ABSTRACT

Title of Thesis: CONTRIBUTIONS TO THE AERODYNAMIC OPTIMIZATION OF A COAXIAL ROTOR SYSTEM

Degree Candidate: Monica Syal

Degree and Year: Masters of Science, 2008

Thesis directed by: Professor J. Gordon Leishman
Department of Aerospace Engineering

The present work analyses the aerodynamic complexities involved in the design of a coaxial rotor system in an attempt to maximize its performance in hover and forward flight. The aerodynamic methodologies of the simple momentum theory (SMT), the blade element momentum theory (BEMT), and a free vortex wake method (FVM) are used to help study this problem. It is shown that because of the inter-rotor aerodynamic interference effects, as well as the requirement of a torque balanced operating condition, the two rotors of the coaxial system generally operate at different thrust and different aerodynamic loadings. Therefore, for an optimally performing coaxial system, the geometric designs of the two rotors can expected to be different. To this end, parametric studies were performed to understand the effects of changes in inter-rotor spacings, blade twist, and blade planforms on both the upper and lower rotors.

A more formal optimization was attempted by coupling FVM with an opti-

mizer to find the best rotor geometry (if any) to maximize the figure of merit in hover or to minimize the total power required in forward flight. It was shown that the performance of the coaxial rotor system can, indeed, be improved significantly by having different blade geometries on the upper and lower rotors. However, it was also shown that the blade twist distribution has more significant effects on the rotor performance as compared to the blade planform shapes. The baseline geometry for all the optimization analyses had untwisted blades on both rotors.

It was shown that a higher inter-rotor spacing is desired to reduce the interference effects between the two rotors in hovering flight. However, the spacing distance can be limited by the increased rotor weight and increased parasitic drag in forward flight. The results also show that a high blade twist is desired on the upper rotor to reduce the induced losses of the coaxial system, whereas a high blade twist on the bottom rotor increases the induced losses of the coaxial system.

In forward flight, the results showed that at high advance ratios the aerodynamic interactions between the two rotors become smaller, and both rotors behave almost as isolated rotors. Parametric studies were also performed to study the effects of changing linear twist rates on both the rotors of the coaxial system in forward flight. The results showed that the total power required at an advance ratio of 0.25 is insensitive to the changes in the blade twist on upper and lower rotors. This outcome also showed that the optimum blade shapes obtained for hovering flight also offered better performance in forward flight.

CONTRIBUTIONS TO THE AERODYNAMIC OPTIMIZATION OF A COAXIAL ROTOR SYSTEM

by

Monica Syal

Thesis submitted to the Faculty of the Graduate School of the
University of Maryland, College Park in partial fulfillment
of the requirements for the degree of
Masters of Science
2008

Advisory Committee:

Professor J. Gordon Leishman, Chairman/Advisor
Professor Roberto Celi
Associate Professor James Baeder

Acknowledgments

I would like to take this opportunity to acknowledge everyone who has helped me in the course of my work in the University of Maryland. I am deeply grateful to my advisor and mentor, Prof. J. Gordon Leishman for critically evaluating my work and always motivating me to look at things from a different perspective. His enthusiasm towards this work always inspired me to give my level best in all respects. I would also like to express my sincere thanks to my committee, Professors James Baeder and Roberto Celi for their support and encouragement. I am specially thankful to Dr. Celi for his constant help in understanding the issues related to optimization. His ideas greatly led to the improvement of the present work. I would like to express my gratitude towards Dr. V. T. Nagaraj for the interesting discussions which helped me to delve deeper into the problem.

I am grateful to Dr. Shreyas Ananthan for his constant help during the course of this research. I am thankful to Dr. Manikandan Ramasamy for the enthusiatic technical discussions. I would also like to thank my friends and colleagues at the Rotorcraft center, Arun, Vinod, Moble, Abhishek, Vikram and Asitav for their help and company over the last two years. Special thanks to my friends Satinder and Neha for always being there for me through all the good and bad times.

Finally this acknowledgment will not be complete without the mention of my parents and siblings who have always supported me and inspired me to work harder.

Table of Contents

List of Tables

List of Figures

NOMENCLATURE

A	Rotor disk area (for one rotor), m^2
A_3	Lower rotor contracted slipstream wake area, m^2
c	Blade chord, m
c_1	Constant used to weight induced power over profile power in optimization
c_0	Blade root chord, m
c_1	Blade tip chord, m
C_d	Sectional drag coefficient
C_{d_0}	Minimum or zero-lift profile drag coefficient
C_l	Sectional lift coefficient
C_{l_α}	Sectional lift-curve-slope, rad^{-1}
C_P	Rotor power coefficient, $= P/\rho A\Omega^3 R^3$
C_Q	Rotor torque coefficient, $= Q/\rho A\Omega^2 R^3$
C_T	Rotor thrust coefficient, $= T/\rho A\Omega^2 R^2$
$C_{T_{\text{req}}}$	Target thrust coefficient of coaxial rotor system
C_W	Weight coefficient, $= W/\rho A\Omega^2 R^2$
d_1, d_2	Coefficients in profile drag equation
dl	Length of a vortex segment, m
dv	Velocity induced at a point P given by Biot–Savart law, ms^{-1}
f	Exponent in Prandtl tip loss function
F	Prandtl tip loss function
F	Objective function used in optimization
FM	Rotor system figure of merit
g	Inequality constraint
H	Equality constraint
i, j, k	Unit vectors along the coordinate axes
I	Influence coefficient matrix used in Weissinger-L model
I	Number of trim iterations required in MFW

I_β	Flapping moment inertia of the blade, kg m^2
$I_{\max}$	Maximum number of iterations allowed for trim in MFW
I_B	Influence coefficient matrix for bound circulation
I_{NW}	Influence coefficient matrix for near-wake circulation
J	Jacobian matrix
k_β	Flapping spring stiffness, Nm rad^{-1}
$\dot{m}$	Mass flow rate, kg/s
M	Number of inequality constraints in optimization problem
M_β	Flapping moment at the blade hinge, Nm
n	Revolutions per second
N	Number of design variables
N_b	Number of blades (for one rotor)
N_s	Number of spanwise segments along the rotor blade
P	Rotor power, kW
P_i	Induced power, KW
P_{ideal}	Ideal (minimum) induced power, KW
Q	Rotor torque, Nm
r	Radial distance of a point on the blade from the rotation axis, m
$\mathbf{r}$	Position vector of collocation point, m
$\mathbf{r}_0$	Initial position vector of collocation point, m
r_b	Radial distance of breakpoint in linear twist distribution on rotor blade, m
$\mathbf{r}_p$	Displacement vector from vortex segment of length dl to point P
r_t	Radial distance of taper starting point on rotor blade, m
R	Rotor radius, m
s	Inter-rotor spacing distance, m
S	Cross-sectional area of the vortex filament, m^2
$\mathbf{S}$, $\mathbf{S}_1$, $\mathbf{S}_2$, $\mathbf{S}_3$	Optimization search directions
t	Time, s
t_0	Initial time, s
T	Rotor thrust, N

TR	Taper ratio on blade
v	Induced velocity, $\mathrm{m\,s^{-1}}$
$\mathbf{V}$	Velocity vector at collocation point, $\mathrm{ms^{-1}}$
V_∞	Axial flight velocity, $\mathrm{ms^{-1}}$
$\mathbf{V}_\infty$	Forward flight speed of the helicopter, $\mathrm{ms^{-1}}$
$\mathbf{V}_B$	Induced velocity component from bound circulation, $\mathrm{ms^{-1}}$
$\mathbf{V}_{FW}$	Induced velocity component from free-vortex trailers, $\mathrm{ms^{-1}}$
$\mathbf{V}_{NW}$	Induced velocity component from near wake trailers, $\mathrm{ms^{-1}}$
$\mathbf{V}_{\mathrm{ind}}$	induced velocity resulting from wake effects, $\mathrm{ms^{-1}}$
w	Slipstream velocity, $\mathrm{ms^{-1}}$
W	Vehicle weight, N
x, y, z	Cartesian coordinates, m, m, m
$\mathbf{x}$	Vector of control input parameters
$\mathbf{X}$	Design variable vector used in optimization
$\mathbf{X}^*$	Optimum design obtained using optimizer
$\mathbf{y}$	Response vector

Greek Symbols

$\overset{\star}{\alpha}$	Number of steps in a given search direction $\mathbf{S}$
β_0	Blade coning angle, rad
β_{1c}	Longitudinal flapping angle, rad
β_{1s}	Lateral flapping angle, rad
β_p	Blade pre-cone angle, rad
Γ	Circulation associated with a vortex filament, $\mathrm{m^2 s^{-1}}$
κ	Rotor induced power factor (single rotor)
κ_{int}	Interference-induced power factor for a coaxial rotor system
λ	Non-dimensional average inflow velocity, $v/\Omega R$
λ_∞	Non-dimensional axial velocity, $\mathbf{V}_\infty/\Omega R$

μ	Advance ratio
ν_β	Non-dimensional rotating blade flapping frequency
ν_h	Hover induced velocity, ms^{-1}
ν_i	Induced velocity, ms^{-1}
$\Delta\zeta$	Discretization along spatial direction, rad
$\Delta\psi$	Temporal or azimuthal discretization, rad
Ω	Rotational speed of the rotor, $\mathrm{rad\,s}^{-1}$
ϕ	Inflow angle, rad
ρ	Air density, $\mathrm{kg\,m}^{-3}$
σ	Rotor solidity, $N_b c/\pi R$
σ_e	Thrust weighted equivalent solidity
θ	Blade pitch, rad
θ	Push-off factor in Method of Feasible Directions
θ_0	Collective blade pitch, rad
θ_{1c}	Lateral cyclic pitch, rad
θ_{1s}	Longitudinal cyclic pitch, rad
θ_{tw}	Linear blade twist, $\mathrm{rad\,m}^{-1}$
θ_{off}	Offset in twist rate at breakpoint, $\mathrm{rad\,m}^{-1}$
ω_0	Non-rotating blade flapping frequency, $k_\beta/I_\beta\Omega^2$, $\mathrm{rad\,s}^{-1}$
ω_β	Rotating blade flapping frequency, $\mathrm{rad\,s}^{-1}$

Subscripts

l	Refers to lower (or rear) rotor
u	Refers to upper (or front) rotor

Superscripts

$\dot{(\,)}$	Time derivative ($= \partial/\partial t$)
$\overset{\star}{(\,)}$	Azimuthal derivative ($= \partial/\partial\psi = \Omega\partial/\partial t$)
coax	Refers to coaxial system
l	Refers to lower (or rear) rotor
u	Refers to upper (or front) rotor
k	Refers to the optimization iteration number

List of Abbreviations

BEMT	Blade Element Momentum Theory
CFD	Computational Fluid Dynamics
DL	Disk Loading
DV	Design Variables
DOT	Design Optimization Tools
FMM	Fast Multipole Methods
FVM	Free Vortex Methods
LHS	Left-Hand Side
MFD	Modified Feasible Directions
MFW	Maryland Free Wake
PC2B	Predictor-Corrector 2^{nd}-order Backward difference
RHS	Right-Hand Side
SLP	Sequential Linear Programming
SQP	Sequential Quadratic Programming
SMT	Simple Momentum Theory
TPP	Tip Path Plane

Chapter 1

Introduction

A coaxial rotor, which is defined as a pair of counter-rotating rotors that spin about a common shaft axis, is not a new concept. This technology dates back to the eighteenth century when the idea of a coaxial rotor was perhaps first conceived by Mikhail Lomonosov of Russia from a pair of counter-rotating Chinese tops. Their device was powered by a string wound around the rotor shaft, and connected to a form of crossbow. The first helicopter patent seems to have been awarded to Henry Bright in 1859 for his coaxial rotor design. Since then, other attempts were made to explore rotary-wing flight using coaxial rotors. The first human-carrying prototype helicopters using coaxial rotors were developed in the 1910s by Ellehammer (Fig. 1.1), Berliner, d'Ascaino (Fig. 1.2), and others. In 1936, Louis Breguet (Fig. 1.3) was to build the first successful helicopter with a coaxial rotor design. References 1 and 2 suggest that since then at least 45 prototype coaxial rotor helicopters have been built, not all of them successful though. The first successful American coaxial helicopter was developed by Hiller Aircraft in 1944 (Ref. 3), although this machine did not progress beyond the prototype stage. The overwhelming success of Sikorsky's single rotor configuration in the early 1940s sidelined all other types of rotor configurations by 1950. Since 1945, the single rotor or conventional configuration has accounted for over 95% of all production

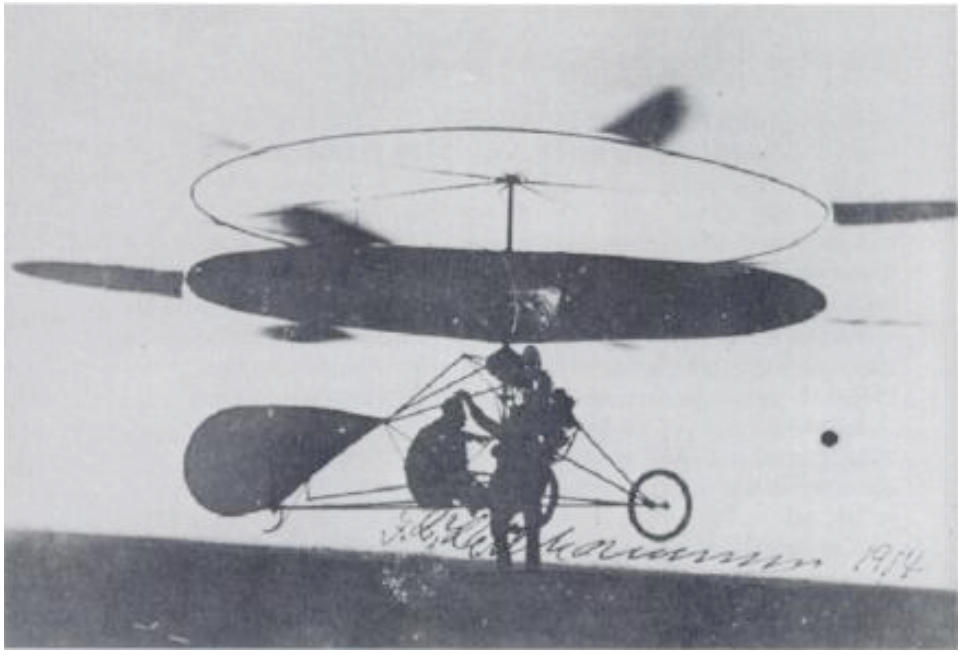

Fig. 1.1: Ellehammer built a coaxial rotor helicopter in 1914. It was the first helicopter ever to be photographed in sustained free-flight, clear of the ground (Ref. 25).

helicopters.

The relative advantages of a coaxial rotor system over a conventional one (i.e., single main rotor and tail rotor configuration) however, continue to attract attention. These advantages include the ability to have a smaller overall rotor diameter to carry a given weight and achieve a given level of performance than would be possible when using a single rotor. Because a coaxial rotor system does not need a separate anti-torque system, there can also be some savings in airframe weight. However, there will always be design trades between the coaxial and conventional helicopter configurations.

In the 1970s, Sikorsky Aircraft used coaxial rotors for its X-59 Advancing Blade Concept (ABC) (Ref. 4), but it never went into production. The Kamov

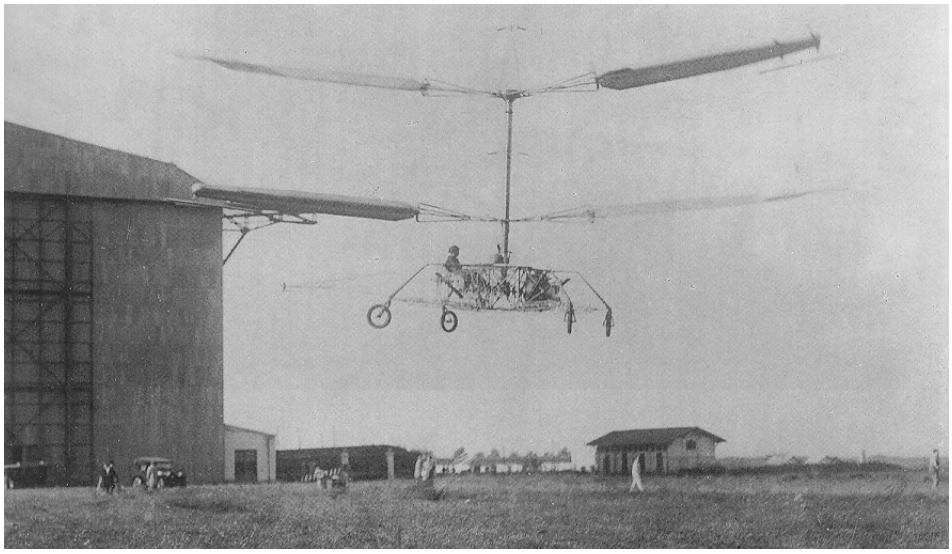

Fig. 1.2: Corradino d' Ascanio's built coaxial machine in 1930, which used servo-tabs to twist the blades and cyclically change their lift (Ref. 25).

Fig. 1.3: The technically successful coaxial helicopter built by Breguet-Dorand in 1935 (Ref. 25).

company from Russia is the only successful producer of coaxial helicopters, starting from Ka-8 in 1947 to the Ka-50 combat helicopter in the 1990s (Ref. 5). With the successful production of the Ka-50 (Fig. 1.4), there has been a renewed interest in the development of coaxial rotor systems, and not just for helicopters. In 2002, Baldwin Technology proposed the use of coaxial proprotor for its Mono Tilt Rotor (MTR) design, which hovers like a helicopter and the rotors tilt forward to act as a propeller in cruise flight—see Ref. 6 and 7 for further details. Sikorsky Aircraft has recently again proposed the use of coaxial rotor for a variety of helicopters, including MAVs, heavy-lift transporters, and a high-speed technology demonstrator (Ref. 12).

The present work is an attempt to further understand the aerodynamics of coaxial rotors, and to develop a robust methodology to optimize the blade geometry of a coaxial rotor to achieve maximum performance in both hover and forward flight. This introductory chapter discusses the motivation behind this work, presents briefly the previous work done on coaxial rotors, defines the targets of the present work, and finally describes the outline of the present thesis.

1.1 Motivation

A coaxial rotor design can offer several significant advantages over the single main rotor tail rotor (i.e., conventional) configuration. Perhaps, the most important of these advantages is the relatively smaller size of a coaxial rotor. Coaxial rotor systems can be made about 30–40% smaller in diameter compared to a single rotor configuration when operating at the same disk loading, despite the fact that two

Fig. 1.4: Kamov Ka-50 (Source: www.richard-seaman.com).

rotors need to be used. The more compact rotor design has proven attractive for prototype micro air vehicles (MAVs) (see Refs. 8 and 11), and for naval purposes where vehicle size or "footprint" is a major constraint. Moreover, with the coaxial design the additional power requirements for the tail rotor to provide anti-torque can now be used to provide vertical lifting capabilities. However, these advantages with the coaxial are offset to some extent by the aerodynamic losses resulting from rotor-on-rotor aerodynamic interference. Furthermore, the downwash flow from a coaxial rotor in hover is higher than that for a single rotor configuration with same disk loading. Therefore, the performance of a coaxial rotor in hover is, at best, comparable to that of a single rotor. There is also a somewhat higher mechanical complexity associated with a coaxial rotor, combined with a relatively higher rotor weight fraction, both of which can be factors that play against the selection of a coaxial rotor system over a single rotor and tail rotor configuration.

A relatively high inter-rotor spacing is generally required to reduce the aerodynamic interference between the two rotors of a coaxial to improve its performance in hover. However, a higher inter-rotor spacing deteriorates the performance significantly in forward flight because of the parasitic drag from the exposed rotor shafts, not to mention other issues such as increased hub and rotor weight. The inter-rotor spacing must also be sufficient enough to avoid blade collisions between the two rotors over the entire operational flight envelope, and this usually demands a relatively high inter-rotor spacing (i.e., as usual on the Kamov helicopters). Considering all these factors, it is obvious that there cannot be one coaxial rotor design that can provide both the best hovering performance and also the best forward flight performance.

The motivation behind the present work was to devise a design methodology that can help to design more efficient coaxial helicopters than those used currently. The principles of optimizing a single rotor system (i.e., using twist, taper and airfoil shapes) is well understood, whereas the optimization of coaxial rotor turns out to be a much more complicated problem. Notice that in a coaxial rotor system (Fig. 1.5), a major portion of the lower rotor operates in the wake from the upper rotor. The coaxial rotor system must also operate at torque balance at any specific thrust condition, so that there is no residual yawing moment on the helicopter. As a result, the induced velocity at the lower rotor is higher compared to that produced on the upper rotor, and also the upper and lower rotors also operate at different thrusts. Therefore, the different flow environments and operating conditions of the two rotors suggests that both rotors of a coaxial rotor system will need to have

Fig. 1.5: Kamov Ka-32 coaxial helicopter, the rotor wake being rendered visible by natural condensation effect, and showing the interference of the flow between the two rotors (Ref. 25).

different geometric designs to maximize its overall performance.

Because the two rotors of a coaxial rotor system are generally operating at torque balanced condition, the thrust carried by the two rotors is different. Generally the lower rotor experiences higher induced losses so that the upper rotor has to carry more thrust to achieve the torque balance. Because the upper rotor also operates at a higher mean lift coefficient, this also means that the stall margins of both the rotors are different if the rotors use the same solidity and airfoil sections. Usually the upper rotor will dictate the stall margin of the rotor system because it shares a greater part of the total thrust. To maintain the stall margins so that neither

rotor by itself will limit performance, an optimum rotor will have to have different solidities on the two rotors, i.e., the upper rotor will need a higher solidity than the lower rotor. This suggests that the planform shapes for the optimum coaxial system will be different for both the rotors. Therefore, it is clear that the performance, and hence any design of the two rotors in a coaxial system, are coupled to each other and a robust and numerically efficient optimization method is required.

1.2 Literature Survey

It is obvious that any design of a coaxial rotor system requires the use of a methodology that can solve accurately for the flow physics in the interference region between the upper and lower rotors. However, this methodology must be computationally expedient to be used in the process of design. This section explains the previous work done to study the aerodynamics of coaxial rotors, and finally leading to the development of the specific methodology to be used in the present work.

1.2.1 Experiments

Coleman (Ref. 13) has presented a good summary of the experimental work performed on coaxial rotors in the United States, Russia, Japan, Britain, and Germany. This report also addresses the issues of rotor separation distance, load sharing ratio between the two rotors, wake structure, blade solidity effects, etc. However, there are only a few experimental measurements available for full-scale rotors. In

1951 at NACA Langley, Harrington (Ref. 14) conducted experiments on two full-scale coaxial rotor geometries to examine their static-thrust performance. Dingeldein (Ref. 15) performed forward flight measurements to measure performance using one of the rotors from Harrington experiments. More recent experimental work on coaxial rotors has been conducted by McAlister et al. (Ref. 9, 10), confirming the difficulties in quantifying coaxial rotor performance and in measuring the nature of the interfering rotor flow fields. Felipe (Ref. 11) has also performed performance measurements on a micro coaxial air vehicle at torque equilibrium for different trim and operating conditions. It was found that the performance of the upper rotor was only marginally affected by the lower rotor at spacings larger than 35% of the rotor radius, and that the upper rotor produced about 60% of the total thrust.

These aforementioned experiments have provided a reasonably good understanding of the aerodynamics of the coaxial rotor systems, along with confirming the higher induced losses and aerodynamically lower efficiency of the lower rotor. However, because of the expensive infrastructure required to set up new experiment with coaxials, the use of numerical methods is highly beneficial for design studies if these methods can be properly validated.

1.2.2 Numerical Studies

Coleman (Ref. 13) provides a discussion on the limited theoretical work performed on coaxial rotor performance. Harrington (Ref. 14) and Dingeldein (Ref. 15)

used the single rotor blade element momentum theory and extended it to coaxial rotors in hover. The results only showed some modest level of predictive capability. Other theoretical analyses of coaxial rotor performance (albeit relatively limited), has been conducted mainly by Andrew (Ref. 16), Saito & Azuma (Ref. 17), Zimmer (Ref. 18), Valkov (Ref. 19) and a few others—again see Coleman (Ref. 13) for a summary of most of the early work.

Leishman (Ref. 20) derived the momentum theory and the blade element momentum theory (BEMT) analysis for coaxial rotors (Refs. 26 and 27) in hover. These analysis have shown very good agreement with experimental results. Leishman (Ref. 20) also used the BEMT to study the aerodynamic issues in the design of a coaxial rotor. Bagai (Ref. 21) used free vortex methods to study the performance of twin rotor systems (i.e., coaxial, tandem and tiltrotors). This approach showed good agreement with wake measurements. Being a three-dimensional analysis, the method solves for the complicated flow physics that are associated with the interference region between the coaxial rotors. This approach is computationally more intensive than the BEMT because it solves for the three-dimensional flow field, but it provides a trimmed solution using only a hour or so of computer time.

Recently, the study of the aerodynamic of coaxial rotors has been performed using computational fluid dynamics (Ref. 24). Despite the advantages in solving for the finer details in the flow field, this methodology cannot be used for design and optimization studies. Specifically, the computational cost required to obtain trimmed solution using Reynolds-Averaged Navier–Stokes (RANS) solver is extremely high for coaxials; it takes about six weeks to find one trimmed solution on a fine grid

using 14 quad-core duo processors. This means that it would take years of computer time to get a rotor design using CFD if it were to be coupled with an optimizer. Secondly, it is known that the CFD solvers have issues with preserving vorticity. This issue becomes more important when the effects of the wake of upper rotor have to be accounted for on lower rotor. Additionally, the generation of the grids required in CFD is a significant challenge. For design studies, the requirement would be to automate the generation of grids, which is still a research area in CFD.

Out of all the above mentioned approaches, the present work uses mainly the free vortex method (FVM) to help to design an optimum coaxial rotor. This is primarily because this approach is computationally faster than CFD but provides a much better fidelity than the BEMT. The FVM provides a complete three-dimensional analysis of the flow field, taking into account the flow physics in the interference region. However, the BEMT was also used in this work to provide the FVM with initial conditions to minimize the overall design time.

1.3 Objectives of the Present Work

The goal of the present work was to devise a methodology with good aerodynamic fidelity to help optimize the performance of coaxial rotors in both hover and forward flight. The specific objectives were:

1. To study the aerodynamics of the coaxial rotor system using the BEMT and FVM. This involved validating the FVM methodology, and examining through parametric studies the effects of blade twist, taper, rotor spacing and thrust

sharing on the performance of coaxial rotor systems.

2. To develop a design methodology to help determine the optimum coaxial rotor geometry to achieve a given level of performance. Considering the various interdependent factors that will determine the performance of a coaxial rotor as a system, this process was approached using a formal optimization method.

3. The final objective was to examine different blade twist and taper distributions to optimize the geometries of both the rotors of the coaxial system in hover and in forward flight to achieve the best levels of performance.

1.4 Outline of Thesis

This thesis is divided into five chapters. The first chapter describes the need for the optimization of the blade geometry for a coaxial rotor. It discusses previous work done to help understand the aerodynamics and performance of coaxial rotors, and explains the objectives of the present work. The second chapter describes the mathematical and numerical methodology used to study the problem of coaxial rotor optimization. This methodology includes the use of the simple momentum theory, blade element momentum theory, and free vortex methods. The present work uses the free vortex method called the MFW, developed at the University of Maryland (see Ref 22). This chapter then explains the coupling between the Maryland Free Wake (MFW) and an optimization method called design optimization tools (DOT). The third chapter discusses the formulation of the optimization problem for the coaxial rotor system. This chapter explains the manner with which the different

optimization parameters are defined in the present work. The fourth chapter discusses the numerous results that were found in the present study. The fifth and final chapter of this thesis gives a summary of the conclusions drawn from the present study, and recommendations for future research are also discussed.

Chapter 2

Methodology

Overview

This chapter discusses the mathematical models used to study the aerodynamics and performance of coaxial rotor systems, and the manner in which these models were used in the blade shape optimization study. The coaxial rotor problem was first approached using the Simple Momentum Theory (SMT) and the Blade Element Momentum Theory (BEMT), followed by a more advanced Free Vortex Method (FVM). The SMT and BEMT are mathematically parsimonious, computationally expedient, and reasonably well-validated against performance measurements. More importantly, these models provide a robust modeling basis from which to initiate a rotor design solution for further analysis. The FVM method has also been well validated, although it is considerably more computationally expensive than either of the SMT or the BEMT. The FVM also forms a robust and aerodynamically more rigorous basis to perform an optimization process, but it requires a good initial condition to both ensure convergence and to conserve computer time. These initial conditions were mostly obtained using the BEMT.

After studying the aerodynamics of the coaxial rotor system, the optimization of its geometry to give maximum aerodynamic efficiency in hover was attempted by coupling the FVM with a formal optimization method called Design Optimization

Tools (DOT). This chapter is divided into five sections. The first four sections discuss the SMT, BEMT, FVM and DOT, respectively, and the final section describes the coupling process between the FVM and DOT.

2.1 Simple Momentum Theory Analysis of Coaxial Rotors

The Simple Momentum Theory (SMT) provides the most parsimonious flow model to study the hovering performance of a coaxial rotor system. The main assumptions behind the derivation of the SMT for coaxial rotors are essentially those used for single rotors. First and foremost, the flow field is assumed to be one-dimensional, incompressible, and inviscid. While perhaps relatively sweeping assumptions, the validity of the SMT has been well-proven for the performance analysis of helicopter rotors. The main advantage of the SMT, however, is that it provides results for the minimum power consumption of the rotor(s) under a given set of conditions, and so provides a datum against which the efficiency of a real rotor can be measured. When extended to a model coaxial rotor at a given operating condition (e.g., at a total system thrust), the SMT can provide estimates of the thrust and power sharing between the two rotors for a specified trim state, e.g., at a given total system thrust and at a torque balanced condition.

The control volume assumed with the SMT starts above the upper rotor and ends below the lower rotor of coaxial system, and is limited on the sides by the edges of the two rotor disks, as shown in Fig. 2.1. The equations of mass, momentum and energy conservation in integral form are used to derive the thrust and power

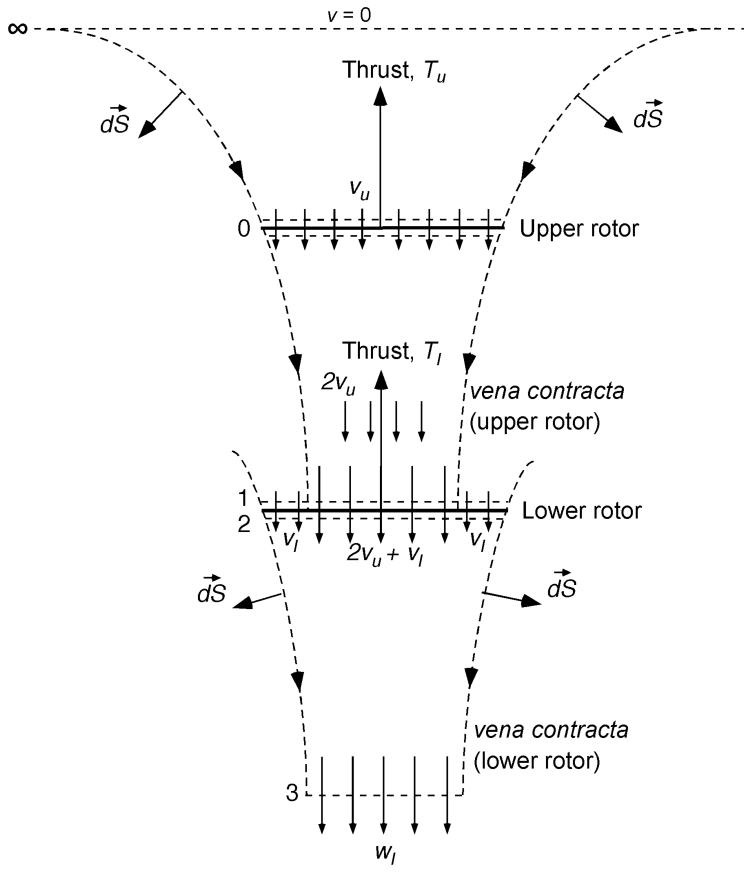

Fig. 2.1: Flow model showing the coaxial rotor system with lower rotor in the vena contracta of the upper rotor (Ref. 26).

expressions for the coaxial rotor. The losses determined from the SMT analysis are all induced in nature and hence, as previously mentioned, the results obtained from this theory represent the datum against which to measure the operating efficiency of a coaxial rotor system.

The four primary cases of interest for the analysis of the coaxial rotors are:

Case 1: The two rotors rotating in the same plane (practically, they would be very near to each other with minimal rotor spacing) and operated at equal thrusts.

Case 2: The two rotors in the same plane of rotation and operated at equal and

opposite torques, i.e., at a torque balance.

Case 3: The two rotors rotating at equal thrusts, with the lower rotor operating in the fully developed slipstream of the upper rotor.

Case 4: Two rotors rotating at equal and opposite torques, with the lower rotor in the fully developed slipstream (i.e., the *vena contracta*) of the upper rotor.

Reference 26 gives a detailed discussion and a full derivation of all of these cases in terms of the induced power requirements, as well as the thrust sharing. Practically, there is always a finite spacing between the two rotors in a coaxial system to avoid blade collisions between the two rotors. Also, the two rotors will generally operate at equal and opposite torques to provide zero net torque to the helicopter when it is operating in steady flight conditions. Therefore, for all the cases mentioned above, Case 4 is of primary practical importance, and so it is discussed in this thesis in more detail. However, solutions for all the cases are required to assess the effects of the rotor-on-rotor spacing on the performance of the coaxial rotor system.

Figure 2.1 shows the flow field of a coaxial rotor with the lower rotor operating in the *vena contracta* of the upper rotor. Thrusts shared by upper and lower rotors are represented by T_u and T_l, respectively. Because, the upper rotor is not directly affected by the wake of the lower rotor, it can be treated as a single rotor that is connected to the lower rotor only through the need for a torque balance. The

induced velocity and the work done by the upper rotor are given by

$$v_u = \sqrt{\frac{T_u}{2\rho A}} \tag{2.1}$$

and

$$P_u = 2\rho A v_u^3 \tag{2.2}$$

respectively.

Because the lower rotor is placed in the fully developed slipstream of the upper rotor, the velocity on the inner half region of the lower rotor is $(2v_u + v_l)$ and on the outer half it is v_l (see Fig. 2.1). The total mass flow rate through the lower rotor is given as

$$\dot{m} = \rho\frac{A}{2}(2v_u + v_l) + \rho\frac{A}{2}v_l = \rho A(v_u + v_l) \tag{2.3}$$

Therefore, the average of the induced velocity through the lower rotor is simply $(v_u + v_l)$. In Fig. 2.1, the slipstream velocity from the coaxial system is represented by w_l. By means of momentum conservation, the thrust on the lower rotor is given by

$$T_l = \rho A(v_u + v_l)w_l - 2\rho A v_u^2 \tag{2.4}$$

The work done on the air by the lower rotor can be written as

$$P_l = T_l(v_u + v_l) \tag{2.5}$$

The increase in the kinetic energy of the flow through the lower rotor is

$$T_l(v_u + v_l) = \frac{1}{2}\rho A(v_u + v_l)w_l^2 - \frac{1}{2}\rho A v_u(2v_u)^2 \tag{2.6}$$

Because in Case 4 both of the rotors are operating with equal and opposite torques (i.e., at a torque balance), then

$$T_u v_u = T_l(v_u + v_l) \tag{2.7}$$

Multiplying Eq. 2.4 by $v_u(v_u + v_l)$ and also using Eq. 2.5 gives

$$P_l \left(2v_u + v_l\right) = \rho A \left(v_u + v_l\right)^2 v_u w_l \tag{2.8}$$

Using $P_u = 2\rho A v_u^3 = P_l$ in Eq. 2.6 gives

$$P_l = \frac{1}{4}\rho A \left(v_u + v_l\right) w_l^2 \tag{2.9}$$

Substituting Eq. 2.9 into Eq. 2.8 and rearranging gives

$$w_l = 4v_u \left(\frac{v_u + v_l}{2v_u + v_l}\right) \tag{2.10}$$

Substituting w_l in Eq. 2.6 and solving gives $v_l = 0.4375 v_u$. The thrust sharing ratio is then

$$\frac{T_u}{T_l} = \frac{v_u + v_l}{v_u} = 1 + \frac{v_l}{v_u} = 1.4375 \tag{2.11}$$

It is interesting to note that the slipstream velocity in this case becomes $w_l = 2.359 v_u = 1.64(v_u + v_l)$, and the slipstream area A_3 becomes $0.6096A$. This means that the area of the fully contracted slipstream is not as much as that obtained for a single rotor (which is $0.5A$), i.e., it is greater in this coaxial rotor case (i.e., Case 4) by 22%.

To quantify the rotor-on-rotor interference losses with coaxial rotors, an interference-induced power factor, κ_{int}, is introduced, as discussed in Ref. 20. This factor relates the performance of a coaxial rotor system to two isolated rotors operating separately but at the same disk loading as for the two rotors of the coaxial system. The interference-induced factor can be defined as

$$\kappa_{\text{int}} = \frac{(P_i)_{\text{coax}}}{(2P_i)_{\text{isolated}}} \tag{2.12}$$

The interference factor, κ_{int}, in Case 4 can be obtained in two ways for the same specified disk loading:

Case 4a

In this case, the basis of comparison is with two isolated rotors, each operating at thrust, T, where $2T = T_u + T_l$. The interference-induced power factor can be written as

$$\kappa_{\text{int}} = \frac{(P_i)_{\text{coax}}}{(2P_i)_{\text{isolated}}} = \frac{P_u + P_l}{2T\sqrt{\dfrac{T}{2\rho A}}} = \frac{P_u + P_l}{2\left(\dfrac{T^{3/2}}{\sqrt{2\rho A}}\right)} \tag{2.13}$$

Now, $P_u = P_l$ at the torque balance, and also $T = (T_u + T_l)/2$ and $T_u/T_l = 1.4375$, so that

$$\kappa_{\text{int}} = \frac{2P_u}{2\dfrac{\left(\dfrac{T_u + T_l}{2}\right)^{3/2}}{\sqrt{2\rho A}}} = 2\sqrt{2}\left(\frac{T_u}{T_l}\right)^{3/2}\left(1 + \frac{T_u}{T_l}\right)^{-3/2} = 1.2810 \tag{2.14}$$

Case 4b

In this case, the basis of comparison is with two isolated rotors, each operating at thrust equal to that shared by the upper and lower rotors (i.e., T_u and T_l, respectively) of the coaxial system at torque balance. Therefore, the disk loadings of the isolated single rotors and the coaxial rotor are same. The interference-induced power factor in this situation is

$$\kappa_{\text{int}} = \frac{(P_i)_{\text{coax}}}{(2P_i)_{\text{isolated}}} = \frac{P_u + P_l}{\dfrac{T_u^{3/2}}{\sqrt{2\rho A}} + \dfrac{T_l^{3/2}}{\sqrt{2\rho A}}} \tag{2.15}$$

Table 2.1: Summary of minimum interference-induced power factors for coaxial rotors operating under different conditions.

Case No.	Interference induced power factor, k_{int}
1	1.4142
2	1.4142
3	1.2808
4a	1.2810
4b	1.2657

Again, $P_u = P_l$ at the torque balance, so that

$$\begin{aligned} \kappa_{\text{int}} &= \frac{2P_u}{\frac{T_u^{3/2}}{\sqrt{2\rho A}} + \frac{T_l^{3/2}}{\sqrt{2\rho A}}} = \frac{2T_u^{3/2}}{T_u^{3/2} + T_l^{3/2}} \\ &= \frac{2\left(\frac{T_u}{T_l}\right)^{3/2}}{\left(\frac{T_u}{T_l}\right)^{3/2} + 1} = 1.2657 \end{aligned} \tag{2.16}$$

In this case, the value of κ_{int} is slightly lower than that found in the previous case where both the isolated rotors shared equal thrust.

Table 2.1 gives a summary comparison of the induced interference-factors for the coaxial rotors in each of the assumed cases. For detailed derivations of κ_{int} in the first three cases—see Ref. 26. Table 2.1 shows that for Cases 1 and 2 when the planes of rotation of the two rotors are coplanar, κ_{int} has a maximum value of 1.414

(or $\sqrt{2}$). As rotor spacing spacing increases, the interference losses between the two rotors decrease. For the case in which the lower rotor is placed in the fully developed slipstream of the upper rotor, κ_{int} reaches a minimum value of 1.265. These results from the SMT now set the datum to perform comparisons of efficiency with real coaxial rotors.

2.2 Blade Element Momentum Theory

The Blade Element Momentum theory (BEMT) is a hybrid analysis based on an equivalence between the circulation and momentum theories of lift. Initially developed for airplane propellers, it was first used for helicopters by Gustafson & Gessow (Ref. 29). Unlike the SMT, which assumes that the inflow must be uniform over the rotor disk (i.e., a one-dimensional theory), the BEMT solves for the non-uniform inflow over the rotor blades (i.e., it is a two-dimensional theory). It is assumed that the successive annuli on any one rotor disk have no mutual impact on each other.

The assumed BEMT flow model is shown in Fig. 2.2, with the lower rotor placed in the *vena contracta* of the upper rotor. Because, the wake of the upper rotor is not directly affected by the wake of the lower rotor, its inflow equation can be obtained using the same principles of the BEMT that have been developed for a single rotor (see Ref. 27) operating in the axial climb velocity, V_∞, and is written as

$$\lambda_u(r,\lambda_\infty) = \sqrt{\left(\frac{\sigma_u(r)\ C_{l_\alpha}}{16F} - \frac{\lambda_\infty}{2}\right)^2 + \frac{\sigma_u(r)\ C_{l_\alpha}}{8F}\theta_u(r)r} - \left(\frac{\sigma_u(r)\ C_{l_\alpha}}{16F} - \frac{\lambda_\infty}{2}\right) \quad (2.17)$$

where $\theta_u(r)$ and $\sigma_u(r)$ are the blade pitch and solidity distributions, respectively, at

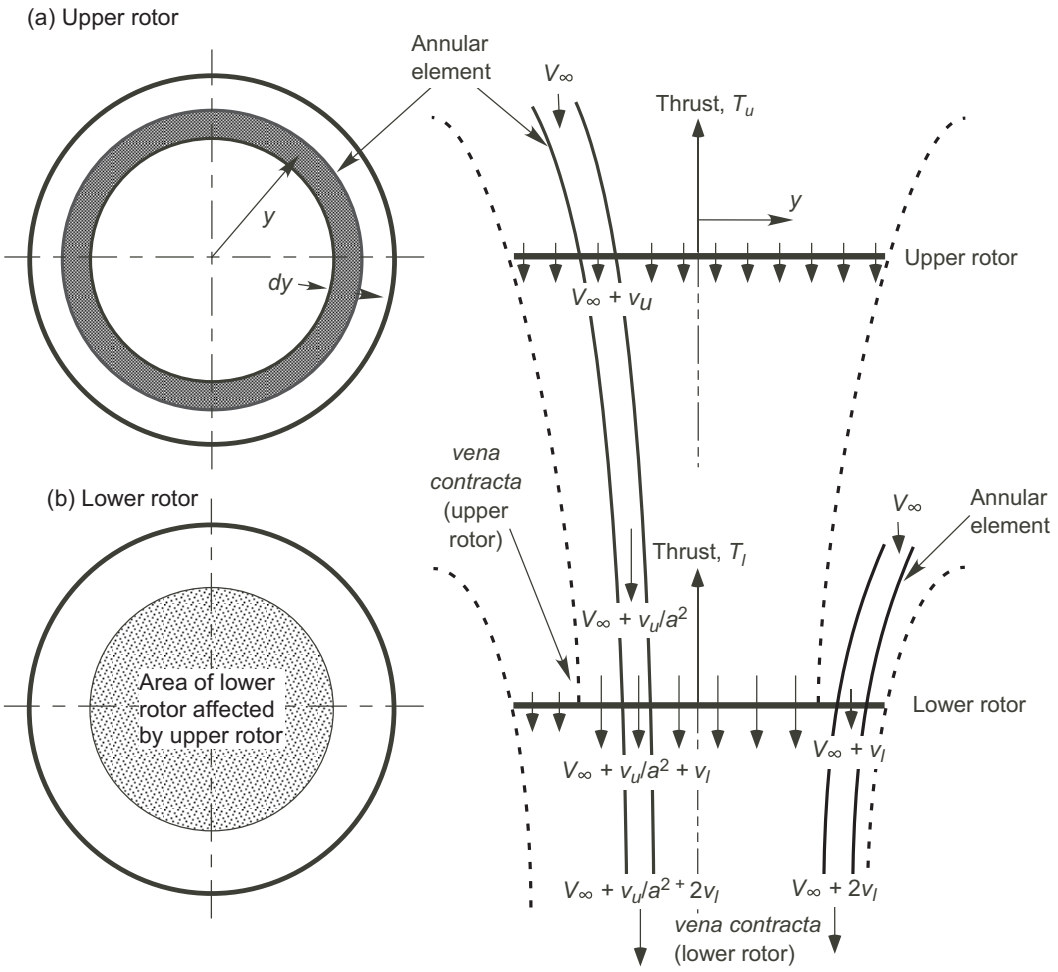

Fig. 2.2: Flow model used for the BEMT analysis (Ref. 20).

any radial section on the upper rotor. The blade tip loss effects are included in the present analysis using Prandtl tip-loss function—see Ref. 27. The final result can be expressed in terms of a correction factor, F, as

$$F = \left(\frac{2}{\pi}\right)\cos^{-1}\left(\exp(-f)\right) \tag{2.18}$$

where f is given in terms of the number of blades N_b and the radial position of the blade element, r, by

$$f = \frac{N_b}{2}\left(\frac{1-r}{r\phi}\right) \tag{2.19}$$

and ϕ is the inflow angle, which is given by $\lambda(r)/r$ for a small angle approximation. Notice that the expression for F depends upon the rotor inflow, so Eqs. 2.17, 2.18 and 2.19 are solved iteratively starting from $F = 1$ and then updating its value over subsequent iterations until convergence is achieved.

Only a part of the lower rotor operates in the slipstream generated by the upper rotor. Therefore, the lower rotor can be modeled as an isolated rotor, operating partially in the axial climb velocity equal to the slipstream velocity of the upper rotor. The slipstream velocity, w_u, from the upper rotor depends upon the slipstream area, A_c, and can be written, using continuity assumptions, as

$$w_u = V_\infty + \left(\frac{A}{A_c}\right) v_u \tag{2.20}$$

In the ideal case, the slipstream area is $\frac{A}{2}$, which means that axial velocity into the inner region of the lower rotor is $V_\infty + 2v_u$.

Applying the principles to the lower rotor, its inflow equation can be written as

$$\begin{aligned} \lambda_l(r, \lambda_\infty) \;\; = \;\; & \sqrt{\left(\frac{\sigma_l(r)\; C_{l_\alpha}}{16F} - \frac{\lambda_u}{2}\right)^2 + \frac{\sigma_l(r)\; C_{l_\alpha}}{8F}\theta_l(r)r} \\ & - \left(\frac{\sigma_l(r)\; C_{l_\alpha}}{16F} - \frac{\lambda_\infty + (A/A_c)\lambda_u}{2}\right) \quad \text{for } r \leq r_c \end{aligned} \tag{2.21}$$

where r_c is the assumed wake contraction radius of the upper rotor when it impinges the lower rotor, i.e., $r_c = 0.707$ in the ideal case, and θ_l is the blade pitch distribution on the lower rotor. For points outside the area, A_c, that are unaffected by the upper

rotor (i.e., for $r > r_c$), the inflow distribution is given by solving

$$\lambda_l(r, \lambda_\infty) = \sqrt{\left(\frac{\sigma_l(r)\ C_{l_\alpha}}{16F} - \frac{\lambda_\infty}{2}\right)^2 + \frac{\sigma_l(r)\ C_{l_\alpha}}{8F}\theta_l(r)r} - \left(\frac{\sigma_l(r)\ C_{l_\alpha}}{16F} - \frac{\lambda_\infty}{2}\right) \quad \text{for } r > r_c \tag{2.22}$$

After finding the inflow distribution over both the rotors, the thrust and power for each can be found by integrating the airloads along the blade. The thrust on the upper rotor is

$$C_{T_u} = \int_{r=0}^{r=1} dC_{T_u} = \frac{1}{2}\int_r^1 \sigma_u\ c_l\ r^2\ dr, \tag{2.23}$$

with the corresponding power as

$$C_{P_u} = \int_{r=0}^{r=1} \lambda_u\ dC_{T_u} + \int_0^1 \frac{1}{2}\sigma_u\ C_d r^3\ dr \tag{2.24}$$

The thrust on the lower rotor is

$$C_{T_l} = \int_{r=0}^{r=1} dC_{T_l} = \frac{1}{2}\int_0^1 \sigma_l\ c_l\ r^2\ dr, \tag{2.25}$$

with the power given by

$$C_{P_l} = \int_{r=0}^{r=1} \lambda_l\ dC_{T_l} + \int_0^1 \frac{1}{2}\sigma_l\ C_d r^3\ dr \tag{2.26}$$

Because the coaxial rotor system operates at the torque balance condition at a specified system thrust, these two conditions (i.e., thrust balance and torque balance) must be satisfied to obtain the trimmed solution. More information on the trim methodology is given in Section 2.3.3. The collective angles on both the rotors

are adjusted iteratively until the required thrust and torque balance conditions are satisfied.

The BEMT provides a very efficient and effective tool to study the aerodynamics of coaxial rotors with different planform shapes and twist distributions. Reference 20 gives a detailed analysis of the use of the BEMT to help find an optimum design of the blade shapes. In the present study, this methodology has been used to better understand the aerodynamics of coaxial rotors, and thus help to further optimize the shapes of the two rotors. However, because of the complexity of the flow physics involved in the interference region, this problem was studied in more detail using a free-vortex wake analysis, as explained in the following section.

2.3 Free-Vortex Method

Free-vortex wake models solve for the vortex strengths in the evolving wake geometry. The vortex field behind each blade is represented by trailing vortex filaments. Experiments have shown that tip vortices form the dominant structures inside the vortex wake—see Ref. 25. Therefore, for the present work, the far wake below the rotor was approximated by modeling only the tip vortices. Correlation studies have also shown a very good agreement between experimental results and the FVM results by modeling only the tip vortices. This assumption also reduces the computational cost significantly by limiting the number of velocity field computations that are performed using the Biot–Savart law.

In the FVM, the curved tip vortex filaments are discretized into straight line

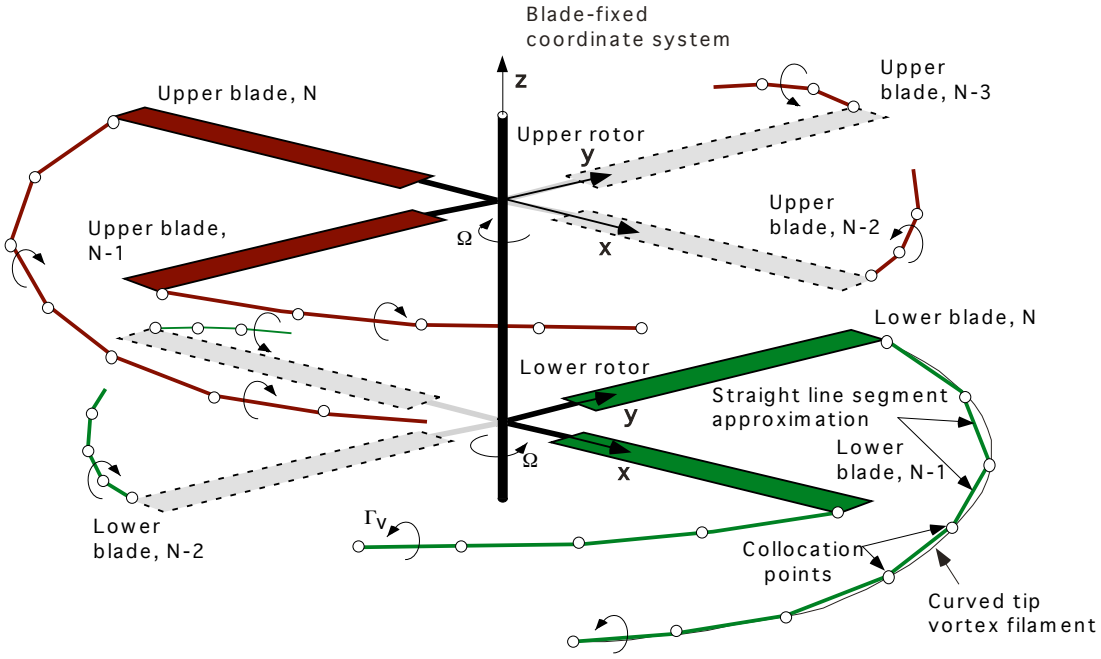

Fig. 2.3: Schematic showing the wake of the coaxial rotor system.

segments by linking the Lagrangian markers used to represent the flow field. Figure 2.3 shows the tip vortex filaments of the coaxial rotor system discretized using Lagrangian markers. Reference 30 shows that the induced velocity field computed using straight-line segmentation of the vortex filaments is second-order accurate when sufficiently high levels of discretizations are used. The initial strength of the vortex filaments is governed by blade loading, i.e., by the distribution of circulation over the blades. Solving for the wake geometry at different blade azimuth locations, coupled with the computation of the induced velocity field and its effects on the rotor blades, defines the free wake solution.

2.3.1 Blade Aerodynamic Model

The rotor is modeled using N_b blades, which are assumed to be rigid beams, but can execute fully independent flapping motion in a time-accurate manner. The rotor blades are modeled using a Weissinger-L model—see Ref. 31—which is essentially a lifting surface model with one chordwise element. This model represents the blades with multiple horseshoe vortices. Each blade is divided into N_s spanwise segments, and the bound vortex strength along each segment is assumed to be constant. The bound vortex is located at blade 1/4-chord, and the flow tangency condition is applied at 3/4-chord—see Fig. 2.4. While the bound vortex strength is constant along each blade segment, it is allowed to vary from one segment to another. Therefore, circulation must be trailed at the ends of each segment. The strengths of the trailers can be found out by using Helmholtz laws of conservation of vorticity at the end of j^{th} blade segment, and is given by

$$\Gamma_t|_j = \Gamma_b|_j - \Gamma_b|_{j+1} \tag{2.27}$$

In the FVM, the trailed vorticity system comprises two parts: a near wake and a far wake. The near wake trailers are assumed to be rigid and fixed to the blade, and are truncated at $\Delta\psi = 30°$. The far wake consists of tip vortex (a root vortex can also be modeled if required) released from each blade tip. Shed vorticity can be modeled as additional filaments, but this too adds to the computational cost. Therefore, unsteady effects resulting from changes in the angle of attack are modeled using the indicial method—see Ref. 32 for a detailed description.

The strength of the bound circulation along the blade span is calculated by

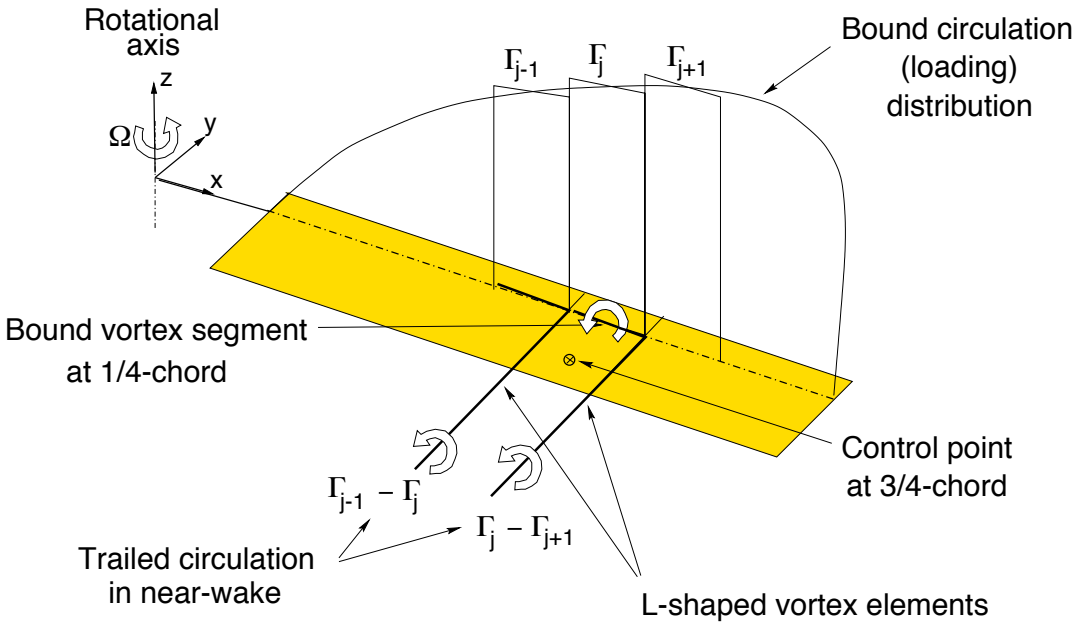

Fig. 2.4: Schematic of the Weissinger-L model used to represent the blade (Ref. 32).

satisfying flow tangency at the blade control points. This means that the component of incident velocity perpendicular to the i^{th} blade segment at the 3/4-chord position is exactly zero, i.e.,

$$\mathbf{V}_i \cdot \mathbf{n}_i = 0 \qquad i = 1, 2, ..., i_{max} \tag{2.28}$$

where $\mathbf{V}_i = \mathbf{V}_\infty + \mathbf{V}_{man} + \mathbf{V}_B + \mathbf{V}_{NW} + \mathbf{V}_{FW}$. The far wake velocity ($\mathbf{V}_{FW}$), and maneuver velocity ($\mathbf{V}_{\text{man}}$), are calculated using the Biot–Savart law. Notice that the velocities induced by the bound vortex ($\mathbf{V}_B$), and the near wake trailers ($\mathbf{V}_{NW}$) at the blade control points depend upon the bound circulation strength, and are computed using influence coefficient matrices.

The velocity induced by the bound vortex segment of strength Γ_j at the i^{th}

blade control point can be expressed as

$$V_{B_i} = \sum_{j=1}^{N_s} I_{B_{ij}} \Gamma_j \tag{2.29}$$

and the velocity induced by the near wake trailer at an i^{th} blade control point can be expressed as

$$V_{NW_i} = \sum_{j=1}^{N_s} I_{NW_{ij}} \Gamma_j \tag{2.30}$$

The influence coefficient matrices, I_B and I_{NW}, depend on the blade geometry—see Ref. 31 for details. Substituting Eqs. 2.29 and 2.30 into Eq. 2.28 gives

$$[I]\{\Gamma_j\} = \{(\mathbf{V}_\infty + \mathbf{V}_{man} + \mathbf{V}_{FW}) \cdot n\}_i \tag{2.31}$$

The bound circulation is thus obtained by the inversion of the influence coefficient matrix, I, i.e.,

$$\{\Gamma_j\} = [I]^{-1}\{(\mathbf{V}_\infty + \mathbf{V}_{man} + \mathbf{V}_{FW}) \cdot n\}_i \tag{2.32}$$

After calculating the bound vortex strength, the blade lift distribution can be computed using Kutta–Joukowski (K–J) theorem. The profile drag is computed using Beddoes' two-dimensional, non-linear airfoil model—see Ref. 33. Blade flapping moments, rotor thrust, and torque are obtained by integrating the airloads over all the segments and around the rotor azimuth.

Notice that blade flapping depends upon the blade aerodynamic response, and hence on the wake solution. Also, the wake blade attachment boundary condition is determined by the blade flapping response. This necessitates the coupling of the blade flapping to the rotor wake solution. Because the blade is assumed to be rigid

and undergoing flapping about a hinge, the flapping equation is given by

$$\overset{\star\star}{\beta} + \nu_\beta^2 \beta = \frac{M_\beta}{I_\beta \Omega^2} + \frac{\omega_0^2}{\Omega^2} \beta_p \tag{2.33}$$

Equation 2.33 can also be written as a set of first-order ordinary differential equations (ODEs) in the matrix form as Eq. 2.34—see Ref. 34 for details.

$$\frac{d}{d\psi} \begin{Bmatrix} \overset{\star}{\beta} \\ \beta \end{Bmatrix} + \begin{bmatrix} \nu_\beta^2 & 0 \\ 0 & 1 \end{bmatrix} \begin{Bmatrix} \overset{\star}{\beta} \\ \beta \end{Bmatrix} = \begin{Bmatrix} \frac{M_\beta}{I_\beta \Omega^2} + \frac{\omega_0^2}{\Omega^2} \beta_p \\ 0 \end{Bmatrix} \tag{2.34}$$

Equation 2.34 is solved by a technique that is explained in the following section.

2.3.2 Free-Wake Solution

The crux of a free-vortex method is to model the convection of vorticity in the wake as accurately as possible. This is achieved by tracking Lagrangian markers. These markers are placed on the vortex filaments, and are linked to each other using straight line segmentation. The vortex filaments are modeled in the manner shown in Fig. 2.5. The movement of the Lagrangian markers is governed by the three-dimensional, incompressible Navier–Stokes equations, which can be written in the form of the vorticity transport equation, as given in Eq. 2.35, i.e.,

$$\frac{D}{Dt} (\vec{\omega}) = \left(\vec{\omega} \cdot \vec{\nabla} \right) \vec{V} + \nu \Delta \cdot \vec{\omega} \tag{2.35}$$

This equation determines the rate of change of vorticity of a fluid element in terms of the instantaneous values of vorticity $\vec{\omega}$ and velocity $\vec{V}$. The left-hand-side term gives the substantive derivative of vorticity, which provides both time rate-of-change of vorticity and its convection rate. The first term on the right-side of Eq. 2.35 is

the strain term. This term provides the change in the length of vortex filament as it is convected. The second term on the right-side of Eq. 2.35 gives the diffusion of vorticity because of the viscosity of the fluid.

In the free-wake modeling, the vorticity is confined within the tip vortex, and the flow outside is assumed to be inviscid. Therefore, under the assumptions of incompressible, inviscid and irrotational flow, Eq. 2.35 reduces to

$$\frac{d}{dt}(\mathbf{r}) = \mathbf{V}(\mathbf{r}) \tag{2.36}$$

and gives the motion of fluid particles on the vortex filaments in the local velocity field $\mathbf{V}$—see Ref. 34.

The vector $\mathbf{r}$ in Eq. 2.36 gives the position of the Lagrangian markers in the vortical wake. In the blade fixed coordinate system, the time rate of change of fluid elements can be expressed in terms of rate of change of $\mathbf{r}$ with blade azimuth, ψ (temporal) and wake-age, ζ (spatial). Therefore, Eq. 2.36 can be written in the form of a partial differential equation as

$$\frac{\partial \mathbf{r}}{\partial \psi} + \frac{\partial \mathbf{r}}{\partial \zeta} = \frac{\mathbf{V}}{\Omega} \tag{2.37}$$

This equation is solved using finite difference approximations. The vortex field is discretized in space and time with step sizes of $\Delta\zeta$ and $\Delta\psi$, respectively. The right-hand side of Eq. 2.37 comprises of the local velocity vector at any point in the flow field, which includes free-stream effects (i.e., $\mathbf{V}_\infty$) and induced effects (i.e., $\mathbf{V}_{\text{ind}}$) resulting from wake effects (including rotor-on-rotor interference), the bound circulation on the blade, and possible flight maneuvers (not considered in

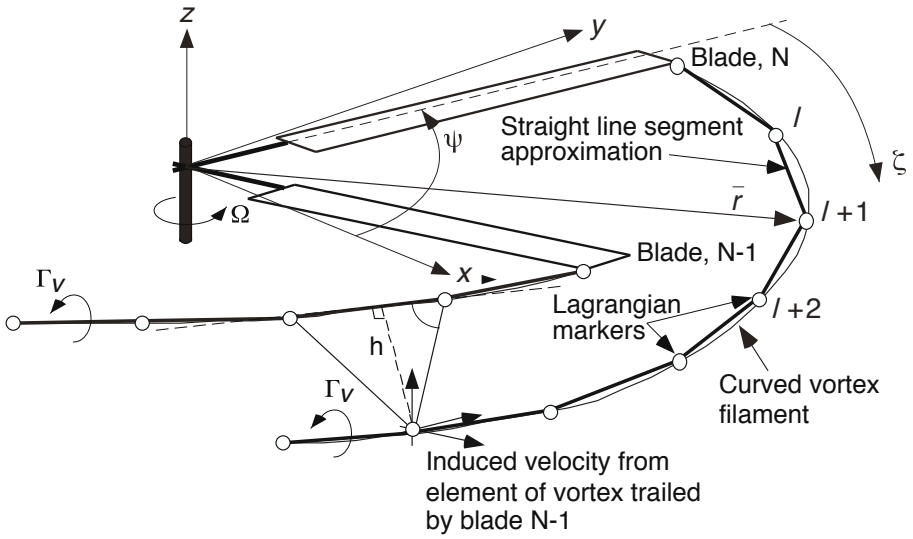

Fig. 2.5: Schematic showing the Lagrangian markers used to represent the rotor wake. Source: Ref. 35.

this thesis). The finite difference equation can be written in the form

$$D_\psi(\mathbf{r}) + D_\zeta(\mathbf{r}) = \frac{\mathbf{V}_\infty}{\Omega} + \frac{1}{\Omega}\sum_{j=1}^{j=N_v} \Delta\mathbf{V}_{\mathrm{ind}_j} \tag{2.38}$$

Equation 2.38 is solved in the present analysis using time-accurate, predictor-corrector (PC2B) scheme, developed by Bhagwat (Ref. 35) at the mid-point of each grid cell (i.e., at $\psi + \Delta\psi/2, \zeta + \Delta\zeta/2$), as shown in Fig. 2.6. This algorithm uses five-point central discretization in space and two-point backwards discretization in time, as given by Eqs. 2.39 and 2.40, respectively. These numerical approximations are second-order accurate in space and time.

$$D_\zeta(\mathbf{r}) = \frac{\mathbf{r}(\psi+\Delta\psi,\zeta+\Delta\zeta) + \mathbf{r}(\psi,\zeta+\Delta\zeta) - \mathbf{r}(\psi+\Delta\psi,\zeta) - \mathbf{r}(\psi,\zeta)}{2\Delta\zeta} \tag{2.39}$$

$$D_\psi(\mathbf{r}) = \frac{3\mathbf{r}(\psi+\Delta\psi,\zeta) - \mathbf{r}(\psi,\zeta) - 3\mathbf{r}(\psi-\Delta\psi,\zeta) + \mathbf{r}(\psi-2\Delta\psi,\zeta)}{4\Delta\psi} \tag{2.40}$$

The self- and mutually-induced velocities on the right-hand side of Eq. 2.38

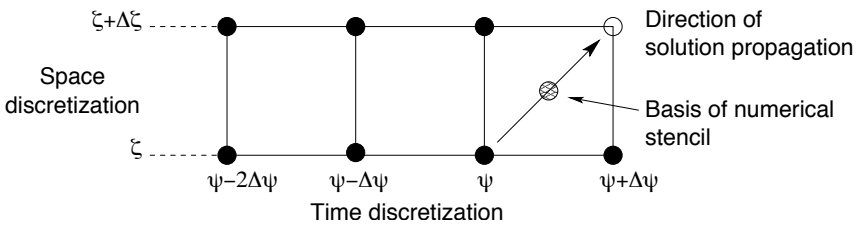

Fig. 2.6: Schematic showing the stencil for PC2B finite difference approximation. (Ref. 32).

from the N_v vortex filaments are approximated by using Biot–Savart law (Ref. 36,Ch. 2, pp. 93–94). The Biot–Savart law gives the velocity induced by a vortex segment of length dl and strength Γ_v, at a point P, which is at a distance $\mathbf{r}_p$ from the vortex filament as

$$d\vec{v} = \frac{\Gamma_v}{4\pi}\left(\frac{d\vec{l}\times\mathbf{r}_p}{|\mathbf{r}_p|^3}\right) \tag{2.41}$$

Then the total induced velocity at point P is integrated as given in Eq. 2.38.

2.3.3 Rotor Trim Methodology

The aerodynamic response of a coaxial rotor is a highly coupled function of the blade control angles, the resulting aerodynamic environment at the rotors, and their aerodynamic interference. Changes in the blade collective also affect the flapping response of each rotor, and the changes in the blade cyclic affect the total rotor thrust and thrust sharing between the rotors of a coaxial. The coaxial rotors must be trimmed to obtain a converged solution at a torque balance condition. The following trim methodology considers an isolated coaxial rotor system without the effects of a fuselage. The procedure is based on the Newton–Raphson method, and

is the same as discussed in Ref. 32.

2.3.3.1 Single Rotor Trim Methodology

The rotor control input vector, $\mathbf{x}$, comprising of blade collective θ_0 lateral cyclic θ_{1c} and longitudinal cyclic θ_{1s} angles (i.e., $\mathbf{x} = \{\theta_0, \theta_{1c}, \theta_{1s}\}^T$), is updated in the trim procedure using a Newton–Raphson approach to solve the rotor aerodynamic environment such that the desired response response vector $\mathbf{y}$ comprising of thrust and orientation of the rotor tip-path-plane (TPP) (i.e., $\mathbf{y} = \{C_T, \beta_{1c}, \beta_{1s}\}^T$) is obtained.

The change in the response vector $\mathbf{y}(\mathbf{x} + \Delta\mathbf{x})$ is approximated using a Taylor series expansion, as given by

$$\mathbf{y}(\mathbf{x} + \Delta\mathbf{x}) = \mathbf{y} + [\mathbf{J}]\Delta\mathbf{x} + \dots \tag{2.42}$$

The trim Jacobian matrix, $\mathbf{J}$ is expressed as

$$\mathbf{J} = \frac{\partial \mathbf{y}}{\partial \mathbf{x}} = \begin{bmatrix} \dfrac{\partial C_T}{\partial \theta_0} & \dfrac{\partial C_T}{\partial \theta_{1c}} & \dfrac{\partial C_T}{\partial \theta_{1s}} \\ \dfrac{\partial \beta_{1c}}{\partial \theta_0} & \dfrac{\partial \beta_{1c}}{\partial \theta_{1c}} & \dfrac{\partial \beta_{1c}}{\partial \theta_{1s}} \\ \dfrac{\partial \beta_{1s}}{\partial \theta_0} & \dfrac{\partial \beta_{1s}}{\partial \theta_{1c}} & \dfrac{\partial C_T \beta_{1s}}{\partial \theta_{1s}} \end{bmatrix} \tag{2.43}$$

The updated perturbation is then obtained by re-arranging Eq. 2.42 to give

$$\Delta\mathbf{x} = [\mathbf{J}]^{-1} \begin{Bmatrix} C_T - C_{T_{req}} \\ \beta_{1c} \\ \beta_{1s} \end{Bmatrix} \longrightarrow 0 \tag{2.44}$$

where $C_{T_{\text{req}}}$ is the target total thrust coefficient of the rotor system.

The trim is performed by using an initial guess of the input control vector, which is then updated by solving Eq. 2.44. The Jacobian matrix is calculated using a first-order forward difference approximation. This approximation is performed by first calculating the initial response vector based on the initial guess at the input vector. The input vector is then perturbed, and the response vector is re-calculated to find the Jacobian matrix. Because the Jacobian calculation is a relatively expensive computation, it is calculated only as frequently as needed in the trim procedure.

2.3.3.2 Coaxial Rotor Trim Methodology

The trim approach can be extended to coaxial rotors with two sets of collective and cyclic pitch angles, and these will be coupled because of the interference between the aerodynamics of the two rotors. In fact, because of the interfering flows, both rotors will typically operate at different thrust conditions and different disk loadings at the torque balanced condition. Therefore, the coaxial system must be trimmed to satisfy the following two conditions:

1. Thrust balance: The net rotor thrust obtained by the coaxial system must counter-balance the components of weight and drag forces of the system. In most cases, it is sufficient to assume that thrust equals aircraft weight.

2. Torque balance: The net yaw moment on the aircraft as a system must be zero. If the contributions other than that of the rotor are neglected, then the torque produced by the upper rotor must be counter-balanced by the lower rotor.

For coaxial rotor systems, the control input vector and the response vector

can be defined using

$$\mathbf{x} = \begin{Bmatrix} \theta_0^u \\ \theta_{1c}^u \\ \theta_{1s}^u \\ \theta_0^l \\ \theta_{1c}^l \\ \theta_{1s}^l \end{Bmatrix} \quad \text{and} \quad \mathbf{y} = \begin{Bmatrix} \sum C_T \\ \sum C_Q \\ \beta_{1c}^u \\ \beta_{1s}^u \\ \beta_{1c}^l \\ \beta_{1s}^l \end{Bmatrix} \tag{2.45}$$

In these equations the superscript u represents upper rotor, and the superscript l represents lower rotor of the coaxial system. The Jacobian matrix for the coaxial rotor system can then be defined as

$$\mathbf{J} = \frac{\partial \mathbf{y}}{\partial \mathbf{x}} = \begin{bmatrix} \frac{\partial \sum C_T}{\partial \theta_0^u} & \frac{\partial \sum C_T}{\partial \theta_{1c}^u} & \frac{\partial \sum C_T}{\partial \theta_{1s}^u} & \frac{\partial \sum C_T}{\partial \theta_0^l} & \frac{\partial \sum C_T}{\partial \theta_{1c}^l} & \frac{\partial \sum C_T}{\partial \theta_{1s}^l} \\ \frac{\partial \sum C_Q}{\partial \theta_0^u} & \frac{\partial \sum C_Q}{\partial \theta_{1c}^u} & \frac{\partial \sum C_Q}{\partial \theta_{1s}^u} & \frac{\partial \sum C_Q}{\partial \theta_0^l} & \frac{\partial \sum C_Q}{\partial \theta_{1c}^l} & \frac{\partial \sum C_Q}{\partial \theta_{1s}^l} \\ \frac{\partial \beta_{1c}^u}{\partial \theta_0^u} & \frac{\partial \beta_{1c}^u}{\partial \theta_{1c}^u} & \frac{\partial \beta_{1c}^u}{\partial \theta_{1s}^u} & \frac{\partial \beta_{1c}^u}{\partial \theta_0^l} & \frac{\partial \beta_{1c}^u}{\partial \theta_{1c}^l} & \frac{\partial \beta_{1c}^u}{\partial \theta_{1s}^l} \\ \frac{\partial \beta_{1s}^u}{\partial \theta_0^u} & \frac{\partial \beta_{1s}^u}{\partial \theta_{1c}^u} & \frac{\partial \beta_{1s}^u}{\partial \theta_{1s}^u} & \frac{\partial \beta_{1s}^u}{\partial \theta_0^l} & \frac{\partial \beta_{1s}^u}{\partial \theta_{1c}^l} & \frac{\partial \beta_{1s}^u}{\partial \theta_{1s}^l} \\ \frac{\partial \beta_{1c}^l}{\partial \theta_0^u} & \frac{\partial \beta_{1c}^l}{\partial \theta_{1c}^u} & \frac{\partial \beta_{1c}^l}{\partial \theta_{1s}^u} & \frac{\partial \beta_{1c}^l}{\partial \theta_0^l} & \frac{\partial \beta_{1c}^l}{\partial \theta_{1c}^l} & \frac{\partial \beta_{1c}^l}{\partial \theta_{1s}^l} \\ \frac{\partial \beta_{1s}^l}{\partial \theta_0^u} & \frac{\partial \beta_{1s}^l}{\partial \theta_{1c}^u} & \frac{\partial \beta_{1s}^l}{\partial \theta_{1s}^u} & \frac{\partial \beta_{1s}^l}{\partial \theta_0^l} & \frac{\partial \beta_{1s}^l}{\partial \theta_{1c}^l} & \frac{\partial \beta_{1s}^l}{\partial \theta_{1s}^l} \end{bmatrix} \tag{2.46}$$

Finally, the updated perturbation vector can be written as

$$\Delta\mathbf{x} = [\mathbf{J}]^{-1} \left\{ \begin{array}{c} \sum C_T - C_{T_{\text{req}}} \\ \sum C_Q \\ \beta_{1c}^u \\ \beta_{1s}^u \\ \beta_{1c}^l \\ \beta_{1s}^l \end{array} \right\} \longrightarrow 0 \tag{2.47}$$

2.4 Optimization Methodology

The principles behind the optimization of the blades for a single rotor in hovering flight are very well understood—see Ref. 25. The goal is to design the shapes of the blades to minimize induced and profile losses, and therefore to maximize aerodynamic efficiency. However, the optimization of the geometry of a coaxial rotor is a more complex problem because of rotor-on-rotor interference. Furthermore, the aerodynamics of coaxial rotors is usually aperiodic because of the rotor-on-rotor interference effects. It is known that the upper rotor affects the aerodynamics of the lower rotor, but the degree to which the lower rotor affects the aerodynamics of the upper rotor is unclear. However, it is clear that the two rotors of the coaxial system operate at torque balance when other sources of yaw moment are neglected, and so share a different proportion of the total thrust. Because of this, both rotors operate at different disk loadings. Therefore, there are inter-dependent parameters that participate in the optimization problem.

The optimization of the blade shapes of the coaxial rotors must be done using a

robust and efficient optimization methodology. In the present work, the optimization of a coaxial rotors was performed using a formal optimization method called Design Optimization Tools (DOT). This section describes the general optimization problem, and the specific algorithms used in the optimization process.

2.4.1 General Optimization Problem

The optimization problem involves solving a nonlinear, constrained problem. The objective is to find a set of design variables that minimizes a suitable objective function subject to certain constraints. Mathematically this can be defined as Minimize:

$$F(\mathbf{X}) \tag{2.48}$$

subject to:

$$g_j(\mathbf{X}) \leq 0 \qquad j = 1, 2, ..., M \tag{2.49}$$

and

$$\mathbf{X}_i^l \leq \mathbf{X}_i \leq \mathbf{X}_i^u \qquad i = 1, 2, ..., N \tag{2.50}$$

In these equations, $\mathbf{X}$ is the vector of design variables, which defines the design space in which the optimization is to be performed. Equation 2.48 defines the objective function $F(\mathbf{X})$ that is to be minimized. This means finding the set of design variables $\mathbf{X}^*$ that minimizes the objective function. For problems requiring the function to be maximized, $-F(\mathbf{X})$, can be minimized instead.

Equation 2.49 defines the set of M constraints that should be satisfied while

minimizing the objective function. A constraint at some design variable $\mathbf{X}$ is considered "satisfied" if its value is negative, "violated" if its value is positive, and "active" if its value is zero at $\mathbf{X}$. The portion of the design space in which all the constraints are satisfied is called the "feasible region". The portion where even one constraint is violated is called the "infeasible region." Equation 2.50 defines the side constraints, i.e., the upper and lower limits of the design variables.

A general optimization procedure can be defined in the following steps:

1. Start with an initial design $\mathbf{X}^k = \mathbf{X}^0$ at $k = 0$.
2. Find a suitable search direction, say $\mathbf{S}^k$.
3. Perform a one-dimensional minimization along $\mathbf{S}^k$ to find $\alpha^\star$.
4. Update the design vector as $\mathbf{X}^{k+1} = \mathbf{X}^k + \alpha^* \mathbf{S}^k$.
5. Check for convergence.
6. Repeat the procedures from step 2 until convergence is achieved.

There are various constrained optimization algorithms such as the Method of Feasible Directions (MFD), Sequential Linear Programming (SLP), and Sequential Quadratic Programming (SQP) methods, which are very effective in finding the minimum of the defined function. DOT gives the flexibility to use any of these algorithms to help solve a specific type of optimization problem. In the present work, the Method of Feasible Direction (MFD) method was used.

2.4.2 Optimization Basics

The three critical steps of any optimization algorithm are explained here. The details of all of these algorithms can be found in Ref. 38.

2.4.2.1 Finding Search direction

The MFD is based on finding "usable-feasible" search direction that reduces the value of the objective function and keeps the design vector in the feasible region. The concept of such a direction can be explained as follows:

1. $\boldsymbol{S}^k$ *must be feasible*: This means that any small positive move along $\mathbf{S}^k$ should lead the updated design in the feasible region. Mathematically, this can expressed as

$$\nabla g_j(\mathbf{X}^k) \cdot \mathbf{S}^k \leq 0 \tag{2.51}$$

   Figure 2.7(a) shows the design space with two constraints $g_1(\mathbf{X})$ and $g_2(\mathbf{X})$ active at $\mathbf{X}^k$. The direction $\mathbf{S}^k$ takes the solution into the feasible region, and hence it satisfies the first condition.

2. $\boldsymbol{S}^k$ *must be usable*: This means that any small positive move along $\mathbf{S}^k$ must reduce the value of the objective function, $F(\mathbf{X}^k)$. Mathematically, this behavior can be expressed as

$$\nabla F(\mathbf{X}^k) \cdot \mathbf{S}^k \leq 0 \tag{2.52}$$

The feasible-usable direction is such that both of the conditions given by Eqs. 2.53 and 2.52 are satisfied. Figure 2.7(b) shows the concept of feasible-usable

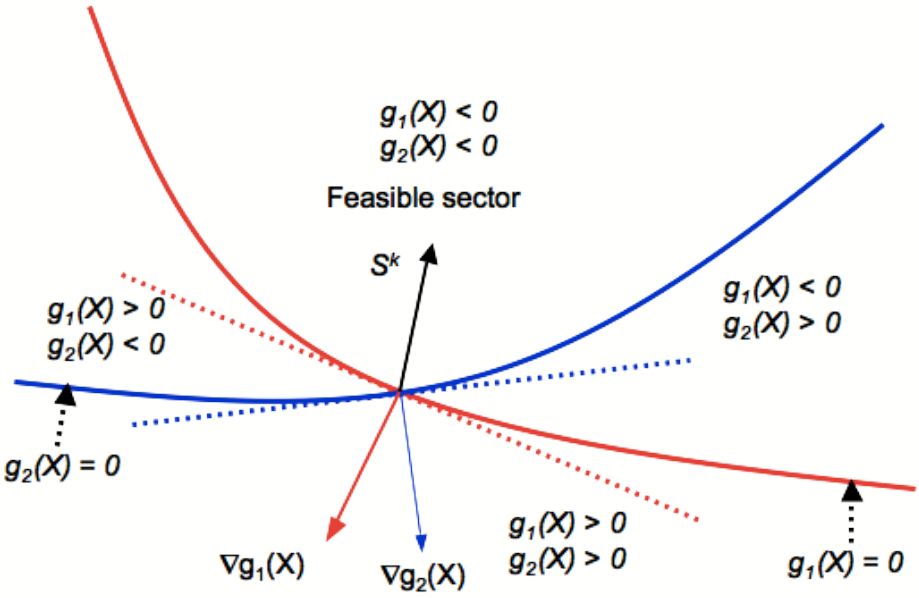

(a) Feasible directions

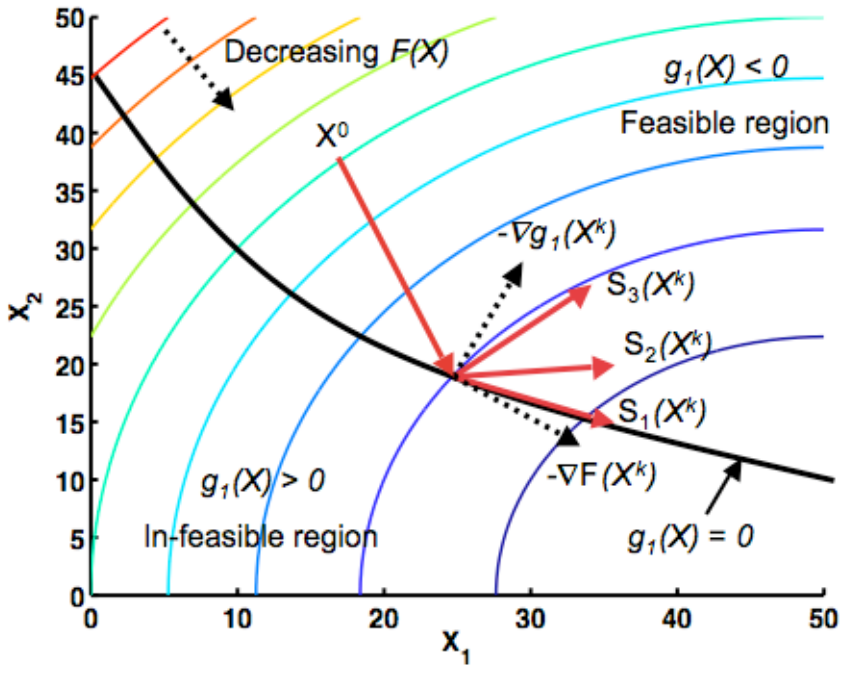

(b) Modified usable-feasible directions

Fig. 2.7: Usable-feasible direction in the MFD

directions and the feasible-usable sector. The search directions $\mathbf{S}_1^k$, $\mathbf{S}_2^k$ and $\mathbf{S}_3^k$ in Fig. 2.7(b) are feasible-usable directions. Out of all the feasible-usable directions, the search direction should be chosen that drives the solution to the optimum design in the minimum number of iterations.

Even a small step along the search direction that is very close to the constraint ($\mathbf{S}_1^k$) can lead the solution into the infeasible region. In this case, extra iterations may be required to bring solution back in the feasible sector. A search direction perpendicular to $-\nabla F(\mathbf{X})$ (i.e., along $\mathbf{S}_3^k$ in Fig. 2.7(b)) will make the optimization process relatively slow, hence again increasing the number of iterations.

The Method of Feasible Directions (MFD) algorithm works on the concept of push-off factor (i.e., θ), and modifies the feasibility condition using

$$\nabla \mathbf{g}_j(\mathbf{X}^k) \cdot \mathbf{S}^k - [\nabla F(\mathbf{X}^k) \cdot \mathbf{S}^k]\theta \leq 0 \tag{2.53}$$

If the search direction $\mathbf{S}^k$ is close to being perpendicular to $\nabla F(\mathbf{X}^k)$, this means that $\nabla F(\mathbf{X}^k) \cdot \mathbf{S}^k$ is very small and it prevents too large of a push-off factor. If $\mathbf{S}^k$ is very close to $-\nabla F(\mathbf{X}^k)$, then $F(\mathbf{X}^k) \cdot \mathbf{S}^k$ is large, and so the push-off factor will increase and the direction $\mathbf{S}^k$ will be pushed away from the constraint.

2.4.2.2 One-Dimensional Minimization

At any step k, given a knowledge of the starting design vector, $\mathbf{X}^{k-1}$, and search direction, $\mathbf{S}^k$, the requirement is to perform one dimensional minimization along $\mathbf{S}^k$ and to find the minimum of the function along this direction, i.e., $\mathbf{X}^k$ ($= \mathbf{X}^{k-1} + \alpha^\star \mathbf{S}^k$). Here, $\alpha^\star$ is a measure of how far from $\mathbf{X}^{k-1}$ the minimum lies on

$\mathbf{S}^k$. This value is found by computing the bounds on $\alpha^\star$ along $\mathbf{S}^k$ that will keep the solution inside the feasible region. The details of this approach can be found in Ref. 38.

After the bounds on $\alpha^\star$ are determined, a one-dimensional minimization is performed by interpolating $\alpha^\star$ between the bounds and fitting a linear, quadratic or cubic polynomial, depending upon the availability of the design solutions at which the function values are known.

2.4.2.3 Convergence to the Optimum

In DOT there are several criteria to determine convergence. These criteria are discussed here only briefly and the details can be found in Ref. 38.

1. *Maximum number of iterations*: DOT usually converges between 5 to 10 iterations, depending on the nonlinearity of the problem. In the present work, the maximum number of iterations that DOT is allowed to perform is set to a hard limit of 40 to avoid unnecessary computations.

2. *No feasible solution*: If the initial design is inside the infeasible region, and even after trying for some fixed maximum number of times the solution remains in the infeasible region, then DOT terminates the optimization and assumes that there is no feasible solution to the problem.

3. *Point of diminishing returns*: If the relative decrease in the objective function is less than a specified value for a specified number of consecutive iterations, then the optimization is terminated.

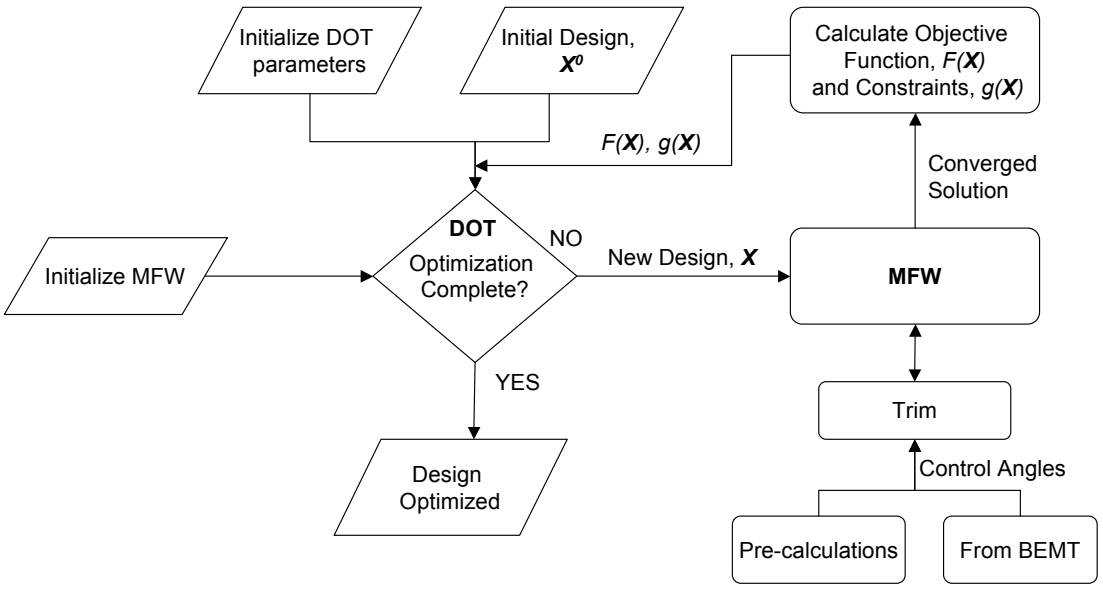

Fig. 2.8: Coupling between MFW and DOT.

4. *Kuhn–Tucker conditions*: If the Kuhn–Tucker conditions are satisfied, the optimization is terminated. More information on these conditions can be found in Ref. 38

2.5 Coupling between MFW and DOT

There is a coupling process needed between the Maryland Free Wake (MFW) and DOT (see Fig. 2.8), which is used to help find the optimum geometry of the coaxial rotor system. DOT provides MFW with the design vector. The MFW computes the trimmed, converged aerodynamic solution for the coaxial and passes the objective function and constraints back to DOT. This information is used by DOT to compute the next search direction, or to perform the one-dimensional minimization, as needed.

An initial coaxial rotor design was decided through a preliminary parametric

study performed using the BEMT. The MFW then computes the blade geometry parameters using the design provided by DOT. The trim Jacobian matrix given by Eq. 2.46 is re-computed for each updated design, and the rotor is trimmed at each MFW iteration. The time-accurate solution for the wake is determined until aerodynamic convergence is achieved.

Because the flow field around a coaxial rotor is generally aperiodic, the thrust and power fluctuate slightly in trim. Therefore, it was difficult to establish a very tight numerical tolerance on convergence. As described previously, convergence was determined on the basis of the total torque coefficient or the system figure of merit (depending upon what parameter was chosen as the objective function). The solution was considered to be converged when the values of the torque coefficient (or FM) did not change by more than 0.001% for five successive rotor revolutions. This converged solution was then used to re-calculate the objective function and the constraints, which were then returned to DOT.

2.6 Summary

This chapter discussed the methodologies that were used to study the aerodynamics of the coaxial rotors in the present study. It has explained the assumptions used in the formulation of each of the methods, and has also discussed the strengths of each of them. The trim methodology made it clear that for the coaxial helicopter to operate at zero torque condition, the aerodynamics of the two rotors are coupled to each other such that the torques produced by both rotors are equal and opposite.

This requires both rotors to operate at different thrust conditions. To this end, the designs of the two rotors could also be different to achieve the "best" or optimum performance in both hover and forward flight. Therefore, there are several design parameters, e.g., twist and planform shapes of the two rotors that participate in the optimization process. The optimization in the present work was done using a formal DOT optimizer. This chapter then explained the basics of a general optimization process. Finally, the coupling between the MFW and the DOT optimizer was discussed. The next chapter explains in details the specific objective functions, the design variables, and the constraints that were used in the present study to perform the blade geometry optimization of a coaxial rotor in both hover and forward flight.

Chapter 3

Formulation of the Optimization Problem

3.1 Overview

This chapter explains the formulation of the optimization problem for the coaxial rotor systems. The algorithm used to study the optimization of a coaxial rotor geometry has been described in the previous chapter (see Section 2.4 for details). The DOT optimizer is a mathematical tool that helps to find an optimum solution when it is provided with an objective function (that should be minimized or maximized) and defined sets of design variables (i.e, descriptions of the blade shapes). To make the optimization possible, the objective function, design variables, and constraints must be chosen carefully. Also, DOT is a general optimization algorithm that can be applied to any problem that needs to be optimized. However, the optimum that it provides may or may not be the actual physical solution of the problem. Therefore, the constraints must be formulated carefully such that solutions are not sought in any non-physical regions.

The optimization of a coaxial rotor geometry involves more complexities compared to a single rotor optimization, mainly because of the inter-dependence of the performance of both rotors arising from the interfering flow-fields. As already known from the single rotor optimization (see Ref. 37, Chapter 2, pp. 65–69), the induced power can be minimized by changing the twist distribution on the blades such that

the inflow becomes more uniform. The profile power can also be minimized by choosing the planform shape and airfoil sections such that all the blade sections operate at their best lift-to-drag ratios. Applying the same principles for the aerodynamic optimization of a coaxial rotor geometry in the hover flight condition, first the effect of twist was studied, followed by planform optimization. The results, however, are not completely linearly superimposable.

3.2 Objective Function

The focus was to maximize the aerodynamic performance of a coaxial rotor operating in hovering or forward flight. Maximizing the efficiency means maximizing the system figure of merit or minimizing the total required power for a given value of thrust or disk loading. This section explains the objective functions used in the present study in both hover and forward flight.

3.2.1 Power Required

The total required power coefficient, as given by Eq. 3.1, should be minimized to maximize power loading (i.e., to maximize the value of T/P), i.e.,

$$C_{P_{reqd}} = \left(C^u_{P_i} + C^l_{P_i}\right) + \left(C^u_{P_0} + C^l_{P_0}\right) \tag{3.1}$$

In forward flight, the induced and profile power distributions vary with blade azimuthal position. Therefore, the objective was to minimize the total power averaged over the complete revolution after the steady state trimmed solution was obtained.

Because the blade twist distribution affects the inflow over both the rotors,

when optimizing blade twist the goal is primarily to minimize the induced losses. However, in the case of a coaxial rotor, the change in the twist distribution also indirectly affects the profile power because the results must be obtained at torque balance. Therefore, while optimizing the form of the blade twist distribution, the objective function may be formulated such that the induced power coefficient is weighted more heavily relative to the profile power coefficient. The resulting objective function can be defined as

$$F(\mathbf{X}) = c_1 \left(C^u_{P_i} + C^l_{P_i} \right) + (1 - c_1) \left(C^u_{P_0} + C^l_{P_0} \right) \tag{3.2}$$

where c_1 is a constant that varies from 0 to 1 and determines the relative weighting given to the fraction of induced and profile power contributions.

The gradients of the objective function, $\nabla F(\mathbf{X})$, which are used to find the search direction (see Section 2.4), are computed using finite difference approximations.

3.2.2 Figure of Merit

The figure of merit, FM, is a metric used to compare the relative hovering performance of different rotors to the "ideal" performance provided by the SMT at the same rotor operating conditions. The FM for a single rotor is defined as the ratio of the ideal hover induced power to the actual power required, i.e.,

$$FM = \frac{P_{\text{ideal}}}{\kappa P_{\text{ideal}} + P_0} \quad < \quad 1 \tag{3.3}$$

This result can also be written as

$$FM = \frac{1}{\kappa + \dfrac{P_0}{P_{\text{ideal}}}} = \frac{1}{\kappa + \dfrac{\sqrt{2}\rho}{T}\dfrac{P_0}{\sqrt{DL}}} \tag{3.4}$$

Notice from Eq. 3.4 that even if operating at same thrust condition, the comparison of the efficiencies of any two rotors should be done at same disk loading. For same thrust, a rotor with a higher disk loading will produce a higher value of FM, all other parameters being the same. To avoid any bias in the results, the comparison of any two rotor systems (i.e., single to coaxial), therefore, must be done at the same disk loading.

The two rotors in the coaxial rotor system operate at unequal thrust values, and hence at unequal disk loadings. Therefore, the FM of a coaxial rotor system should be a metric that considers the unequal thrust sharing between the two rotors. To obtain the expression of FM for a coaxial rotor, the minimum power as given by the SMT should represent the ideal power. The ideal power, P_{ideal}, for a coaxial system can be written as

$$P_{\text{ideal}} = \kappa_{\text{int}} 2\left(P_{\text{iso}}\right) = \kappa_{\text{int}}\left(\frac{T_u^{3/2}}{\sqrt{2\rho A}} + \frac{T_l^{3/2}}{\sqrt{2\rho A}}\right) \tag{3.5}$$

where κ_{int} is the interference-induced power factor, as explained previously in Section 2.1 (Case 4b). In this case, the comparison is made against two isolated rotors each operating at thrusts equal to those of the upper and lower rotors, respectively at the sharing condition. This gives the value of κ_{int} as 1.2656 (see Table 2.1). The ideal power for the coaxial rotor becomes

$$P_{\text{ideal}} = 1.2656\left(\frac{T_u^{3/2}}{\sqrt{2\rho A}} + \frac{T_l^{3/2}}{\sqrt{2\rho A}}\right) \tag{3.6}$$

The *FM* expression for coaxial rotors, therefore, becomes

$$FM = \frac{1.2657 \frac{C_{T_l}^{3/2}}{\sqrt{2}} \left[\left(\frac{C_{T_u}}{C_{T_l}} \right)^{3/2} + 1 \right]}{C_{P_{\text{meas}}}} \tag{3.7}$$

The development of the figure of merit expression given by Eq. 3.7 is discussed in more detail in Ref. 26.

Because the computation of the figure of merit or total power required at each rotor revolution is an iterative process, the values of these parameters fluctuate slightly about their mean values. In this case, the convergence of the MFW solution was seeked when the relative error between values of figure of merit or total power required becomes smaller than 0.001% consecutively for five rotor revolutions.

3.3 Design Variables

In the present study, the objective was to maximize the *FM* of the coaxial rotors for the hover case, and to minimize the total power required for the forward flight case. From the optimization of the geometry of a single rotor, it is known that twist, taper (planform) and airfoil selection are the key parameters that must be adjusted to maximize the rotor performance. For a coaxial system, the performance levels of both the rotors must be optimized. Therefore, these parameters were used as primary design variables. In forward flight, the inter-rotor spacing becomes another parameter that should be optimized, although the range of practical spacings for a coaxial rotor (at least on a helicopter) may be dictated by factors other than aerodynamics (e.g., the need to avoid inter-blade collisions between the rotors). This

section explains the design variables used to achieve these goals in both hover and forward flight conditions.

3.3.1 Twist Optimization

Because the induced losses on both the rotors of the coaxial system are different, the optimum blade twist needed should be different on both the rotors to maximize overall coaxial system performance. As already known from the optimization of a single rotor geometry, hyperbolic blade twist distribution (or something close to that) minimizes the induced losses in hover or in axial flight. The equivalent optimum coaxial rotor has been considered by Leishman (Ref. 20). In this case, the upper rotor has a hyperbolic form but the lower rotor has a double hyperbolic form; the break in the twist distribution on the lower rotor corresponds to the point on the blades where the wake boundary from the upper rotor impinges on the lower rotor. Therefore, a linear twist distribution was implemented first, and then nonlinear twist distribution was studied.

3.3.1.1 Linear Twist Distribution On Both Rotors

Because a linear twist distribution is a fairly good approximation at the blade tip, to the hyperbolic twist distribution both the rotors were initially linearly twisted. The design variable vector in this case consists of the twist rates on upper and lower rotors, respectively, and can be written as

$$\mathbf{X} = \left\{\theta^u_{\text{tw}},\ \theta^l_{\text{tw}}\right\}^T \tag{3.8}$$

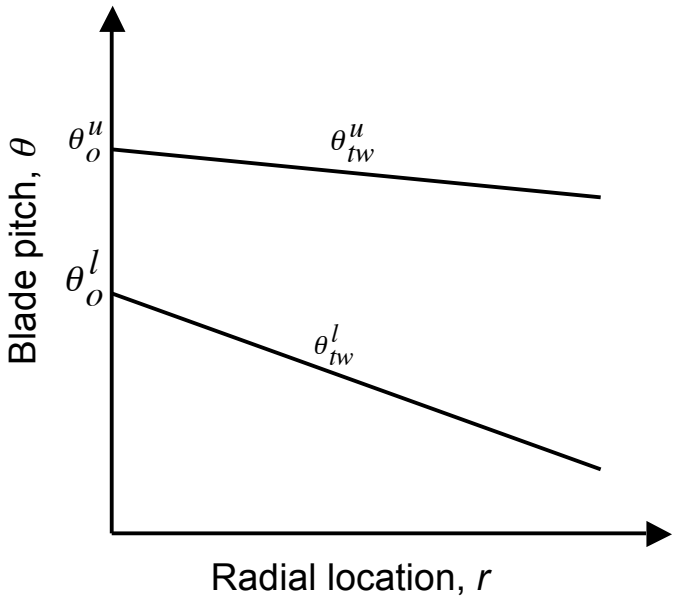

Fig. 3.1: Linear twist distribution on upper and lower rotor blades.

This problem will be referred to as the "2-design variable" problem. The twist distribution on the upper and lower rotors can be represented as shown in Fig. 3.1, and can be expressed as

$$\theta^u(r) = \theta_0^u + \theta_{\text{tw}}^u r \tag{3.9}$$

and

$$\theta^l(r) = \theta_0^l + \theta_{\text{tw}}^l r \tag{3.10}$$

on upper and lower rotors, respectively. The variables θ_0^u and θ_0^l are the collective pitch angles on upper and lower rotors, respectively.

3.3.1.2 Nonlinear Twist Distribution On Both Rotors

Because of the rotor-on-rotor interference, the inflow distribution on both the rotors of a coaxial system is highly non-linear compared to the single rotor twist

distribution. As seen from Fig. 4.6, the inflow on the lower rotor is higher within the region where the wake from the upper rotor impinges upon it. Therefore, the blades on the lower rotor were twisted nonlinearly in the following ways.

1. 6-Design Variable Problem

   In this case, the blade twist on both of the rotors was represented using two linear twist rates. Therefore, the blade twist distribution can be represented by three design variables: two linear twist rates and one breakpoint, as shown in Fig. 3.2(a). The design vector can be represented as

$$\mathbf{X} = \left\{\theta_{\text{tw}}^{u1},\ \theta_{\text{tw}}^{u2},\ \theta_{\text{tw}}^{l1},\ \theta_{\text{tw}}^{l2},\ r_b^u,\ r_b^l\right\}^T \tag{3.11}$$

   where r_b^u and r_l^b are the breakpoints on upper and lower rotors, respectively. The variables $\theta_{\text{tw}}^{u1},\ \theta_{\text{tw}}^{u2}$ are the linear twist rates inboard and outboard of the breakpoint on the upper rotor, respectively, and, $\theta_{\text{tw}}^{l1},\ \theta_{\text{tw}}^{l2}$ are the linear twist rates inboard and outboard of the breakpoint on lower rotor, respectively.

   In this case, the twist distribution on both the rotors is given by Eq. 3.12

$$\theta(r) = \begin{cases} \theta_0 + \theta_{\text{tw}}^1 r & \text{if } r \le r_b \\ \theta_0 + \theta_{\text{tw}}^1 r_b + \theta_{tw}^2 (r - r_b) & \text{if } r > r_b \end{cases} \tag{3.12}$$

2. 8-Design Variable Problem

   In this case, the twist distribution on each rotor was represented using four design variables: 2 linear blade twists, one breakpoint and twist offset per blade. The twist distributions are given by Fig. 3.2(b). The design vector can

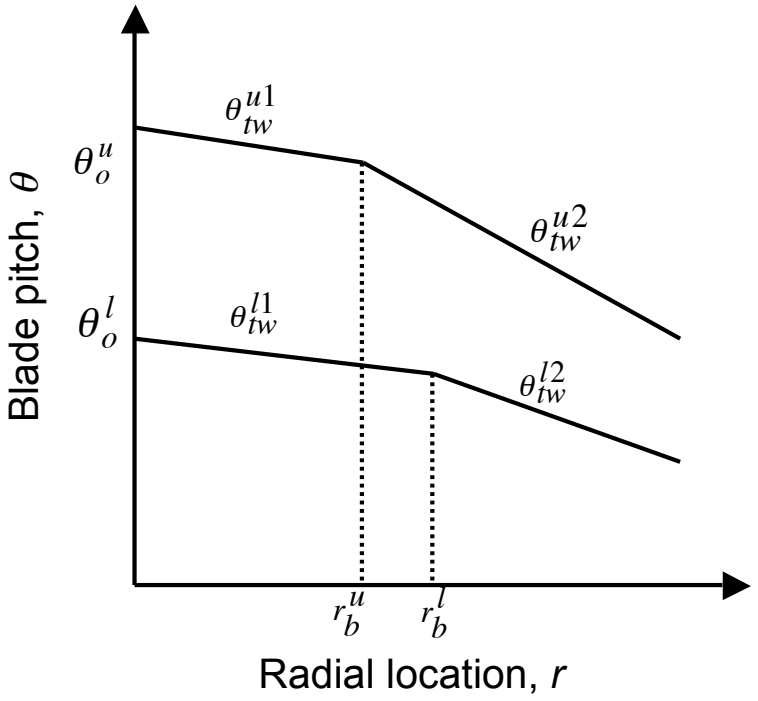

(a) 6-design variable problem

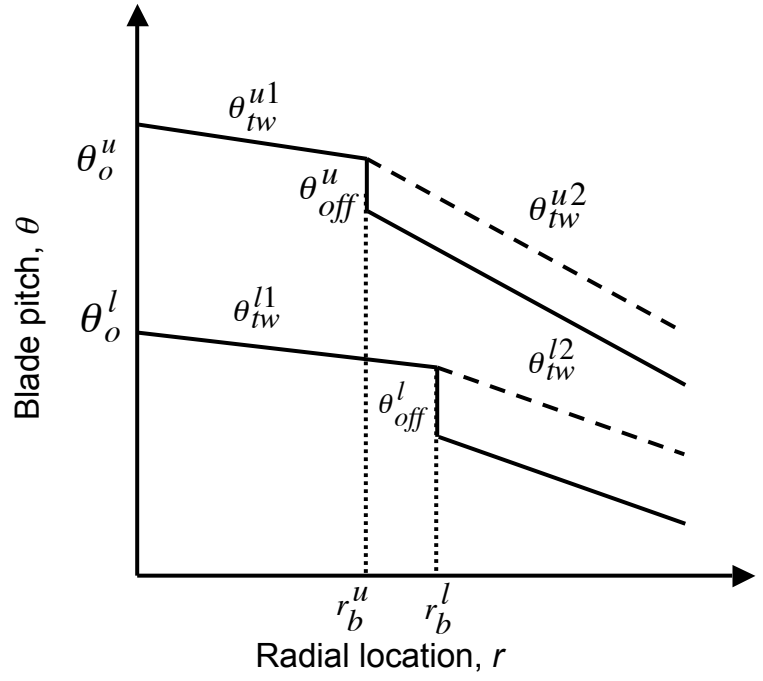

(b) 8-design variable problem

Fig. 3.2: Non-linear twist distribution on upper and lower rotors

be written as

$$\mathbf{X} = \left\{\theta^{u1}_{\text{tw}},\ \theta^{u2}_{\text{tw}},\ \theta^{l1}_{\text{tw}},\ \theta^{l2}_{\text{tw}},\ r^{u}_{b},\ r^{l}_{b},\ \theta^{u}_{\text{off}},\ \theta^{l}_{\text{off}}\right\}^{T} \tag{3.13}$$

where θ^{u}_{off} and θ^{l}_{off} are the offsets in the twist rates on the upper and lower rotors at the breakpoints, respectively.

The twist distribution on both the rotors can be given by

$$\theta(r) = \begin{cases} \theta_0 + \theta^{1}_{\text{tw}} r & \text{if } r \leq r_b \\ \theta_0 + (\theta^{1}_{\text{tw}} + \theta_{\text{off}}) r_b + \theta^{2}_{tw}(r - r_b) & \text{if } r > r_b \end{cases} \tag{3.14}$$

3.3.2 Planform Optimization

The two rotors of a coaxial system operate at different disk loadings; usually, the upper rotor shares a higher fraction of the total system thrust coefficient. This also means that upper rotor dictates the stall margin of the coaxial as a system. Therefore, to maximize the stall limits of the optimum coaxial rotor, the solidities on both the rotors will need to be different.

The solidity of each rotor can be expressed as a function of the taper ratio TR of the rotor blade, the point r_t where taper starts, and the root chord c_0 on each set of blades—see Fig. 3.3. Notice that in the present analysis, the taper ratio (TR) is defined as the ratio of root chord (c_0) to the tip chord (c_1), i.e.,

$$TR = \frac{c_0}{c_1} \tag{3.15}$$

The performance of the coaxial systems with different planform shapes were compared such that the thrust weighted equivalent solidity (Ref. 25) of the total

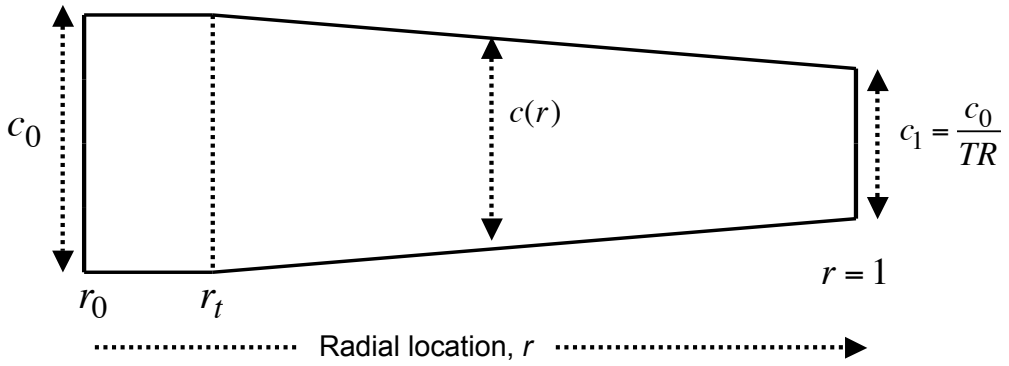

Fig. 3.3: Radial distribution of blade chord for a linearly tapered blade.

system remains constant. The thrust weighted solidity of the coaxial system (i.e., σ_e^{coax}) can be written as a sum of the equivalent solidities on the upper and lower rotors, i.e.,

$$\sigma_e^{\text{coax}} = \sigma_e^{\text{u}} + \sigma_e^{\text{l}} \tag{3.16}$$

where the equivalent solidities can further be written as

$$\sigma_e = \frac{3N_b}{\pi R} \int_0^1 c(r)\ r^2 dr \tag{3.17}$$

and

$$c(r) = \begin{cases} c_0 & r \le r_t \\ c_0 \left[1 + \left(\dfrac{\dfrac{1}{TR} - 1}{1 - r_t} \right) (r - r_t) \right] & r > r_t \end{cases} \tag{3.18}$$

The design variable vector can be written as

$$\mathbf{X} = \left\{ TR^u,\ r_t^u,\ c_0^u,\ TR^l,\ r_t^l,\ c_0^l \right\}^T \tag{3.19}$$

where the superscripts "u" and "l" denote the upper and lower rotor variables, respectively.

3.3.3 Inter-Rotor Spacing Distance Optimization

The induced losses in both the hover and forward flight conditions depend upon the inter-rotor spacing distance between the two rotors. In hovering flight, the wakes from the two rotors interact with each other, and the induced losses rotor-on-rotor interference are higher. At higher forward speeds the interaction between the wakes of the two rotors reduce. Therefore, a higher inter-rotor spacing is desired in hovering flight to reduce the induced losses as compared to forward flight. Moreover, at high forward speeds, a high inter-rotor spacing distance increases the parasitic drag of the coaxial rotor system because of the exposed shaft. Therefore, inter-rotor spacing distance must also become one of the design variables for forward flight optimization. Although, generally the inter-rotor spacing distance will be decided based on factors other than aerodynamics, such as to avoid inter-blade collisions between the rotors.

3.4 Constraints

As mentioned previously, constraints must be used to restrict the optimizer from picking designs that drive the solution into a non-physical domain. This section describes the two types of constraints that were used in the present study—the behavior and side constraints.

3.4.1 Behavior Constraints

The behavior constraints are the inequality constraints that define the nature of the problem. In the present study, the requirement was to obtain a trimmed solution in the physical domain. These conditions have been modeled mathematically as two behavior constraints.

3.4.1.1 Trim Constraint

This constraint determines that for the design chosen whether or not the solution is able to trim the rotors. The maximum number of iterations allowed for trim was limited to 20. Usually, with the initial collective guess provided by the BEMT, the MFW takes 3 to 7 iterations to converge. The constraint is given by

$$g_1(\mathbf{X}) = \mathrm{I} - \mathrm{I}_{\max} \tag{3.20}$$

where $I_{\max}$ is the maximum iterations allowed to trim, which was set to 20 for the present study, and I is the number of iterations taken to trim. If $g_1(\mathbf{X}) \leq 0$, the solution is trimmed, and the design is in the feasible region. When $g_1(\mathbf{X}) > 0$, the constraint is not satisfied and the design will be in the infeasible region. The optimizer then updates the design and brings it back into the feasible region.

3.4.1.2 *FM* Constraint

The second aerodynamic constraint is that the figure of merit of the coaxial system should always be less than unity. Because the objective of the problem is to maximize the figure of merit (FM), the optimizer can pick some nonphysical designs

such that FM becomes greater than 1. Mathematically, this can be defined as

$$g_2(\mathbf{X}) = FM - 1 \tag{3.21}$$

3.4.1.3 Equivalent Thrust Weighted Solidity Constraint

As explained previously, the blade planform optimization was performed such that the net thrust weighted solidity of the coaxial system remains constant, i.e.,

$$\sigma_e^{\text{coax}} = \sigma_e^{\text{u}} + \sigma_e^{\text{l}} \tag{3.22}$$

where σ_e^{u} and σ_e^{l} are the thrust weighted solidities of the upper and lower rotors, respectively. This means that the design vectors as given by Eq. 4.25 should be chosen such that the total system weighted thrust solidity remains constant. This equality constraint can be written as

$$h(\mathbf{X}) = \left(\frac{\sigma_e^{\text{u}}(\mathbf{X}) + \sigma_e^{\text{l}}(\mathbf{X})}{\sigma_e^{\text{coax}}} \right) - 1 \tag{3.23}$$

3.4.2 Side constraints

Side constraints set the lower and upper bounds on the design variables. These basically limit the design space where DOT searches for an optimum. The upper and lower side constraints ($\mathbf{X}^u$ and $\mathbf{X}^l$, respectively) used in the present study are given as follows.

For a 2-design variable problem, the side constraints are given as

$$\mathbf{X} = \left\{ \begin{array}{c} \theta_{\text{tw}}^u \\ \\ \theta_{\text{tw}}^l \end{array} \right\}, \qquad \mathbf{X}^l = \left\{ \begin{array}{c} -40^\circ \\ \\ -40^\circ \end{array} \right\} \text{ and } \qquad \mathbf{X}^u = \left\{ \begin{array}{c} 40^\circ \\ \\ 40^\circ \end{array} \right\} \tag{3.24}$$

For a 6-design variable problem, the side constraints are given as

$$\mathbf{X} = \begin{Bmatrix} \theta_{\text{tw}}^{u1} \\ \theta_{\text{tw}}^{u2} \\ \theta_{\text{tw}}^{l1} \\ \theta_{\text{tw}}^{l2} \\ r_b^u \\ r_b^l \end{Bmatrix}, \qquad \mathbf{X}^l = \begin{Bmatrix} -40^\circ \\ -40^\circ \\ -40^\circ \\ -40^\circ \\ 0 \\ 0 \end{Bmatrix} \text{ and } \qquad \mathbf{X}^u = \begin{Bmatrix} 40^\circ \\ 40^\circ \\ 40^\circ \\ 40^\circ \\ 1 \\ 1 \end{Bmatrix} \tag{3.25}$$

For an 8-design variable problem, the side constraints are given as

$$\mathbf{X} = \begin{Bmatrix} \theta_{\text{tw}}^{u1} \\ \theta_{\text{tw}}^{u2} \\ \theta_{\text{tw}}^{l1} \\ \theta_{\text{tw}}^{l2} \\ r_b^u \\ r_b^l \\ \theta_{\text{off}}^u \\ \theta_{\text{off}}^l \end{Bmatrix}, \qquad \mathbf{X}^l = \begin{Bmatrix} -40^\circ \\ -40^\circ \\ -40^\circ \\ -40^\circ \\ 0 \\ 0 \\ -5^\circ \\ -5^\circ \end{Bmatrix} \text{ and } \qquad \mathbf{X}^u = \begin{Bmatrix} 40^\circ \\ 40^\circ \\ 40^\circ \\ 40^\circ \\ 1 \\ 1 \\ 5^\circ \\ 5^\circ \end{Bmatrix}. \tag{3.26}$$

3.5 Summary

This chapter explained in detail the objective functions, the design variables, and the constraints used to define the problem of optimizing coaxial rotor system. The objective in hover was to maximize the figure of merit, and in forward flight

it was to minimize the total power required. The design variables comprised of the blade shape parameters that defined the geometry of blades on both the rotors. These variables included twist rates and planform shapes on both the upper and lower rotors, along with the inter-rotor spacing distance. The next chapter presents the results obtained from the parametric studies that were performed to optimize the blade shapes in both hover and forward flight, also discussing the optimization results obtained by coupling BEMT with DOT and the MFW with DOT.

Chapter 4

Results

4.1 Validation of the Aerodynamic Methods

The results from the three mathematical models used in the present study (i.e., the SMT, BEMT and MFW) were validated against the measurements conducted by Harrington (Ref. 14) on two nominally full scale rotor systems, which are referred to as Rotor 1 and Rotor 2 in Ref. 20. Both had two 25 ft diameter rotors. The Rotor 1 had a solidity of 0.027 per blade, and Rotor 2 had solidity 0.076 per blade. The blades on Rotor 1 were untwisted but tapered in planform (approximately taper ratio of 3:1) and thickness—see Fig. 4.1(a). The blades on Rotor 2 were untwisted and tapered only in thickness-to-chord ratio—see Fig. 4.1(b). The inter-rotor spacing of Rotor 1 was 0.1864 R, and of Rotor 2 was 0.16 R. This section presents the validation results for the SMT, BEMT and MFW against these data.

4.1.1 Validation of the Simple Momentum Theory

The SMT results for coaxial rotors, as described in Chapter 2, defines the minimum induced power losses that can be expected from any coaxial system. Therefore, it sets the datum to compare the performance of real coaxial rotors. Figures 4.2(a) and 4.2(b) show the hovering power polars obtained by using the SMT with Harrington's measurements on both the single rotor and coaxial Rotors 1 and 2. The

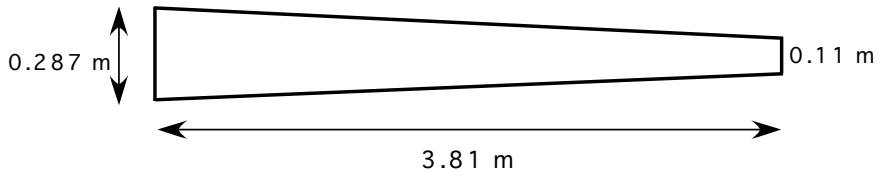

(a) Rotor blade of Harrington Rotor 1

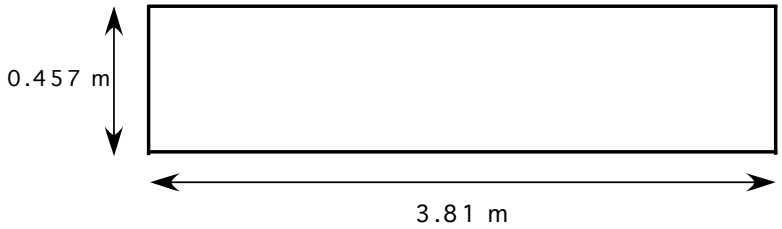

(b) Rotor blade of Harrington Rotor 2

Fig. 4.1: Schematic showing rotor blades for Harrington rotor 1 and 2. (Note: figure not to scale)

single rotor represents one of the two rotors of the coaxial systems that was analyzed in isolation.

The theoretical power required by a single rotor operating at thrust coefficient, C_T, is given by the modified momentum theory as

$$C_P = \frac{\kappa C_T^{3/2}}{\sqrt{2}} + \left(\frac{\sigma C_{d_0}}{8}\right) \tag{4.1}$$

where κ is determined through least-squares correlation with single rotor thrust and power measurements, and C_{d_0} is determined from either two-dimensional airfoil data or implied from the rotor power required at the zero thrust condition.

The power required by an equivalent single rotor system with the same disk loading and solidity as a coaxial system, and operating at $W = T_u + T_l$, is given by

$$C_P = \frac{2\kappa\left(\frac{C_W}{2}\right)^{3/2}}{\sqrt{2}} + 2\left(\frac{\sigma C_{d_0}}{8}\right) = \frac{\kappa C_W^{3/2}}{2} + \frac{\sigma C_{d_0}}{4} \tag{4.2}$$

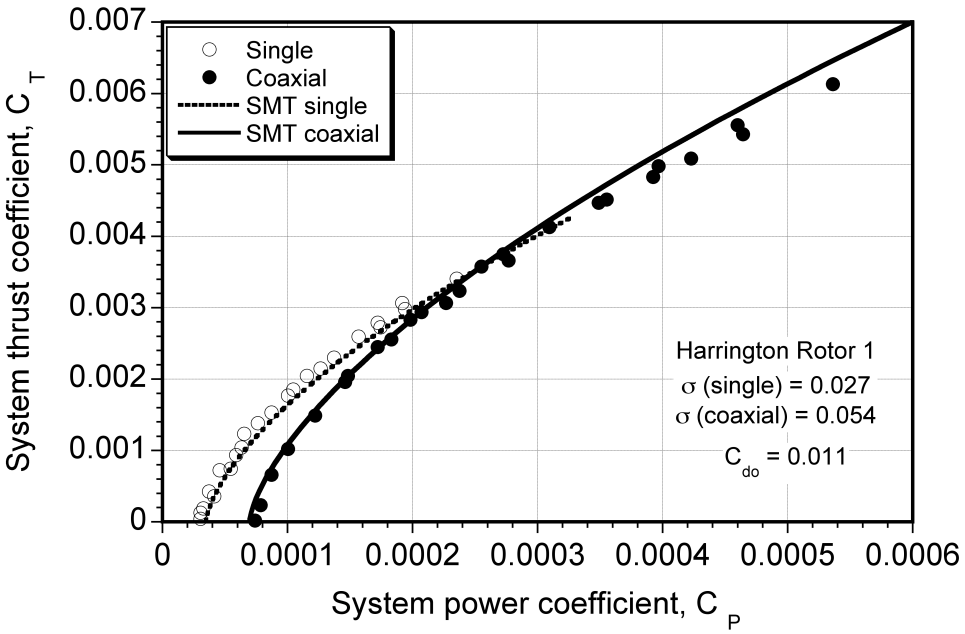

(a) Power polar for Harrington Rotor 1

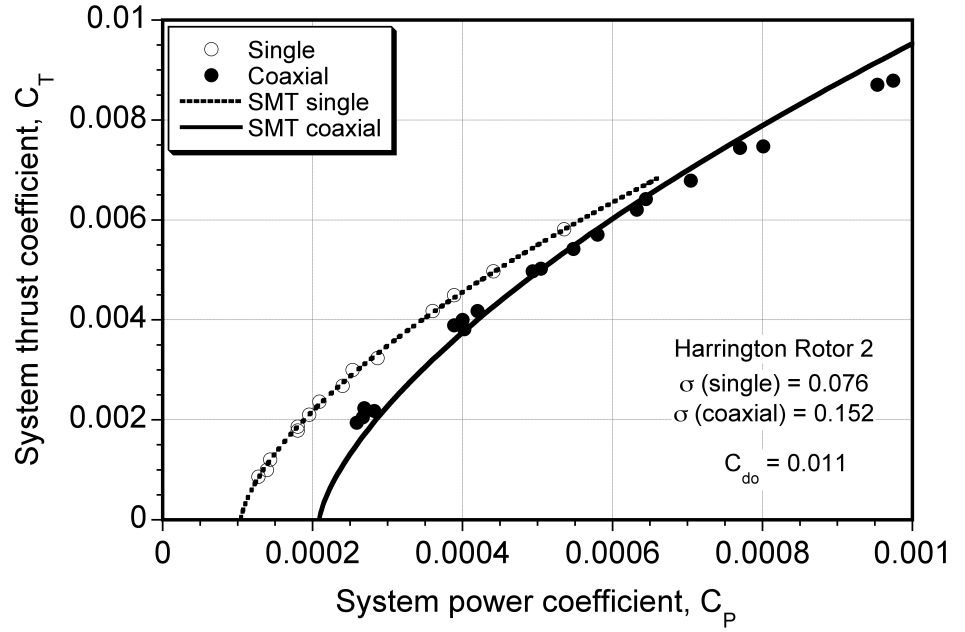

(b) Power polar for Harrington Rotor 2

Fig. 4.2: Comparison of power polars of the Harrington rotor geometries using the SMT and measurements.

The corresponding power for the coaxial rotor system can be calculated using

$$C_P = \frac{\kappa_{\text{int}}\ \kappa(C_{T_u} + C_{T_l})^{3/2}}{2} + \left(\frac{\sigma C_{d_0}}{4}\right) = \frac{\kappa_{\text{int}}\ \kappa C_W^{3/2}}{2} + \left(\frac{\sigma C_{d_0}}{4}\right) \tag{4.3}$$

where the induced interference factor κ_{int} of 1.28 was assumed in this case on the basis of the results shown previously in Table 2.1.

The momentum theory generally underpredicts measured performance for both single and coaxial rotors, but can be modified using an increment in sectional profile drag that is a function of blade element angle of attack, i.e., by using

$$C_d = C_{d_0} + d_1\alpha + d_2\alpha^2 \tag{4.4}$$

where $d_1 = 0.021$ and $d_2 = 0.65$ are based on NACA 0012 airfoil section measurements. In this case, the power required for the equivalent single rotor can be approximated as

$$C_P = \frac{\kappa C_W^{3/2}}{2} + \left(\frac{\sigma C_{d_0}}{4}\right) + \left(\frac{2d_1}{3C_{l_\alpha}}\right) C_W + \left(\frac{2d_2}{\sigma C_{l_\alpha}^2}\right) C_W^2 \tag{4.5}$$

and the power required for the coaxial is

$$C_P = \frac{\kappa_{\text{int}}\ \kappa C_W^{3/2}}{2} + \left(\frac{\sigma C_{d_0}}{4}\right) + \left(\frac{2d_1}{3C_{l_\alpha}}\right) C_W + \left(\frac{2d_2}{\sigma C_{l_\alpha}^2}\right) \left(C_{T_u}^2 + C_{T_l}^2\right) \tag{4.6}$$

Equation 4.6 was used to calculate the power required for the two coaxial rotor systems, as shown in Figs. 4.2(a) and 4.2(b). The results show that the power polars as predicted by the SMT are in reasonably good agreement with the measurements.

4.1.2 Validation of Blade Element Momentum Theory

Figures 4.3(a) and 4.3(b) show the power polars of Harrington Rotors 1 and 2 that were obtained by using the BEMT. The BEMT gives a better prediction of

the power required for a given thrust when compared to the SMT. This is primarily because BEMT is a two-dimensional analysis that solves for the non-uniform inflow over the rotor blades. In the present analysis, the viscous drag was assumed to be a function of blade section angle of attack, as given by Eq. 4.4. Also, to account for blade tip losses, Prandtl's tip loss factor (see Eqs. 2.18 and 2.19) was implemented in the present calculations. Unlike the SMT, however, the BEMT does not make any assumption about the values of κ and its value computed as a part of the solution process.

It is interesting to note that κ varies with the system operating state, i.e., with thrust in this case. Figure 4.4 shows the variation of the total induced power factor with the blade loading coefficient, C_T/σ, for the single and coaxial rotor systems (Harrington Rotor 1), with and without tip losses. The induced power factor of the single rotor (with tip losses) is approximately 1.1, though it varies slightly with C_T/σ. The induced power factor for the Harrington Rotor 1 with tip losses varies from 1.34 to 1.38 within the normal range of C_T/σ. Total induced power factor of 1.38 gives an interference-induced power factor of 1.26, which is consistent with the results from the SMT—see Table 2.1.

4.1.3 Validation of Free Vortex Method

Figures 4.5(a) and 4.5(b) show the comparison of the power polars obtained using the MFW with measurements for the Harrington Rotor 1 and 2, respectively. The results show that MFW is in good agreement with the measurements. Figure 4.6

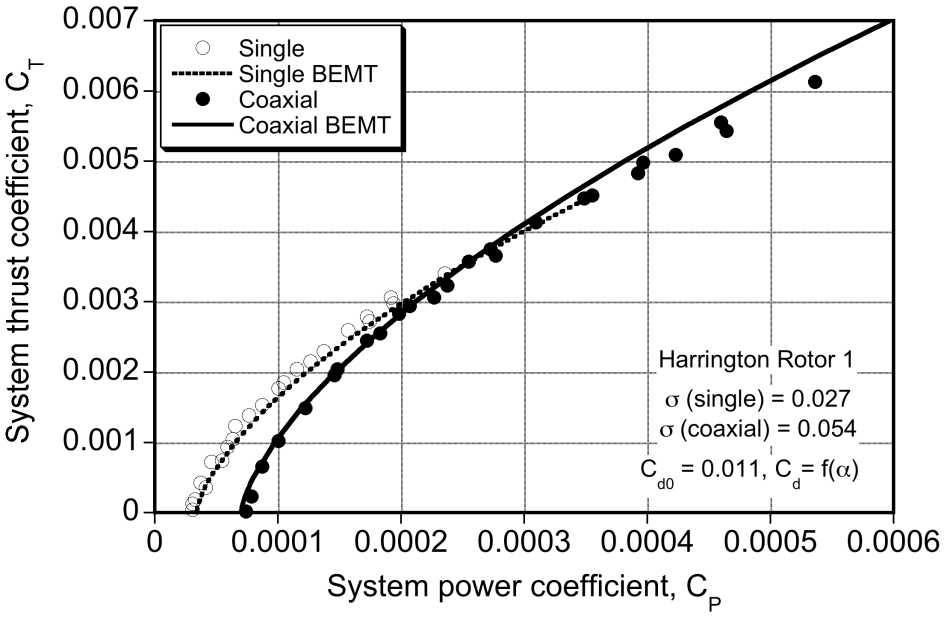

(a) Power polar for Harrington Rotor 1

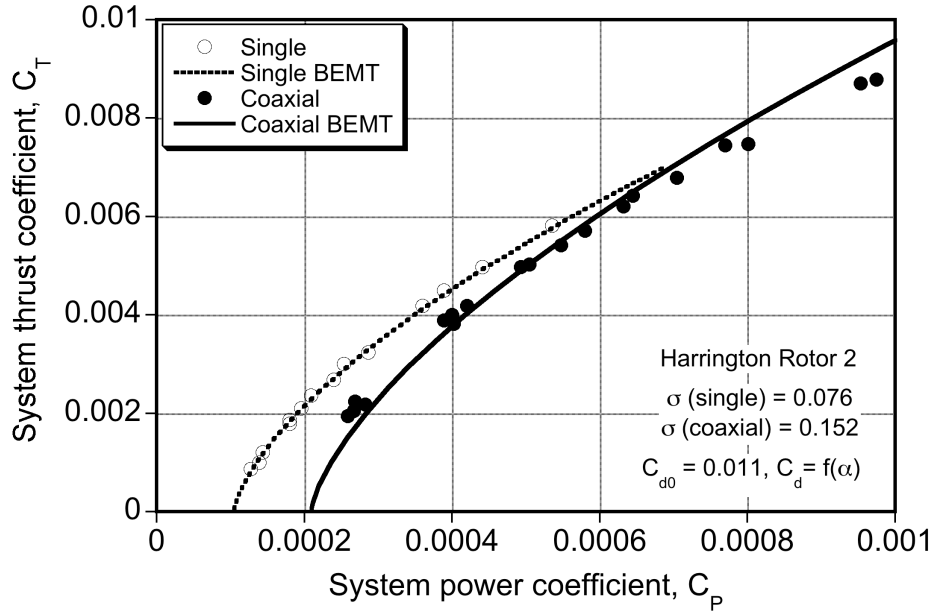

(b) Power polar for Harrington Rotor 2

Fig. 4.3: Comparison of power polars for the Harrington rotor geometries obtained using the BEMT with measurements.

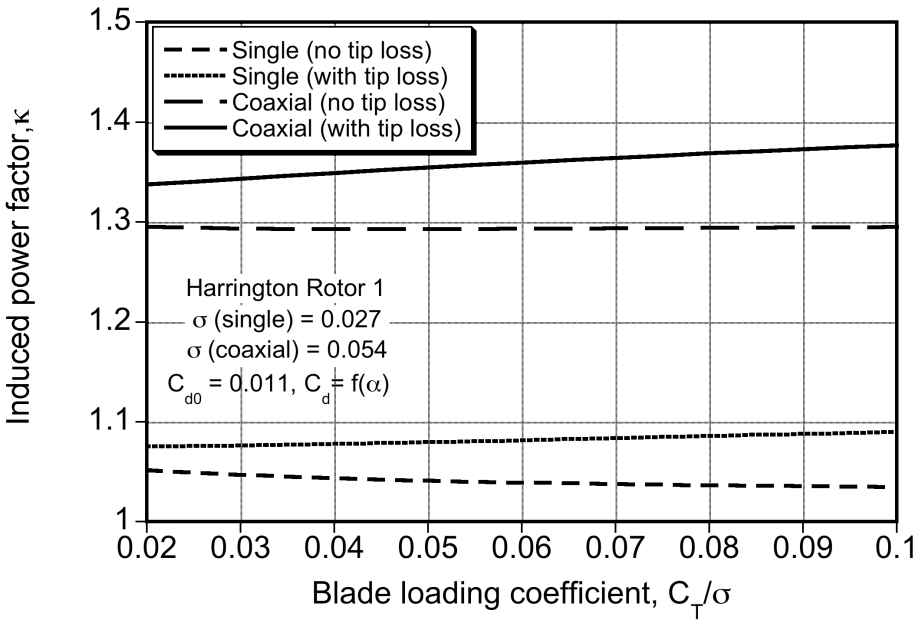

Fig. 4.4: Variation of induced power factor with blade loading coefficient for single and coaxial rotors of the Harrington Rotor 1 system.

shows the wake geometry of upper and lower rotors, in this case considering only the tip vortices from the two blades of each rotor. This shows that the wake from the upper rotor passes through the lower rotor smoothly without much loss of its helical structure. These results are consistent with the flow visualization experiments of Taylor (Ref. 39) and McAlister (Ref. 40), where the interfering wakes from the two rotors appear to remain fairly distinct. However, the flow fields from the two rotors still interact with each other. Notice that the flow models used for the SMT and BEMT analysis are also well justified from the wake geometry given in Fig. 4.6 using the MFW.

Because of the unavailability of the measurements showing the spanwise distribution of airloads on the blades of both upper and lower rotors of the coaxial system,

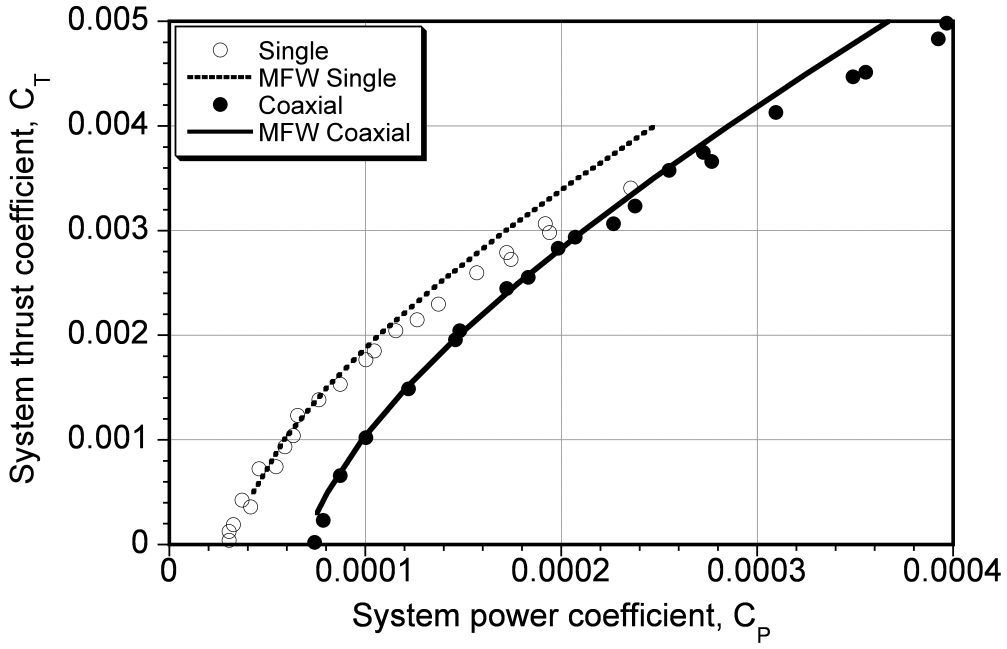

(a) Power polar for Harrington Rotor 1

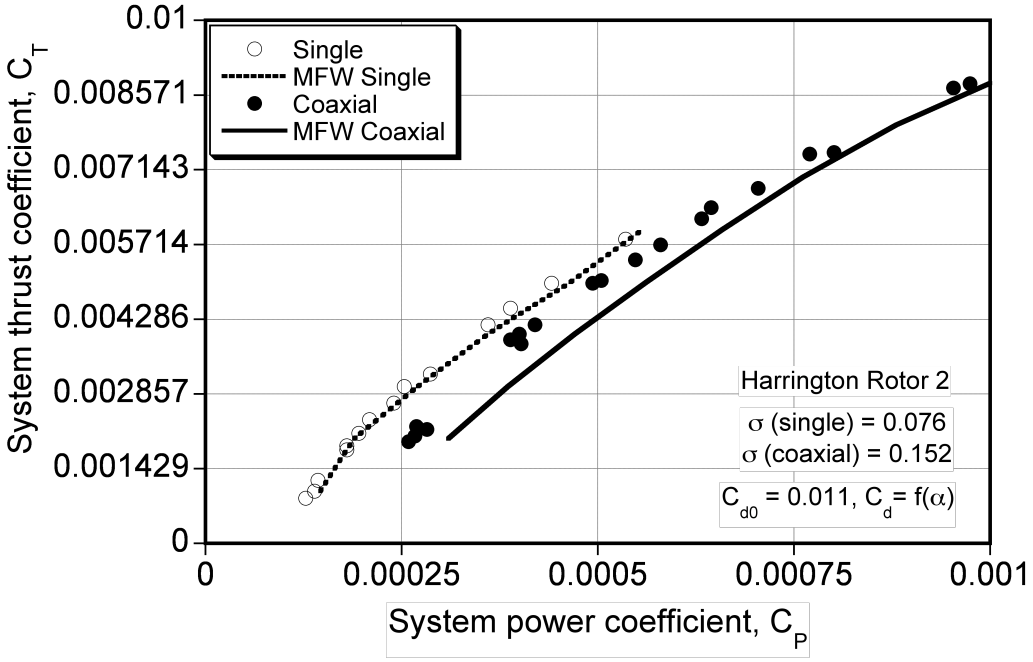

(b) Power polar for Harrington Rotor 2

Fig. 4.5: Comparison of power polars for the Harrington rotor geometries with MFW and measurements.

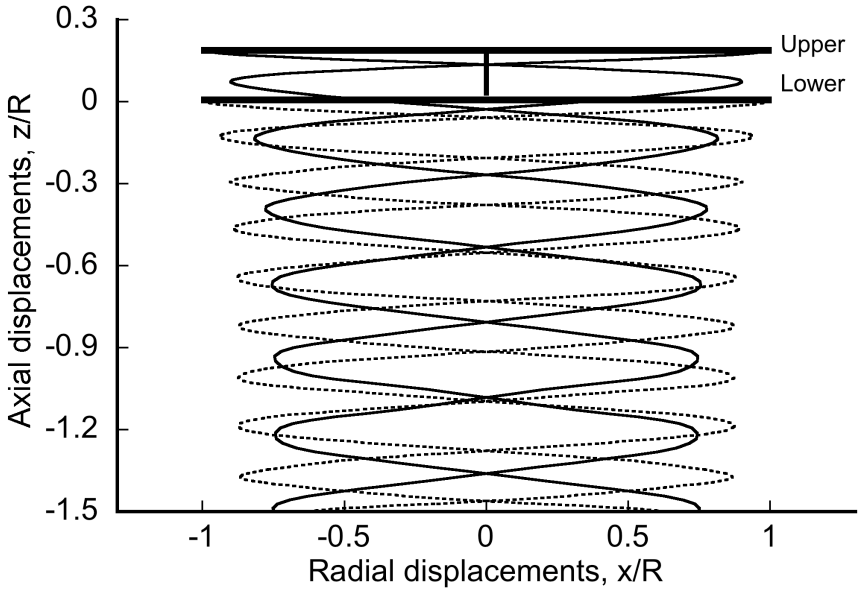

Fig. 4.6: Wake geometry of the Harrington Rotor 1 in hover at $C_T = 0.004$.

the airloads predicted by FVM were compared with those given by the BEMT. In this case, the Harrington Rotor 1 operating at $C_T = 0.004$ was used. The BEMT calculations were performed by assuming the upper wake contraction ratio of 0.82, as predicted by FVM.

Figure 4.7 shows the predicted inflow distribution over the upper and lower rotors of the Harrington Rotor 1 using the FVM and the BEMT. The inflow on the lower rotor is higher than the upper rotor in the region where the slipstream of the upper rotor impinges on the lower rotor. Outside this region, where the lower rotor is not affected by the upper rotor, the inflow reduces and is almost the same as that found on the upper rotor. Notice that the Prandtl tip loss factor used in the BEMT analysis gives good agreement with the tip losses compared to the loading produced by the FVM. Because the BEMT accounts for the effects of the lower rotor on the performance of the upper rotor only through torque balance, the inflow

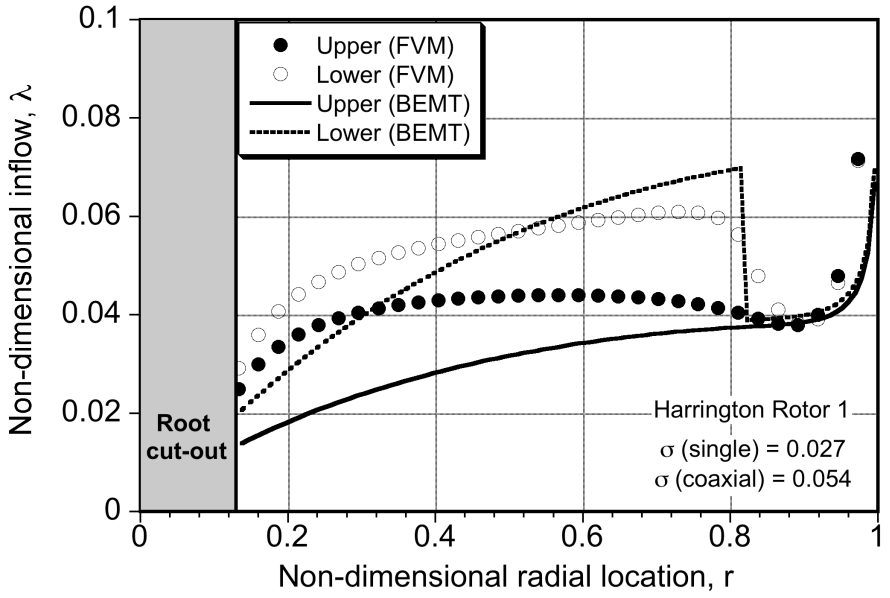

Fig. 4.7: Predicted spanwise inflow distribution on the upper and lower rotors of the Harrington Rotor 1 at $C_T = 0.004$.

predicted on the upper rotor using these two analysis (i.e., BEMT and FVM) is different. The predictions made by the two methodologies also differ in the region on the lower rotor where the wake from the upper rotor impinges upon it, and also toward the root region of the blades. However, considering the fact that the BEMT is a two-dimensional flow methodology and it takes only a few seconds to solve the flow model compared to FVM which is a three-dimensional analysis and takes about an hour to compute flow, BEMT emerges as an efficient and effective tool for the initial optimization of the coaxial rotor geometry.

Figures 4.8 shows the predicted thrust distribution over the upper and lower rotors of the Harrington Rotor 1 using the FVM and BEMT. The results show good agreement. As was suggested by the SMT analysis, at the torque balanced condition the upper rotor carries higher thrust than the lower rotor. This is clear from the

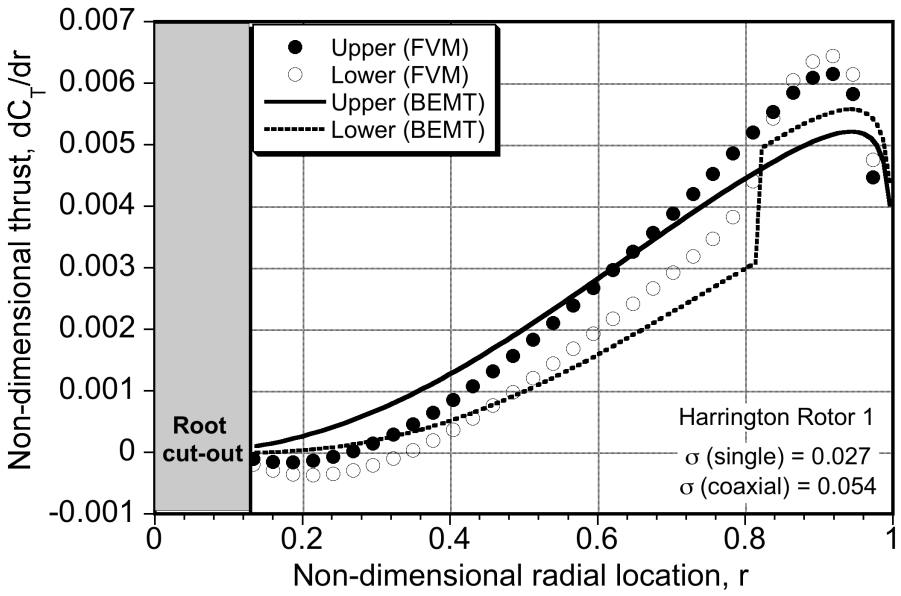

Fig. 4.8: Predicted spanwise thrust distribution on the upper and lower rotors of the Harrington Rotor 1 at $C_T = 0.004$.

results in Figs. 4.7 and 4.8, which show that because the inflow over the inboard part of the lower rotor is higher, it carries lower thrust. Over the outer part of the lower rotor, the thrust becomes equal to the upper rotor in that region. Notice that the thrust on the root section of the upper and lower rotors, as predicted by FVM, is negative; this is because of the higher inflow at these locations.

Figure 4.9 shows the predicted local lift coefficient distribution over the upper and lower rotors of the Harrington Rotor 1 when using the FVM and BEMT. The results show reasonable agreement. The BEMT predicts higher lift coefficients towards the inboard region because it accounts for the lower inflow in that region (being a two-dimensional model). The lift coefficients on both the rotors as predicted by FVM are negative towards the root sections. Notice from Fig. 4.9 that only the tip region can be operating near its best lift-to-drag ratios, which will re-

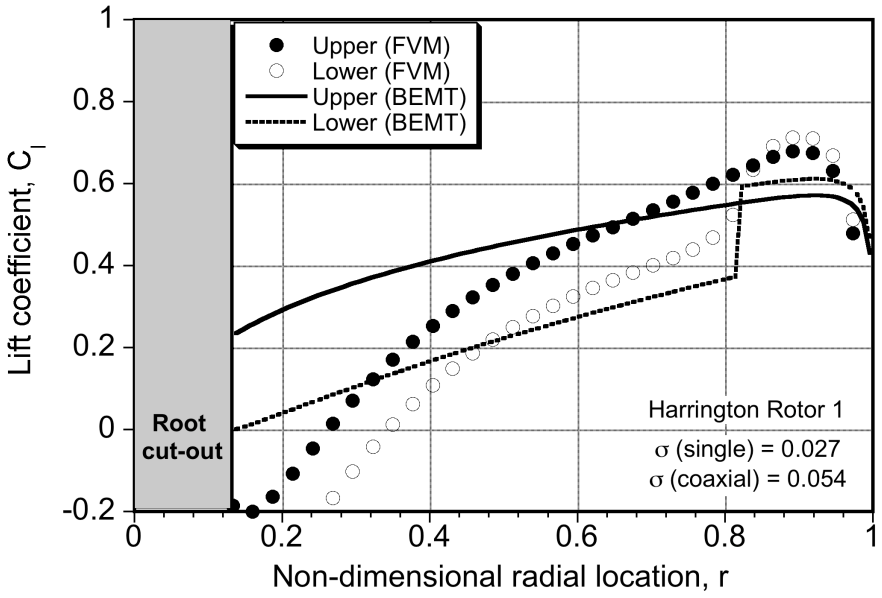

Fig. 4.9: Predicted spanwise lift distribution on the upper and lower rotors of the Harrington Rotor 1 at $C_T = 0.004$.

sult in a higher profile power requirement for the rotors than would otherwise be possible.

Figure 4.10 shows the predicted induced torque distribution over the upper and lower rotors of the Harrington Rotor 1. Again, the BEMT and FVM show good agreement. The induced power distribution on the lower rotor is slightly higher than that on the upper rotor in the region where the wake from the upper rotor impinges upon it.

4.2 Performance Analysis

This section discusses the results obtained by using BEMT and FVM to study the performance of coaxial rotors at different thrust conditions. These studies were

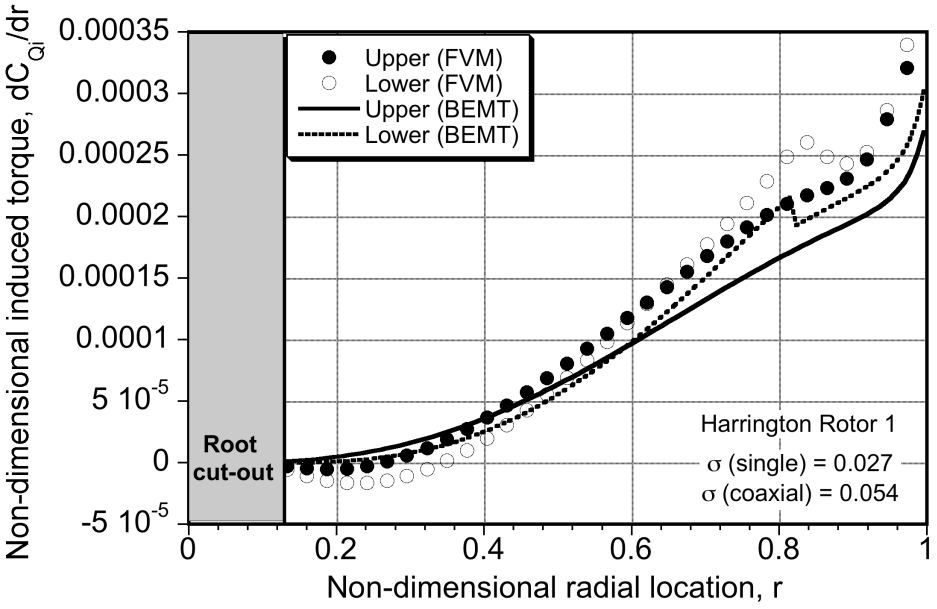

Fig. 4.10: Predicted spanwise induced torque distribution on the upper and lower rotors of the Harrington Rotor 1 at $C_T = 0.004$.

performed using the Harrington Rotor 1 coaxial system. It should be noted that all the results presented are for trimmed flight conditions such that the coaxial system operates at a specified net thrust and the torques of the rotors are equal and opposite to each other.

Table 4.1 shows the variation of trimmed collective blade pitch on the upper and lower rotors to achieve the torque balance. To trim the coaxial system at higher thrusts, the collective angles on both the rotors must increase. The collective blade pitch angle required by the lower rotor is higher than the upper rotor because the lower rotor operates with a higher induced velocity (resulting from the influence of the wake from upper rotor). The collective pitch angles obtained by using BEMT and FVM show good comparison with each other. Because the FVM can completely

Table 4.1: Collective angles of trimmed upper and lower rotors at different system thrust conditions.

Case	C_T	θ_0 (upper) BEMT	θ_0 (lower) BEMT	θ_0 (upper) FVM	θ_0 (lower) FVM
1	0.0003	1.1797°	1.4672°	1.7414°	2.1700°
2	0.0005	1.6775°	2.0382°	2.1950°	2.6470°
3	0.001	2.7678°	3.2317°	3.1900°	3.6600°
4	0.002	4.6912°	5.2267°	4.9980°	5.4740°
5	0.003	6.465°	6.9985°	6.6030°	7.0090°
6	0.004	8.1597°	8.6547°	8.1000°	8.3900°
7	0.005	9.8012°	10.2374°	9.5250°	9.6810°
8	0.006	11.4062°	11.7684°	10.905°	10.922°

account for the effects of the performance of lower rotor on upper rotor, it predicts a higher inflow on both the rotors than using the BEMT. Therefore, the collective pitch angles obtained when using FVM are higher than those obtained from the BEMT.

Figures 4.11 and 4.12 show the variation of the ratio of thrust shared by upper and lower rotors to the total system thrust $\left(\text{i.e., } \frac{C_{T_u}}{C_T} \text{ and } \frac{C_{T_l}}{C_T}, \text{respectively}\right)$, at the torque balanced condition. These figures show that the ratios $\frac{C_{T_u}}{C_T}$ and $\frac{C_{T_l}}{C_T}$ as

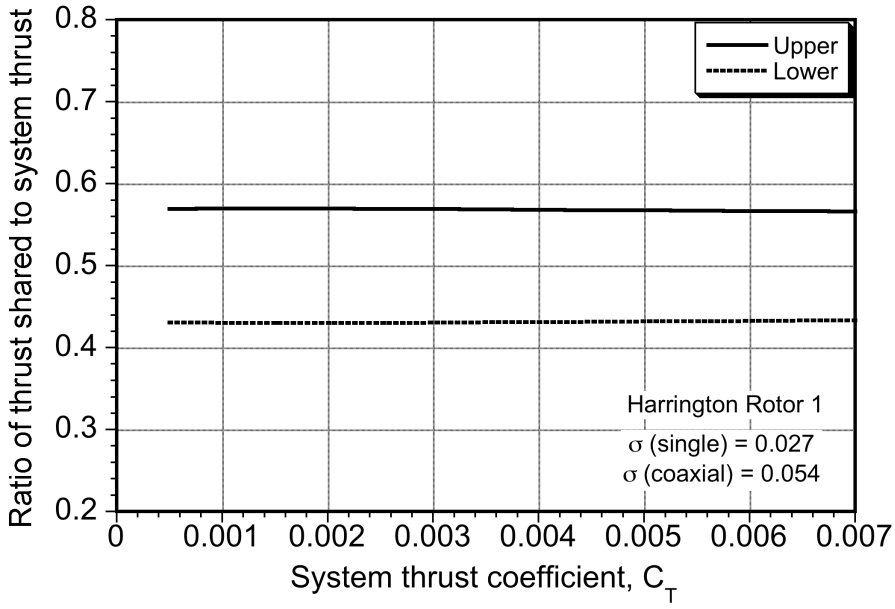

Fig. 4.11: Variation of the thrust shared by upper and lower rotors with system thrust coefficient.(Results are obtained using BEMT.)

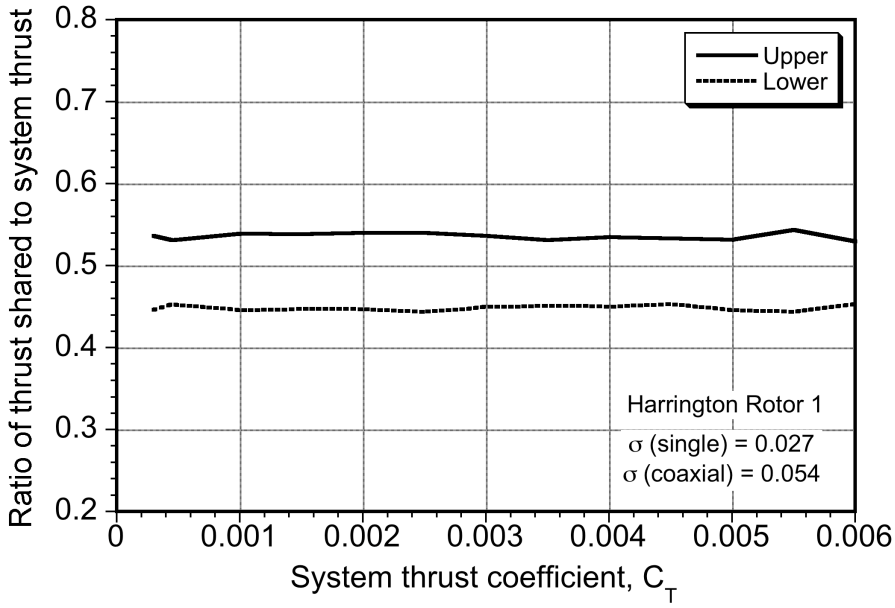

Fig. 4.12: Variation of the thrust shared by upper and lower rotors with system thrust coefficient. (Results are obtained using FVM.)

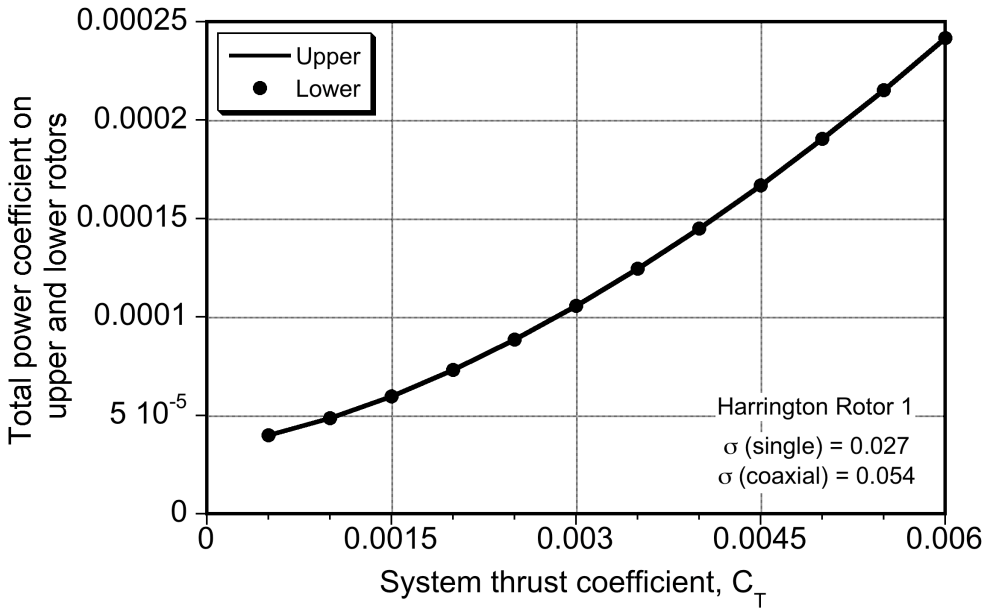

Fig. 4.13: Variation of total power coefficients on upper and lower rotors with system thrust coefficient. (Results are obtained using BEMT.)

obtained from both BEMT and FVM remain almost constant. The BEMT predicts that the upper and lower rotors share 57% and 43% of the total system thrust, respectively. The FVM predicts the share to be 55% and 45% for the upper and lower rotors, respectively. Again, these results show that the BEMT and FVM are generally in good agreement with each other.

Because both the rotors were operated at torque balance, the total power coefficients of both the rotors should be same. Figures 4.14 and 4.13 show that the total power coefficients for the two rotors are equal to within the specified accuracy at all thrust conditions. However, the total power required by both the rotors increases with increases in system thrust.

This result can be further explained using Figs. 4.15 and 4.16, which show that

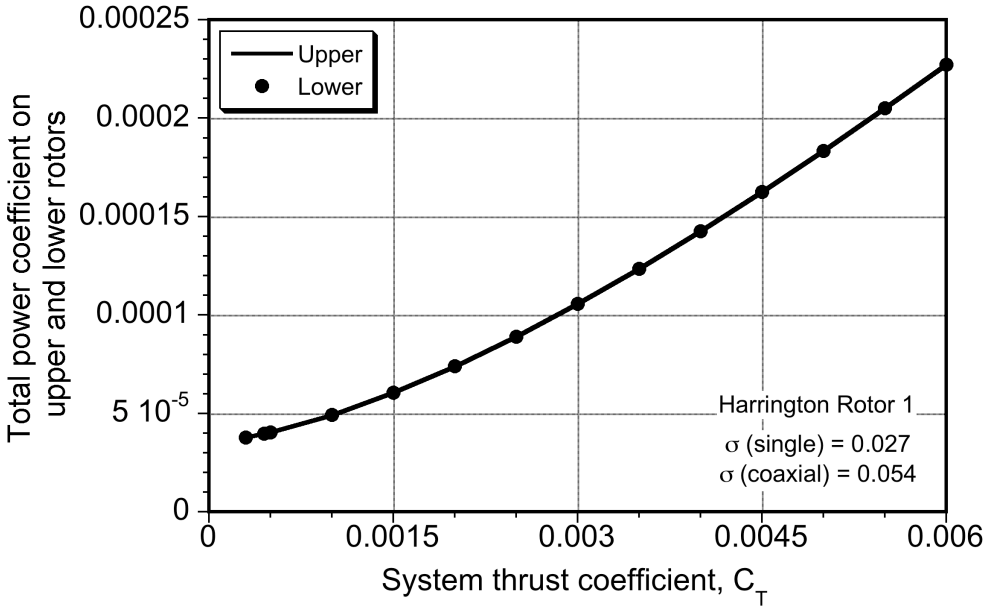

Fig. 4.14: Variation of total power coefficients on upper and lower rotors with system thrust coefficient. (Results are obtained using FVM.)

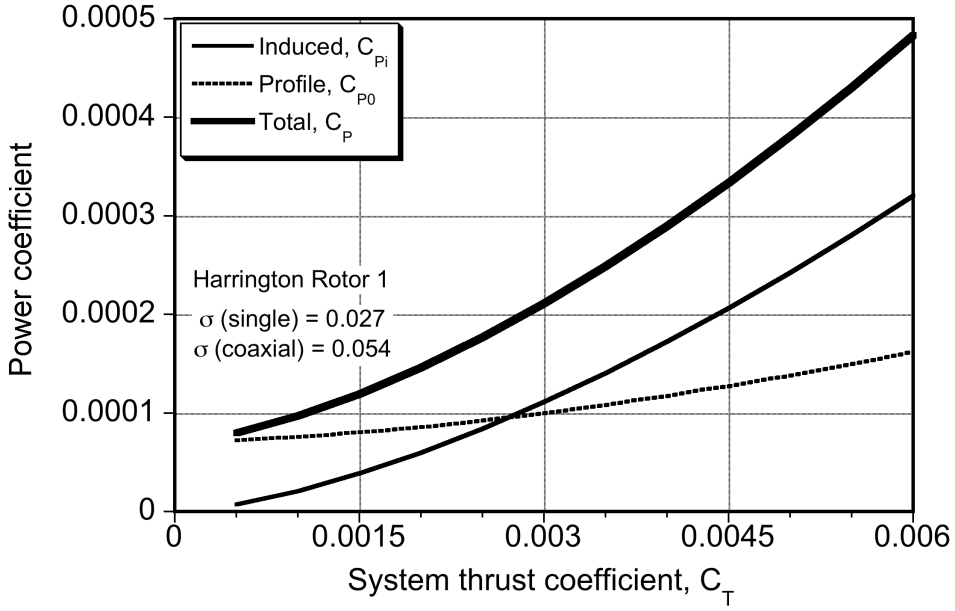

Fig. 4.15: Variation of induced, profile and total power coefficients of the coaxial rotor system with system thrust coefficient. (Results are obtained using BEMT.)

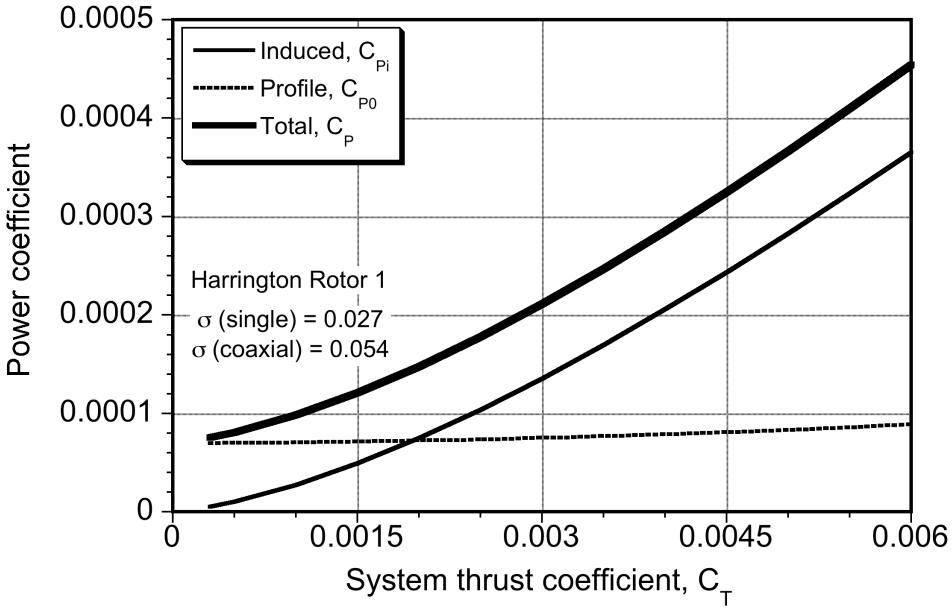

Fig. 4.16: Variation of induced, profile and total power coefficients of the coaxial rotor system with system thrust coefficient. (Results are obtained using FVM.)

the total power required increases with system thrust coefficient. This is because the induced power, which is a major portion of the total power in hover, increases with thrust coefficient. The profile power also increases with thrust coefficient using both of these models, because the local drag coefficient is a function of section angle of attack. In the BEMT, the profile drag is computed using Eq. 4.4, and in the FVM by using Beddoes' nonlinear airfoil model (Ref. 33).

4.3 Rotor Spacing Studies

The FVM has the ability to model the aerodynamic interference region between the upper and lower rotors, hence this method can help to quantify the effects of rotor spacing on the airloads distribution and performance levels of both rotors.

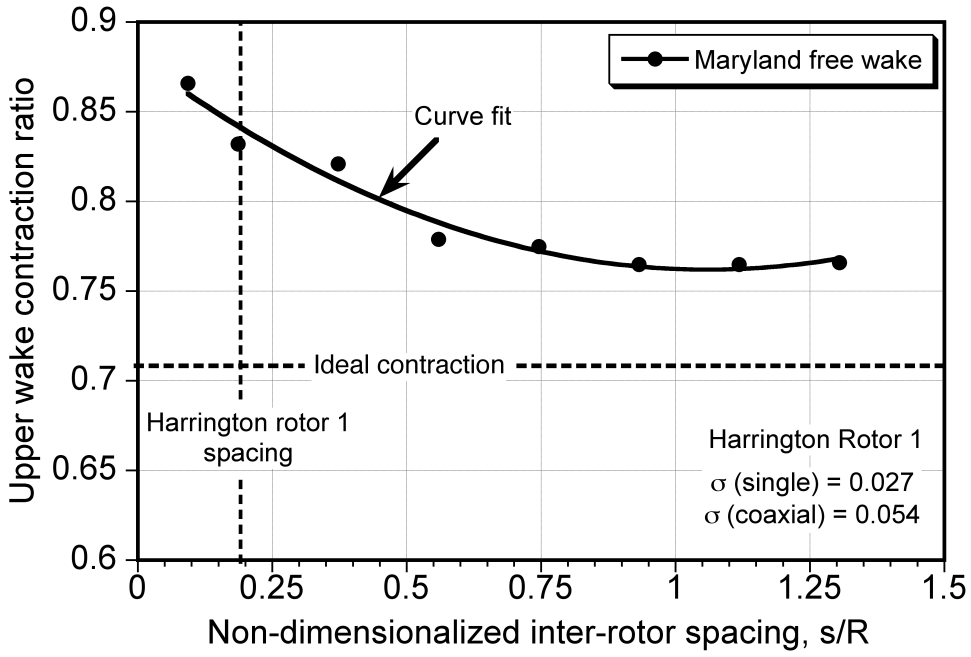

Fig. 4.17: Variation of the upper rotor wake contraction (when it impinges lower rotor) as a function of inter-rotor spacing.

With an increase in the distance between the upper and lower rotors, the upper rotor wake is known to become more significantly contracted when it impinges on the lower rotor, until it becomes fully contracted at higher rotor spacings.

Figure 4.17 shows the variation wake contraction of the upper rotor as a function of the inter-rotor spacing (both parameters are shown as a faction of rotor radius) when it impinges on the lower rotor. The slipstream from the upper rotor becomes almost fully developed when the distance between the two rotors is larger than 75% of the blade radius. The assumption that the lower rotor is placed in the fully developed slipstream of upper rotor may not be such a good one for either of the Harrington rotors because the inter-rotor spacings in these cases are below this spacing threshold.

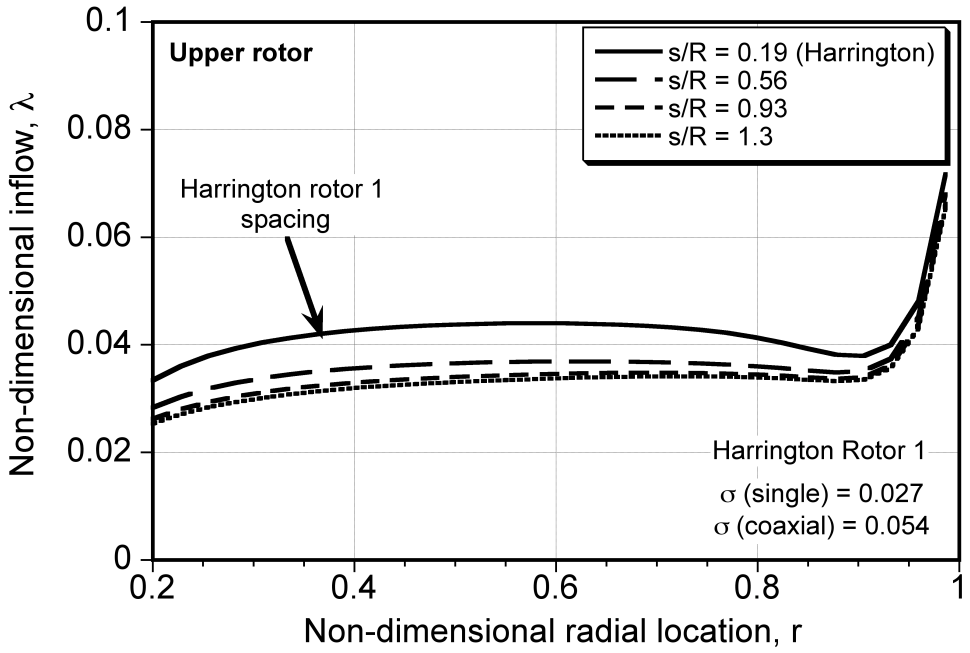

(a) Upper rotor

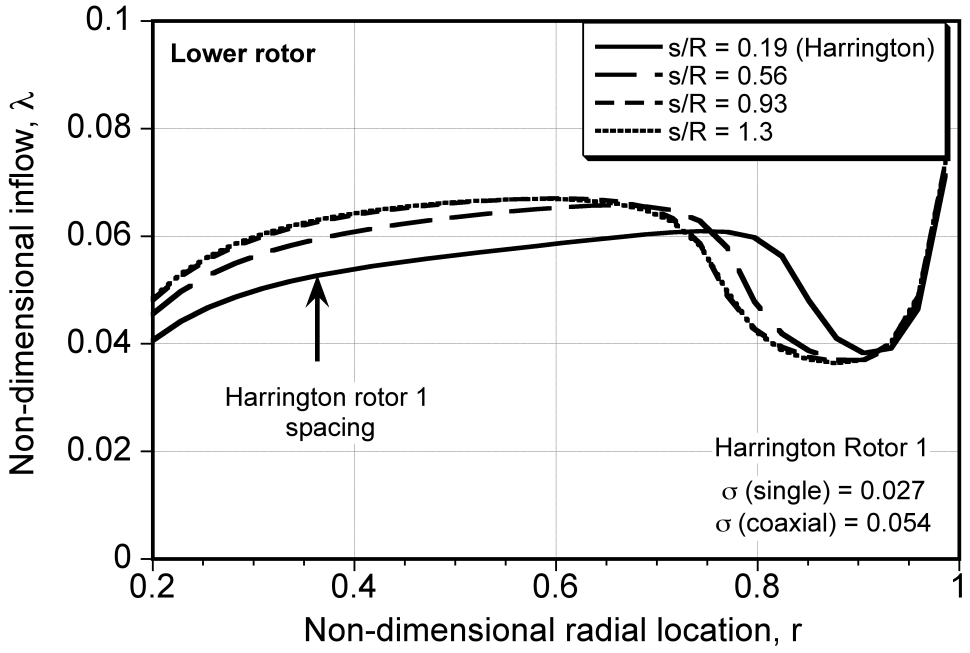

(b) Lower rotor

Fig. 4.18: Spanwise inflow distribution on the upper and lower rotors with different inter-rotor spacings.

It should be mentioned that the airloads distribution, and hence the performance of the two rotors, has an effect on each other in two ways. First, there is a reciprocal effect through the slipstreams or the induced flow fields of the two rotors. Second, there is an effect through the overall system trim at the torque balanced operating condition. Figures 4.18(a) and 4.18(b) show the variation of the spanwise inflow over the upper and lower rotors, respectively, as a function of inter-rotor spacings. As the spacing increases, the inflow on the upper rotor decreases—see Fig. 4.18(a). At the same time, the inflow on the lower rotor increases in the region where the upper rotor wake impinges upon it, and decreases over the areas of the rotor disk that are unaffected by the slipstream from the upper rotor.

The increase in inflow on the lower rotor at higher inter-rotor spacings in the region affected by the upper rotor is a result of the higher slipstream velocities from the upper rotor wake when it impinges on the lower rotor. This can be explained from the principle of conservation of mass, i.e., as the inter-rotor spacings increases the upper rotor slipstream area decreases when it impinges the lower rotor and so the slipstream velocity will also increase. The region on the lower rotor that is unaffected by the wake from the upper rotor behaves normally, i.e., the inflow reduces there as the inter-rotor spacing increases.

The spanwise variation of the time-averaged inflow on the blades of both the rotors as a function of inter-rotor spacing is shown in Fig. 4.19. The average inflow on the upper rotor reduces and then becomes almost constant when the spacing between the two rotors reaches 75% of the blade radius. On the lower rotor, the average inflow increases gradually and then becomes almost constant when spacing

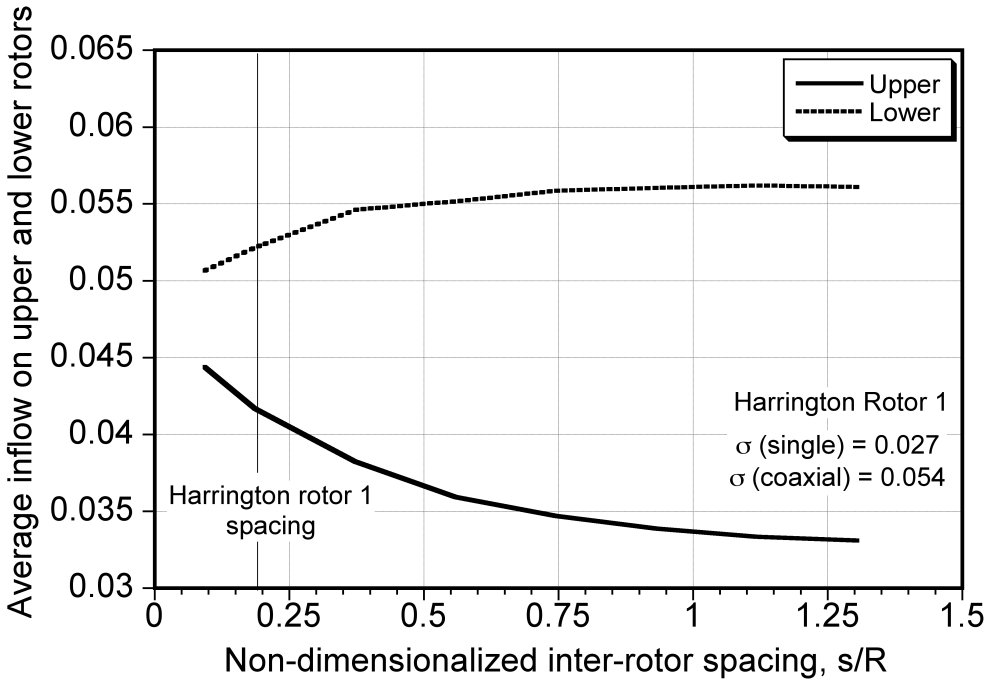

Fig. 4.19: Variation of the average inflows on upper and lower rotors with inter-rotor spacing. (Harrington Rotor 1).

reaches 75% of the blade radius. This gradual increase of the average inflow is a result of the decrease in inflow in the region affected by the upper rotor, which cancels the effect of an increase in the inflow inboard where upper rotor wake impinges upon it—see Fig. 4.18(b). Figure 4.20 shows that the variation of the collective blade pitch angles on both rotors mimics the variation of the average inflow (Fig. 4.19), which would be expected.

As previously mentioned, the rotors of the coaxial operate at a torque balanced condition, so the increase in the induced losses on the lower rotor requires the thrust carried by the upper rotor to increase—see Fig. 4.21(a). On the lower rotor, the thrust decreases in the region where inflow was higher, and increases outside this

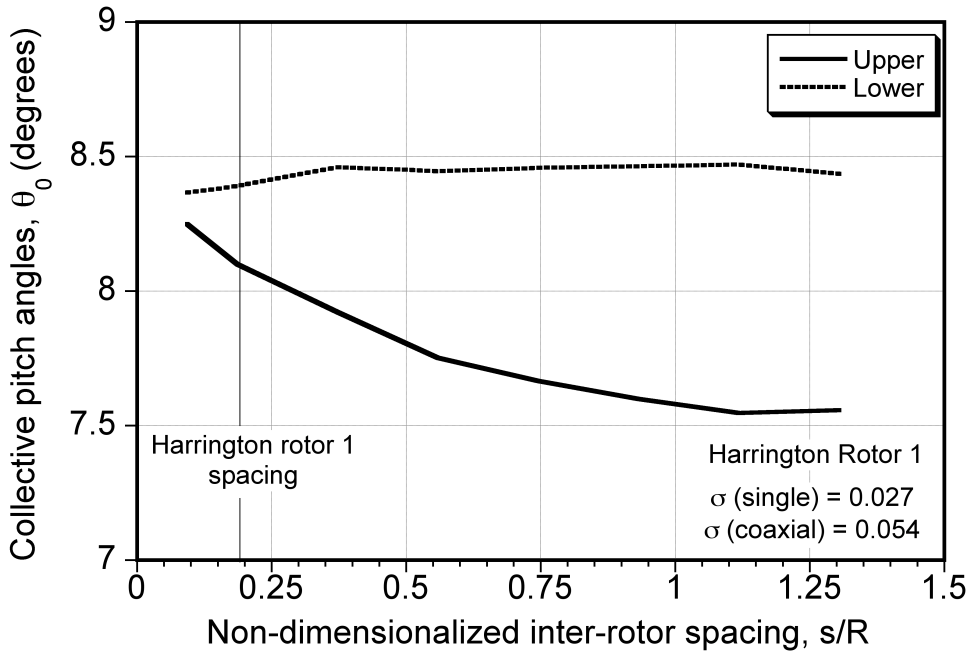

Fig. 4.20: Variation of the collective pitch angles on upper and lower rotors with inter-rotor spacing. (Harrington Rotor 1).

region—see Fig. 4.21(b). The average thrust shared by the rotors as a function of the inter-rotor spacing is shown in Fig. 4.22. Because the average inflow on the lower rotor increases with an increase in the inter-rotor spacing, the thrust carried by the upper rotor increases when the comparison is performed at a torque balance. The thrust carried by the lower rotor decreases to maintain a specified overall system thrust. Notice that the thrust sharing of the rotors become almost constant at higher inter-rotor spacings.

The total power required by both the rotors should be the same so as to maintain a torque balance (assuming the rotational speeds of both rotors are equal). Figure 4.23 shows that the induced power reduces with an increase in the inter-rotor spacing, and the profile power remains almost constant. This results in a net

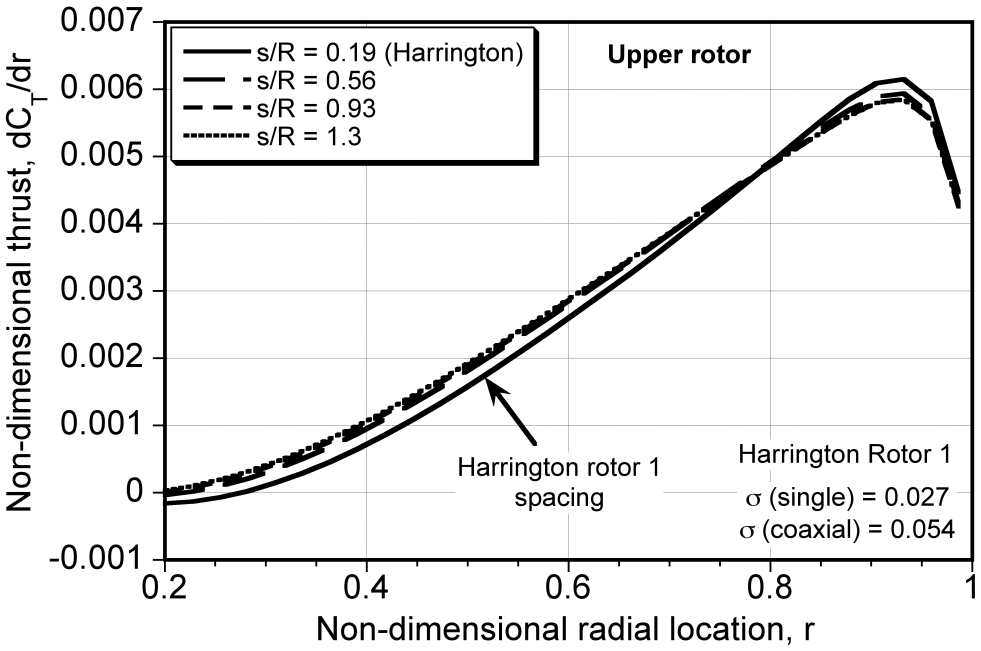

(a) Upper rotor

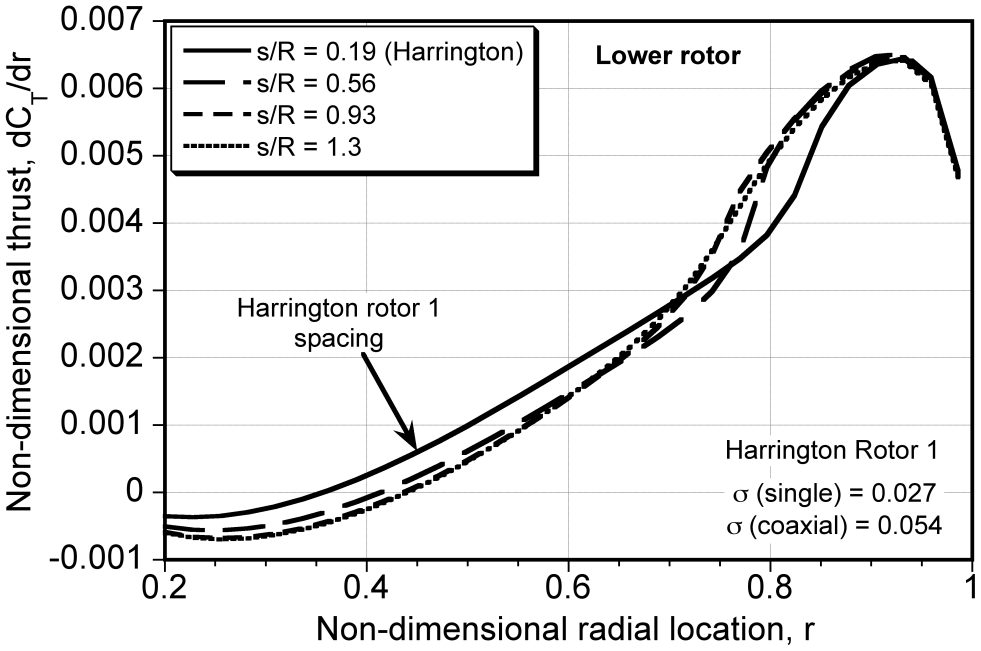

(b) Lower rotor

Fig. 4.21: Spanwise thrust distribution on upper and lower rotors with different inter-rotor spacing. (Harrington Rotor 1).

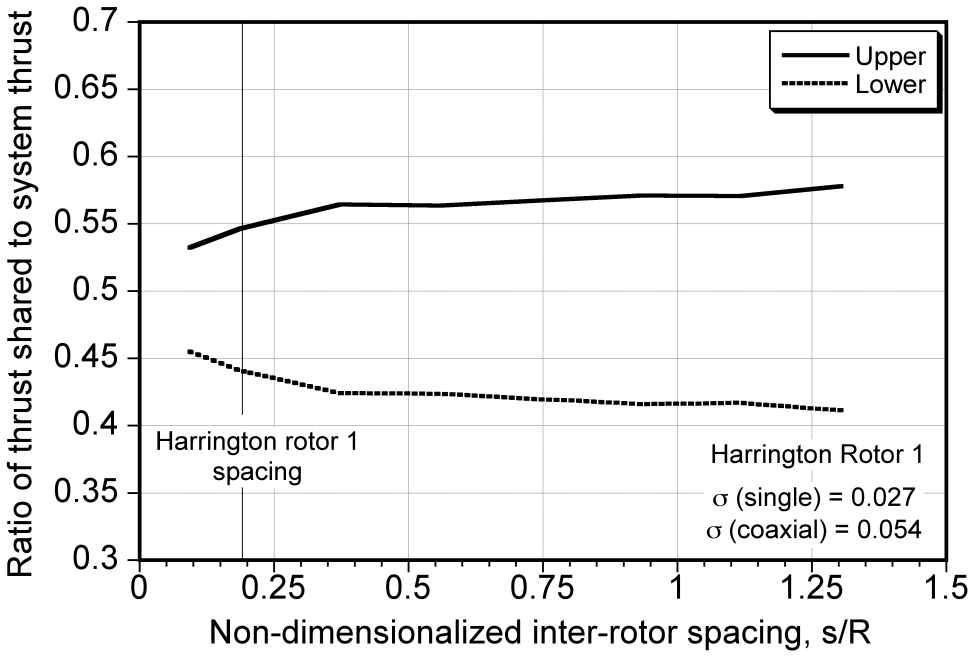

Fig. 4.22: Variation of the average thrusts shared by upper and lower rotors with inter-rotor spacing. (Harrington Rotor 1).

decrease in the total power required for the system at the higher rotor spacings. Therefore, it is apparent that it is the induced part of the total power that drives the overall torque balance, with some smaller contributions from the profile parts.

Figures 4.24(a) and 4.24(b) show the variations of the spanwise distributions of induced power coefficient on the upper and lower rotors, respectively, for different inter-rotor spacings. On the inner regions of the upper rotor, the thrust increases and the inflow decreases with an increase in rotor spacing, causing almost no change in the induced power levels. Whereas on the outer regions, both the thrust and and the inflow reduce, resulting in a decrease in the torque. On the lower rotor, the inflow increases and thrust decreases in the region affected by the slipstream from the upper rotor, resulting in a net decrease in the induced torque. In the regions

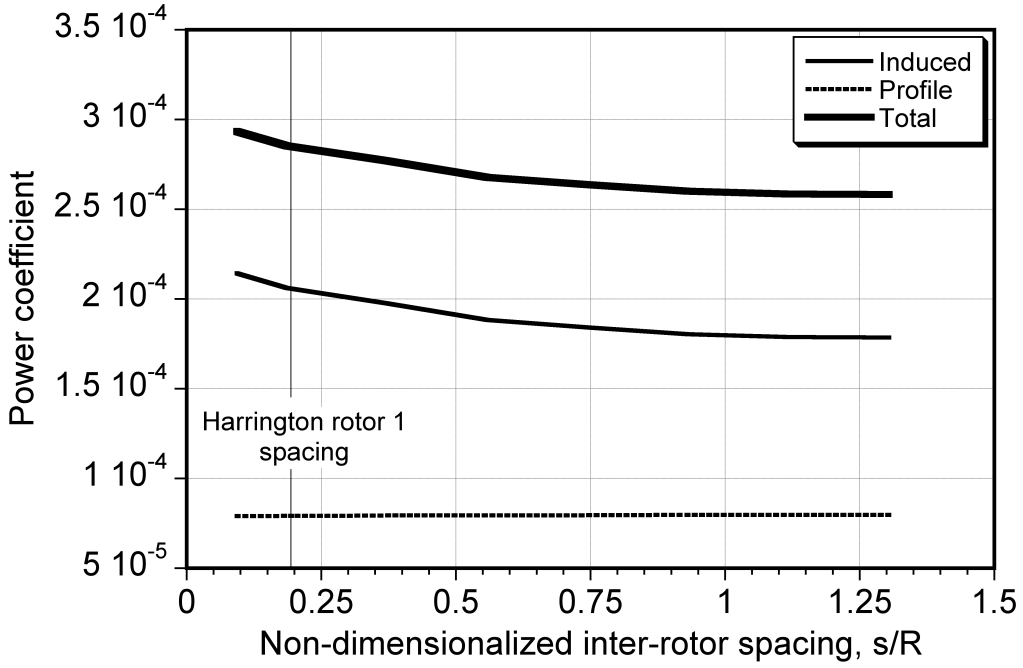

Fig. 4.23: Variation of coaxial rotor system induced, profile and total power coefficients with inter-rotor spacing. (Harrington Rotor 1).

on the lower rotor that are unaffected by the wake from the upper rotor, the inflow decreases and thrust increases, resulting again in a reduction in the induced torque coefficient at higher rotor spacings.

The variation of total induced power coefficient with rotor-on-rotor spacing is shown in Fig. 4.25. Notice that there are some small differences in the induced power coefficients on both the rotors, with the value being higher on the lower rotor. Figure 4.26 shows that the total induced power factor decreases with an increase in the inter-rotor spacing.

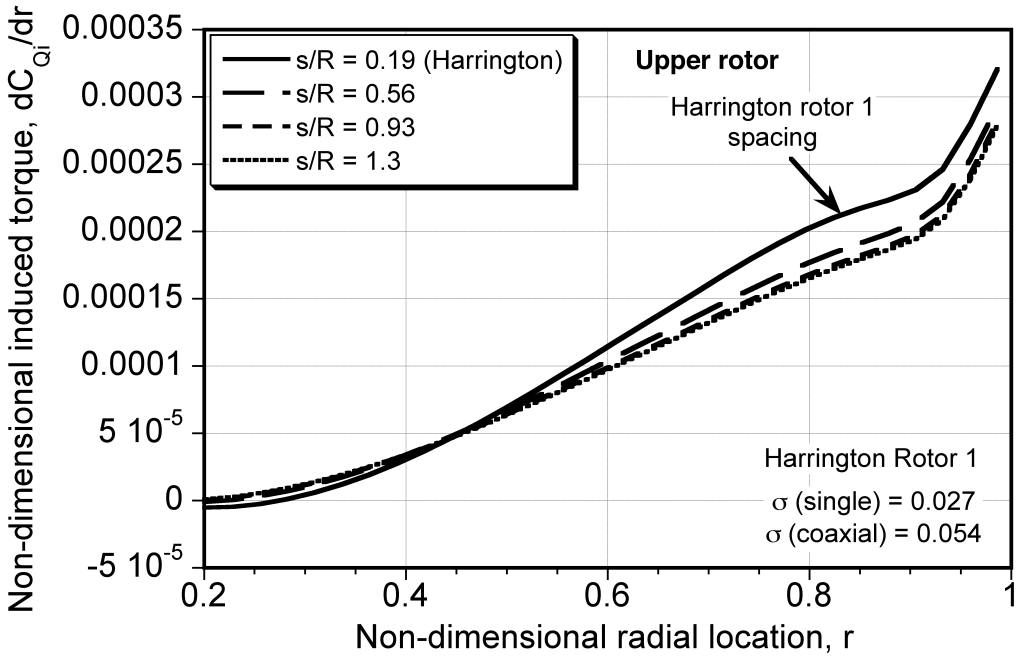

(a) Upper rotor

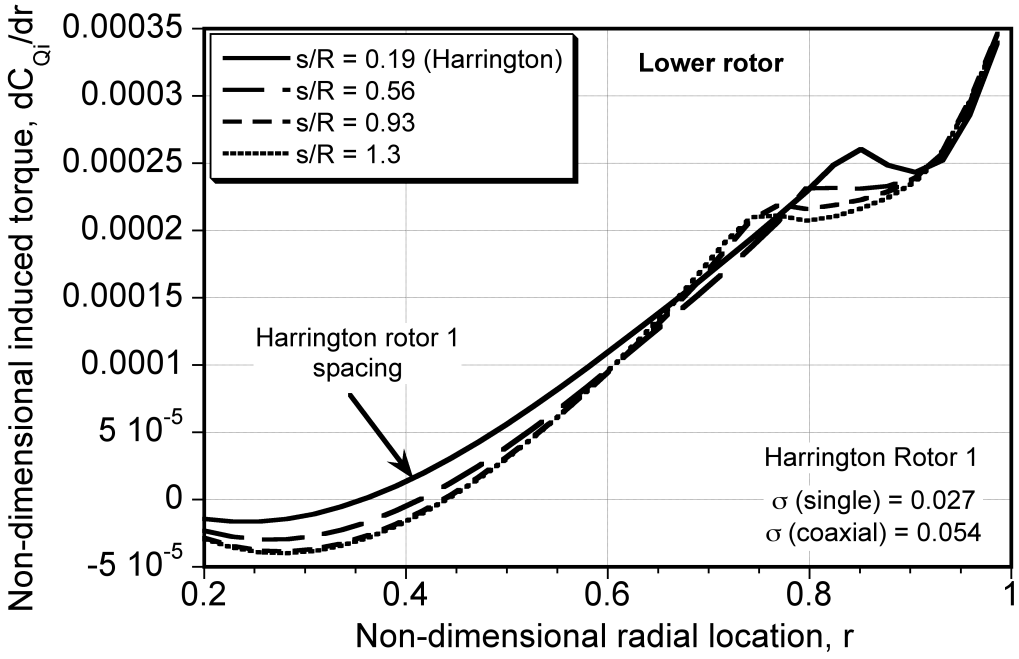

(b) Lower rotor

Fig. 4.24: Spanwise induced torque distribution on upper and lower rotors with different inter-rotor spacings. (Harrington Rotor 1)

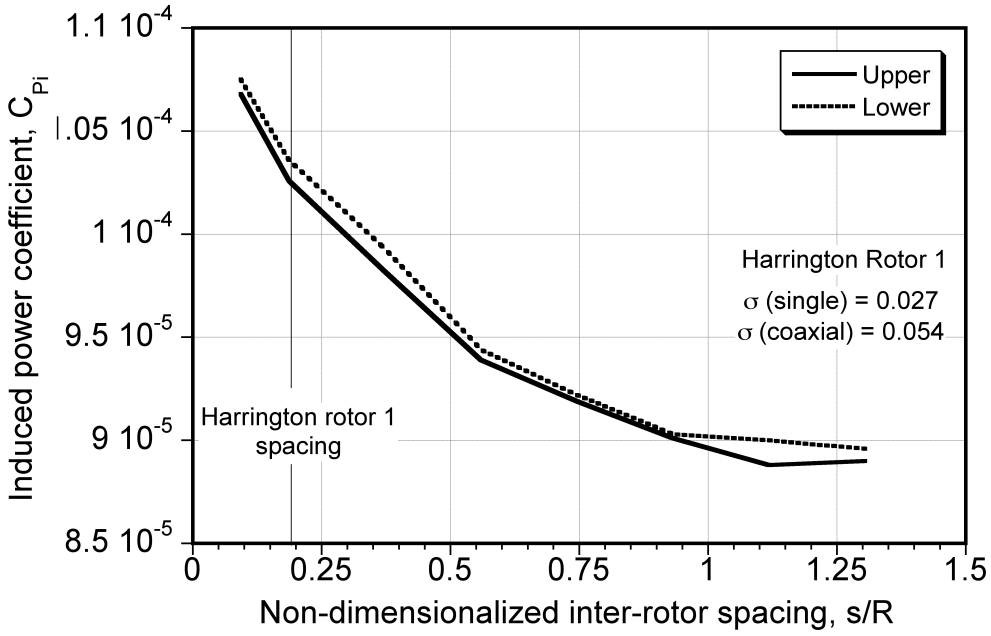

Fig. 4.25: Variation of the induced power coefficients on upper and lower rotor in a coaxial rotor system with inter-rotor spacing. (Harrington Rotor 1).

4.3.1 Effect of the Lower Rotor on the Upper Rotor

With a coaxial rotor system, each rotor affects the performance of the other through the induced flow field and also through the overall trim requirement of the system to maintain torque balance. It is obvious that the upper rotor affects the performance of the lower rotor. However, to what extent the lower rotor affects the performance of the upper rotor is still not well understood. In the formulation of more parsimonious mathematical models such as the BEMT and SMT, it is assumed that the induced flow field of the lower rotor does not affect the performance of the upper rotor. In other words, the resultant flows are obtained by superposition. This means that the lower rotor affects the inflow and thrust distributions on the upper rotor in the process of maintaining an overall trim state at a specified thrust

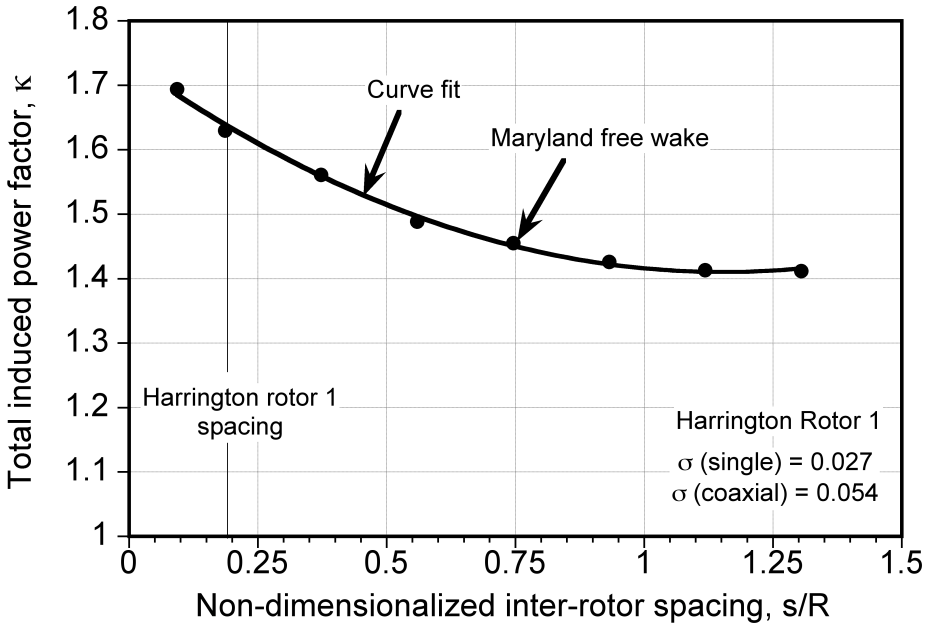

Fig. 4.26: Variation of total induced power factor of the Harrington Rotor 1 with inter-rotor spacing .

condition and at a torque balance.

The free-vortex wake model can solve the complicated flow physics in the interference region and hence, can better quantify the effects of the lower rotor on the upper rotor. As a byproduct, the results can help to validate the assumptions made with the simpler mathematical models like the BEMT. As mentioned previously, each rotor of a coaxial system affects the performance of the other through the need for a trimmed solution at torque balance, and through the induced effects in its slipstream. It is very difficult to isolate these two effects from each other. Therefore, the aim of the present study was to quantify the total effects of the lower rotor on the performance of the upper rotor.

This goal was achieved by isolating the upper rotor from the coaxial system,

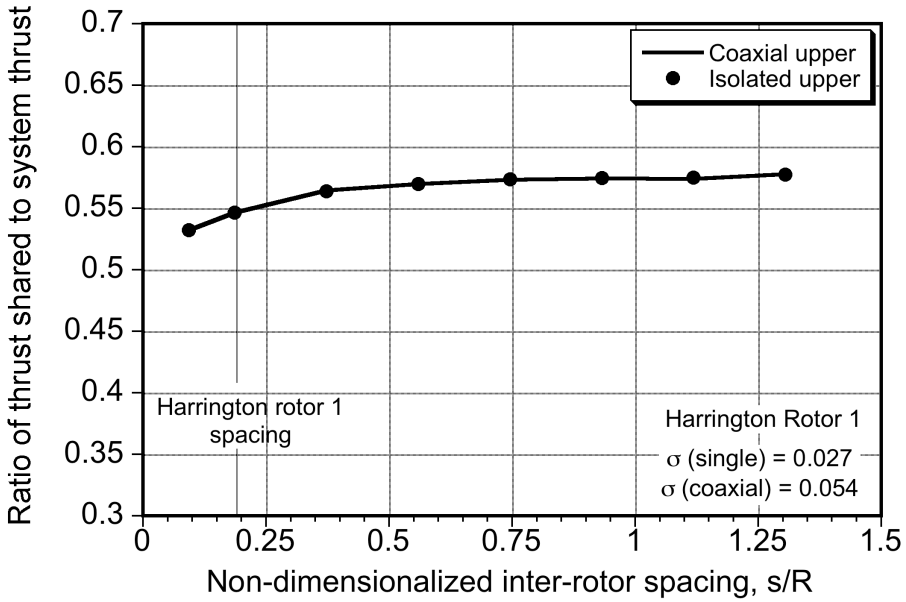

Fig. 4.27: Variation of thrust shared by upper rotor in a coaxial system and as an isolated rotor with inter-rotor spacing.

and analyzing it as a single rotor at the same disk and blade loadings at which it was operating in the coaxial system at the torque balance. By comparing the performance of the upper rotor at different inter-rotor spacings with an isolated rotor (at same disk loading as in the coaxial system at any given inter-rotor spacing), the effects of the lower rotor on the performance of the upper rotor can then be determined.

Figure 4.27 shows the variation of the thrust sharing by the upper rotor at different inter-rotor spacings. Notice that the isolated upper rotor was trimmed to same thrust coefficient for comparison. From here onwards, this isolated rotor (which operates at the same thrust as that shared by the upper rotor of the coaxial system at a specific inter-rotor spacing) will be referred to the equivalent single rotor

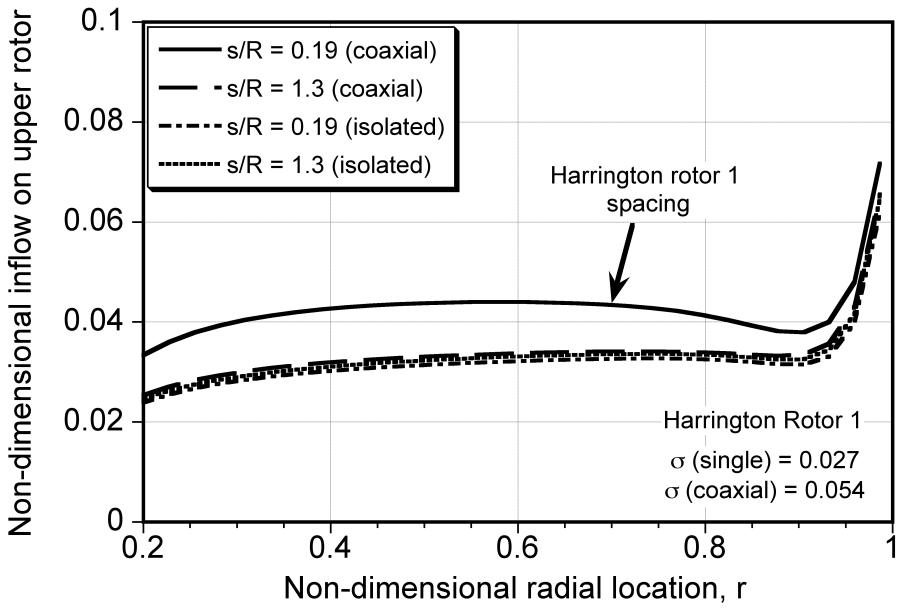

Fig. 4.28: Spanwise inflow variation on the upper rotor in a coaxial system and as an isolated rotor with inter-rotor spacing.

at that thrust condition.

Figure 4.28 shows the variation of the spanwise inflow distribution on the upper rotor compared to the equivalent single rotor for different inter-rotor spacings. At the inter-rotor spacing of the Harrington Rotor 1 (i.e., at $s/R = 0.19$), the inflow on the upper rotor is higher than that on the equivalent isolated single rotor. This shows that the performance of the upper rotor is affected significantly by the lower rotor. At higher inter-rotor spacings, the inflow on the upper rotor reduces and thrust shared by the upper rotor increases—see Fig. 4.27. Because of the increase in thrust sharing by the upper rotor at higher inter-rotor spacings, the inflow on the equivalent single rotor also increases slightly.

Notice that the difference between the inflows for the two cases that were

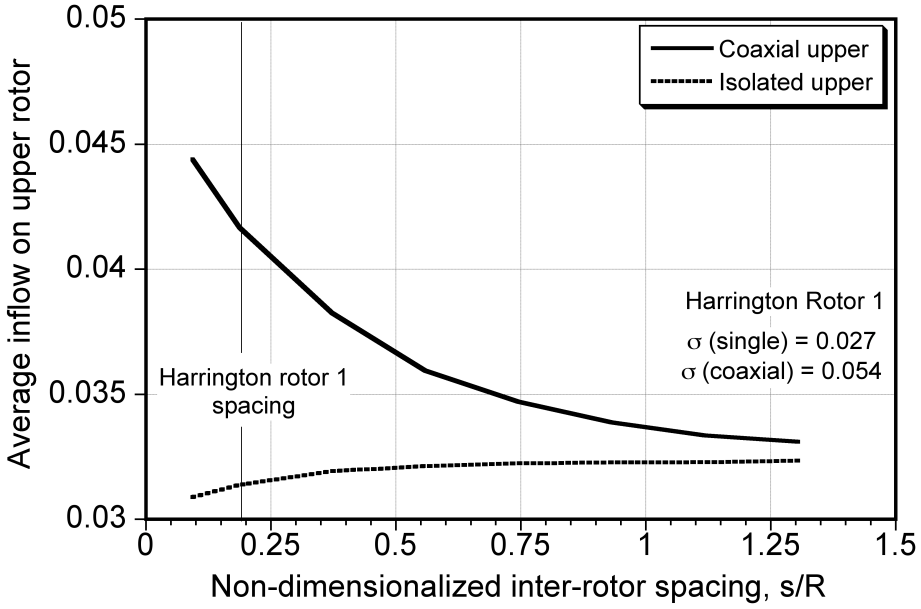

Fig. 4.29: Variation of the average inflow on upper rotor in a coaxial system and as an isolated rotor with inter-rotor spacing.

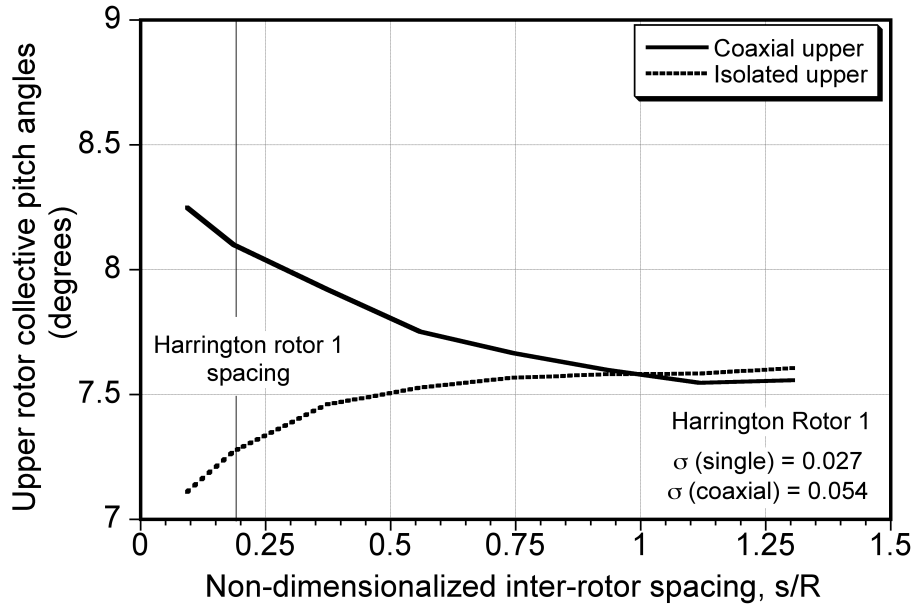

Fig. 4.30: Variation of the upper rotor blade pitch collective angle in a coaxial system and as an isolated rotor with inter-rotor spacing.

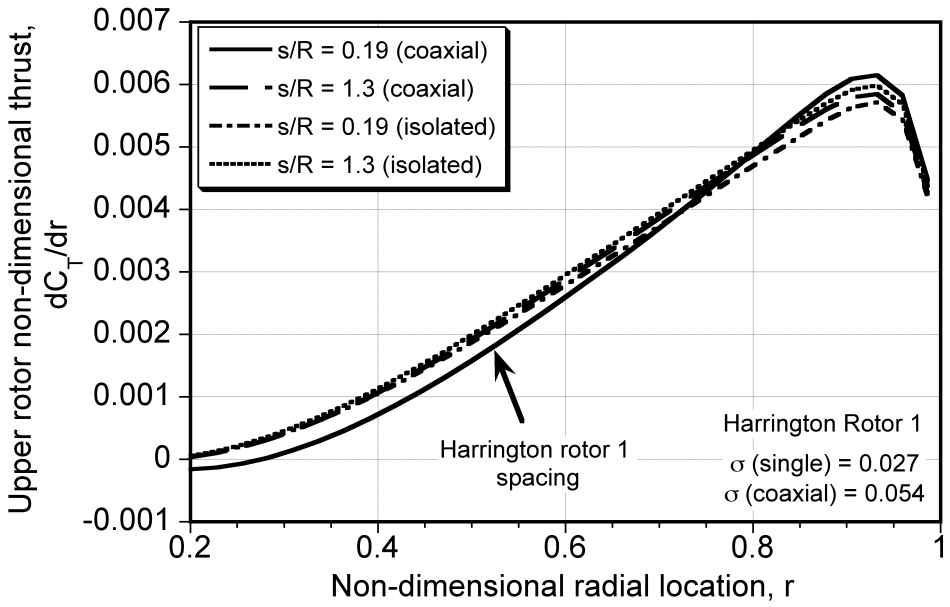

Fig. 4.31: Spanwise thrust distribution on the upper rotor in a coaxial system and as an isolated rotor with inter-rotor spacing.

obtained at same disk loading decreases when a coaxial rotor is operated at higher inter-rotor spacings. This effect can be further seen in Fig. 4.29, which shows the average inflow on the upper rotor and as an isolated rotor (at the same disk loading) at different inter-rotor spacings. The difference between the two inflows reduces at higher inter-rotor spacings. Figure 4.30 shows the variation of the blade collective angles, which were found to vary in the same manner as the average inflow. These results show that the lower rotor does affect the performance of the upper rotor at smaller inter-rotor spacings (e.g., for the Harrington Rotor 1) but the effect reduces significantly as the inter-rotor spacing increases.

Figure 4.31 shows the variation of the thrust sharing on upper rotor and as an equivalent isolated rotor for different inter-rotor spacings. At the Harrington Rotor

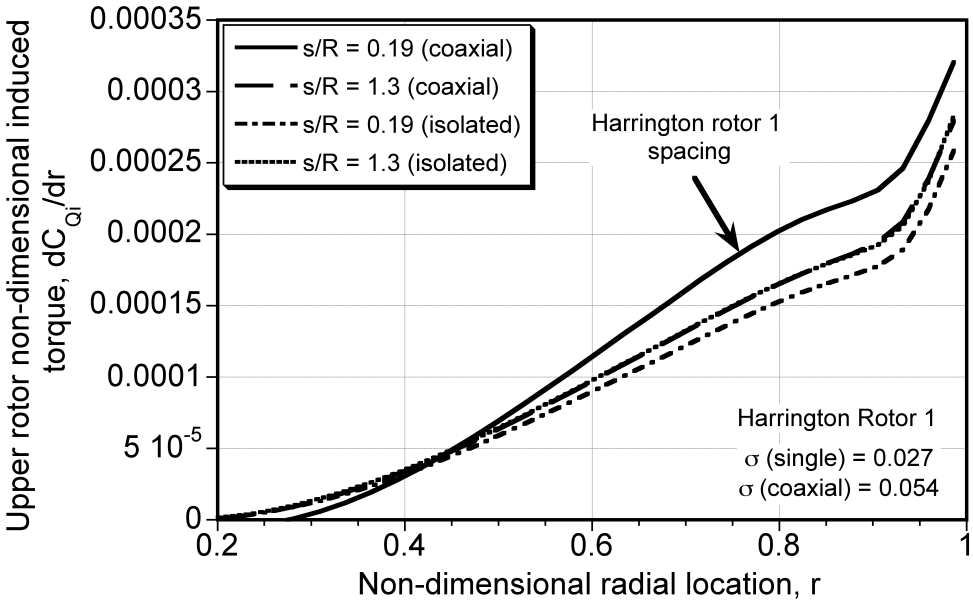

Fig. 4.32: Spanwise induced torque coefficient distribution on the upper rotor in a coaxial system and as an isolated rotor with inter-rotor spacing.

1 inter-rotor spacing (i.e., $s/R = 0.19$), the thrust distribution on the upper rotor is lower over the inboard region than found for the single rotor at same disk loading. Notice that the total thrust on the upper rotor in the coaxial system and as single rotor is same at each inter-rotor spacing. The thrust on the upper rotor increases at higher inter-rotor spacings to balance the torque produced on the lower rotor as a result of the higher induced losses (as explained in the previous section).

Figure 4.32 shows the induced power coefficient distribution on the upper rotor of the coaxial and the equivalent isolated rotor. The difference between the induced powers are significantly higher at the lower spacings. This difference reduces for higher inter-rotor spacings. The variation of the total induced power coefficient for the upper rotor and the equivalent single rotor at different inter-rotor spacings is

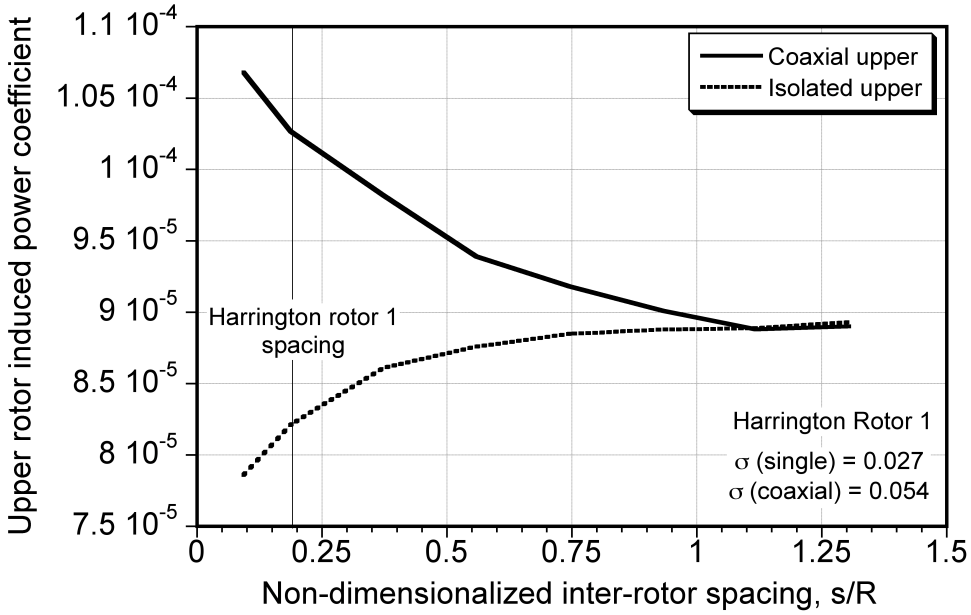

Fig. 4.33: Variation of the upper rotor induced power coefficient in a coaxial system and as an isolated rotor with inter-rotor spacing.

shown in Fig. 4.33. The results clearly show that at higher inter-rotor spacings the difference in induced powers between the upper rotor and equivalent isolated rotor decreases. Therefore, it can be concluded from this study that at smaller rotor-on-rotor distance (e.g., in the case of the Harrington Rotor 1), the lower rotor does indeed affect the performance of the upper rotor.

4.4 The Effects of Blade Twist

Before proceeding towards the optimization of blade twist for a coaxial rotor system, an understanding of the effects of changing blade twist on any one of the rotors on the performance of the coaxial system was necessary. Because the performance of the rotors of a coaxial system are interdependent, how the blade twist on

one rotor affected the performance of the other rotor (and hence the performance of the system) is not well understood.

As has already been suggested in Ref. 20, the optimum coaxial rotor design should minimize the total induced losses of the coaxial system. This condition can be achieved by designing for uniform disk loading on both of the rotors of the coaxial system. This is equivalent to having a linear thrust distribution on both the rotors and uniform inflow distribution on upper rotor, with a double valued uniform inflow distribution on the inner and outer regions of the lower rotor. It was shown in Ref. 20 that in the ideal case, these conditions can be met by having hyperbolic twist distribution on upper rotor and double hyperbolic twist distribution on lower rotor.

Because a linear twist distribution is a good approximation to hyperbolic twist distribution over the outer parts of the blade, in the present study the effects of a linear twist were studied on both the rotors separately. First, only the blades of the lower rotor were twisted linearly, and the changes on upper and lower rotor performance were then analyzed. The upper rotor blades were then twisted linearly (and the lower rotor blades were kept untwisted) and the effects on the performance were analyzed. This study was performed on Harrington Rotor 1 system, using both the BEMT and the FVM, at a thrust coefficient of 0.004. Notice that all the results in the present analysis were obtained such that the torque produced by the upper rotor is balanced by the lower rotor. So besides the wake interference effects between the two rotors, there is a coupling between them to satisfy a torque balance. Notice that the legends in all the figures presented in this section, represent twist rates on

upper and lower rotors, e.g., $-9°/0°$ represents a linear twist rate of $-9°$ per radius, and a lower rotor linear twist rate of $0°$ per radius.

4.4.1 Lower Rotor Twisted Linearly

This section analyses the performance of the coaxial rotor system when the lower rotor blades were twisted linearly (nose down) with the constraint of having a torque balance. It is further divided into two separate sections that discuss the results obtained by using the BEMT and the FVM.

4.4.1.1 BEMT Analysis

BEMT was formulated on the assumption of the linear superposition of flows from the upper and lower rotors of the coaxial system, such that the net torque of the coaxial rotor system is zero. This means that although the effects of the lower rotor wake on the upper rotor are not modeled, the airloads on the lower rotor *does* effect those on the upper rotor through torque balance.

The blade collective angles obtained by trimming the coaxial system, are shown in Fig. 4.34. In the present analysis, all of the results are explained on the basis of the collective angles that are obtained to satisfy the torque balance condition at a specific thrust condition. The results in this figure show that the collective pitch angles on the lower rotor increase linearly with the twist rate. Whereas, the collective pitch angles on the upper rotor remain almost constant.

Twisting the blades of the lower rotor linearly (nose down) increases the blade

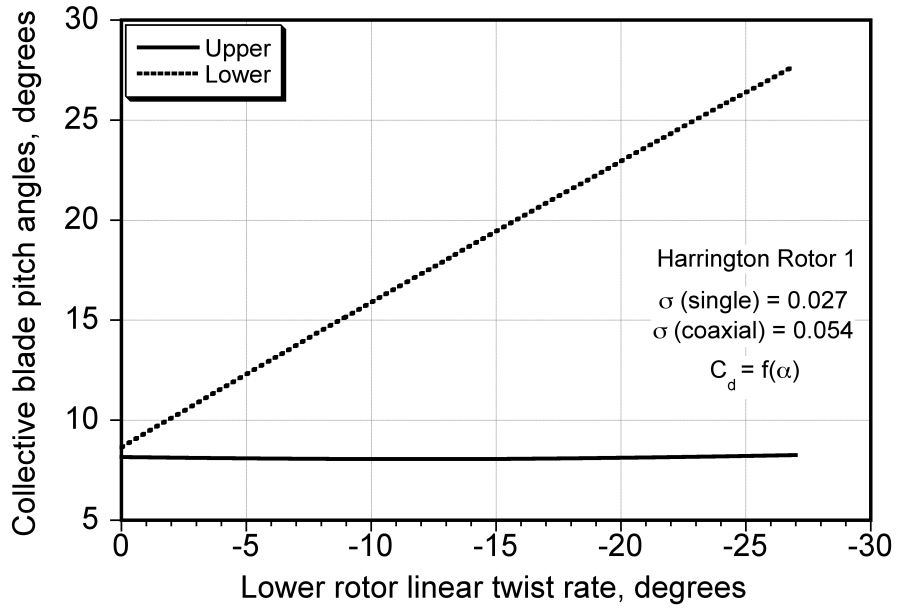

Fig. 4.34: Variation of the collective blade pitch angles on upper and lower rotors with different lower rotor twist rates. (Results obtained using BEMT.)

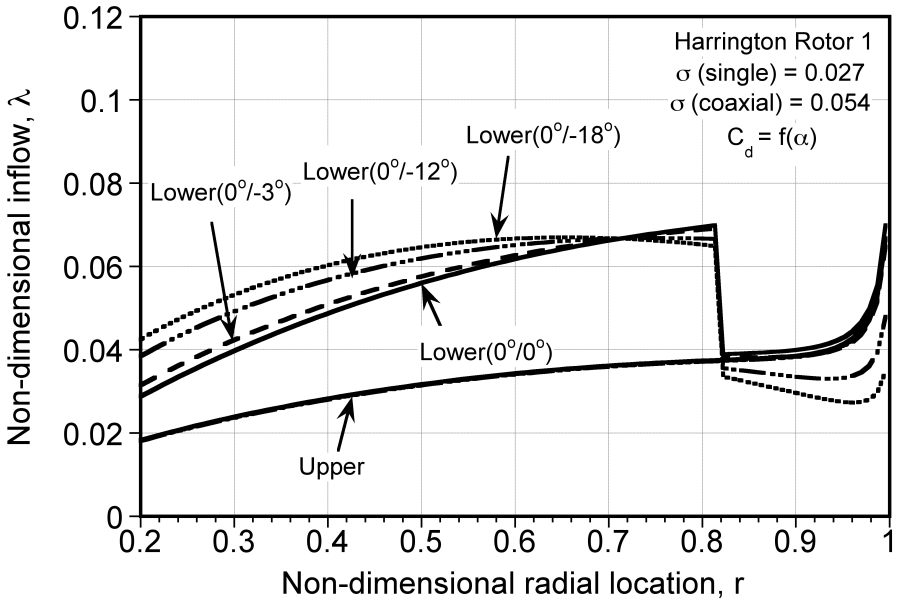

Fig. 4.35: Variation of the spanwise inflow distribution on the upper and lower rotors with different lower rotor twist rates.(Results obtained using BEMT.)

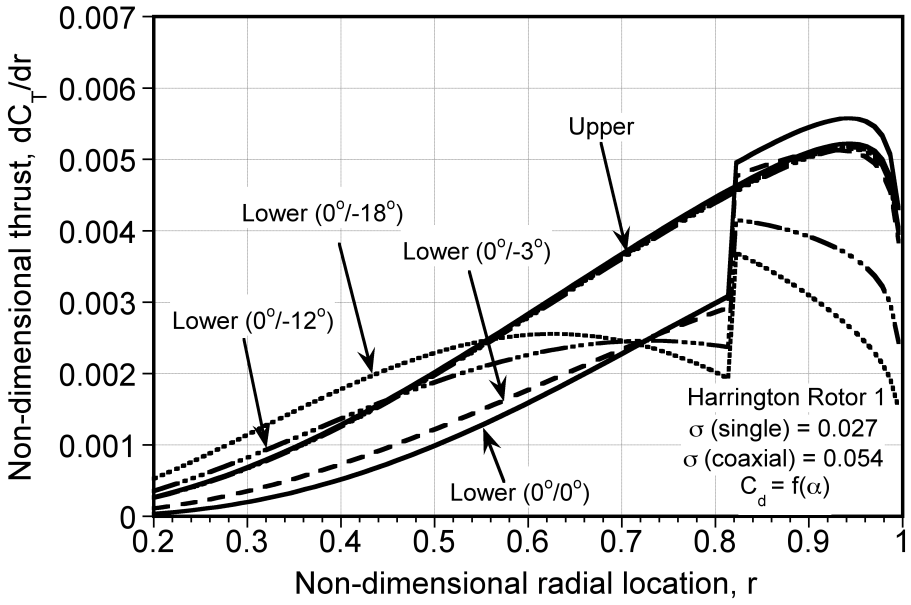

Fig. 4.36: Variation of the spanwise thrust distribution on the upper and lower rotors with different lower rotor twist rates.(Results obtained using BEMT.)

pitch angles towards the inboard sections and decreases them towards the outboard regions. This results in a biased inflow and thrust distribution inboard, which decreases outboard on the lower rotor blades—see Figs. 4.35 and 4.36. Because the upper rotor is affected by the lower rotor only through torque balance, the effects of changing the thrust on lower rotor on the performance of the upper rotor are not very significant.

Because of the effects of upper rotor wake, the inflow on the inboard sections of the lower rotor is higher than at the outer sections. By increasing the twist rate on the lower rotor, the inflow increases more towards the root region than it decreases towards the tip sections. This results in an increased inflow on the lower rotor blades as their twist rate is increased—see Fig. 4.37. The inflow distribution

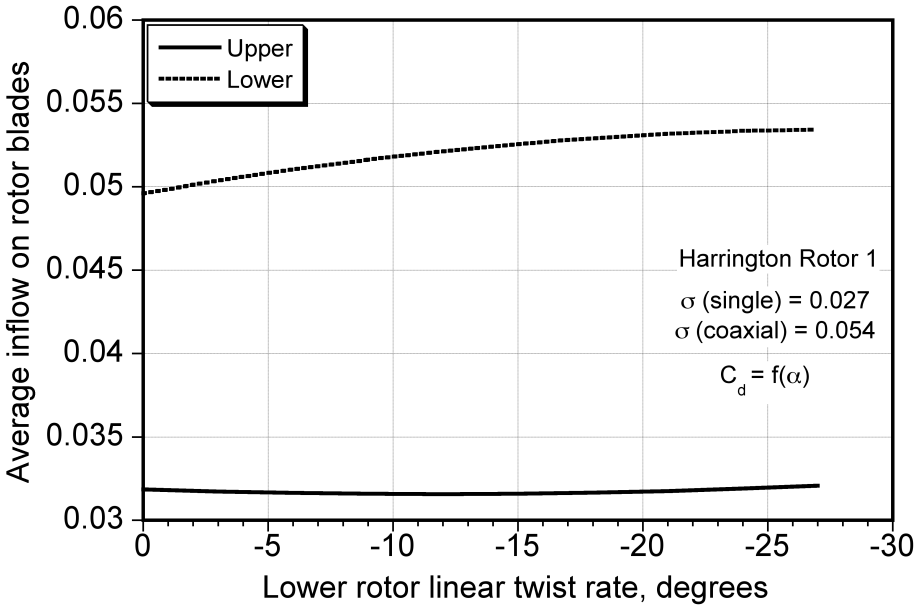

Fig. 4.37: Variation of the average inflow on the upper and lower rotors with different lower rotor twist rates.(Results obtained using BEMT.)

on the upper rotor remains almost constant. Figure 4.38 shows the ratios of the integrated thrusts on upper and lower rotors to the system thrust coefficient. It shows that the thrust shared by the lower rotor increases slightly with increase in its blade twist rate until $-15°$, and then at higher twist rates it again decreases. On the upper rotor, the thrust varies in the manner opposite to the lower rotor to maintain the specified system thrust—see Fig. 4.38.

The spanwise distribution of the induced torque coefficient on both the rotors as a function of nose down twist rate on the lower rotor blades is shown in Fig. 4.39. Figure 4.40 shows the integrated induced power coefficient on both the rotors as a function of twist rate on the lower rotor. This figure shows that the induced power coefficient of the lower rotor increases rapidly with increasing blade twist rate. On

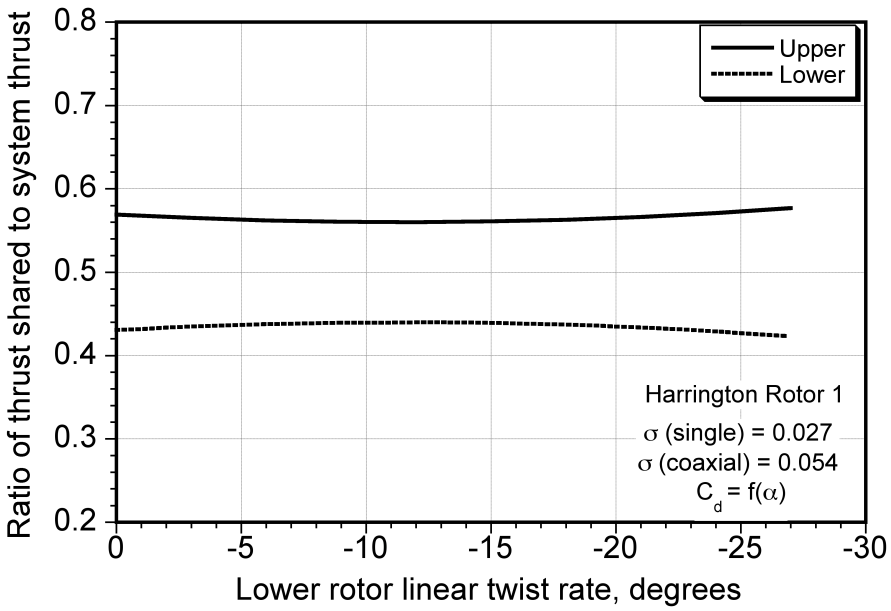

Fig. 4.38: Variation of the ratio of thrust shared by the upper and lower rotors with respect to the total system thrust, with different lower rotor twist rates. (Results obtained using BEMT.)

the upper rotor, the induced power coefficient is not significantly affected. This result is an outcome of the higher increase in inflow distribution inboards of the lower rotor (when its blade twist increases) as compared to the decrease in inflow outboards. It is very interesting to notice that an increase in the twist rate on the lower rotor results in an increase in the induced power coefficient.

In the present analysis, the local profile drag of the blade element was a function of local angle of attack, as given by Eq. 4.4. Therefore, the profile power also changes with twist rate to maintain a torque balance of the coaxial as a system. Figure 4.41 shows the variation of profile power coefficients on the upper and lower rotors with the twist rate on the lower rotor blades. It shows that the profile power

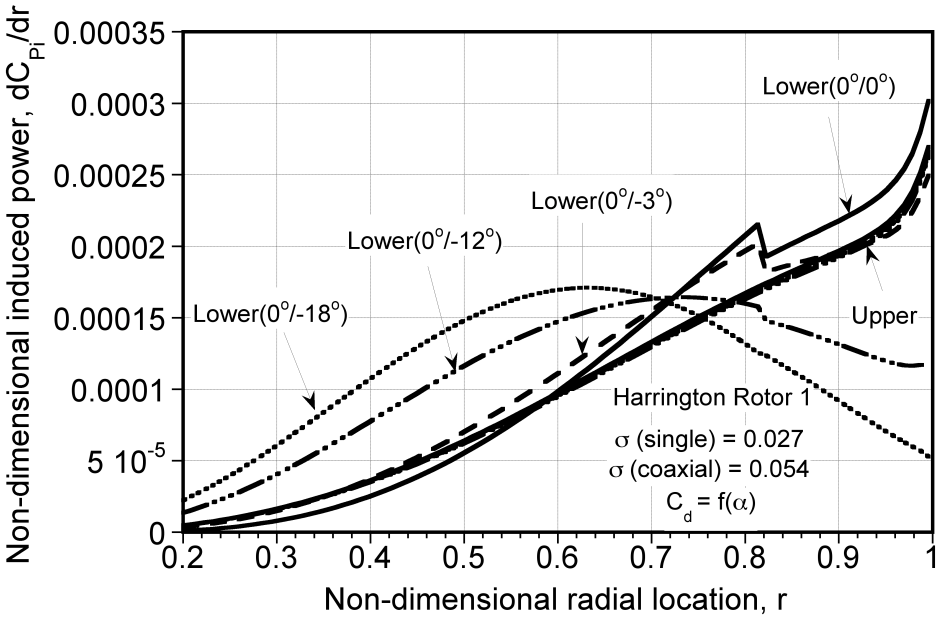

Fig. 4.39: Variation of the spanwise induced power distribution on the upper and lower rotors with different lower rotor twist rates. (Results obtained using BEMT.)

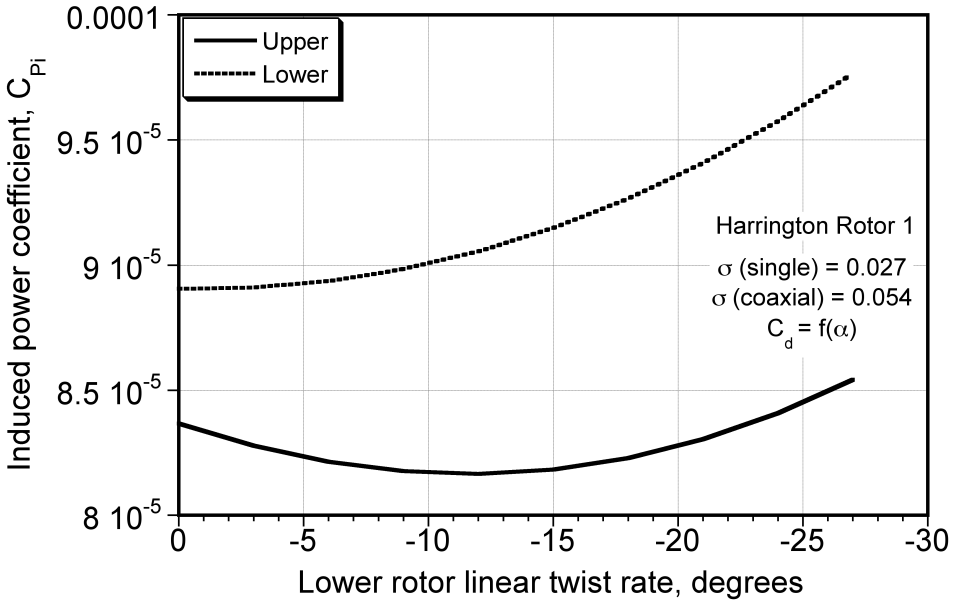

Fig. 4.40: Variation of the induced power coefficient on the upper and lower rotors with increase in linear twist rate on lower rotor blades. (Results obtained using BEMT.)

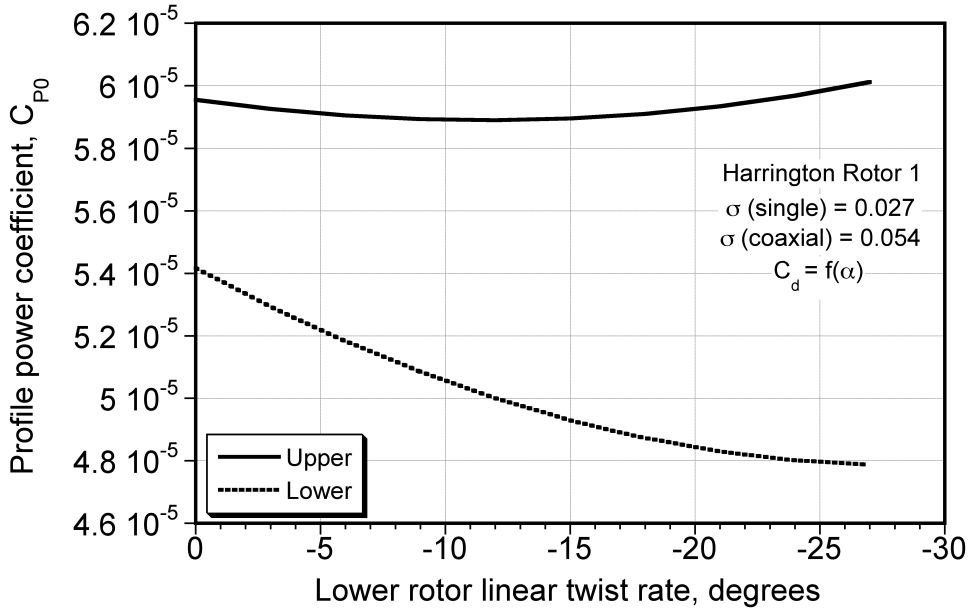

Fig. 4.41: Variation of the profile power coefficient on the upper and lower rotors with increase in linear twist rate on lower rotor blades. (Results obtained using BEMT.)

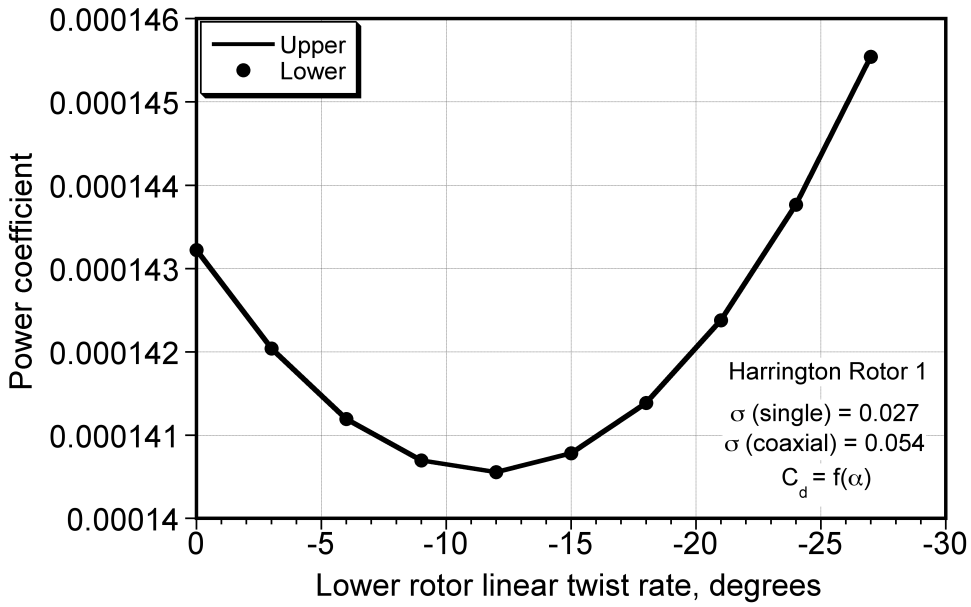

Fig. 4.42: Variation of the total power coefficient (induced plus profile) on the upper and lower rotors with increase in linear twist rate on lower rotor blades. (Results obtained using BEMT.)

coefficient decreases on lower rotor with an increase in its twist rate, whereas on the upper rotor it remains almost unchanged.

Figure 4.42 shows that the total power coefficients (i.e., induced plus profile) on both the rotors are equal at all twist rates, i.e. a torque balance is maintained. Finally, Fig. 4.43 shows the variation of the total system power with an increase in twist rate on the lower rotors. The results in this figure show that the power is minimum when the blades on the lower rotor have a twist rate of $-12°$.

Notice that in this analysis of the coaxial rotor system, an increase in the twist rate of the blades of the lower rotor resulted in an increase in its induced power coefficient and decrease in the profile power coefficient. This result is different from

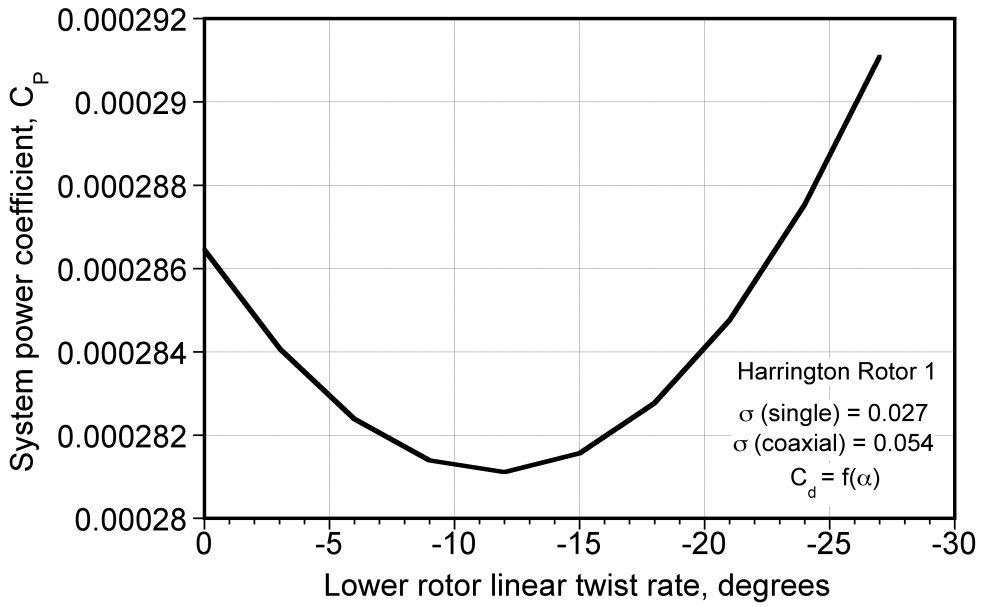

Fig. 4.43: Variation of the total system power coefficient on the upper and lower rotors with increase in linear twist rate on lower rotor blades. (Results obtained using BEMT.)

the behavior obtained with isolated single rotors, where, higher blade twist results in a reduction in the induced losses.

4.4.1.2 FVM Analysis

The effects of blade twist rate variations on the lower rotor of the coaxial system were examined using the FVM. The FVM is a three-dimensional analysis that solves for the effects of the wakes of the two rotors upon each other. The collective blade pitch angles are obtained such that to balance the torque of upper and lower rotors at a specific thrust coefficient. Because the coupling of the performance between the two rotors is relatively complicated, the results in this section

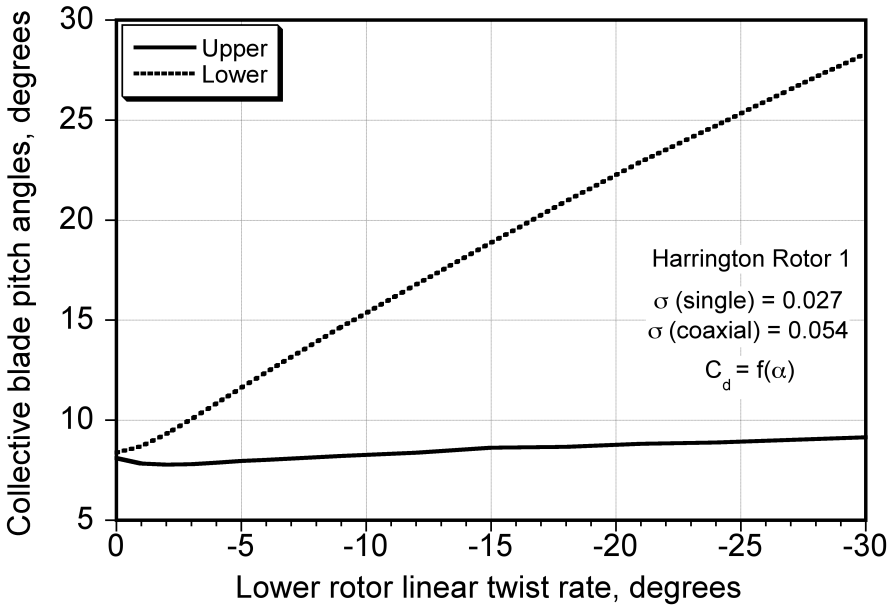

Fig. 4.44: Variation of collective blade pitch angles on the upper and lower rotors with different lower rotor twist rates. (Results obtained using FVM.)

are discussed using the collective obtained in Fig. 4.44. This figure shows that the collective angle on the lower rotor increases with an increase in its twist rate. However, the figure also shows that after a twist rate of -3° is reached, the collective angle on the lower increases more rapidly than for twist rates of between 0 and -3°. The collective pitch on the upper rotor decreases for smaller blade twist rates on the lower rotor (i.e., until -3° is reached in this case), and then increases gradually as the blade twist rate on the lower rotor increases.

Figures 4.45(a) and 4.45(b) show the spanwise inflow distribution over upper and lower rotor blades, respectively, with an increase in the blade twist rate on the lower rotor. The results show that for blade twist rates larger than -3° on the lower rotor, the inflow distributions increase inboard and decrease outboard on

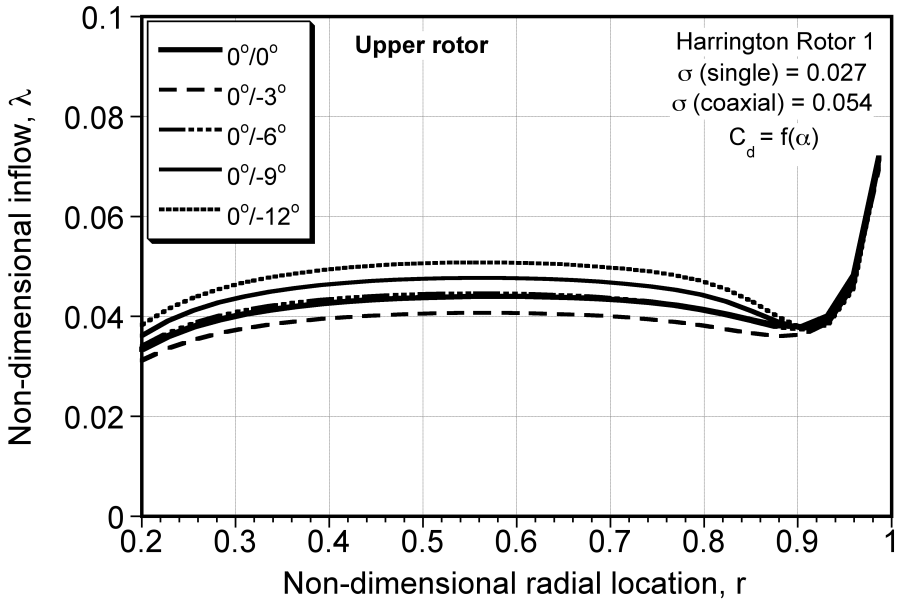

(a) **Upper rotor**

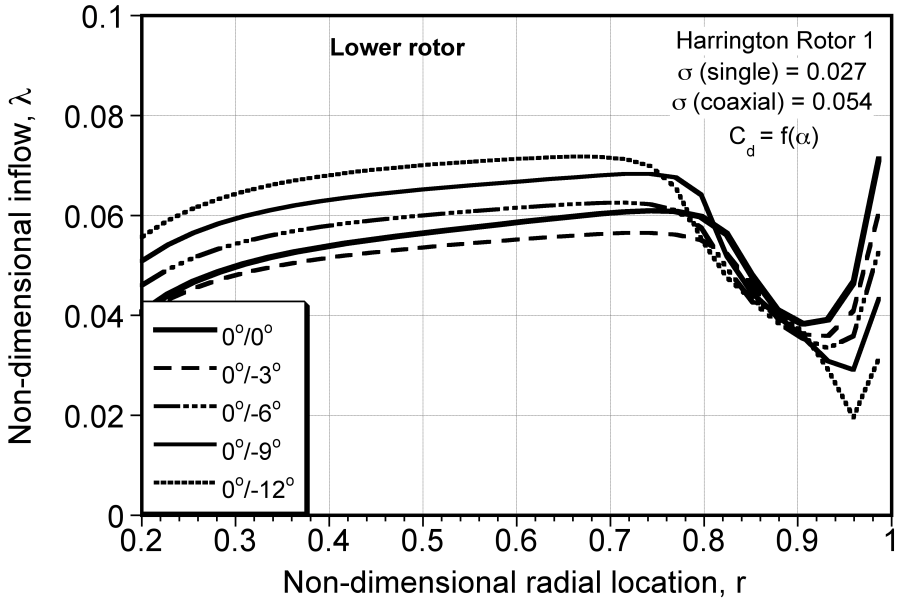

(b) **Lower rotor**

Fig. 4.45: Variation of spanwise thrust distribution on the upper and lower rotors with different lower rotor twist rates. (Results obtained using FVM.)

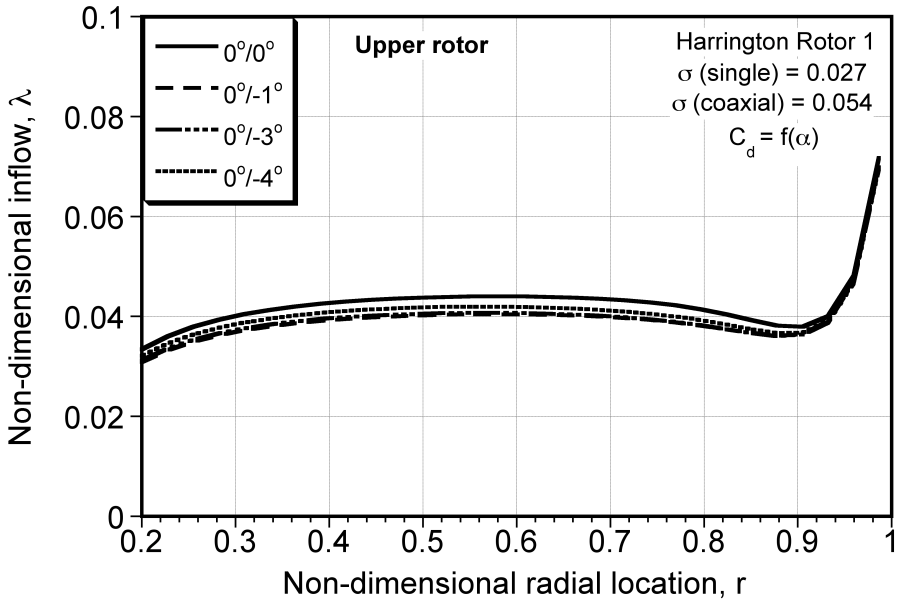

(a) **Upper rotor**

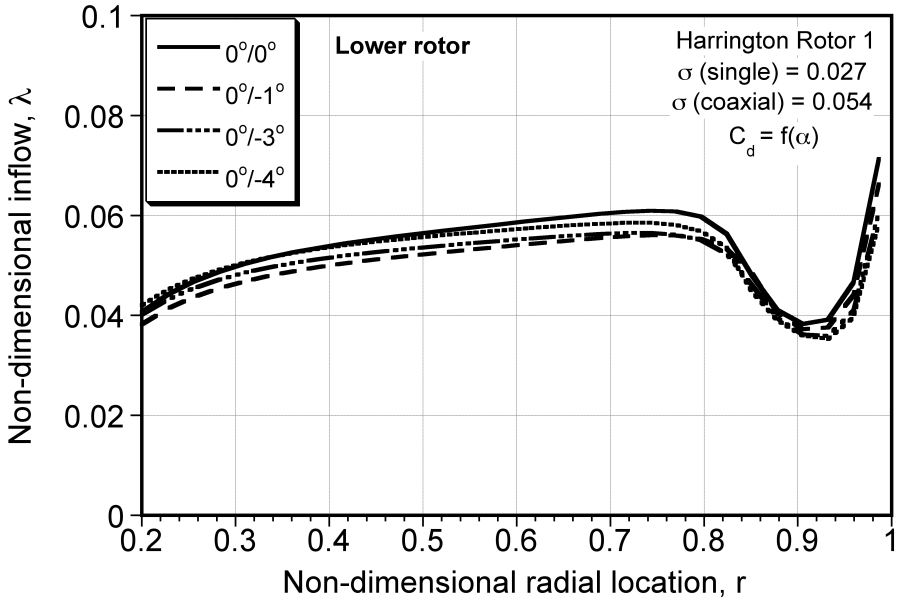

(b) **Lower rotor**

Fig. 4.46: Variation of spanwise thrust distribution on the upper and lower rotors with very small twist rate on lower rotor. (Results obtained using FVM.)

both the rotors. This result is consistent with the BEMT results shown previously in Fig. 4.35. However, at -3° the inflow distribution on both the rotors decrease significantly. To understand this, the rotor performance was analysed for blade twist rates of -1°, -2°, -3° and -4° on the lower rotor. The inflow distributions on the upper and lower rotors are shown in Figs. 4.46(a) and 4.46(b), respectively. The results show that when the lower rotor was given a twist rate of only -1°, the inflow decreases significantly on both rotors. However, at twist rate of -3° it starts to increase on both the rotors. The reason for this behavior is not yet understood. Notice in Fig. 4.44 that the collective angles obtained of the torque balance notably increase on the lower rotor but decrease just by small amount on the upper rotor.

The thrust distributions on both the rotors are shown in Figs. 4.47(a) and 4.47(b) as a function of blade twist rate on the lower rotor. On the lower rotor, the thrust distribution increases inboard and decreases outboard as its twist rate increases. Notice that for a twist rate of -3°, the thrust distribution is more linear than was found for the untwisted lower rotor blades, but as twist rate increases further the thrust distribution again starts to become nonlinear. On the upper rotor, the thrust distribution does not change significantly with increasing blade twist on the lower rotor.

The average inflow on both the rotors is shown in Fig. 4.48. Again, notice that the average inflows on both the rotors are at a minimum for a blade twist rate of -2° and then increase again with twist rate. The reason for this behavior has already been explained. Figure 4.49 shows the ratios of thrust shared by upper and lower rotors. This result also shows that the thrust shared by the upper rotor decreases

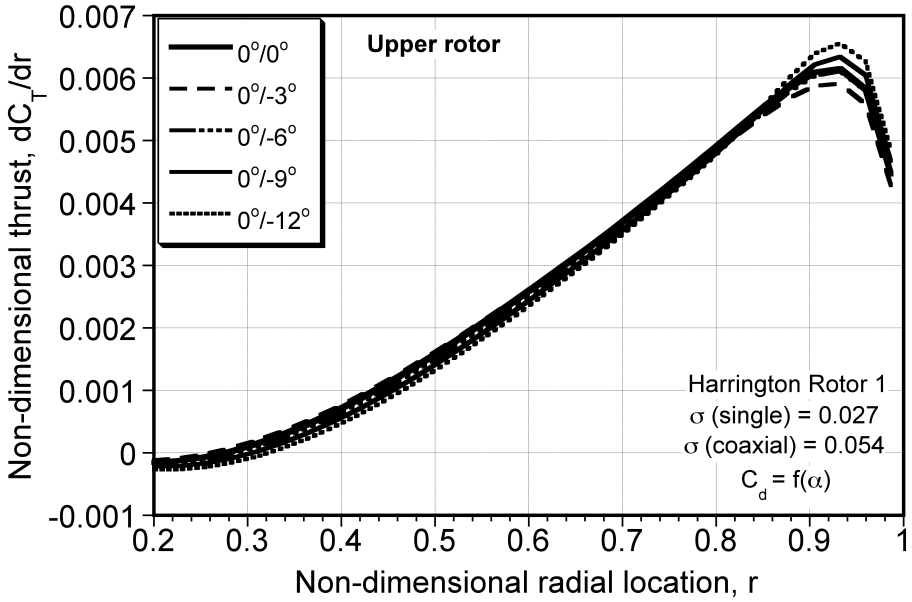

(a) **Upper rotor**

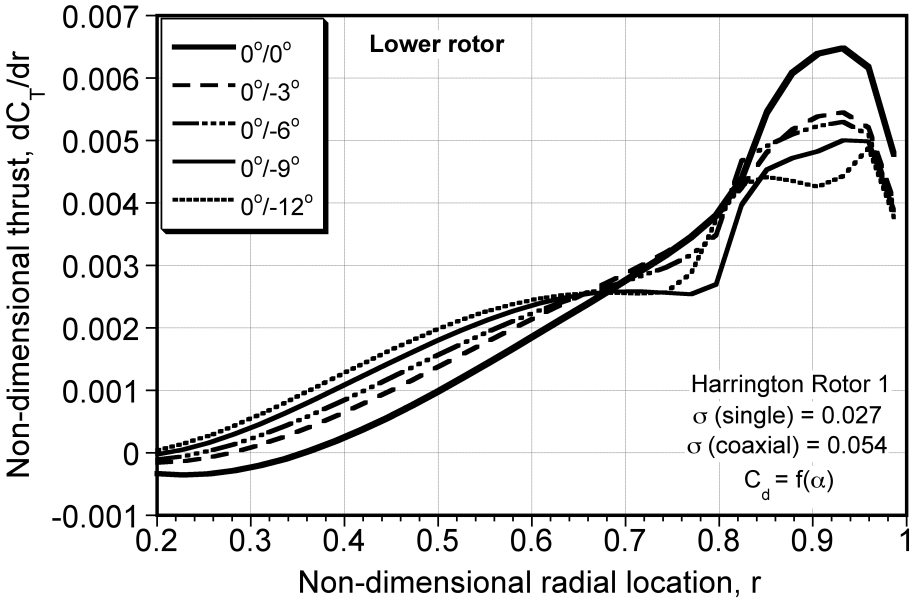

(b) **Lower rotor**

Fig. 4.47: Variation of spanwise thrust distribution on the upper and lower rotors with different lower rotor twist rates. (Results obtained using FVM.)

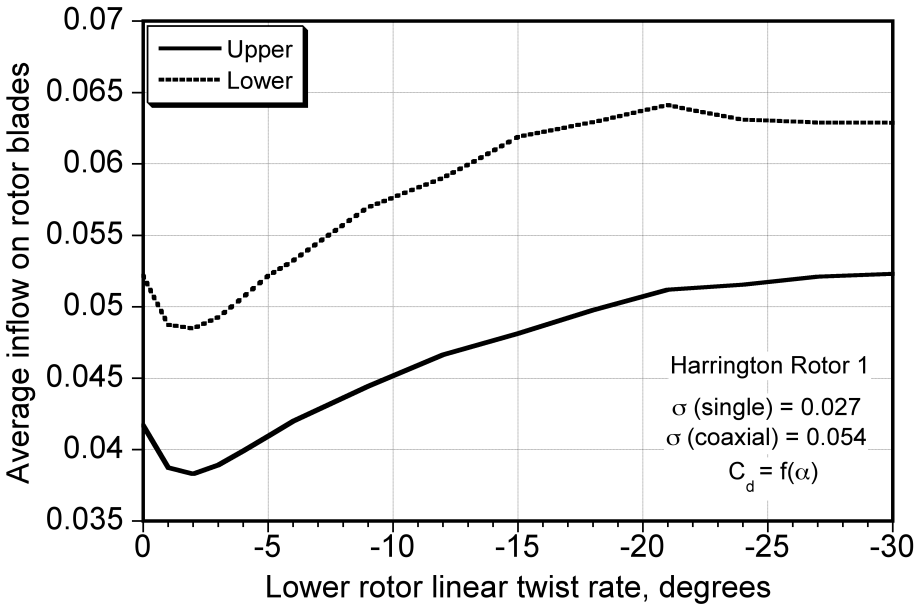

Fig. 4.48: Variation of average inflow on the upper and lower rotors with different lower rotor twist rates. (Results obtained using FVM.)

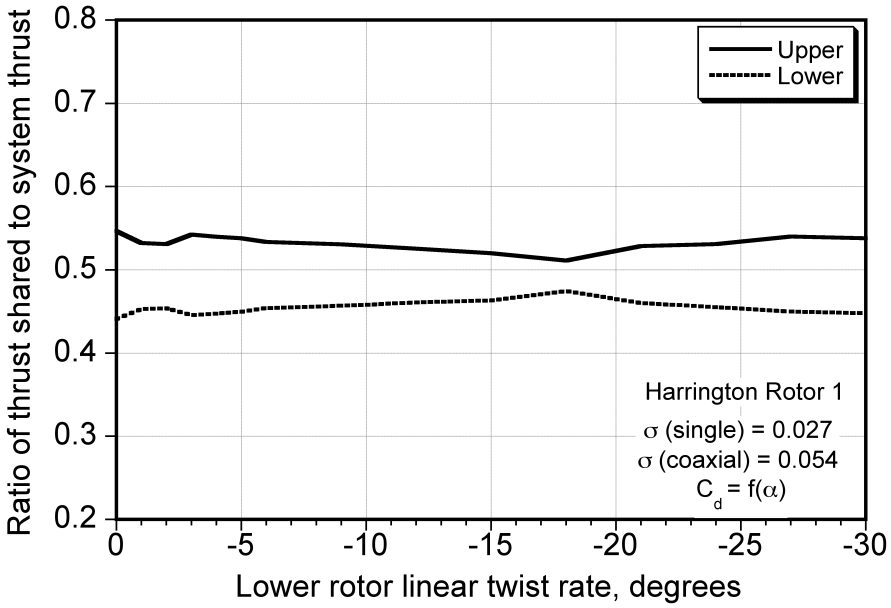

Fig. 4.49: Variation of ratio of thrust shared by the upper and lower rotors wrt. total system thrust, with different lower rotor twist rates.(Results obtained using FVM.)

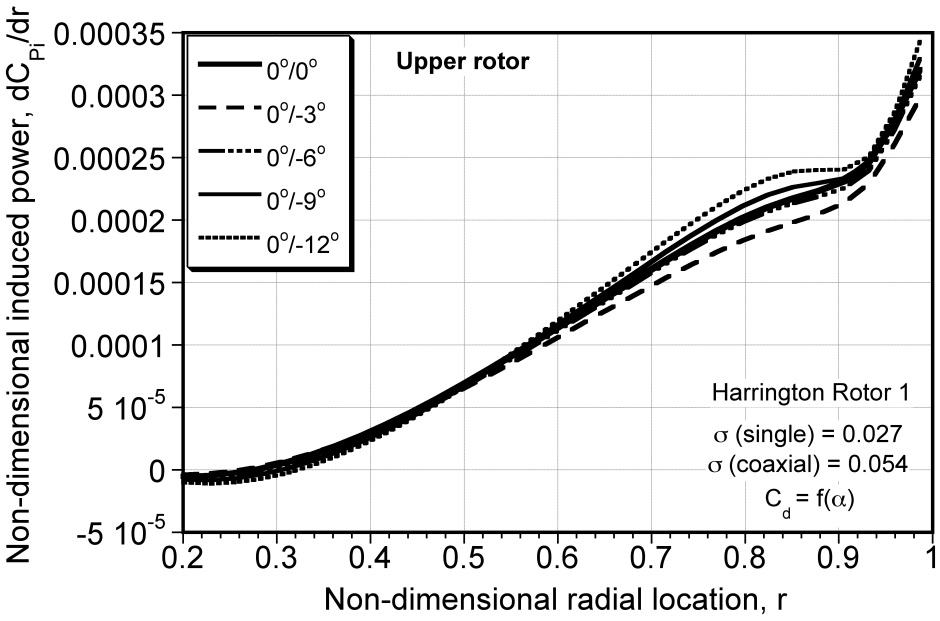

(a) **Upper rotor**

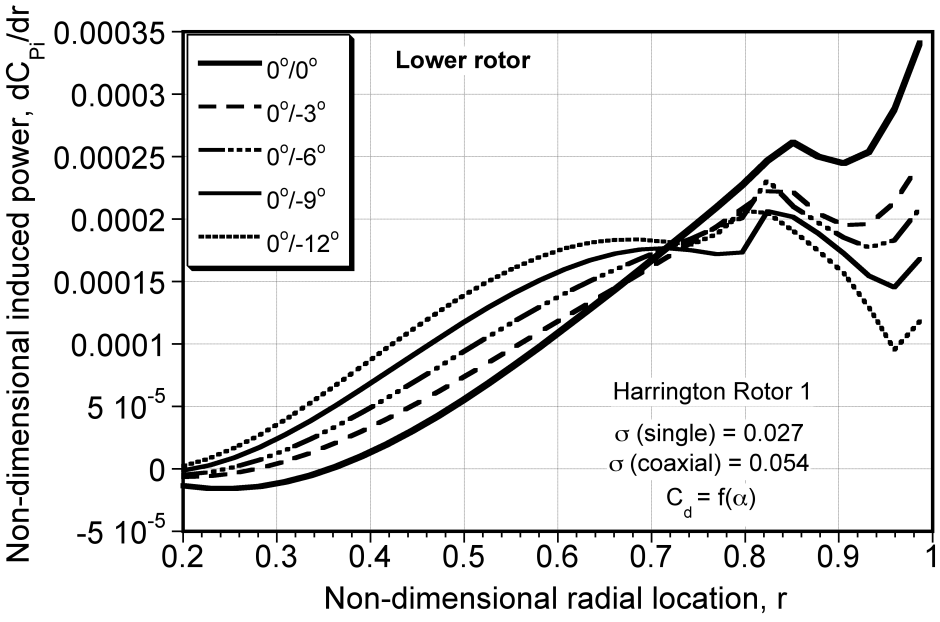

(b) **Lower rotor**

Fig. 4.50: Variation of spanwise induced power distribution on the upper and lower rotors with different lower rotor twist rates. (Results obtained using FVM.)

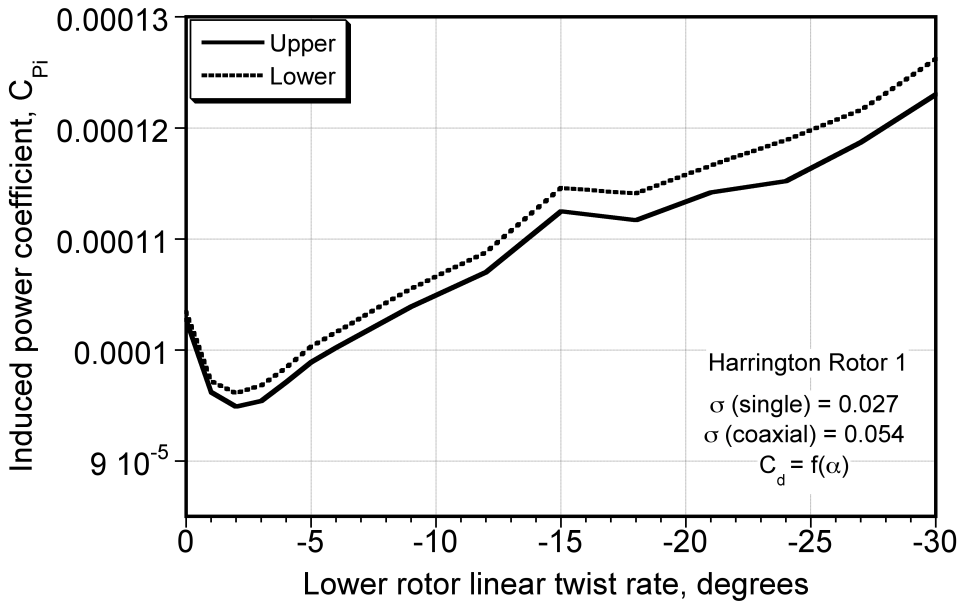

Fig. 4.51: Variation of induced power coefficient on the upper and lower rotors with increase in linear twist rate on lower rotor blades. (Results obtained using FVM.)

for blade twist rates ranging from $-1°$ to $-3°$ because the inflow on the lower rotor decreases, and then it again increases at higher blade twist rates on the lower rotor.

The induced torque distributions on both the rotors of the coaxial system are shown in Figs. 4.50(a) and 4.50(b). On the lower rotor, the induced torque increases inboard as its blade twist increases. On the upper rotor, the induced power coefficient reduces when the blade twist on the lower rotor increases from $0°$ to $-3°$, and then power again increases.

The integrated induced power coefficient on both the rotors is shown in Fig. 4.51. Notice that the induced power on both the rotors decrease when the blade twist increases from $0°$ to $-3°$, and then increases with further increase in blade twist on the lower rotor blades. Figure 4.52 shows that the integrated profile powers on both

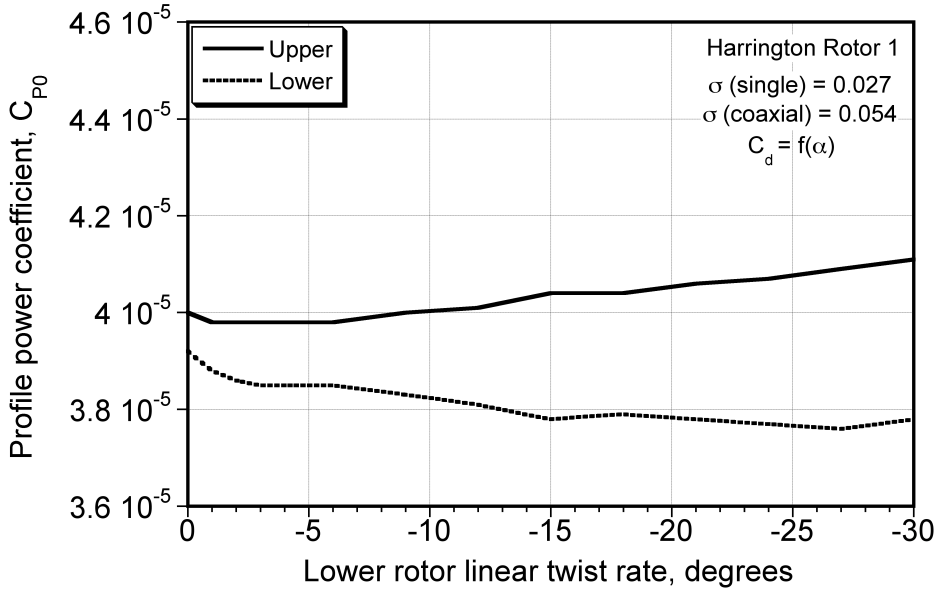

Fig. 4.52: Variation of profile power coefficient on the upper and lower rotors with increase in linear twist rate on lower rotor blades. (Results obtained using FVM.)

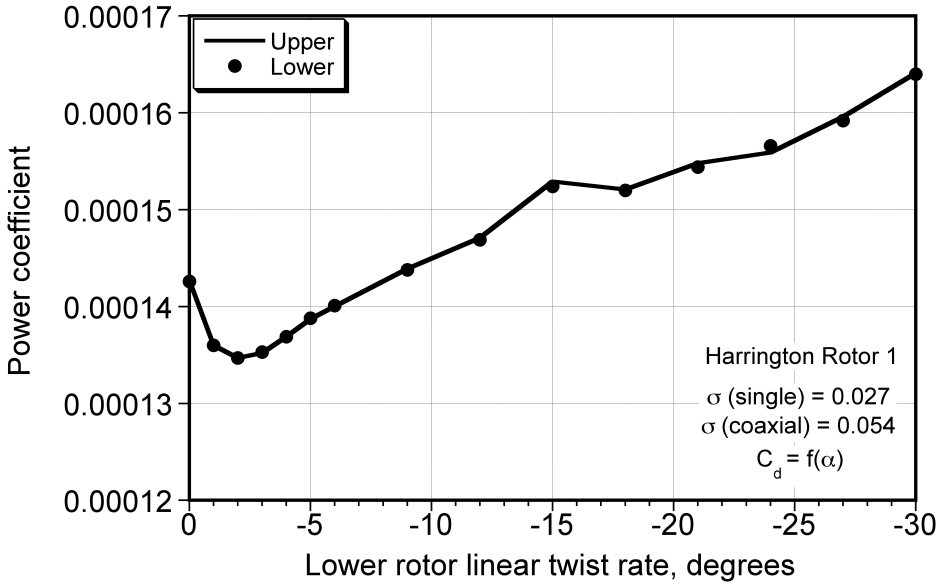

Fig. 4.53: Variation of total power coefficient (induced plus profile) on the upper and lower rotors with increase in linear twist rate on lower rotor blades. (Results obtained using FVM.)

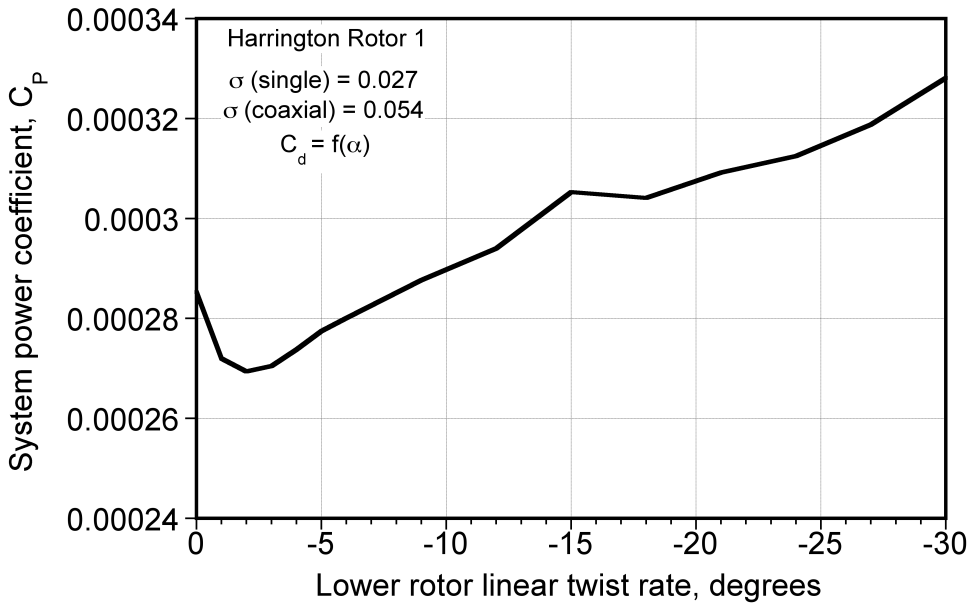

Fig. 4.54: Variation of total system power coefficient on the upper and lower rotors with increase in linear twist rate on lower rotor blades. (Results obtained using FVM.)

the rotors do not change significantly with a change in blade twist on the lower rotor.

Figure 4.53 shows the variation of total power (i.e., induced plus profile) on both the rotors with an increase in blade twist on the lower rotor. The total power on both the rotors are same at all values of blade twist so as to maintain a torque balanced condition. These results also show that for all the blade twist values on the lower rotor, the power requirements on both the rotors reach a minimum with a blade twist rate of $-2°$. The same trends can be seen in the total system power coefficient, shown in Fig. 4.54.

4.4.2 Upper Rotor Twisted Linearly

This section presents results of the analysis of the coaxial rotor performance when the blades of the upper rotor of the Harrington Rotor 1 system were twisted linearly with a twist rate ranging from 0 to 30° (nose down), whereas the lower rotor blades were kept untwisted. The analysis were performed using both the BEMT and the FVM. Again, all the results were obtained at a torque balance.

4.4.2.1 BEMT Analysis

With an increase in the twist rate on the upper rotor blades, the blade pitch angles increase inboard and decrease outboard. To maintain torque balance (see Fig. 4.55) at a specific thrust condition, the collective pitch angle on upper rotor increases and that on lower rotor remains almost constant—see Fig. 4.56. Notice that with both sets of blades being untwisted, the collective blade pitch angles on the lower rotor are slightly higher than the upper rotor. This is because the inflow on the lower is also higher.

Figures 4.57(a) and 4.57(b) show the inflow distribution on the upper and lower rotors, respectively, by using different blade twist values on the upper rotor. The results show that the inflow on both rotors increase inboard, but decrease towards the tip region. On the upper rotor, the inflow becomes almost uniform when using a twist rate of $-9°$. At higher twist rates, the inflow becomes progressively less uniform. The inflow over the lower rotor follows the inflow distribution trends seen on the upper rotor, mainly because it lies in the slipstream wake of the upper rotor.

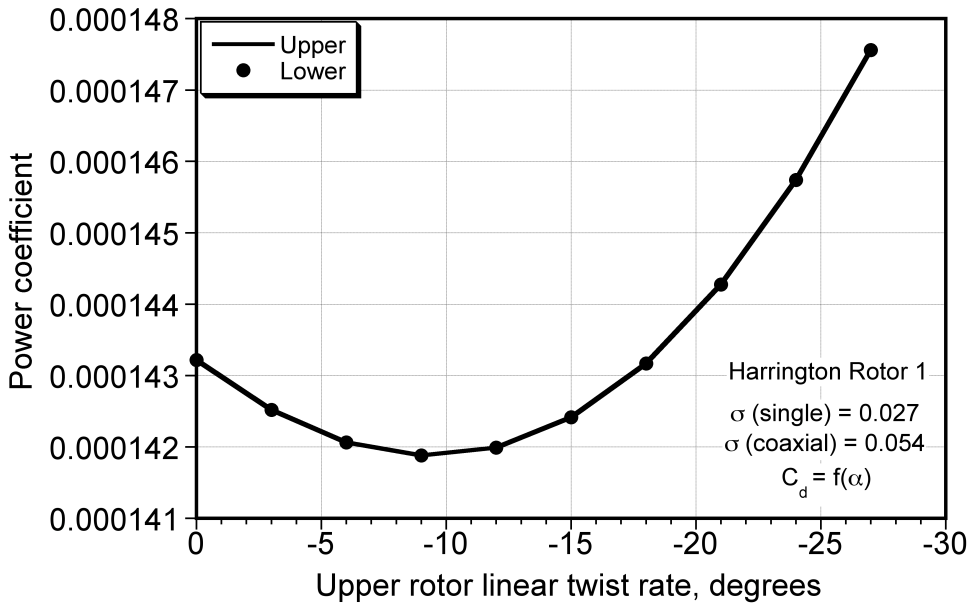

Fig. 4.55: Variation of the total power coefficient on the upper and lower rotors with increase in linear twist rate on upper rotor blades. (Results obtained using BEMT.)

Figure 4.58 shows the variation of the average inflow distribution both the rotors with an increase in linear twist rate on upper blades. The results show that the average inflow on both rotors increases as the blade twist rate increases on the upper rotor blades. However, the inflow increases more rapidly on lower rotor as compared to the upper rotor.

Figures 4.59(a) and 4.59(b) show the thrust distributions on the upper and lower rotors, respectively, in response to a change in the twist distribution on the upper rotor. With an increase in nose down twist on the upper rotor, the thrust distribution on the upper rotor tends to become more linear. For twist rates higher than $-9°$, the thrust begins to become more nonlinearly distributed. On the lower rotor, the thrust distribution decreases inboard with an increase in nose-down blade

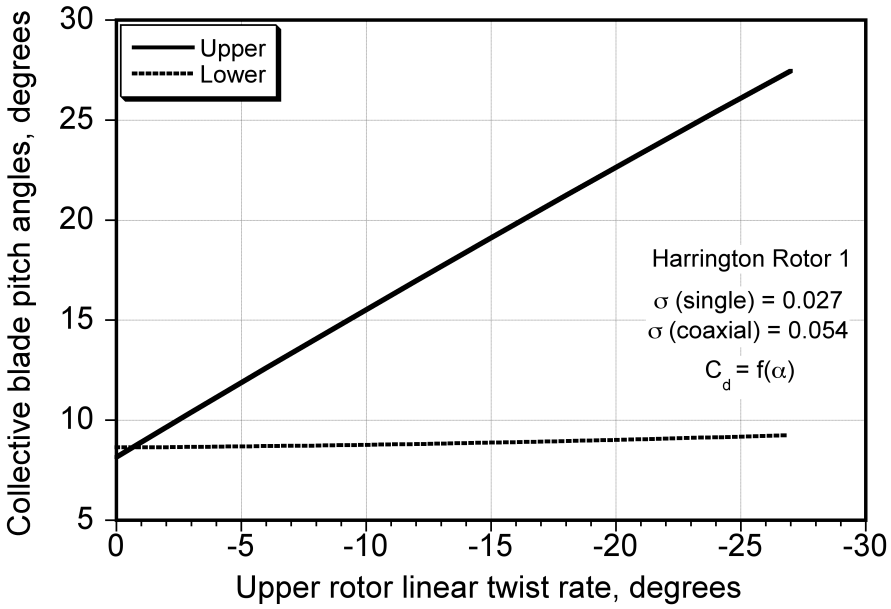

Fig. 4.56: Variation of the collective blade pitch angles on the upper and lower rotors with increase in linear twist rate on upper rotor blades. (Results obtained using BEMT.)

twist on the upper rotor.

Figure 4.60 shows the variation of rotor thrust shared by upper and lower rotors as a function of twist rate on the upper rotor. As can be seen from this figure, the total thrust carried by the upper rotor increases slightly until a twist rate of -15° is reached, and then it starts decreasing again.

Figures 4.61(a) and 4.61(b) show the variations of the spanwise induced power distribution on the upper and lower rotors, respectively, from a change in blade twist on the upper rotor. The induced power coefficient on the upper rotor remains almost constant until a twist rate of -6° is reached, and then it increases rapidly—see Fig. 4.62. On the lower rotor, the inflow increases over the inner sections and

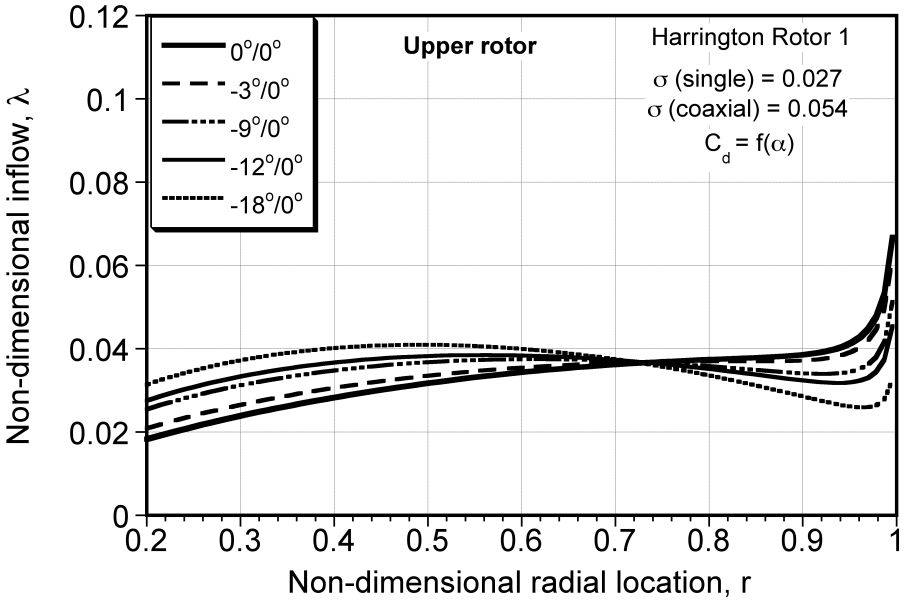

(a) **Upper rotor**

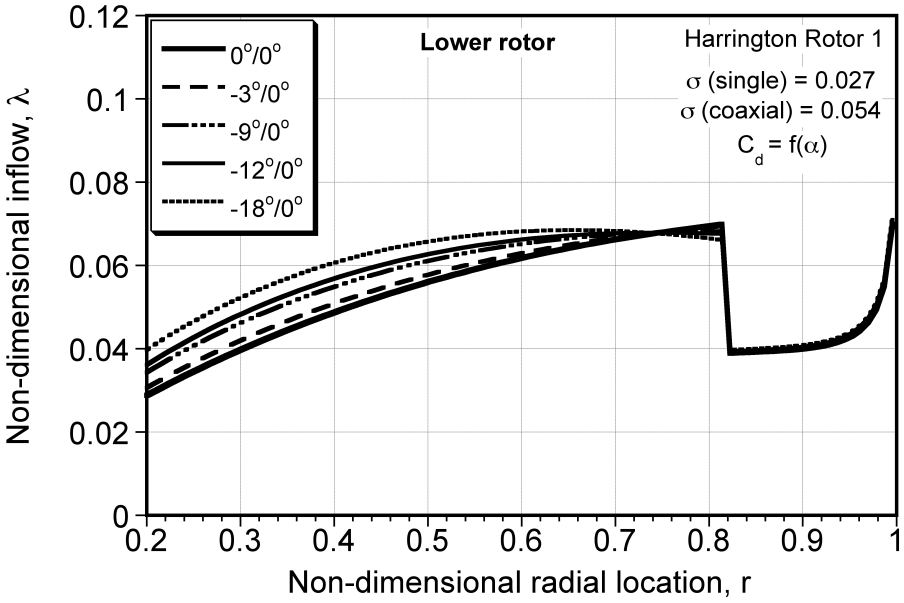

(b) **Lower rotor**

Fig. 4.57: Variation of the spanwise inflow distribution on the upper and lower rotors with different upper rotor twist rates. (Results obtained using BEMT.)

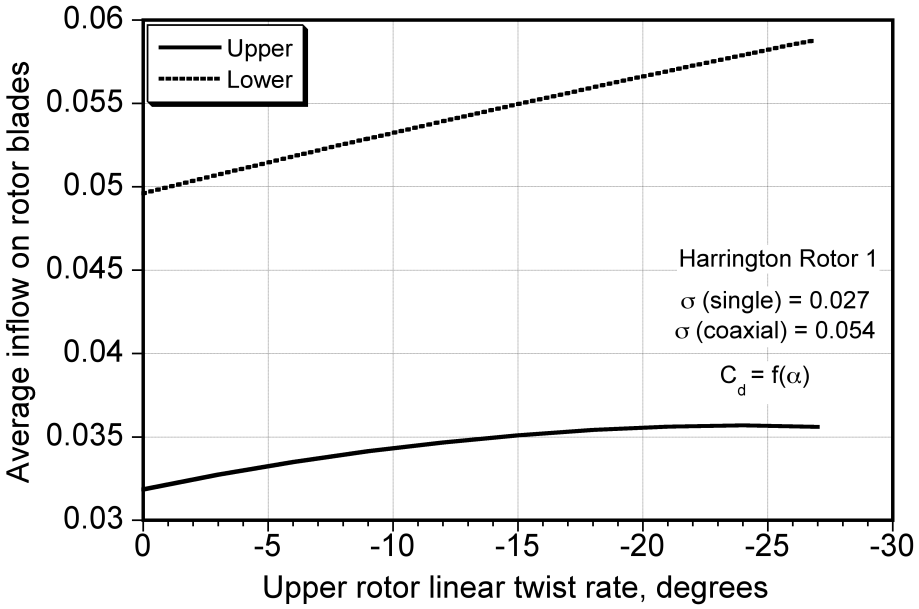

Fig. 4.58: Variation of the average inflow on the upper and lower rotors with increase in linear twist rate on upper rotor blades. (Results obtained using BEMT.)

thrust decreases with an increase in twist rate on the upper rotor, so the induced power coefficient also reduces slightly. The induced power coefficient decreases with an increase in twist on the upper rotor blades until a twist rate of -12° is reached, and then it increases—see Fig. 4.62.

Figure 4.63 shows the variation of profile power coefficient on the upper and lowers of the coaxial system with increase in twist rate on upper rotor blades. The profile power on the upper rotor reduces until a twist rate of -18° is reached, and then it becomes constant. The corresponding profile power coefficient of the lower rotor increases rapidly with an increase in blade twist on the upper rotor. Figure 4.64 shows the variation of total power coefficient of the coaxial system for an increase in blade twist on the upper rotor. The results show that the total power reaches a

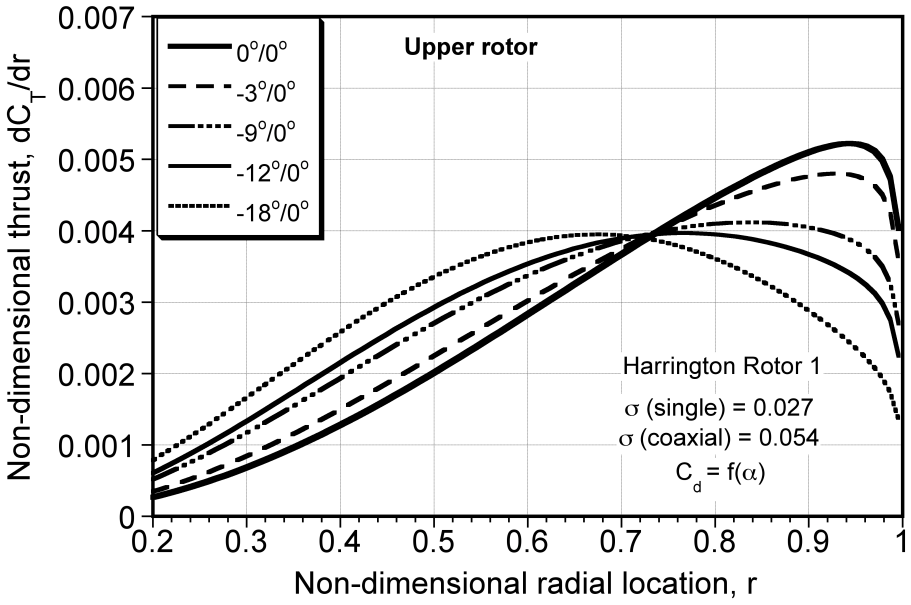

(a) **Upper rotor**

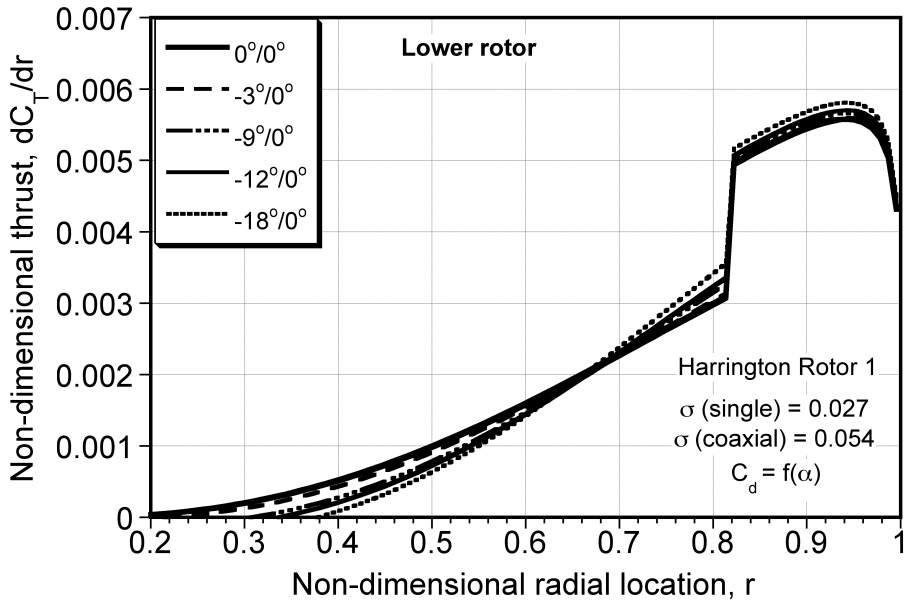

(b) **Lower rotor**

Fig. 4.59: Variation of the spanwise thrust distribution on the upper and lower rotors with different upper rotor twist rates. (Results obtained using BEMT.)

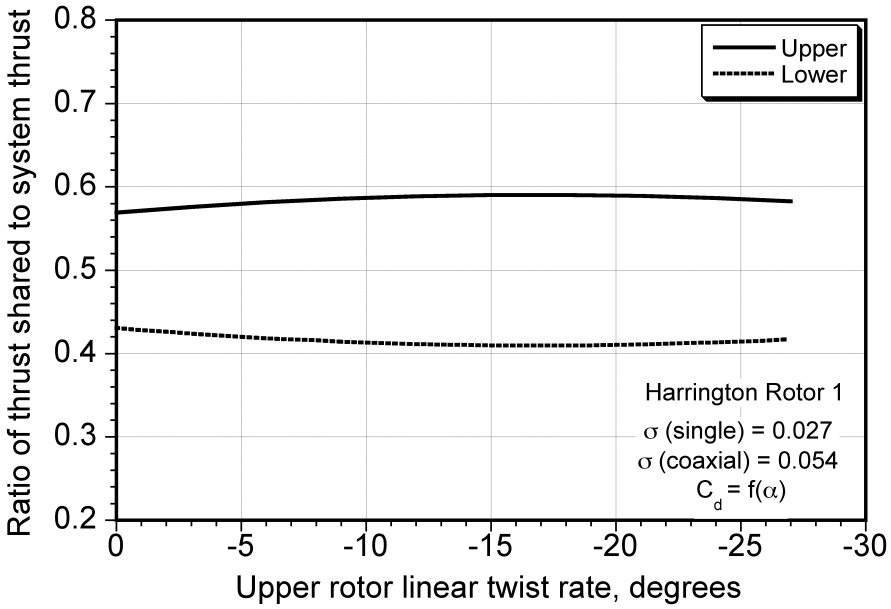

Fig. 4.60: Variation of the ratio of thrust shared by the upper and lower rotors wrt. total system thrust, with increase in linear twist rate on upper rotor blades. (Results obtained using BEMT.)

minimum at a twist rate of $-9°$. This analysis also showed that an increase in the twist on the upper rotor increases the induced power coefficient and decreases the profile power coefficient.

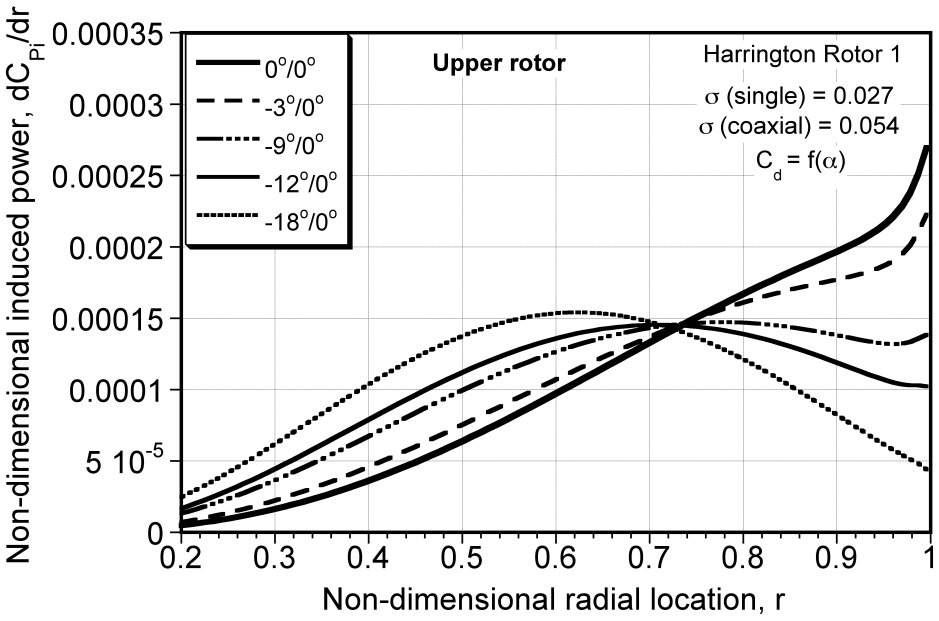

(a) **Upper rotor**

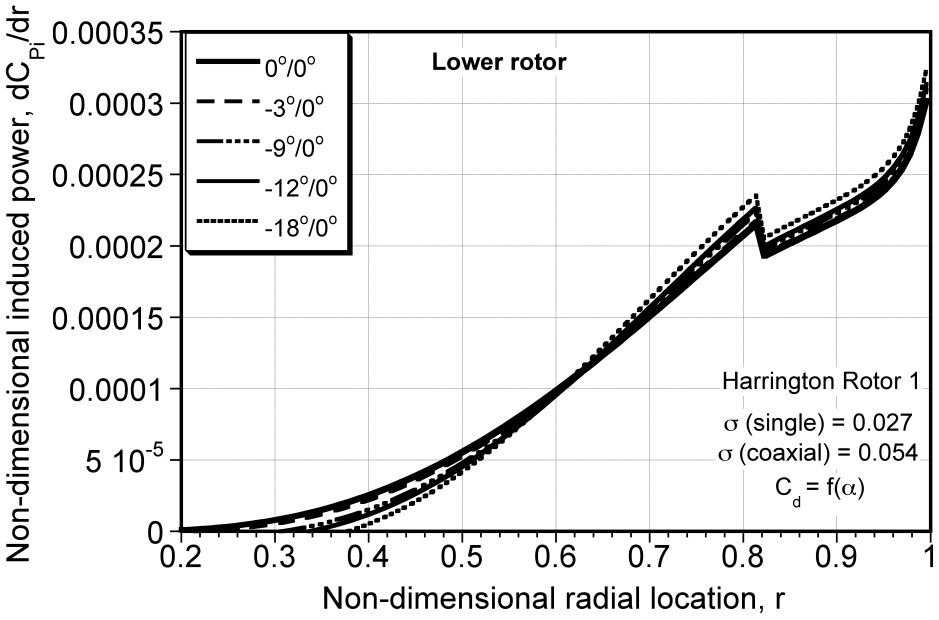

(b) **Lower rotor**

Fig. 4.61: Variation of the spanwise induced power distribution on the upper and lower rotors with different upper rotor twist rates. (Results obtained using BEMT.)

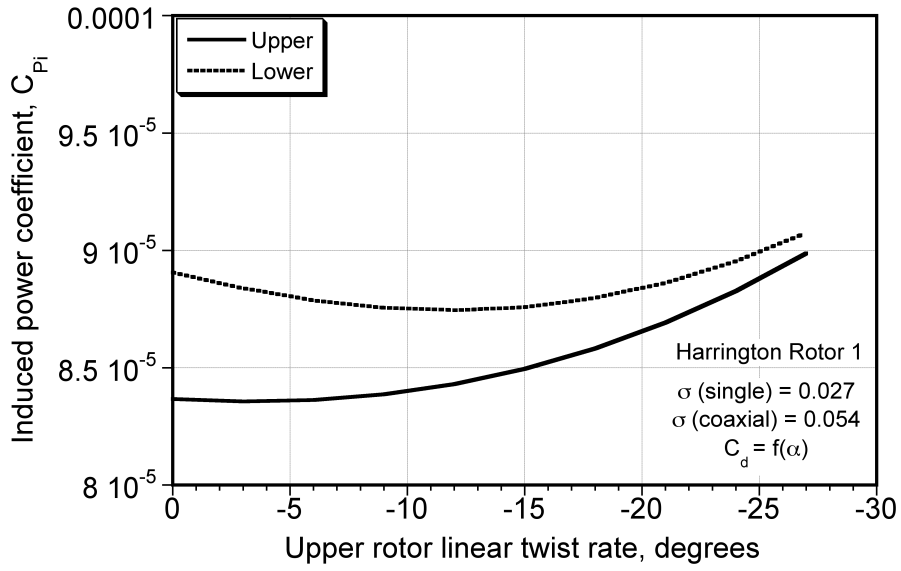

Fig. 4.62: Variation of the induced power coefficient on the upper and lower rotors with increase in linear twist rate on upper rotor blades. (Results obtained using BEMT.)

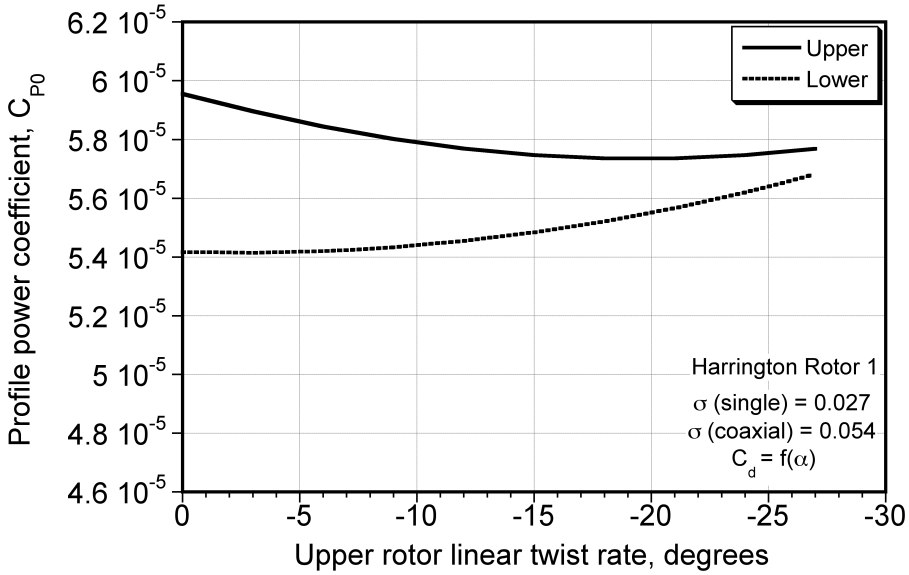

Fig. 4.63: Variation of the profile power coefficient on the upper and lower rotors with increase in linear twist rate on upper rotor blades. (Results obtained using BEMT.)

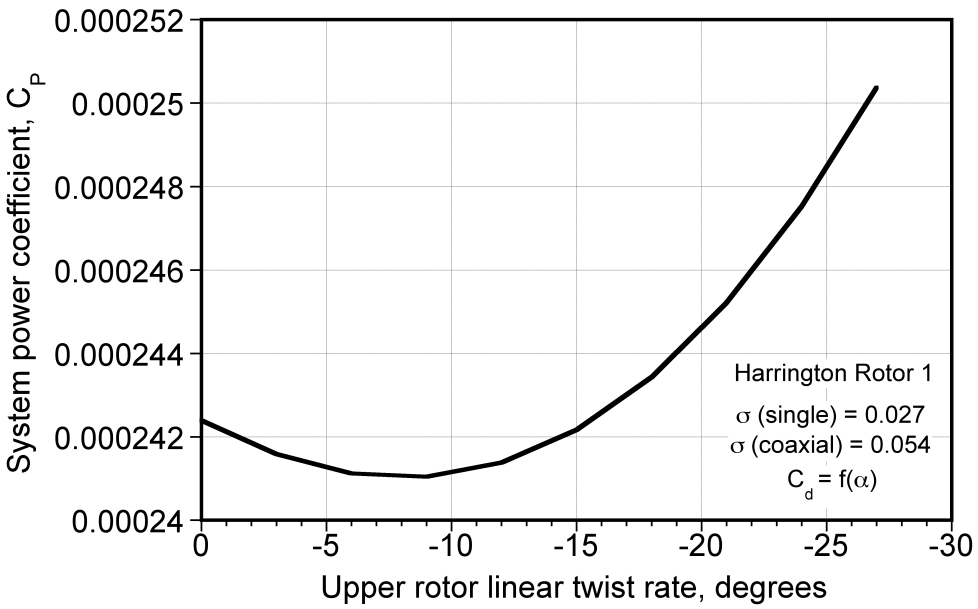

Fig. 4.64: Variation of the total system power coefficient on the upper and lower rotors with increase in linear twist rate on upper rotor blades. (Results obtained using BEMT.)

4.4.2.2 FVM Analysis

This section presents the FVM analysis performed by linearly twisting the blades of the upper rotor. Figure 4.65 shows the collective blade pitch angles obtained from the FVM when the blade twist on the upper rotor was increased from 0° to -30° in steps of -3°. With an increase in the blade twist rate on the upper rotor, the inflow increases at inboard sections and decreases outwards—see Fig. 4.66(a). The inflow on the lower rotor also decreases, but the change here is maximum over the region where the wake boundary from the upper rotor impinges on it. The variation of average inflow on both the rotors with blade twist rate on the upper rotor is shown in Fig. 4.67. This figure shows that the average inflow on both of the rotors decrease, and they become a minimum for blade twist rates on the upper rotor ranging from -18° to -21°.

As mentioned previously, increasing the blade twist on upper rotor biases the thrust distribution toward the inboard sections—see Fig. 4.66(a). The thrust distribution on the lower rotor remains almost constant, except in the areas where upper rotor wake boundary meets the lower rotor—see Fig. 4.66(b). The ratios of the integrated thrusts on both the rotors to the total system thrust are shown in Fig. 4.68. The thrusts shared by both the rotors remain almost constant until a twist rate of -10° is reached on the upper rotor blades, and then it decreases on upper rotor and increases on lower rotor, becoming equal at a twist rate of -21° on the upper rotor.

The induced power coefficient distribution on both the rotors of the Harrington

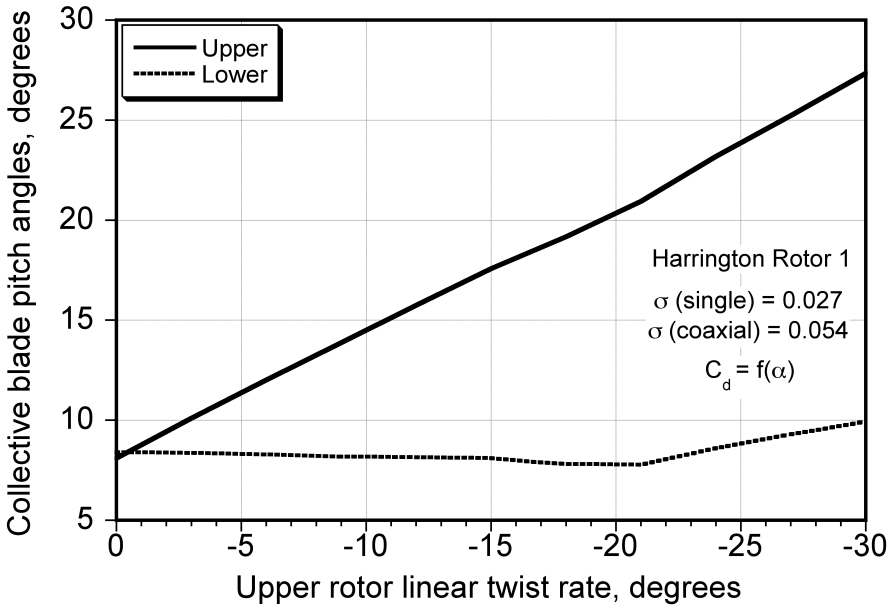

Fig. 4.65: Variation of the collective blade pitch angles on the upper and lower rotors with increase in linear twist rate on upper rotor blades. (Results obtained using FVM.)

Rotor 1 are shown in Figs. 4.70(a) and 4.70(b). The integrated induced power coefficient on both the rotors is shown in Fig. 4.71. This shows that the induced powers on both the rotors decrease with an increase in blade twist rate on the upper rotor and becomes minimum for twist rates between $-18°$ and $-21°$. The profile power coefficients on both the rotors decrease until a blade twist rate of $-21°$ is reached, and then increase rapidly with further increase twist rate—see Fig. 4.72. These results are different from the BEMT results shown in Figs. 4.62 and 4.63, where it was found that the induced power on upper rotor increases with an increase in upper rotor twist rate and the profile power decreases. Finally, the total power coefficient in this case in shown in Fig. 4.74, and shows that the total power reaches

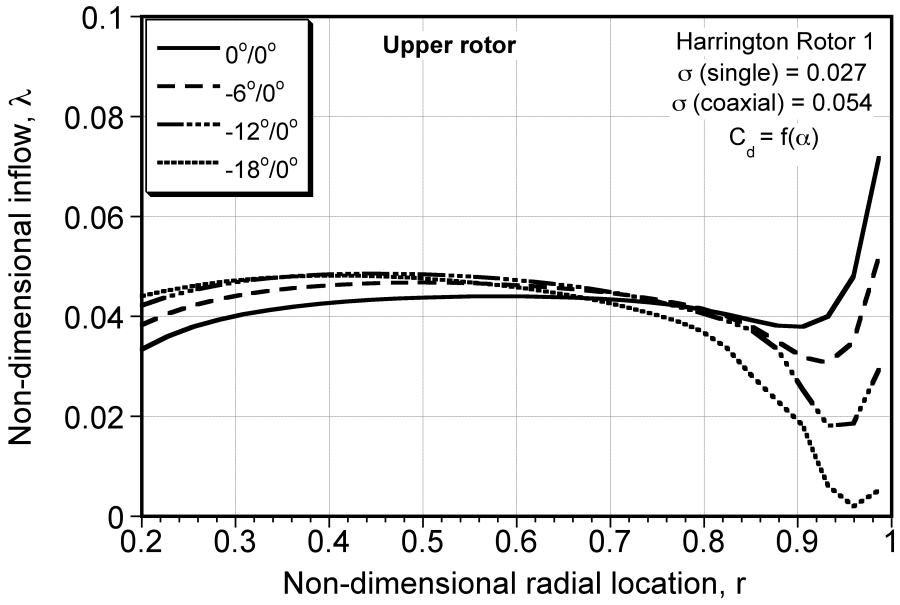

(a) **Upper rotor**

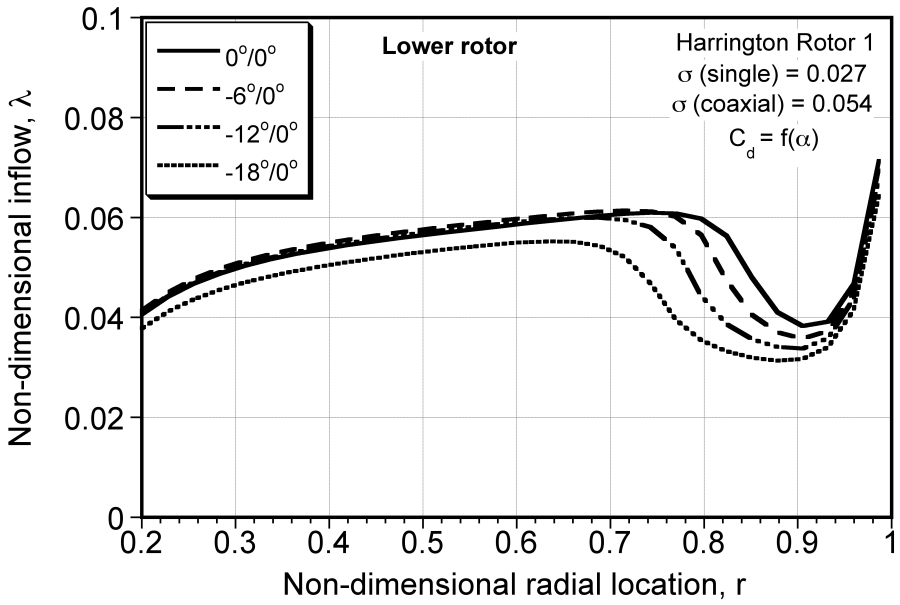

(b) **Lower rotor**

Fig. 4.66: Variation of the spanwise inflow distribution on the upper and lower rotors with different upper rotor twist rates, when lower rotor is not twisted.(Results obtained using FVM.)

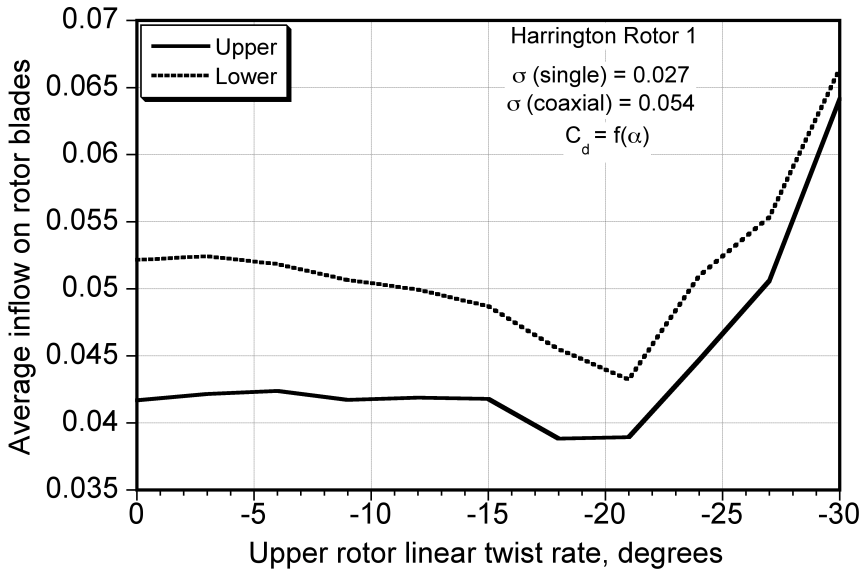

Fig. 4.67: Variation of the average inflow on the upper and lower rotors with increase in linear twist rate on upper rotor blades, when lower rotor blades are not twisted.(Results obtained using FVM.)

a minimum when using a twist rate of -18° on the upper rotor.

4.4.3 Summary of the Effects of Blade Twist

The study that was performed to understand the effects of changes in the twist rates on both rotors of a coaxial system suggest that a higher nose down twist rate is desirable on upper rotor blades to reduce both induced and profile losses. It was found that a nose down twist rate between -18° and -21° is optimum for the upper rotor. The results also suggested that a higher twist rate on the lower rotor blades increases the induced losses, while decreasing the profile power contributions. Therefore, a higher twist rate is not desirable on the lower rotor. It was found that a twist rate of approximately -3° is optimum for the lower rotor. This study

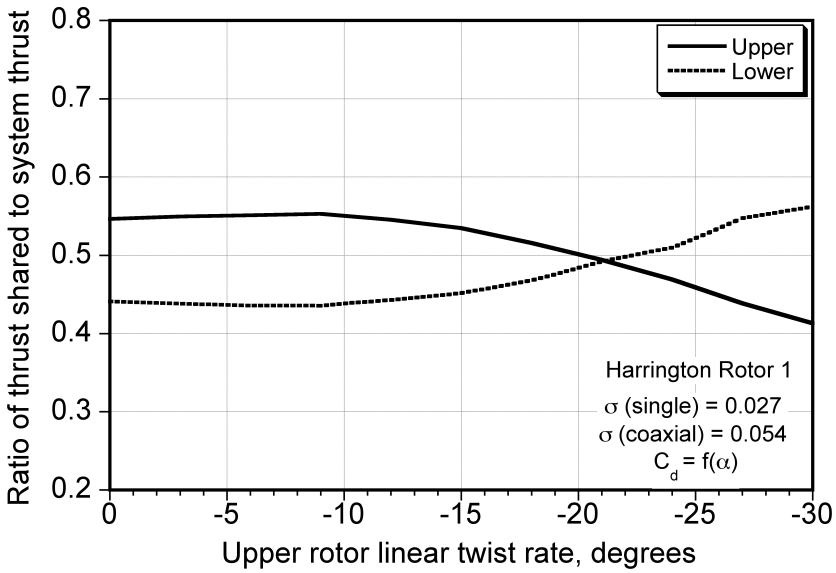

Fig. 4.68: Variation of the ratio of thrust shared by the upper and lower rotors wrt. total system thrust, with increase in linear twist rate on upper rotor blades. (Results obtained using FVM.)

suggested that a major improvement in the performance of a coaxial rotor system can be achieved by twisting the upper rotor blades and trying to optimize their geometry. This meant that the optimum coaxial configuration may not result in the reduction of the interference losses between the two rotors.

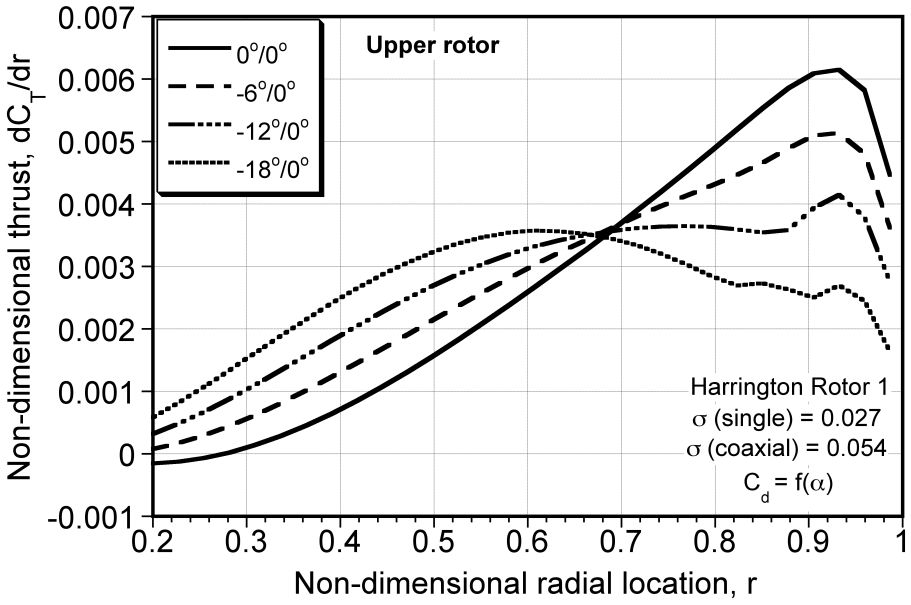

(a) **Upper rotor**

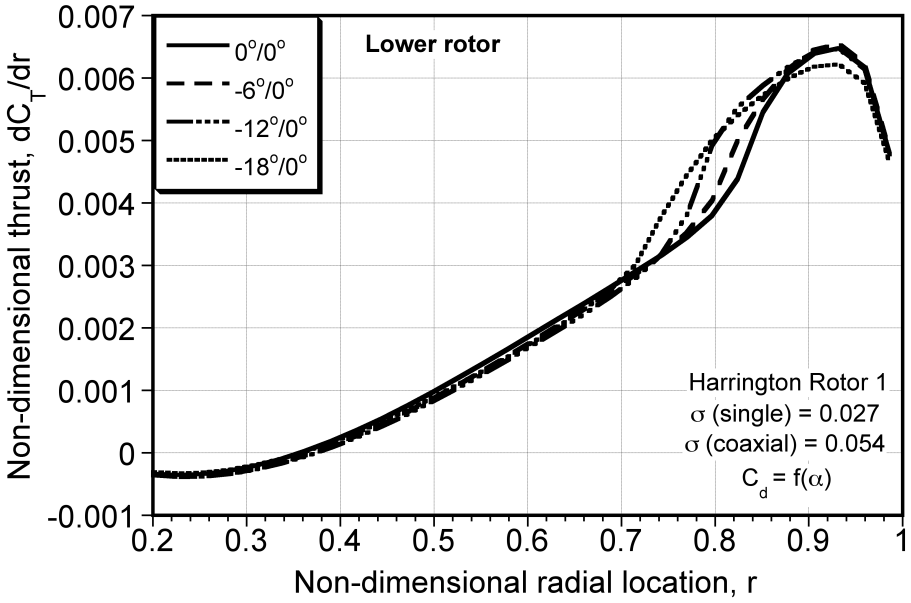

(b) **Lower rotor**

Fig. 4.69: Variation of the spanwise thrust distribution on the upper and lower rotors with different upper rotor twist rates. (Results obtained using FVM.)

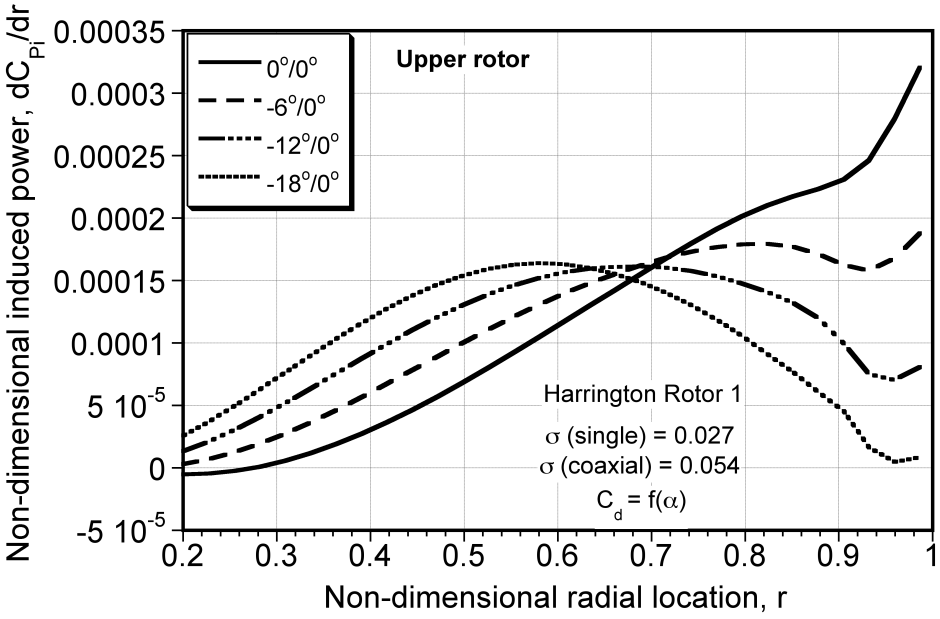

(a) **Upper rotor**

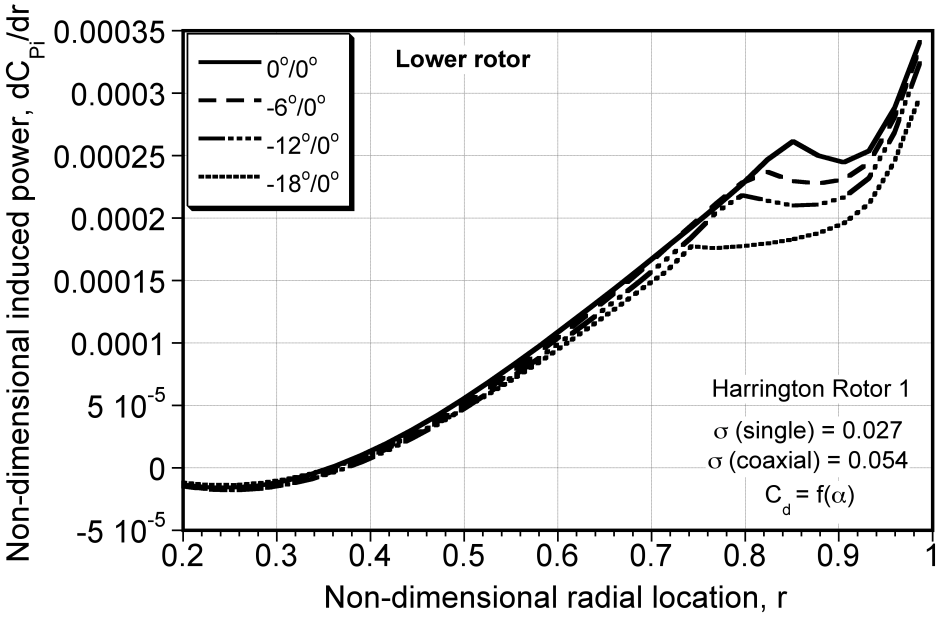

(b) **Lower rotor**

Fig. 4.70: Variation of the spanwise induced power distribution on the upper and lower rotors with different upper rotor twist rates. (Results obtained using FVM)

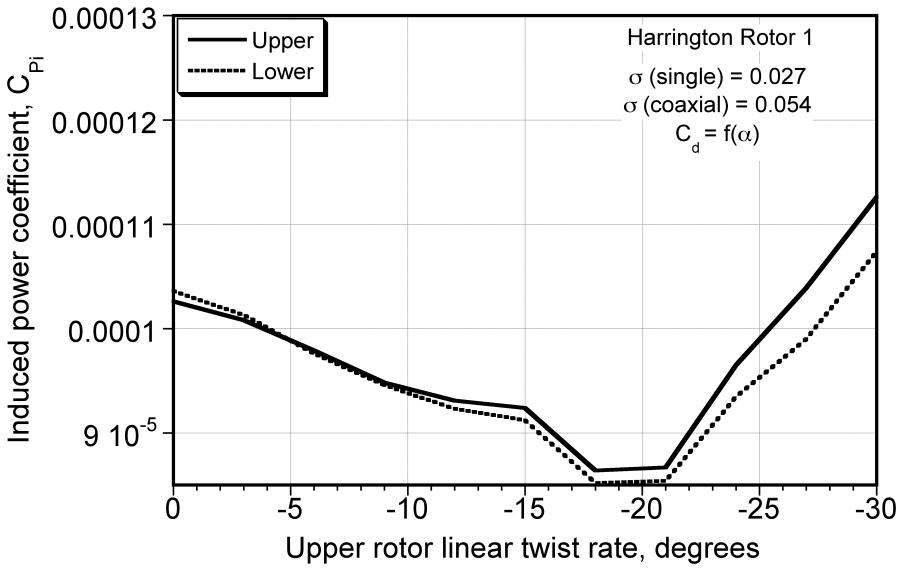

Fig. 4.71: Variation of the induced power coefficient on the upper and lower rotors with increase in linear twist rate on upper rotor blades. (Results obtained using FVM.)

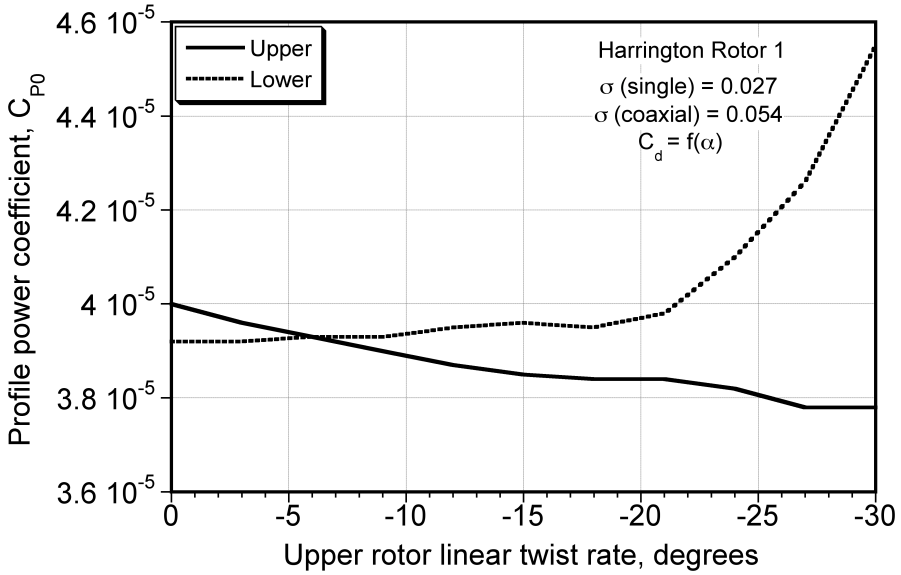

Fig. 4.72: Variation of the profile power coefficient on the upper and lower rotors with increase in linear twist rate on upper rotor blades. (Results obtained using FVM.)

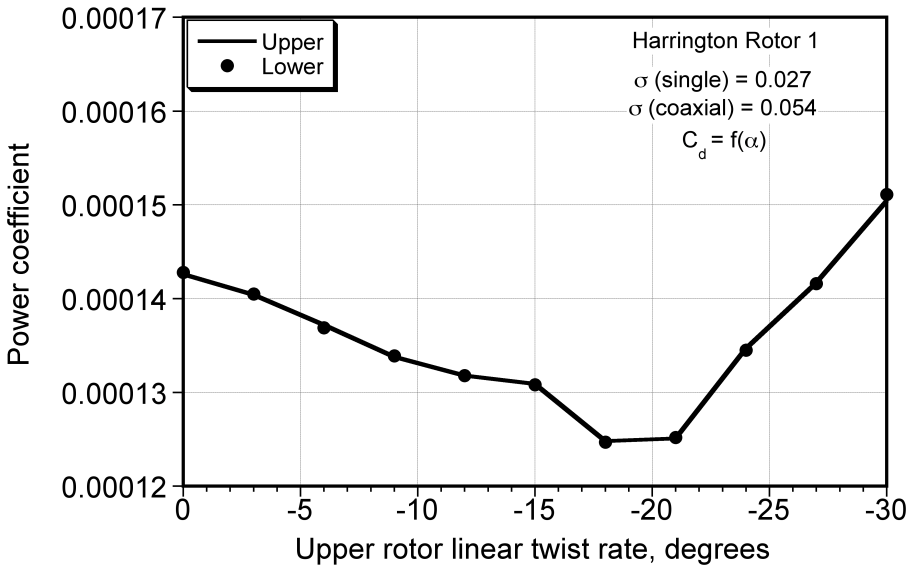

Fig. 4.73: Variation of the total power coefficient (induced plus profile) on the upper and lower rotors with increase in linear twist rate on upper rotor blades. (Results obtained using FVM.)

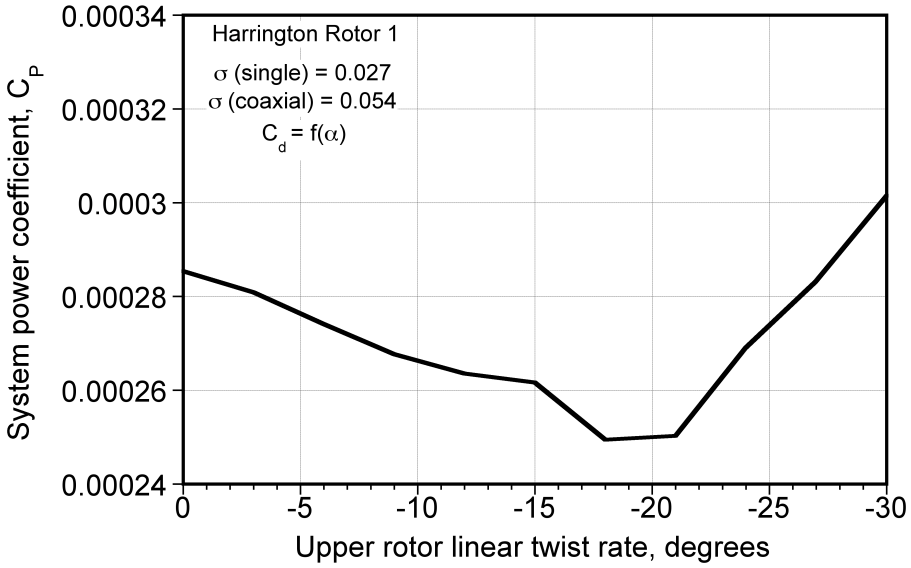

Fig. 4.74: Variation of the total system power coefficient on the upper and lower rotors with increase in linear twist rate on upper rotor blades. (Results obtained using FVM.)

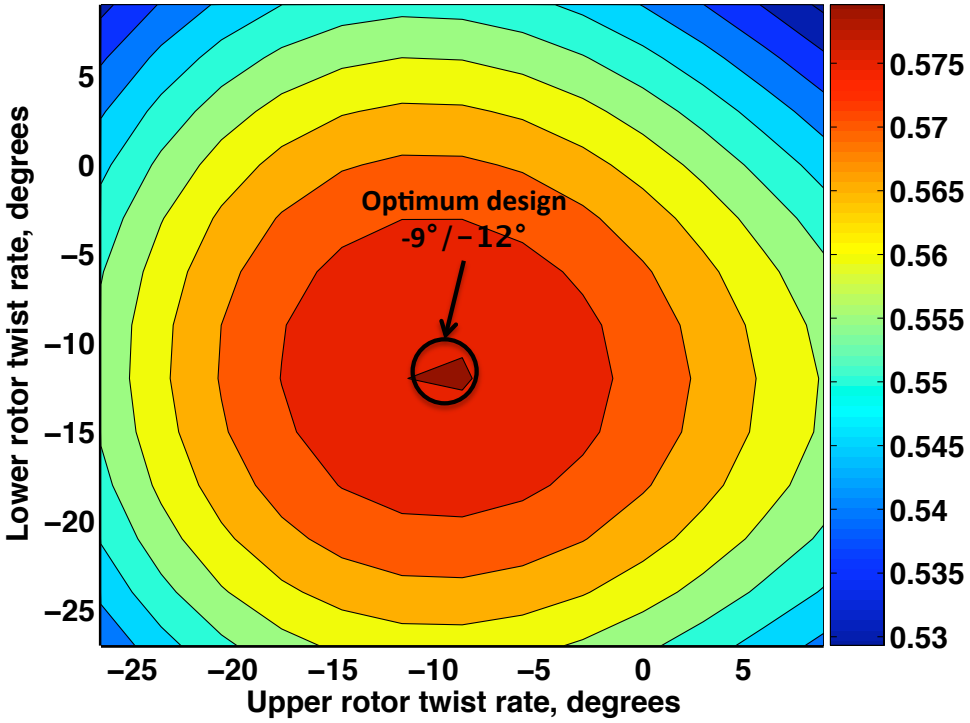

Fig. 4.75: Contour plot of FM over the two-dimensional design space of linear twist rates on upper and lower rotors (produced by the BEMT).

4.5 Blade Shape Optimization Using BEMT

This section discusses the blade shape optimization results obtained by coupling the BEMT with the DOT optimizer. The baseline rotor considered in the present study was the Harrington Rotor 1 system, which has untwisted blades that are linearly tapered in planform. The maximum measured figure of merit of the baseline rotor is 0.5631.

To validate the numerical coupling between the two methods, first parametric computations were done using the BEMT with rotor twist rates ranging from between 9° to −27°, for total of 169 BEMT computations. Figure 4.75 shows the figure of merit contour plot as a function of the linear twist rates on the upper and lower

rotors. The results show that twist rates of -9° and -12° on the upper and lower rotors, respectively, give the maximum figure of merit. This result is consistent with the study performed in the Section 4.4, which also suggests the same optimum for the blade shape.

4.5.1 Linear Twist Distributions: 2-Design Variable Problem

For this case, the blade shape function comprised of linear twist rates on both the upper and lower rotors as given by Eqs. 3.8, 3.9 and 3.10. The objective was to maximize system figure of merit. The figure of merit expression and constraints are given by Eqs. 3.7, 3.20, 3.21 and 3.23. The optimization was performed using several initial blade designs, and for all the initial blade designs, the global optima was found as

$$\mathbf{X}^* = \left\{ \begin{array}{c} -9.2^\circ \\ \\ -11.9^\circ \end{array} \right\} \tag{4.7}$$

The optimum linear twist distribution on the blades of upper and lower rotors as given Eq. 4.7 is shown in Fig. 4.76. The *FM* for this coaxial blade design was 0.5794, which is 3% higher compared to the *FM* of the baseline Harrington rotor 1.

4.5.2 Non-Linear Twist Distributions: 6-Design Variable Problem

In this case, the blade shape function for each rotor comprised of a break point and twist rates defined before and after these breakpoints, as shown previously in Fig. 3.2(a). The corresponding design vector is given by Eq. 3.11. The twist distribution on the blades of both rotors can be given by Eq. 3.12. Like the 2-design

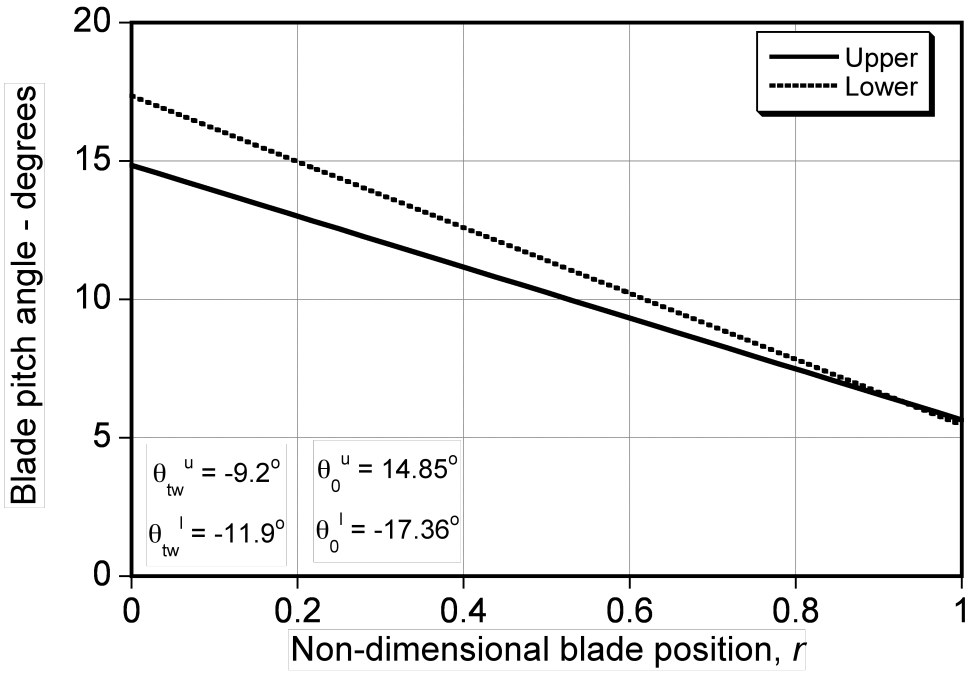

Fig. 4.76: Optimum linear twist distribution on the upper and lower rotor blades as given by BEMT.

variable problem, several initial designs were considered, to test for the existence of local optima. Some of these optimum designs are given in Eqs. 4.8 and 4.9 with the corresponding optimum values of the objective function.

$$\mathbf{X}_1^* = \left\{ \begin{array}{c} -24.3^\circ \\ -4.12^\circ \\ -30.7^\circ \\ -5.63^\circ \\ 0.573 \\ 0.546 \end{array} \right\}, \qquad \mathbf{X}_2^* = \left\{ \begin{array}{c} -31.43^\circ \\ -6.11^\circ \\ -36.8^\circ \\ -6.84^\circ \\ 0.5 \\ 0.5 \end{array} \right\} \text{ and } \qquad \mathbf{X}_3^* = \left\{ \begin{array}{c} -34.1^\circ \\ -4.6^\circ \\ -37.7^\circ \\ -7.13^\circ \\ 0.5 \\ 0.5 \end{array} \right\}$$

$$FM_1 = 0.5846\,, \qquad FM_2 = 0.5849 \qquad \text{and} \qquad FM_3 = 0.5849 \tag{4.8}$$

$$\mathbf{X}_4^* = \left\{ \begin{array}{c} -33^\circ \\ -6^\circ \\ -37.5^\circ \\ -6.8^\circ \\ 0.5 \\ 0.5 \end{array} \right\}, \qquad \mathbf{X}_5^* = \left\{ \begin{array}{c} -45^\circ \\ -6.1^\circ \\ -45^\circ \\ -6.9^\circ \\ 0.5 \\ 0.5 \end{array} \right\} \text{ and } \qquad \mathbf{X}_6^* = \left\{ \begin{array}{c} -40^\circ \\ -5.5^\circ \\ -42.1^\circ \\ -6.3^\circ \\ 0.5 \\ 0.5 \end{array} \right\}$$

$$FM_4 = 0.5850\,, \qquad FM_5 = 0.5852 \qquad \text{and} \qquad FM_6 = 0.5853 \tag{4.9}$$

The twist distribution on upper and lower rotors given by blade designs $\mathbf{X}_1^*$, $\mathbf{X}_3^*$ and $\mathbf{X}_5^*$, are shown in Figs. 4.77(a) and 4.77(b). The results show that for all the local optima given by DOT, the difference between the twist rates before and after the breakpoint is quite significant on both of the rotors, i.e., the inboard sections operate at much higher twist rates than the outboard sections. Also, the twist rate on the lower rotor is slightly higher than the upper rotor for all these blade designs given by Eqs. 4.8 and 4.9. Notice that the FM of the coaxial system obtained from these designs is almost same for all the local optima, and it shows a maximum of 4% increase compared to the baseline geometry FM. These results show that there are local maxima in the design space and perhaps that there is no global maximum that is too different from any local maximum. In other words, an optimum, or near optimum value of FM can be obtained with several different blade designs.

4.5.3 Non-Linear Twist Distributions: 8-Design Variable Problem

The four design variables for each blade in this case comprised of twist rates before and after the breakpoint, the breakpoint itself, and the offset in the blade twist at the break points, as shown in Fig. 3.2(b). As in the 6-DV problem, several initial designs were used, and resulted in different final designs, again indicating non-convexity of the design space. The following design gave maximum figure of merit

$$\mathbf{X}_4 = \{-39^\circ,\ -5.4^\circ,\ -48.5^\circ,\ -5.9^\circ,\ 0.5,\ 0.5,\ 0.98^\circ,\ 0.95^\circ\}^T \qquad (4.10)$$

The *FM* obtained from the blade design given by Eq. 4.10 was 0.5852, which was similar to the one obtained using 6-design variables. This result showed no improvement in the performance of the coaxial system, by increasing the number of design variables from 6 to 8.

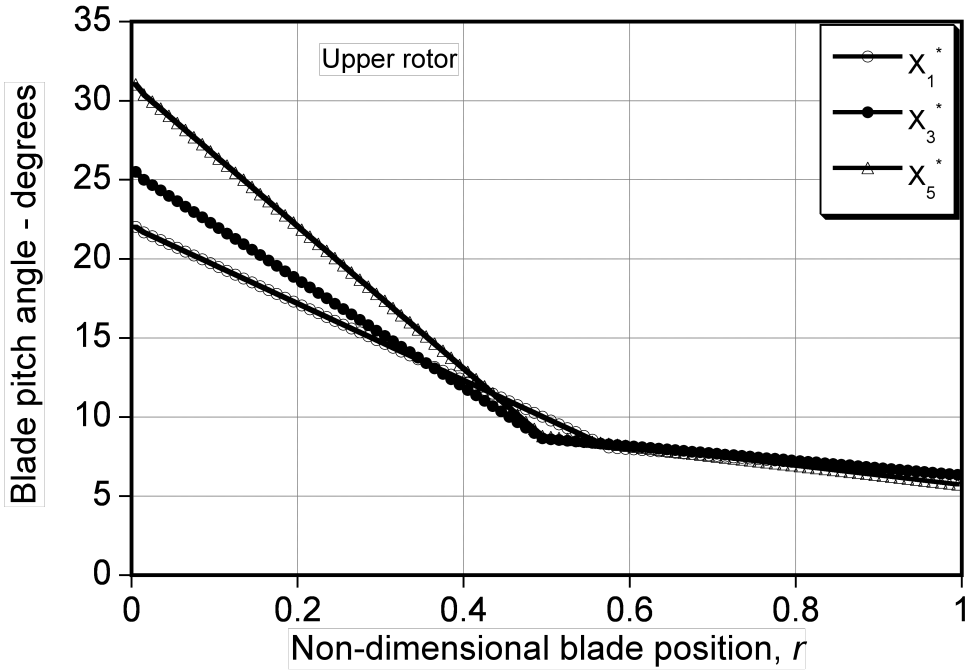

(a) Upper rotor

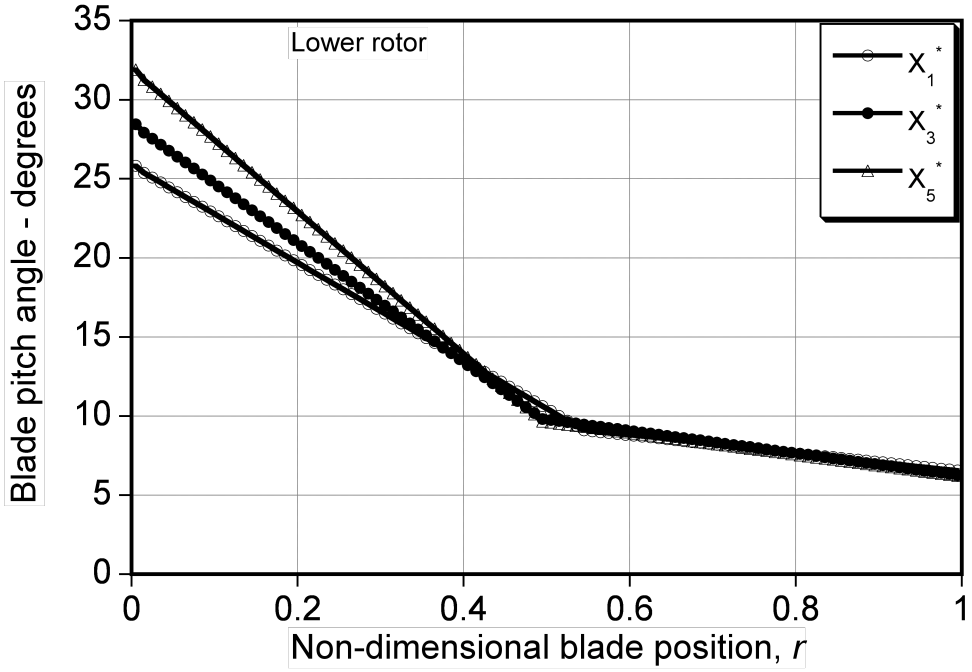

(b) Lower rotor

Fig. 4.77: Nonlinear twist distribution given by 6-design variables obtained using BEMT.

4.6 Optimization Using FVM

This section explains the optimization results that were obtained by coupling the FVM with the DOT optimizer. Like used for the BEMT analysis, the baseline rotor geometry considered in this study was also the Harrington Rotor 1, which has untwisted blades that are linearly tapered in planform. The maximum measured figure of merit of the baseline Harrington Rotor 1 geometry is 0.5631.

To understand the complexity of the optimization problem using the FVM, first the parametric results were obtained by varying linear twist rates on both the rotors from 0° to -30° (nose-down) in steps of -3°. Figure 4.78 shows the contour map of variation in the figure of merit for these cases. Notice that the figure of merit is a more nonlinear and non-convex function of the blade twist rates, compared to the BEMT case. The optimum blade twist is found at -18° and -3° on the upper and lower rotors, respectively, with a figure of merit of 0.6585, which shows a 17% increase over the baseline, although there appears to be a secondary optimum at -20° and -9° twist rates on upper and lower rotors, respectively. Notice that the optima obtained by using BEMT (i.e., $-9^\circ/-12^\circ$ — see Fig. 4.75) and FVM (i.e., $-18^\circ/-3^\circ$) are significantly different. This may be primarily because in BEMT the effect of the lower rotor aerodynamics on the upper rotor is modeled only through torque balance. However, results obtained using FVM in Fig. 4.29 show that lower rotor significantly affects the performance of upper rotor.

Before discussing the optimization results obtained by coupling FVM and DOT, one case is presented to show some details of the optimization process. This is

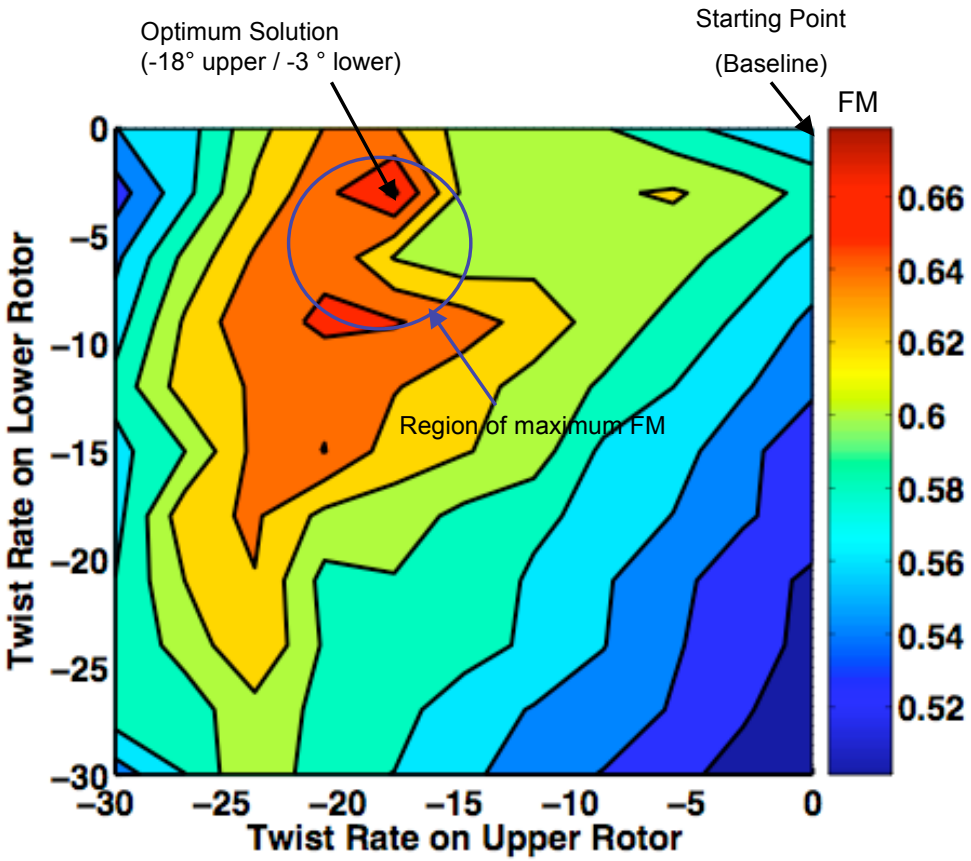

Fig. 4.78: Contour plot of FM over the two-dimensional design space of linear twist rates on upper and lower rotors (produced by the FVM).

a 6-design variable optimization case. Figures 4.79(a), 4.79(b) and 4.80 show some iteration histories for this case. The initial design was

$$\mathbf{X}^0 = \{-20°, -15°, -20°, -15°, 0.5, 0.5\}^T \tag{4.11}$$

The objective was to maximize the figure of merit. Figure 4.79(a) shows that iteration history of the objective function. The final design was

$$\mathbf{X}^* = \{-24.4°, -18.3°, -19.5°, -8.8°, 0.82, 0.86\}^T . \tag{4.12}$$

This gives a figure of merit of 0.665, which is higher by 18% compared to the baseline rotor geometry. This optimization also proceeds such that all of the

constraints are satisfied, as shown in Fig. 4.79(b), therefore the optimization is unconstrained. For this case, the optimization was terminated when the relative difference in the figure of merit at the end of 2 consecutive iterations was less than 0.1 %. A total of 57 functions calls were required to complete the optimization process.

4.6.1 Linear Twist Distribution on both the Rotors: 2 Design Variable Problem

In this case, the design variables comprised of linear twist rates on upper and lower rotors. Notice from Fig. 4.78 that the figure of merit is a nonlinear, and nonconvex function of the blade twist rates. This means that the optimization process depends highly upon the initial blade design chosen to perform optimization. Several initial designs were analyzed, and the optima obtained for all the cases were compared to each other to try to find the global optimum. Two results are presented in the present thesis to appreciate the fact that the process of optimization depends upon the initial design chosen. For the first case, the initial design provided to the optimizer was

$$\mathbf{X}^0 = \{-20^\circ, -20^\circ\}^T \tag{4.13}$$

and the optimum was

$$\mathbf{X}^* = \{-18.6^\circ, -7.7^\circ\}^T \tag{4.14}$$

with a FM of 0.655, which gives a 16% gain over the baseline coaxial system.

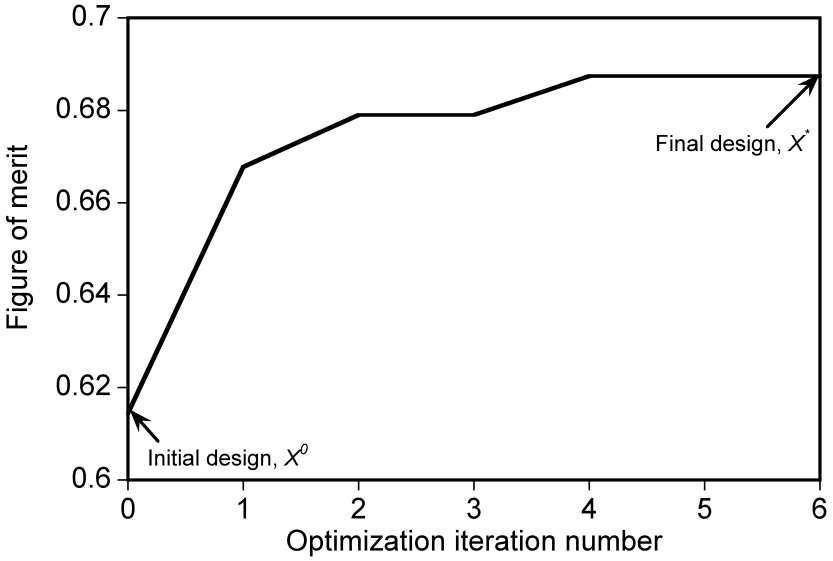

(a) Objective function, i.e., figure of merit

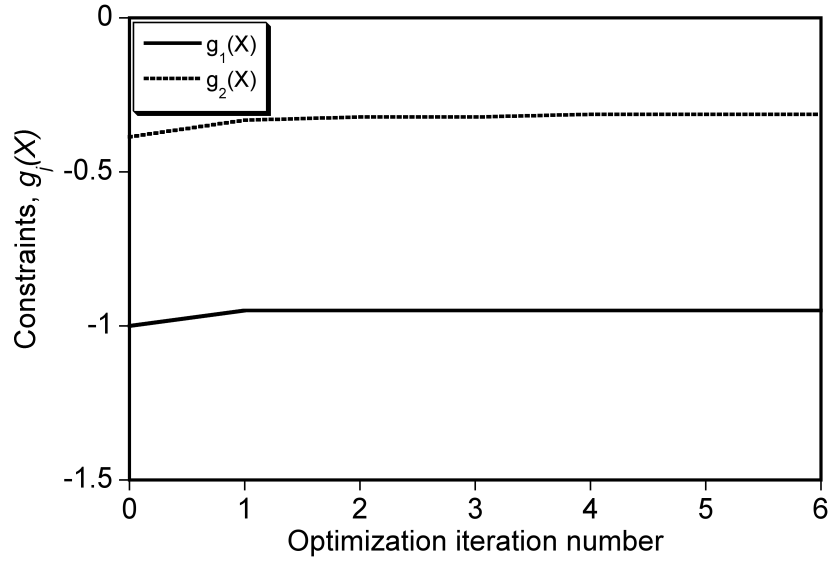

(b) Constraints

Fig. 4.79: Optimization history of a 6-design variable problem.

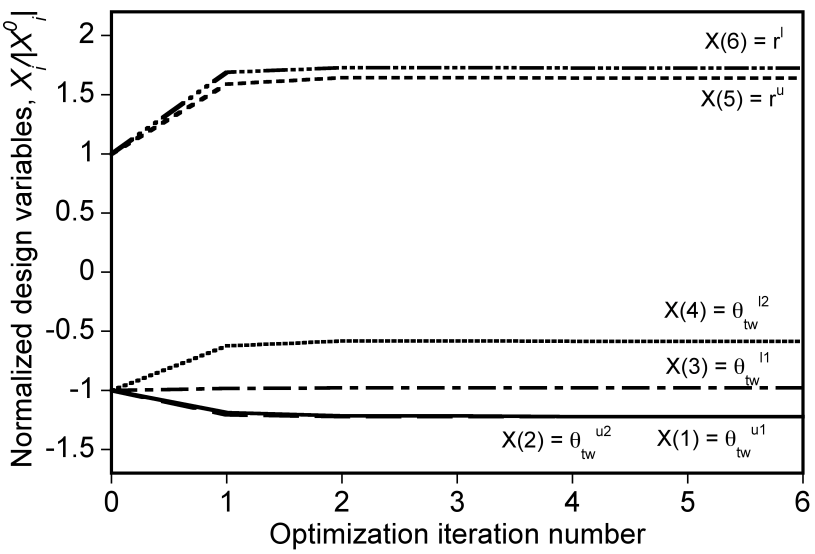

Fig. 4.80: Optimization history of a 6-design variable problem showing the design variables.

For the second case, the initial design was

$$\mathbf{X}^0 = \{-15^\circ, -5^\circ\}^T \tag{4.15}$$

and the optimum was

$$\mathbf{X}^* = \{-17.26^\circ, -3.08^\circ\}^T \tag{4.16}$$

with a FM of 0.6588, which gives a gain of 17% over the baseline. The twist distribution on the blades of both rotors with twist rates given by Eq. 4.14 and 4.16, is shown in Fig. 4.81. Unlike the linear twist rate obtained using the BEMT (i.e., given by Eq. 4.7), the optimum given by the FVM has higher twist on upper rotor blades compared to the lower rotor.

The paths followed by the optimizer to find optimum for these two cases are shown in Figs. 4.82(a) and 4.82(b), respectively. These results are again consistent with the parametric study performed in Section 4.4 to study the effect of twist rate

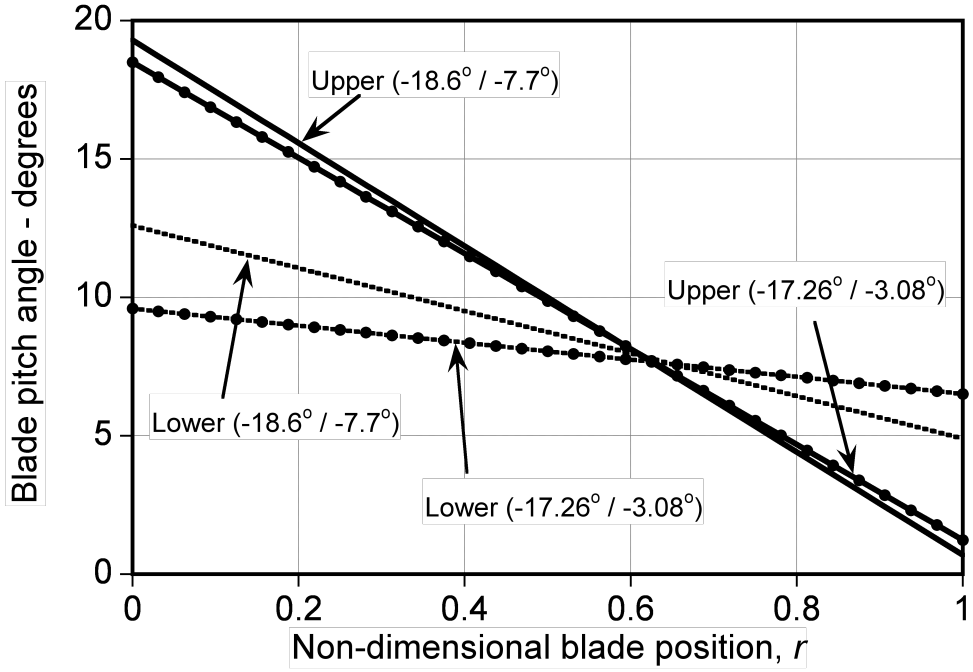

Fig. 4.81: Optimum linear twist distribution on upper and lower rotor blades as given by FVM for two locally optimum designs.

on the efficiency of the coaxial rotor system, which also suggested an optimum close to -18° on the upper rotor and -3° on the lower rotor. For this coaxial rotor design, the variation of the FM with the number of MFW iterations is shown in Fig. 4.83. The result shows that the FM converges to a steady value of 0.6585 within about 30 rotor revolutions (i.e., 60 half revolutions). Notice that as mentioned previously in Section 3.2, the convergence of solution was obtained when the difference between FM reduced by 0.001% consecutively for five rotor revolutions. The objective function was then computed by averaging the FM over these 5 rotor revolutions.

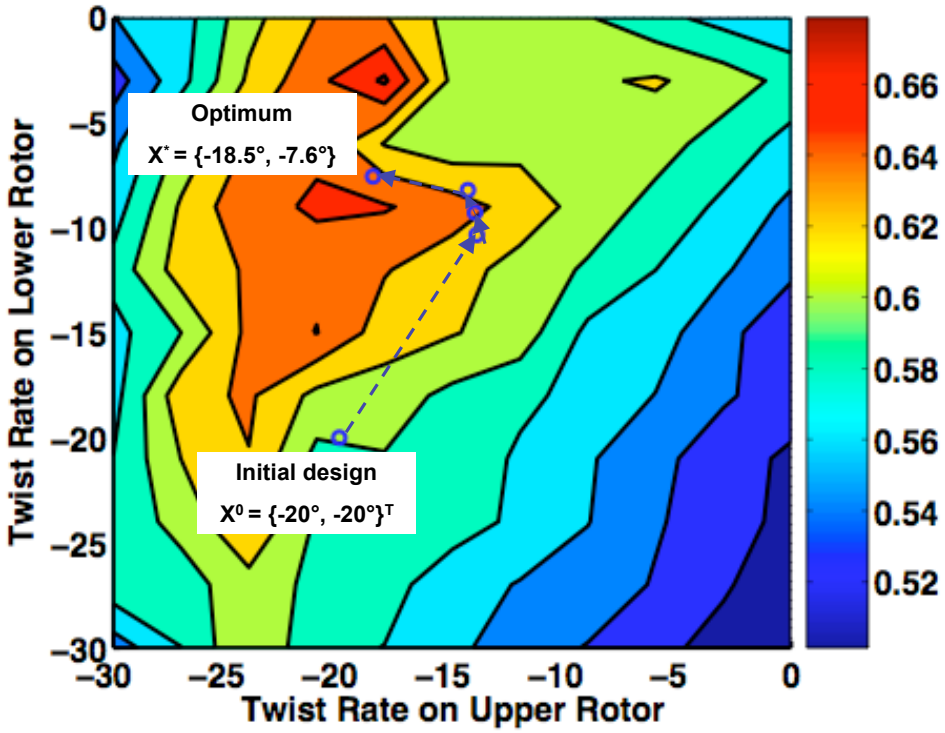

(a) $\mathbf{X}^0 = \{-20°, -20°\}^T$

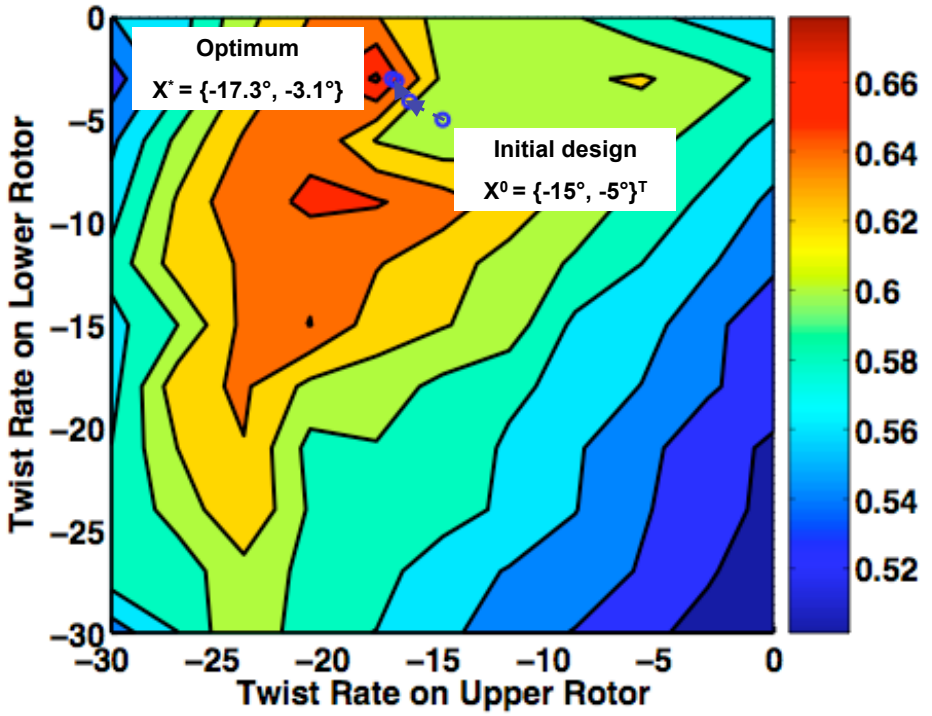

(b) $\mathbf{X}^0 = \{-15°, -5°\}^T$

Fig. 4.82: Representation of the paths followed by the DOT optimizer to obtain the optimum design with two different initial designs, $\mathbf{X}^0$ (produced using the FVM).

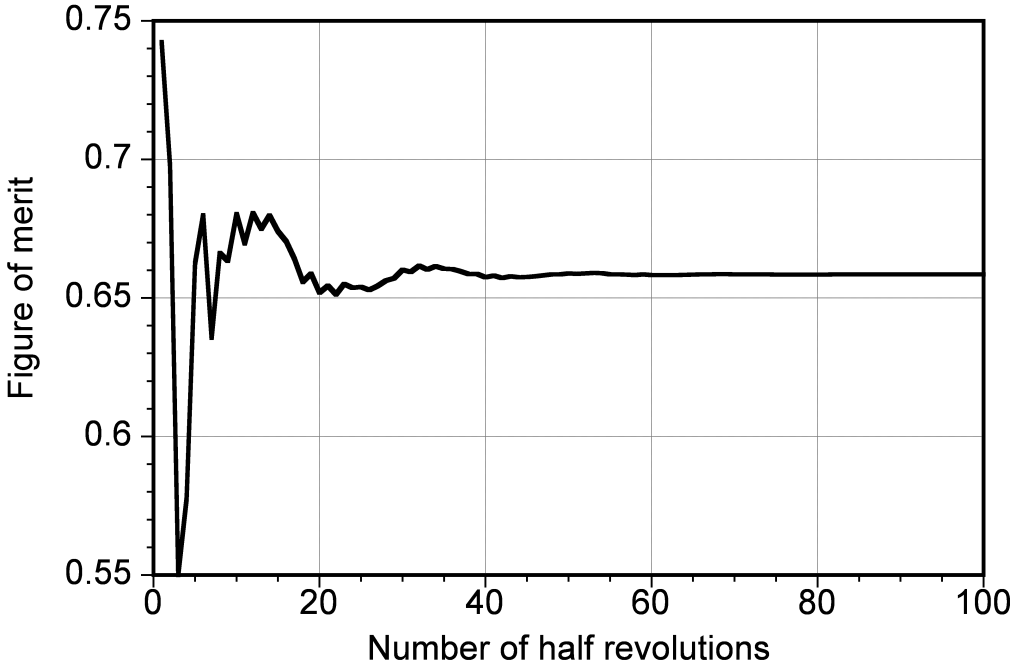

Fig. 4.83: Figure of merit variation with number of half rotor revolutions.

4.6.2 Non-linear Twist Distribution on Both the Rotors—6-Design Variable Problem

The blade shape functions comprised of a spanwise break point and twist rates before and after the breakpoint on both the rotors. As shown previously in the BEMT results, the optimization of the coaxial rotor geometry using 6 design variables is a non-convex problem. In other words, there is more than one combination of design variables that give figure of merit values that are comparable to each other. Notice that unlike the BEMT, which takes just seconds to perform the optimization, using the FVM requires 40–50 hours. Therefore, several initial designs were tried that cover the whole design space. The three results given here are the ones that have the highest figures of merit of all the tried cases.

- Result 1

  The initial design provided to the optimizer was

  $$\mathbf{X}^0 = \{-15^\circ, -15^\circ, -15^\circ, -15^\circ, 0.5, 0.5\}^T \tag{4.17}$$

  and the optimum was

  $$\mathbf{X}^* = \{-17.2^\circ, -17.77^\circ, -8.56^\circ, -6.24^\circ, 0.496, 0.432\}^T \tag{4.18}$$

  with a *FM* of 0.668, which gives a 19% gain over the baseline coaxial system. The optimum blade design has almost linear twist distribution on both the rotors. However, the bottom rotor has a lower twist rate compared to the upper rotor, as was found in the previous section. The twist distribution on both the rotors is shown in Figs. 4.84(a) and 4.84(b), respectively.

- Result 2

  The initial design was

$$\mathbf{X}^0 = \{-21^\circ, -18^\circ, -3^\circ, -3^\circ, 0.8, 0.8\}^T \tag{4.19}$$

  and the optimum was

$$\mathbf{X}^* = \{-19.7^\circ, -18.25^\circ, -2.9^\circ, -2.83^\circ, 0.94, 1.0\}^T \tag{4.20}$$

  with a *FM* of 0.6651, which gives an 18% gain over the baseline coaxial system. This result also gives an almost linear twist distribution on both the rotors as shown in Figs. 4.84(a) and 4.84(b), respectively.

- Result 3

  The initial design was

$$\mathbf{X}^0 = \{-20^\circ, -15^\circ, -20^\circ, -15^\circ, 0.5, 0.5\}^T \tag{4.21}$$

  and the optimum was

$$\mathbf{X}^* = \{-24.4^\circ, -18.3^\circ, -19.5^\circ, -8.8^\circ, 0.82, 0.86\}^T \tag{4.22}$$

  with a *FM* of 0.665, which is higher by 18% compared to the baseline coaxial system. The twist distribution on upper and lower rotor blades is shown in Figs. 4.84(a) and 4.84(b), respectively.

  The results show that for all cases, the twist distribution is higher on the upper rotor compared to the lower rotor. As was found previously from the BEMT analysis, FVM confirms that there is no one blade twist design that gives

optimum performance. However, the *FM* obtained using 6-DV is almost same as that obtained by using 2-DV. This means that *FM* does not increase by increasing the number of parameters used to define the twist shape function.

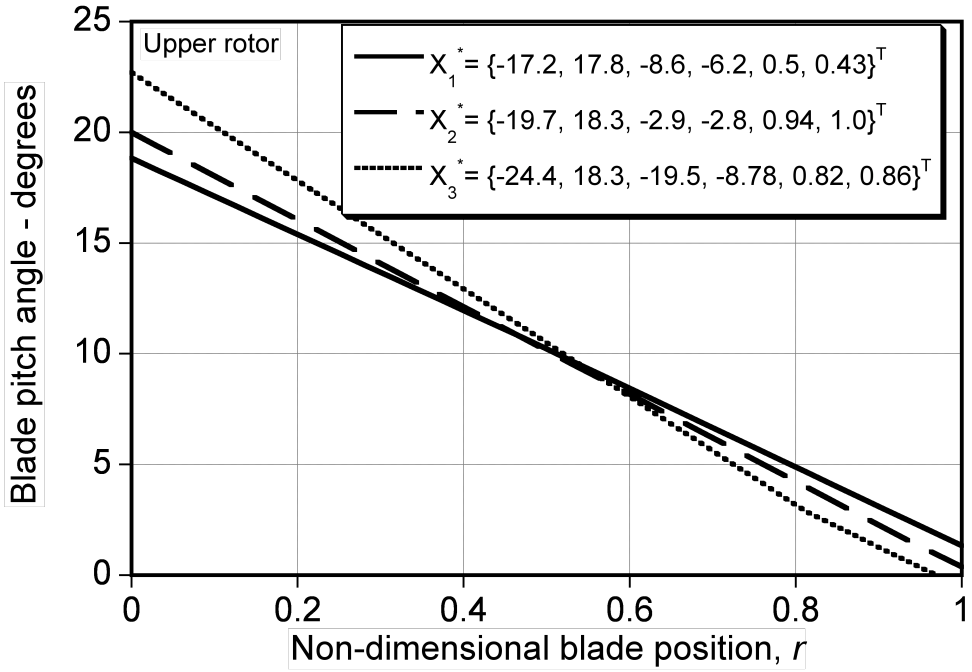

(a) Upper rotor

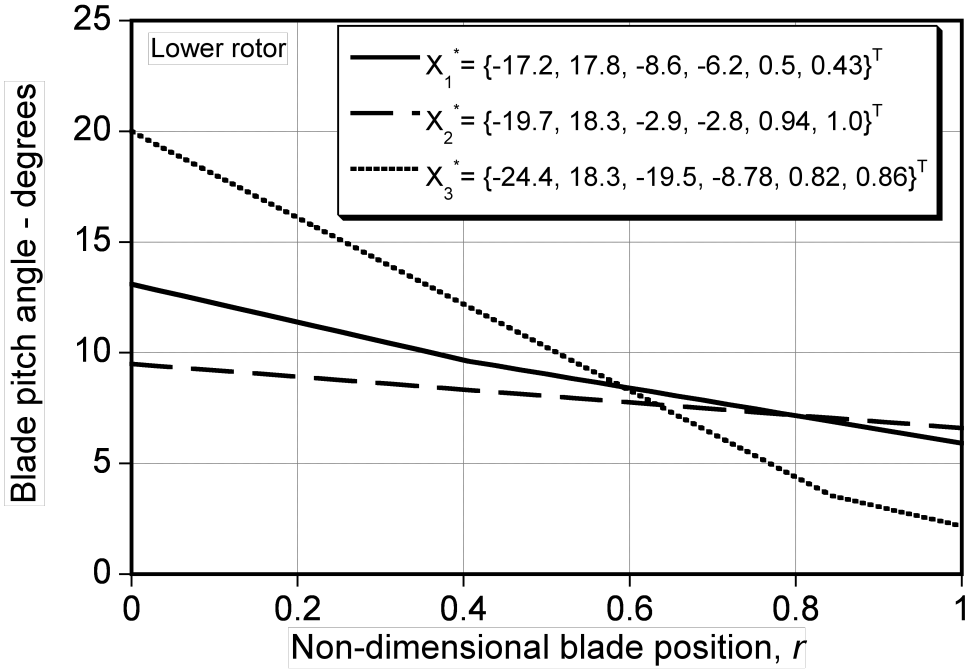

(b) Lower rotor

Fig. 4.84: Nonlinear twist distribution given by 6-design variables obtained by using FVM.

4.7 Blade Planform Variations

This section presents results from the study performed to understand the effects of planform changes on the performance of a coaxial rotor system. The study was performed using Harrington Rotor 1 system as a baseline, with both sets of blades on the rotors being untwisted. The effects of taper ratio and solidity of both the rotors, were analysed. The planform shapes were determined such that the thrust equivalent solidity of the coaxial rotor system remained constant.

This section is divided into two parts discussing the effects of changing taper ratio and solidity on both the rotors, respectively. It should be noted that the thrust weighted solidity of the coaxial was kept constant for all the configurations studied, and all the results are obtained using FVM.

4.7.1 Planform Taper Studies

The planform of the Harrington Rotor 1 system was changed by changing the linear taper on both the rotors, keeping all other geometrical parameters constant. In this study, the taper ratio (i.e., TR_u) on the upper rotor was increased from 1.7 to 5.8. Notice that the taper ratio is defined in Eq. 3.15 as the ratio of the root chord to the tip chord. The taper ratio on the lower rotor was computed by using Eqs. 3.16, 3.17 and 3.18, such that the equivalent solidity of the coaxial rotor system is held constant. The inverse of the taper ratio on the lower rotor is given by

$$\frac{1}{TR_l} = 1 + \left(\frac{1 - r_t^l}{0.75 - r_t^l}\right)\left[\frac{c_e}{c_0^l} - 1 - \frac{c_0^u}{c_0^l}\left\{\left(\frac{1}{TR_u} - 1\right)\left(\frac{0.75 - r_t^u}{1 - r_t^u}\right) + 1\right\}\right] \tag{4.23}$$

where $c_e = \left(\frac{\sigma_e \pi R}{N_b}\right)$ is the thrust weighted equivalent chord of the coaxial rotor

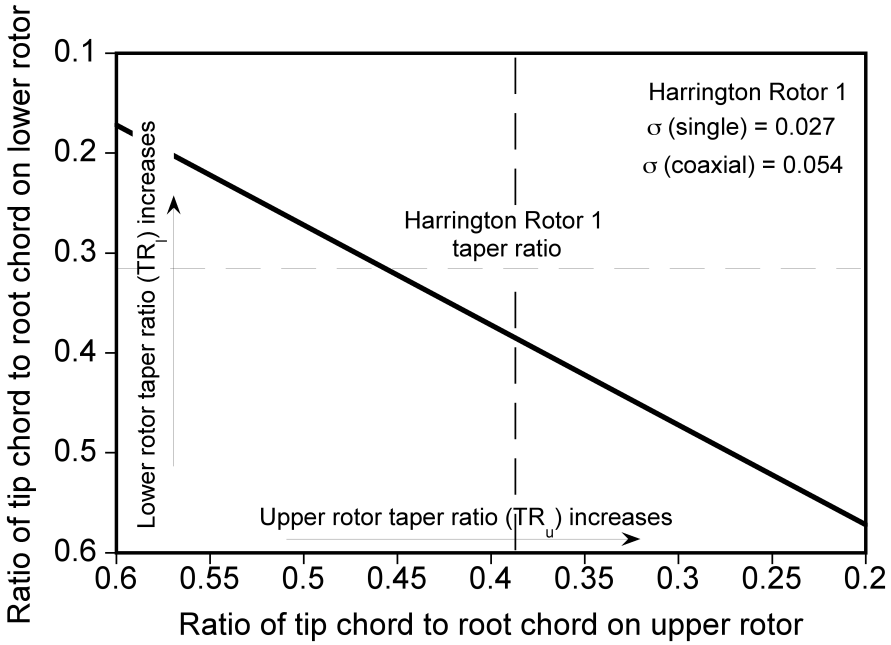

Fig. 4.85: Variation of the taper on lower rotor blades with increase in the taper ratio on upper rotor.

system.

Figure 4.85 shows that the TR on the lower rotor decreases with an increase in the TR on the upper rotor to maintain constant thrust weighted solidity of the coaxial rotor system. The thrust weighted solidity of both the rotors decrease with an increase in their taper ratio—see Fig. 4.86. Also, notice that the thrust weighted solidity of the coaxial system is constant at all taper ratios. At the taper ratios of the Harrington Rotor 1 system, the solidities on both the rotors are equal to 0.027. With an increase in the taper ratio on the upper rotor, its profile power decreases, as shown in Fig. 4.87, whereas the profile power on the lower rotor increases as its taper ratio increases to maintain a total equivalent solidity for the coaxial system. Notice that the power coefficients are normalized by the total power coefficient of

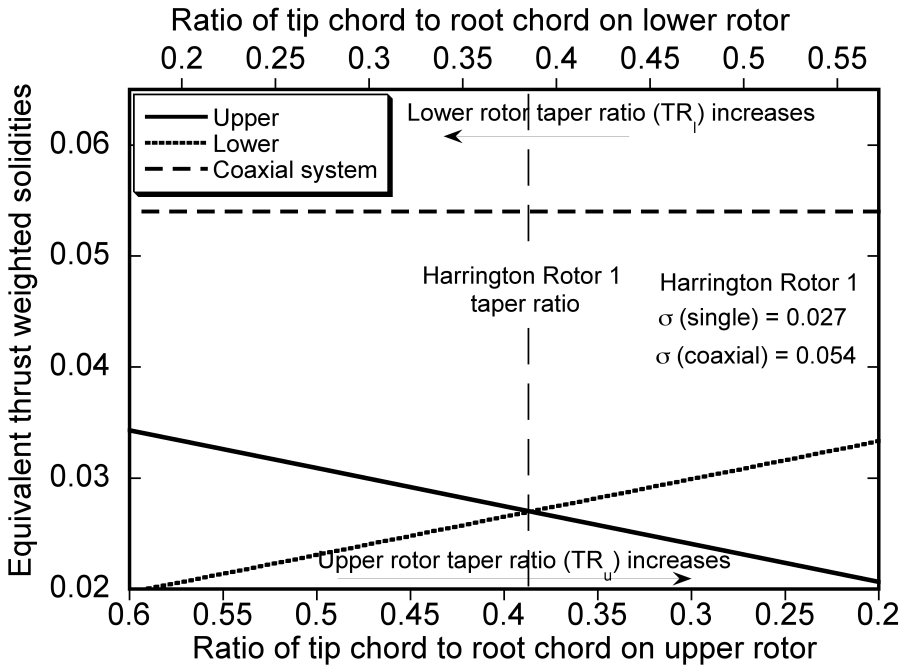

Fig. 4.86: Variation of the thrust equivalent solidities on the upper and lower rotors with changes in blade taper.

the baseline Harrington Rotor 1 system. The induced power on the upper rotor increases with an increase in its blade taper ratio, and so decreases on the lower rotor to maintain torque balance—see Fig. 4.88. Figure 4.89 shows the variation of the normalized total system induced, profile and total (i.e., induced plus profile) power coefficients with an increase in the blade taper ratio on the upper rotor. The results show that the total power remains insensitive to the change in TR, although there is a 1.5% decrease in power coefficient with a TR_u of 3.3:1 and TR_l of 2:1.

The variation of blade loading coefficients for coaxial rotor systems with different taper ratios on both rotors is shown in Fig. 4.90. Because the upper rotor carries a higher thrust, its blade loading coefficient is higher than that of the lower rotor for the baseline Harrington system (which has equal solidities). This also means that

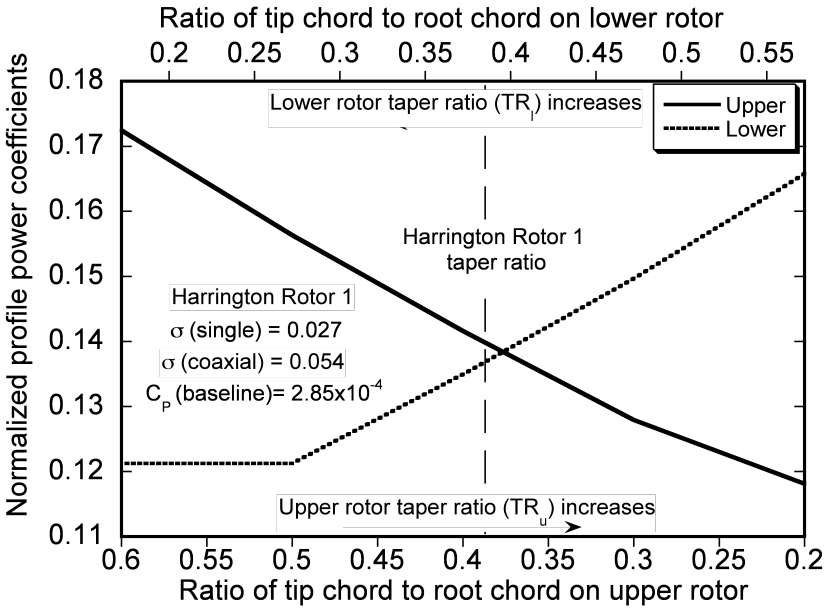

Fig. 4.87: Variation of the normalized profile power coefficient on the upper and lower rotors with changes in blade taper.

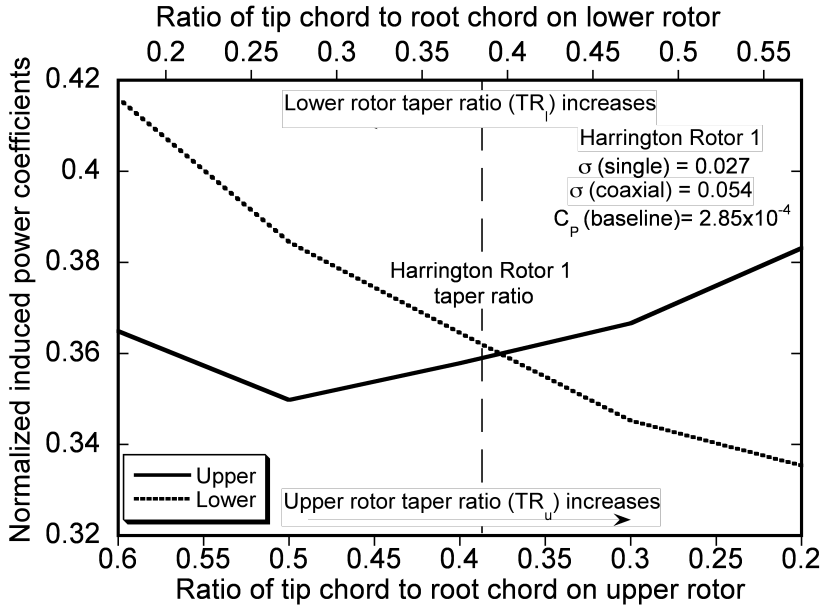

Fig. 4.88: Variation of the normalized induced power coefficient on upper and lower rotors with changes in blade taper.

the upper rotor dictates the stall margins of the coaxial rotor system, and its aerodynamic performance will be more limited than if both rotors had reached their stall limits simultaneously. An optimum coaxial system should be designed to operate with higher stall margins, such that the blade loading coefficients should, preferably, be same on both the rotors. Figure 4.90 shows that the blade loading coefficients on the upper and lower rotors are the same (i.e., $\frac{C_T}{\sigma} = 0.07$) for the coaxial system with taper ratios 2.3:1 and 2.8:1 on the upper and lower rotors, respectively. Notice that the performance of this coaxial geometry is same as the performance of the baseline geometry with the taper ratios equal to 2.6:1 on both of the rotors. Furthermore, the solidities of the upper and lower rotors for this coaxial rotor design are 0.029 and 0.025, respectively, compared to 0.027 on both rotors for the baseline geometry.

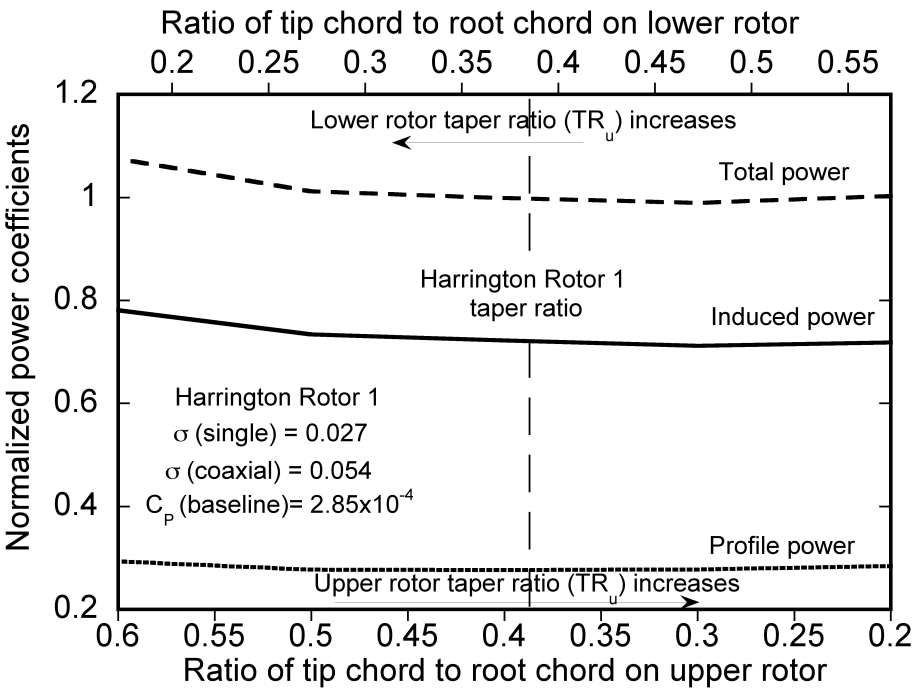

Fig. 4.89: Variation of the normalized system induced, profile and net power coefficients with changes in blade taper.

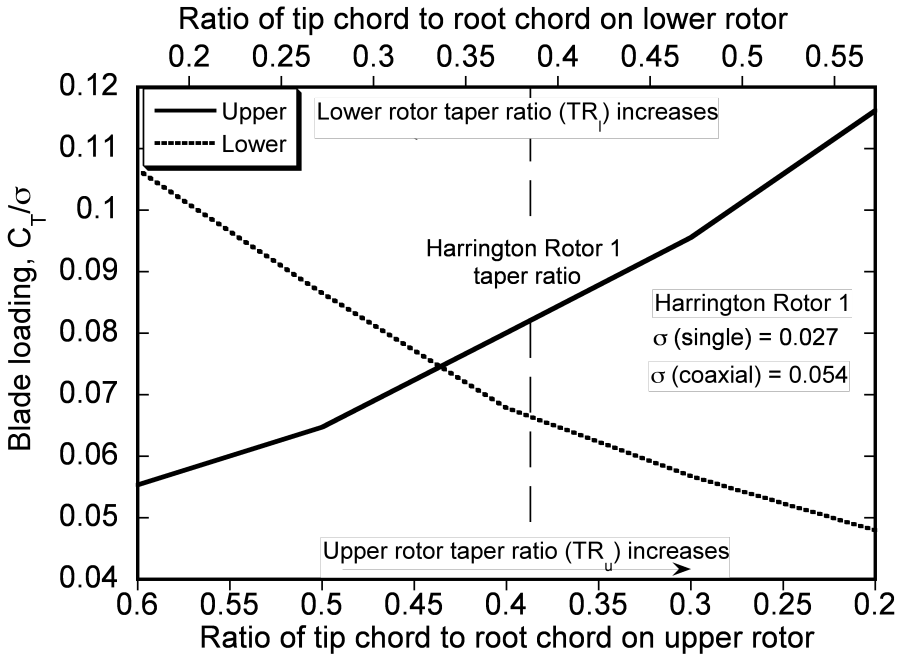

Fig. 4.90: Variation of blade loading with changes in blade taper.

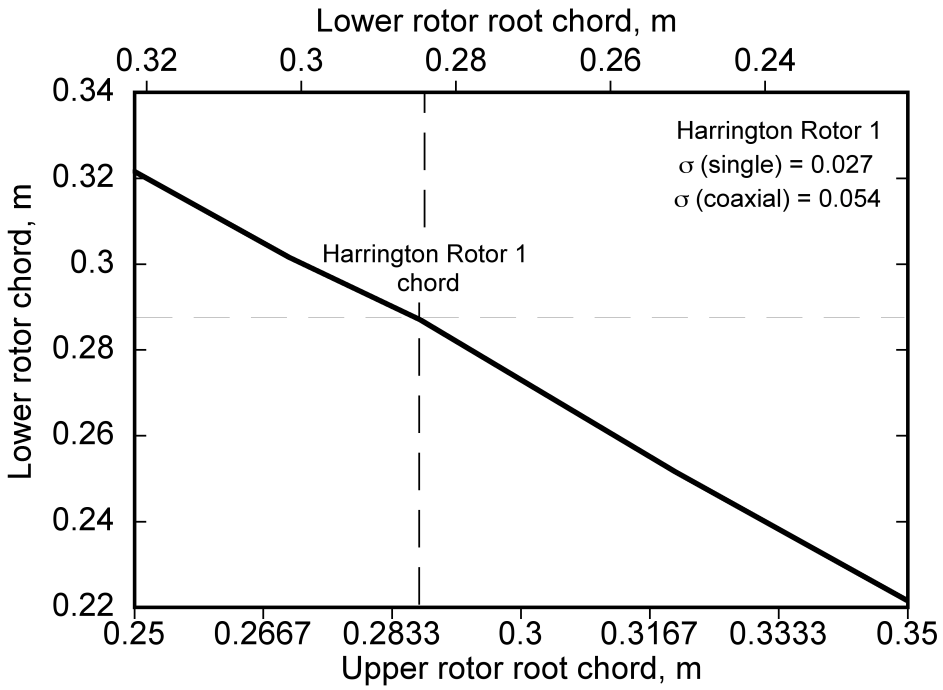

Fig. 4.91: Variation of chord on the lower rotor blades with increase in the upper rotor chord.

4.7.2 Chord Studies

This section discusses the effects of changes in root chord of both the rotors. The root chord on the blades of the upper and lower for Harrington Rotor 1 is 0.287 m (i.e., $0.075R$). In this analysis, the root chord on the upper rotor was increased from 0.25 m (i.e., $0.066R$) to 0.35 m (i.e., $0.092R$), and the chord on the lower rotor was calculated such that the thrust weighted solidity of the coaxial system remained constant. This was achieved by rearranging Eq. 4.23 to give

$$c_0^l = \frac{c_e - c_0^u \left\{ \left(\frac{1}{TR_u} - 1 \right) \left(\frac{0.75 - r_t^u}{1 - r_t^u} \right) + 1 \right\}}{\left\{ \left(\frac{1}{TR_l} - 1 \right) \left(\frac{0.75 - r_t^l}{1 - r_t^l} \right) + 1 \right\}} \tag{4.24}$$

The chord on the lower rotor decreases with an increase in chord on the upper

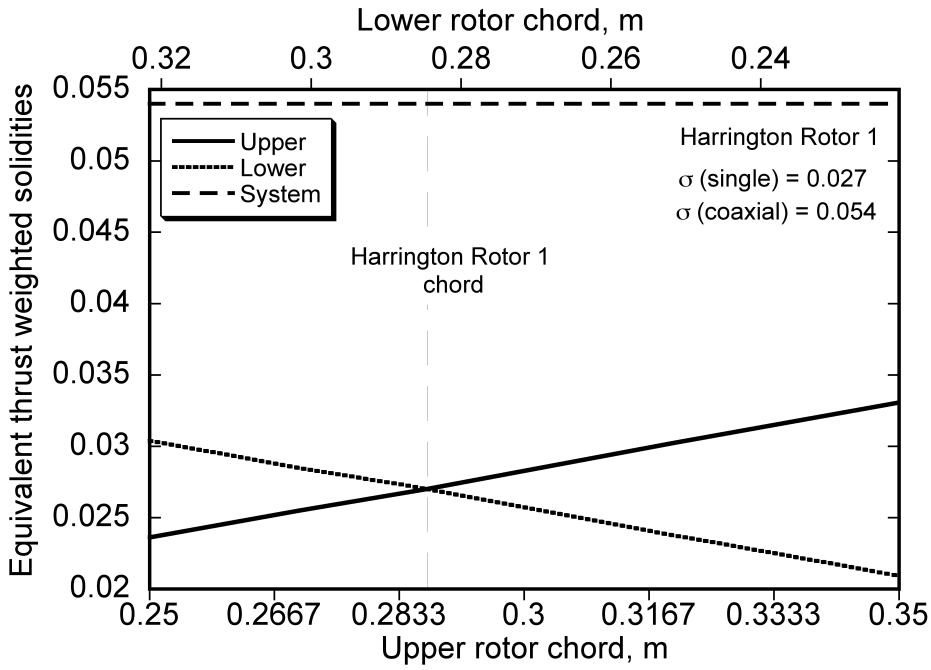

Fig. 4.92: Variation of the thrust equivalent solidities on the upper and lower rotors with root chord.

rotor to maintain a constant thrust weighted solidity of the coaxial system—see Fig. 4.91. The thrust weighted solidities of the upper rotor increases with an increase in its root chord, whereas for lower rotor it decreases as its root chord decreases, as shown in Fig. 4.92. As expected, the profile power increases on the upper rotor (Fig. 4.93) with increasing chord, and decreases on the lower rotor. To maintain torque balance condition, the induced power coefficient decreases on the upper rotor and increases on the lower rotor—see Fg. 4.94. Finally, Fig. 4.95 shows that the total power, the induced power, and the profile power of the coaxial as a system are insensitive to the changes in the chord if done at same equivalent total solidity. Figure 4.96 shows that the blade loading coefficient for both rotors become equal when upper and lower rotors have root chords equal to 0.3 m (i.e., 0.079 R) and

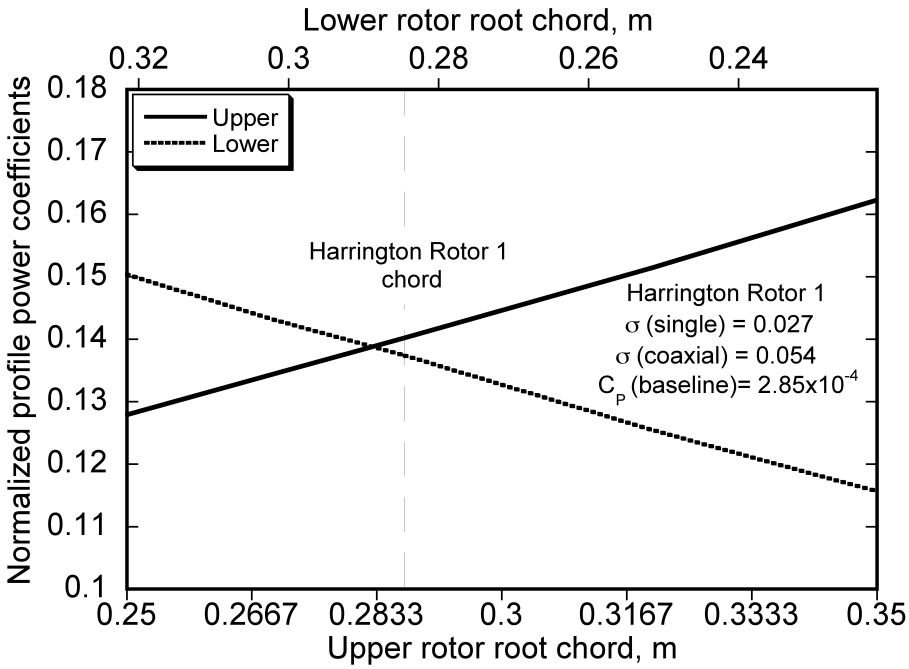

Fig. 4.93: Variation of the profile power coefficient on the upper and lower rotors, normalized with the total power of the baseline geometry, with root chord.

0.27 m (i.e., 0.071 R), respectively, compared to 0.287 m (i.e., 0.075 R) on both of the rotors in the baseline geometry. This coaxial design also offers higher stall margins, with blade loading coefficient equal to 0.07 compared to the upper rotor blade loading coefficient of 0.081 for the baseline geometry. Interestingly, this design also has solidities on the upper and lower rotors that are equal to 0.029 and 0.025, respectively (see Fig. 4.90).

These studies suggest that for the same thrust weighted solidity of the coaxial rotor system at torque balance condition, the performance of the coaxial system is insensitive to changes in taper ratio or blade root chord. However, coaxial design with solidities 0.029 and 0.025 on upper and lower rotors, respectively, offers a better stall margin compared to the baseline coaxial rotor geometry.

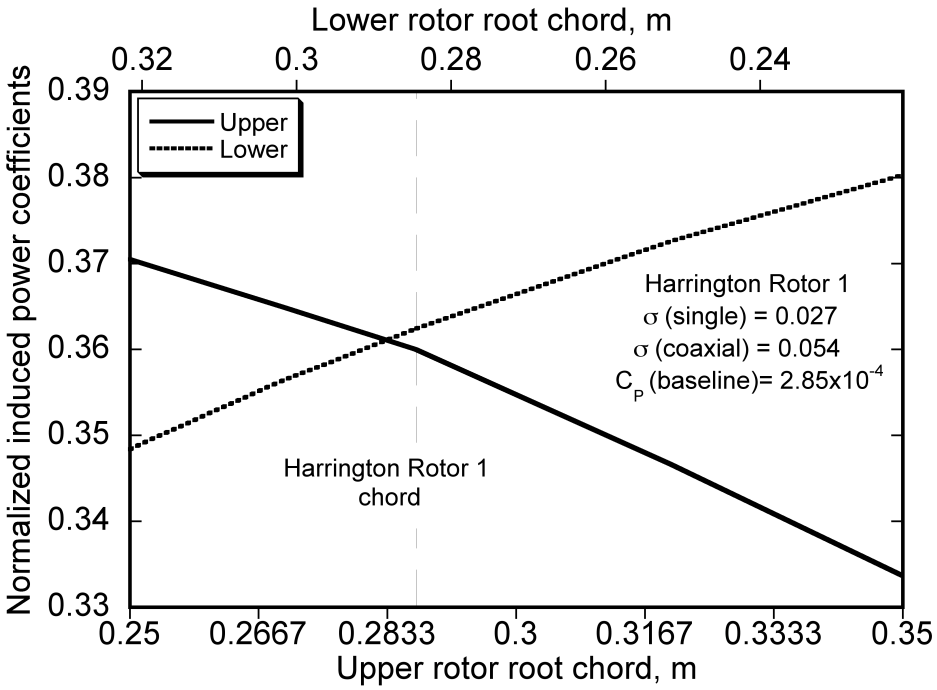

Fig. 4.94: Variation of the induced power coefficient on the upper and lower rotors, normalized with the total power of the baseline geometry, with root chord.

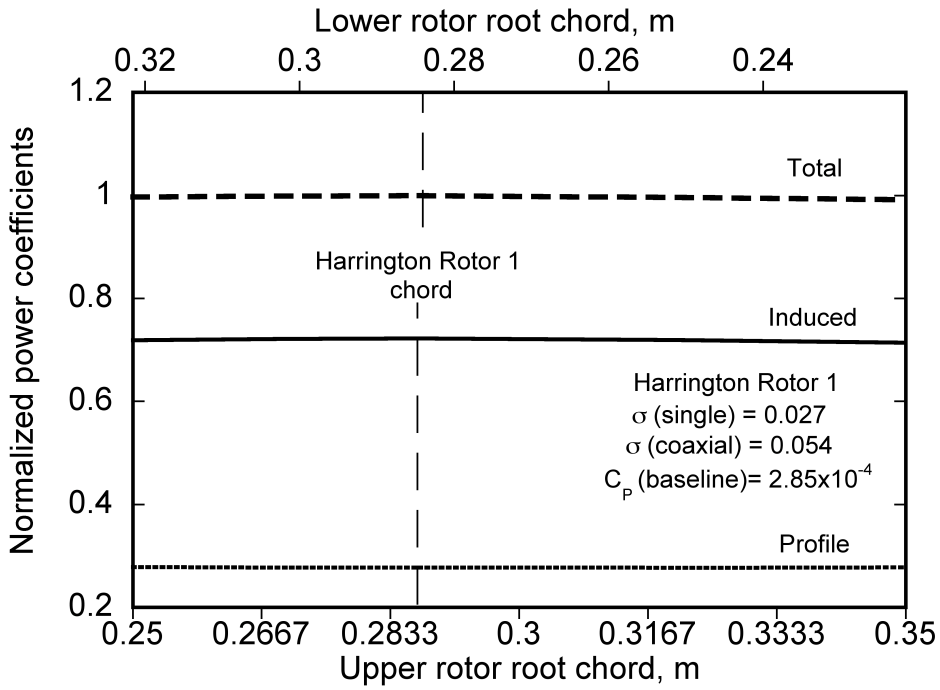

Fig. 4.95: Variation of the system induced, profile and total power coefficients, normalized with the total power of the baseline geometry, with root chord.

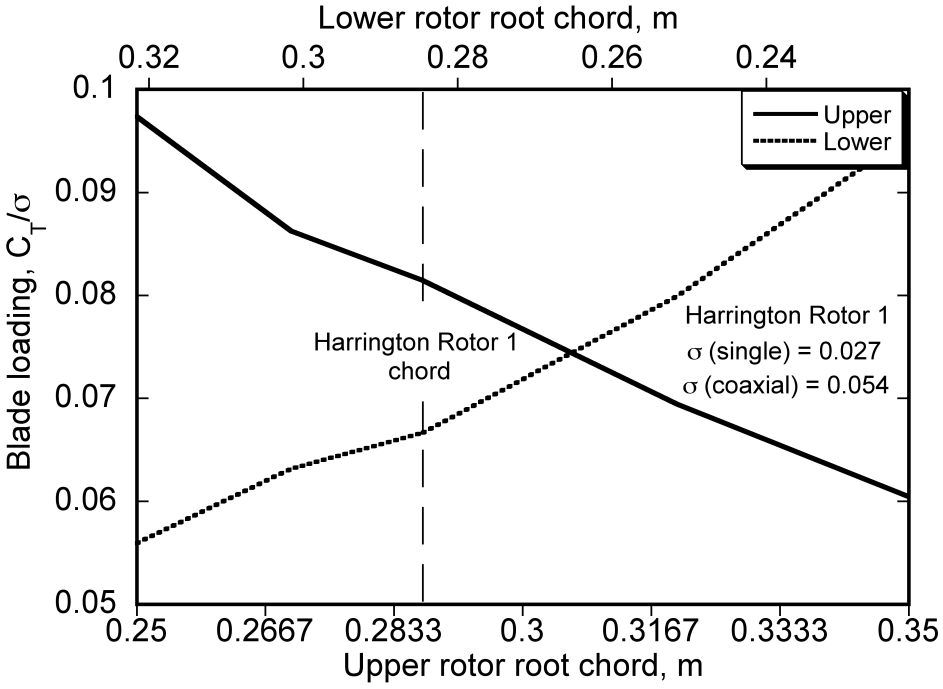

Fig. 4.96: Variation of the blade loading with changes in root chord.

4.8 Forward Flight

This section discusses the results of a study performed to examine the performance of a coaxial rotor system at different forward speeds. It starts with the validation of the forward flight performance predictions, analyzes the changes in wake geometries as predicted by the FVM, and then explains the blade shape optimization process for a specific advance ratio in forward flight.

Figure 4.8 shows the power required as a function of forward speed for the coaxial rotor tested by Dingeldein (see Ref. 15). The tests were done at a constant thrust coefficient of 0.0048 and at a tip speed of 469 ft/s. All the FVM calculations were performed at a torque balance. The effects of fuselage on the propulsive force were calculated by assuming a flat plate area of 10 ft^2, as per the original paper of Dingeldein. The FVM results showed a reasonably good agreement with the measurements over a range of forward speeds.

The predicted wake geometries of the coaxial rotor at advance ratios of between 0.05 and 0.25 are shown in Fig. 4.98. The results show that the interference (intermingling) between the trailed wakes from the upper and lower rotors decreases at higher forward speeds. Therefore, at higher advance ratios both rotors of the coaxial system share almost equal thrusts—see Fig. 4.99. Hence, both the rotors operate at almost same disk loadings at higher forward speeds, and therefore, for best performance the optimum geometries of the two rotors (if obtained) should be essentially the same.

The best blade geometry for forward flight is not intuitively obvious because

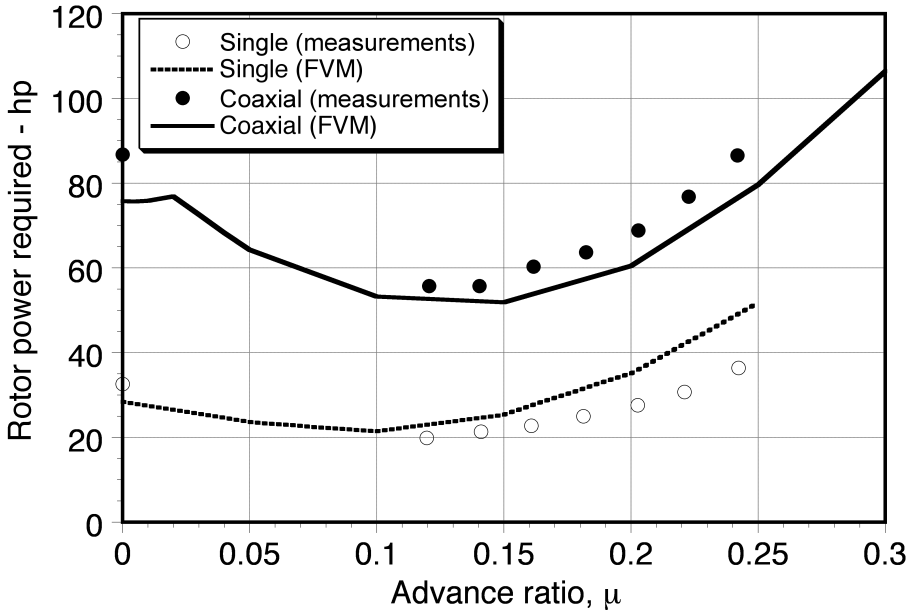

Fig. 4.97: Forward flight performance of the Harrington Rotor 1 at $C_T = 0.0048$ with a tip speed of 469 ft/s.

the flow conditions of the blade vary with azimuth angle. This means that any attempt to optimize the blade shape must be done by considering only the average aerodynamic operating environment. The flow differences between the advancing and retreating sides of the rotor disk are the main issue here; at higher forward speeds the advancing side operates at low angles of attack but higher tip Mach numbers, and the retreating side operates at higher angles of attack and with reverse flow. Furthermore, there will probably be no single blade geometry that will give optimum aerodynamic performance in both hover *and* in forward flight.

An attempt was still made in the present work to optimize the coaxial rotor geometry forward flight. As has already been observed in Section 4.7, the planform changes did not have much effect on the performance of the coaxial rotor system in

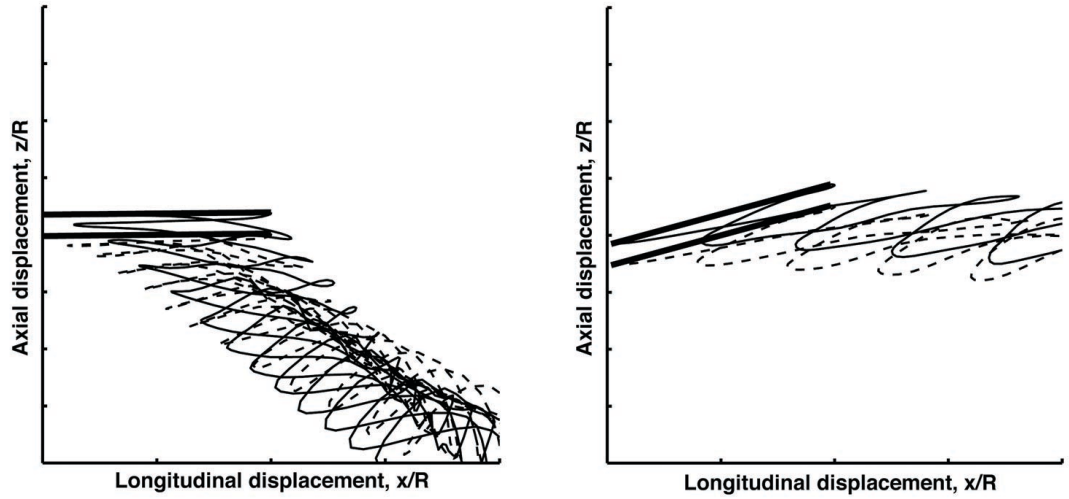

(a) Side view at $\mu = 0.05$

(b) Side view at $\mu = 0.25$

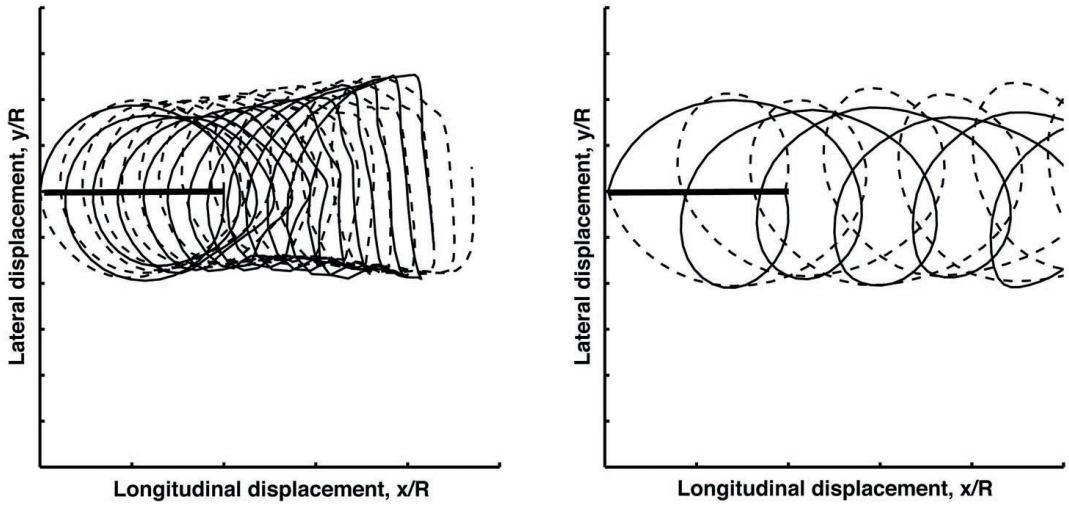

(c) Top view at $\mu = 0.05$

(d) Top view at $\mu = 0.25$

Fig. 4.98: Wake geometries of the Harrington rotor 1 at advance ratios of and 0.25 with C_T of 0.0048.

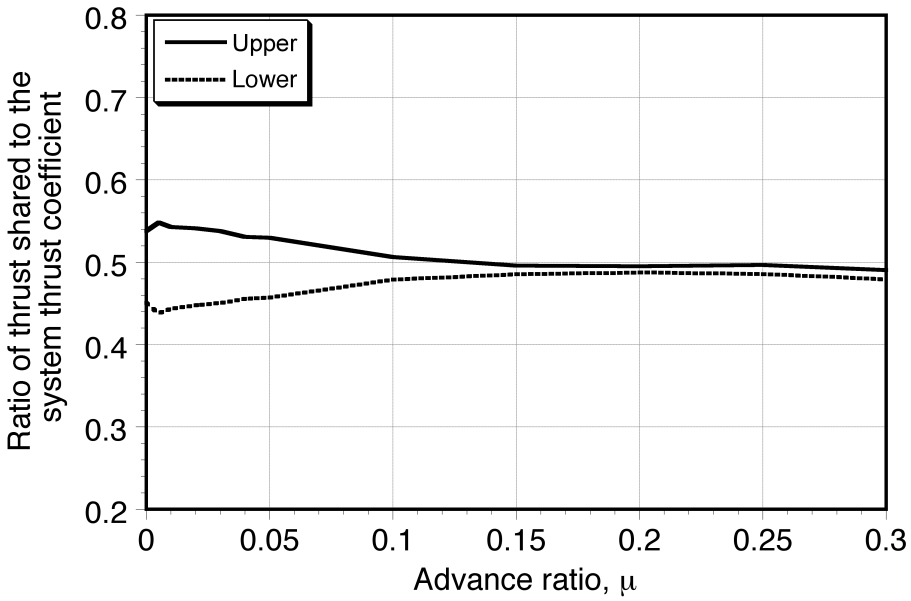

Fig. 4.99: Variation of the ratio of thrust shared by both rotors of the Harrington Rotor 1 with advance ratio at $C_T = 0.0048$ with tip speed of 469 ft/s.

hover. Therefore, blade planform was not considered as an optimization parameter in the forward flight optimization. A preliminary parametric study was conducted by changing the linear twist rates on both the rotors from $+10°$ (nose-up) to $-30°$ (nose-down) in steps of $5°$. The variation of the power required averaged over one rotor revolution with the changes in the blade twist on upper and rotors, is shown in Fig. 4.100. The baseline geometry is the Harrington Rotor 1 system with untwisted blades on both the rotors. As nose-up twist increases, the power required also increases as compared to that of the baseline geometry. With an increase in nose down twist rates on both the rotors, the total power required decreases. However, with higher nose down twist rates on both the rotors, the power required becomes almost insensitive to the changes in blade twist. This means that the optimum

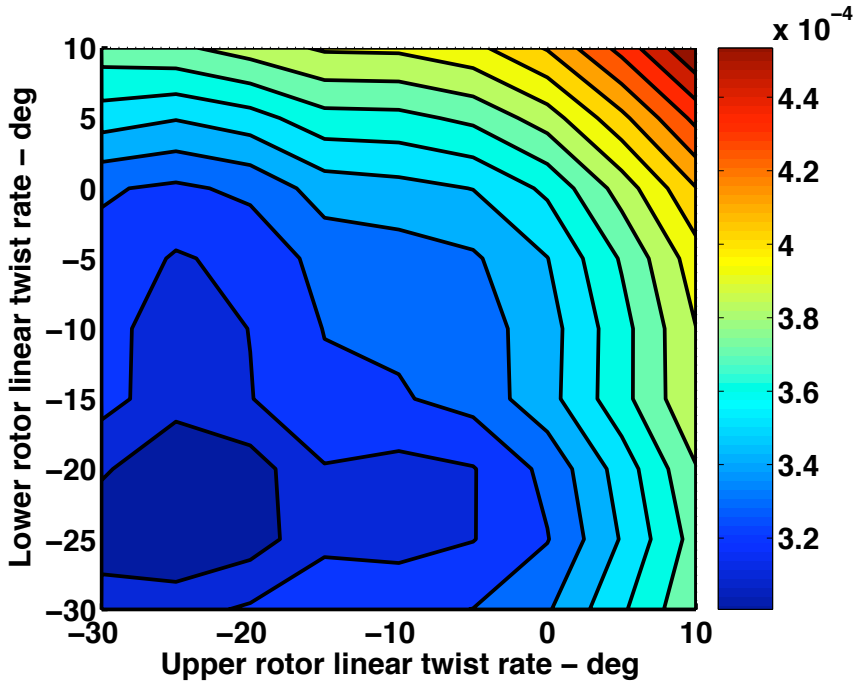

Fig. 4.100: Contour plot showing the variation of total power C_P required for the baseline Harrington Rotor 1 with changes in twist rates on upper and lower rotors at $C_T = 0.0048$, tip speed of 469 ft/s, and advance ratio of 0.25.

configuration obtained in the hover condition should also provide good performance in forward flight.

Furthermore, notice from Fig. 4.100 that results shown in the contour map are almost symmetric about the line on which the twist rates on both the rotors are the same. This shows that at an advance ratio of 0.25, the total power required is same, irrespective of the twist provided to the upper rotor or to the lower rotor. This also means that the aerodynamic interference between the two rotors has reduced significantly at this advance ratio, and the two rotors are more or less working without mutual aerodynamic interference.

The parametric study showed that the total power required becomes almost insensitive to the changes in blade twist at larger values, therefore the optimum obtained from the hover calculations (i.e., twist rate of -18° on upper rotor and -3° on lower rotor) should show good performance in forward flight as well. A comparison of the forward flight performance between the baseline geometry (i.e., untwisted blades on both rotors), hover optimum geometry, and a coaxial rotor system with higher twists equal to -20° on both the rotors is made shown in Figs. 4.101(a), 4.101(b) and 4.102. The results showed that the coaxial rotor designed for maximum performance in hover also requires lower power at higher forward speeds. In fact, such a design reduces the power required by 14% at an advance ratio of 0.25 compared to the baseline coaxial rotor system. The coaxial rotor system with equal twist rates on both the rotors required 7.5% higher power in hover compared to the optimum hover geometry, whereas it required lower power at higher forward speeds, i.e., it required 7.5% lower power at an advance ratio of 0.25 compared to the optimum hover geometry. Also, the lift-to-drag ratio of the hover optimum design is higher at higher advance ratios compared to the baseline geometry as shown in Fig. 4.102. The lift-to-drag ratio of a blade design with nose-down blade twist of 20° on both the rotors is higher compared to baseline as well as hover optimum blade design. Also, notice that for equal twist design, the lift-to-drag is maximum at an advance ratio of 0.25, whereas for the other two designs it was maximum for an advance ratio of 0.2. This means that the speed for maximum range is higher for the blade design with equal twist rates.

Finally, a formal optimization can be attempted using the optimizer. It was

beyond the scope of this work to conduct this study in full detail. To start with, optimization can be performed at one advance ratio, and then it can be extended to the entire flight envelope. The design variable vector can be comprised of blade twist rates, taper ratios and root chord on both rotors, along with inter-rotor spacing distance, and can be written as

$$\mathbf{X} = \left\{\theta_{tw}^{u},\ TR^{u},\ c_0^{u},\ \theta_{tw}^{l},\ TR^{l},\ c_0^{l},\ s/R\right\} \tag{4.25}$$

The objective will be to minimize the average power required or to maximize the lift-to-drag ratio of the coaxial rotor system.

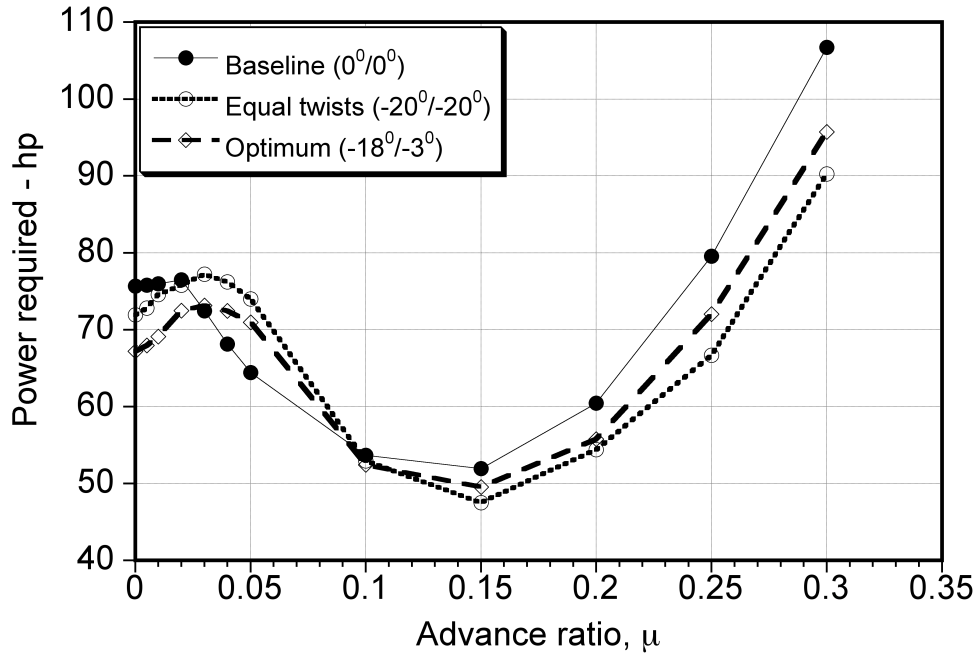

(a) Power required - hp

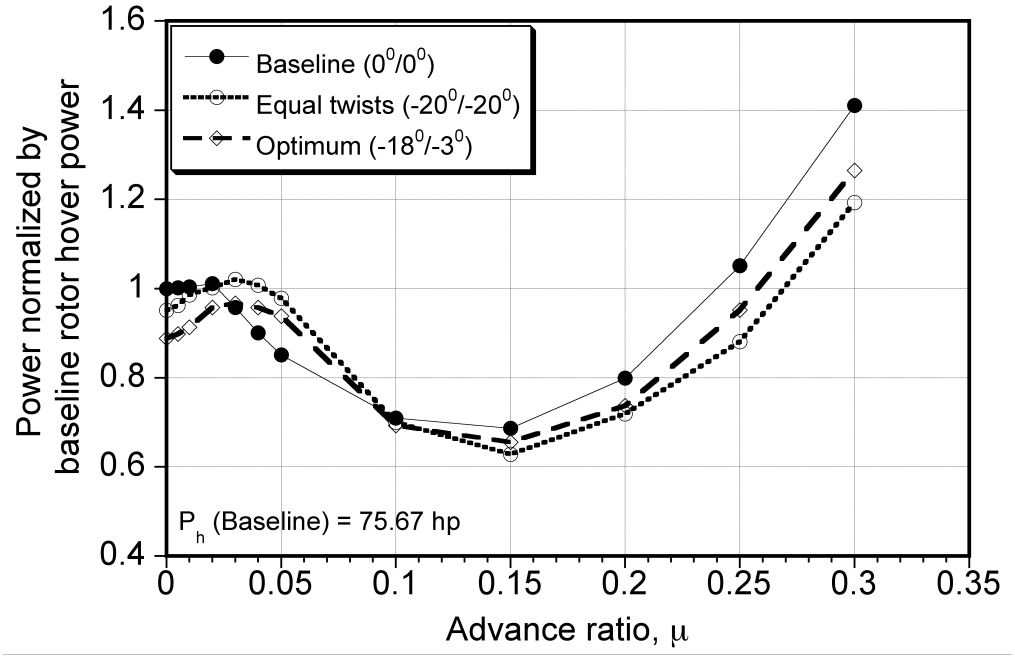

(b) Power required normalized with the baseline geometry hover power

Fig. 4.101: Variation of the power required for the baseline Harrington Rotor 1 with the hover optimum geometry and a coaxial system with equal blade twist rates ($-20°$) on both rotors with advance ratio, at $C_T = 0.0048$ and tip speed of 469 ft/s.

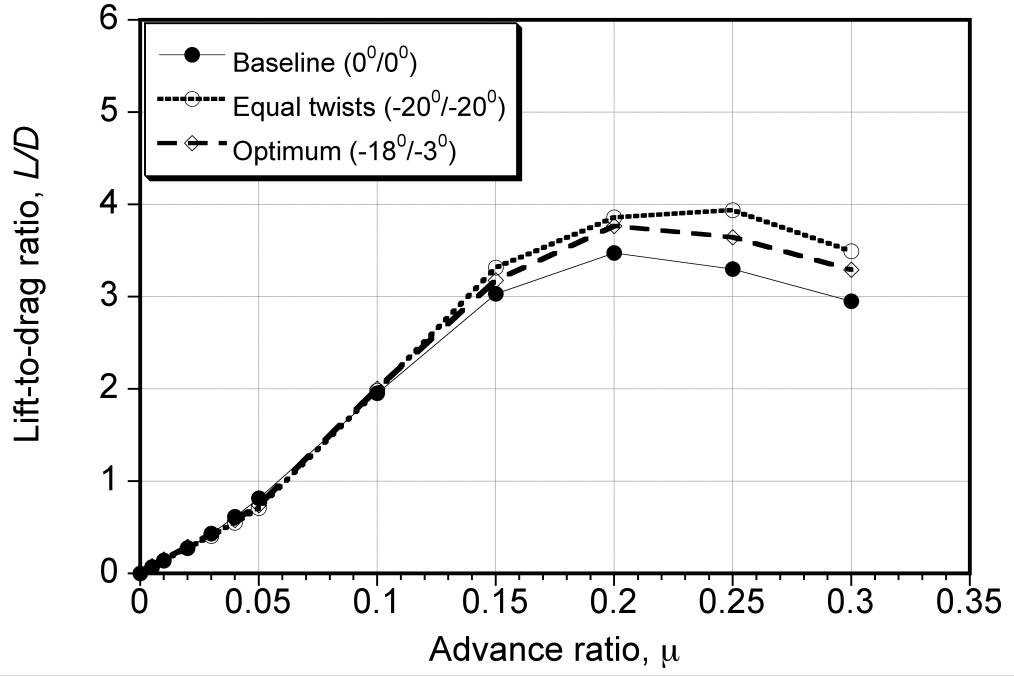

Fig. 4.102: Variation of the lift-to-drag ratio for the baseline Harrington Rotor 1 with the hover optimum geometry and a coaxial system with equal blade twist rates (i.e., $-20°$) on both rotors with advance ratio, at $C_T = 0.0048$ and tip speed of 469 ft/s.

Chapter 5

Conclusions and Future Work

This chapter summarizes the main observations and conclusions drawn from the results found in the present study, and also gives suggestions and recommendations for future work. The study reported in this thesis has attempted to further understand the aerodynamic complexities of counterrotating coaxial rotors, and to try to understand how to make profitable blade and rotor design changes to maximize the performance of a coaxial rotor in both hovering and forward flight. One thing is clear: because of rotor-on rotor flow interference effects, and the fact that a coaxial rotor system must generally operate at a torque balanced condition, then the two rotors of the coaxial system can operate at quite different aerodynamic conditions, especially in hovering flight. Because of these differences, to obtain a true optimum performing coaxial rotor system then the upper and lower rotors can be expected to require different design choices, i.e., different blade shapes.

Clearly, a general goal in maximizing the performance of a coaxial rotor system is to minimize the aerodynamic interference losses between the upper and lower rotors. To this end, parametric studies were conducted to study the effects of changes in inter-rotor spacings, blade twist rates, and blade planforms on the upper and lower rotors. A formal optimization process was also carried out by coupling a free-vortex wake method for the rotor aerodynamics with a set of design optimization tools,

the goal being to find the best rotor geometry (if any) that can give the highest figure of merit in hover and/or the minimum power required in forward flight at one or more forward speeds. The present study showed that the performance of the coaxial rotor system can indeed be increased significantly by changing the twist and planform distributions on both the rotors of the coaxial, and that the upper and lower rotors have different blade twists and planform shapes. However, it was also found that the blade twist distribution has a much more significant effect on the rotor performance compared to any changes in the blade planform shapes.

5.1 Conclusions

The following main observations and conclusions have been drawn from the present study:

1. The methodologies of the simple momentum theory (SMT), the blade element momentum theory (BEMT), and the free vortex wake methods (FVM) were all validated against experimental measurements of full-scale rotor performance for the NACA (Harrington) coaxial Rotors 1 and 2. Experimental measurements of coaxial rotor performance are very limited, the NACA measurements being the only full-scale results available. All of the predictive methods showed reasonably good agreement with the measurements, but the SMT generally under-predicted the power requirements compared to the other two methods. This can be expected, because the SMT incorporates several simplifying assumptions such as uniform inflow, approximations to non-ideal

losses, etc., that limit its capabilities as a predictive tool.

2. The primary value of the SMT (which is an ideal rotor theory) is that it can help set the performance goals needed to attaining maximum aerodynamic performance from a coaxial rotor, in that the interference losses cannot be reduced any further through blade design changes than is determined by the SMT. On one hand, the SMT shows that the induced losses resulting from the interference between the two rotors reach a minimum when the lower rotor operates in the fully developed slipstream of the upper rotor. On the other hand, the induced losses reach a maximum when the two rotors are very close to each other and so they essentially share the same value of induced flow.

3. The predictions of the spanwise airload distributions using the BEMT were validated against the FVM, which showed good overall agreement. These results showed that the BEMT could be used to provide good initial blade designs for the FVM to help reduce the number of rotor geometric iterations required, and so make any subsequent blade shape optimization process much faster. In the present analysis, the BEMT was coupled with the FVM both to provide initial conditions to find the blade pitch and trim state of the rotor system, and also to provide an initial blade design to start the optimization process.

4. The predicted wake structure from the FVM analysis showed that in the hover condition, a substantial fraction of the lower rotor lies in the slipstream of the upper rotor. This observation is used as an assumption within the SMT

and BEMT. Furthermore, the upper rotor wake seems to preserve its helical structure when it passes through the lower rotor but there are still interactions between the two flows. The slipstream of the upper rotor produced a higher inflow at the lower rotor, resulting in higher collective blade pitch angle on the lower rotor to satisfy the torque balance at given net system thrust. At the torque balanced condition, the ratios of the thrusts shared by the upper and lower rotors to the system thrust coefficient were found to remain relatively constant at approximately 55% and 45%, respectively.

5. All of the theories (the SMT, the BEMT and the FVM) showed that higher inter-rotor spacings is desired to reduce the induced losses of the coaxial rotor system in hover. With a higher inter-rotor spacing, a smaller fraction of the lower rotor lies in the slipstream wake generated by the upper rotor, and hence the induced losses of the system as a whole are reduced. Furthermore, it was shown that the effects of the lower rotor on the performance of the upper rotor reduces significantly at higher inter-rotor spacings. At a spacing distance of approximately 75% of the rotor radius, the interference between the two rotors can be minimized. However, this spacing may not be practical in that it will significantly increase rotor system weight. Higher inter-rotor spacings can also result in an increase parasitic drag from the rotor shafts (and exposed control linkages) at higher forward speeds, which will obviously limit the forward flight performance of any helicopter that uses a coaxial rotor system.

6. Parametric studies were performed to understand the effects of blade twist

changes on the performance of the coaxial system in hover. It was found that a larger nose down blade twist on the upper rotor was desired to minimize the induced losses of the coaxial system, whereas a lower nose down blade twist was required on the lower rotor to minimize the induced losses. This is because with higher blade twist rates the inflow increases more inboard and decreases outboard such that total inflow becomes more nonuniform on the lower rotor. It was shown that for the rotor configuration studied in this thesis, linear twist rates of -18° and -3° are required on the upper and lower rotors, respectively, to minimize the net induced losses on the coaxial rotor as a system.

7. Parametric studies were also performed to study the effects of planform changes on both the rotors. Different taper ratios and chord distributions (solidity distribution) were examined such that the total thrust weighted solidity of the coaxial system remained constant. An increase in the taper ratio on one rotor (keeping the root chord constant) decreases the taper ratio on the other to maintain constant thrust weighted solidity of the coaxial system. Increasing taper ratio on one rotor reduces its profile power but also increases the power required on the other rotor. The relative values of the induced powers on the two rotors also change to balance the torque of the system. As a result, the total power of the system was found not to vary significantly with changes in blade planform. However, it was also found that the stall margins of the coaxial rotor system can be improved significantly by 14% (i.e., from 0.08 on the baseline geometry to 0.07) by increasing the solidity on the upper rotor

to 0.029 and reducing it on the lower rotor to 0.025, compared to the baseline geometry with solidities equal to 0.027 on both of the rotors.

8. A formal blade shape optimization was also performed by coupling the BEMT with an optimizer (DOT). The BEMT, which is a two-dimensional model, is computationally efficient to perform such an optimization. However, its use as an aerodynamic tool is limited because of the various simplifying assumptions used in its formulation. The idea of approaching the optimization using the BEMT was to understand the process, and then extend the approach to modeling the aerodynamic interference using the FVM. For blade shape functions comprising of linear twist rates, the BEMT gave a global optimum of -9° and -12° blade twists on upper and lower rotors, respectively, with a corresponding increase of about 4% in the hovering figure of merit. When the rotors were twisted nonlinearly, the optimizer generated several local maxima, depending upon the initial blade design used. The maximum increase in the figure of merit with nonlinear blade twist distributions was found to be 4.5% higher than for the baseline rotor. This preliminary analysis showed that the optimization of the coaxial geometry was a non-convex problem, i.e., it had many local optima corresponding to blade design solutions that gave nearly the same levels of aerodynamic efficiency.

9. The optimization results obtained by coupling the MFW with DOT gave the optimum linear twist on upper and lower rotors as -17.26° and -3.08°, respectively, which were consistent with the results found from the parametric

studies. The rotor figure of merit obtained in this case was about 17% higher than for the baseline blade geometry, which used untwisted blades. Nonlinear twist shape functions using six and eight design variables were also tested using the initial designs provided by the BEMT. The FVM also showed that several different combinations of blade twist could lead to comparable levels of aerodynamic efficiency, with a maximum 18% increase in the figure of merit as compared to the baseline geometry. This means that there was no single optimum coaxial rotor geometry that gives good hover performance. However, the results showed that there is no increase in the figure of merit by twisting blades nonlinearly compared to the linear twist distribution.

10. Overall, increases in hovering efficiency of up to 18% were found possible relative to a baseline rotor with untwisted blades. This is significant, as it could result in an increase in the payload carrying capability of a coaxial rotor helicopter by 35% or more, or an equivalent increase in the fuel load (i.e., for longer range and/or endurance). However, the price to pay for more efficient coaxial system with dissimilar blades and rotors would be higher manufacturing costs. Future studies will have to focus on a better examination of the various design tradeoffs in such a concept.

11. A study was also conducted to predict the performance of a coaxial rotor at different forward speeds. The results showed that the interference between the two rotors reduces with an increase in forward speed, as the wakes from the two rotors become less intermingled. At higher forward speeds, the wakes from

the upper and lower rotors appear more and more like isolated rotor wakes, and the performance of the rotors becomes more similar.

12. Parametric studies were also conducted to understand the effects of changes in the blade twist rates on upper and lower rotors at an advance ratio of 0.25. The results again showed that at this advance ratio, the two rotors behave more as isolated rotors. It was also found that at higher nose down blade twist rates, the total power required becomes almost insensitive to the changes in the twist rate. Therefore, the best blade geometry obtained in hover should also give better performance in forward flight compared to a rotor system using untwisted blades. The forward flight calculations performed on the best hover geometry (i.e., $-18°/-3°$) indeed showed a 14% reduction in the power required in forward flight at low to moderate airspeeds.

13. It can be concluded from this study that although there is no one geometry that can provide "best" performance in *both* hover and forward flights, but there can be one geometry that can provide "optimum" performance in both flight conditions. In this case, the hover optimum blade design also provided significant performance benefits in forward flight at higher advance ratios.

5.2 Future Work

The present work has provided significant insight into the problem of optimizing the shapes of the blades of coaxial rotor to better its performance in both hover and forward flight. While some questions have been answered in that the results have

shown that design optimization can result in improved levels of aerodynamic performance, especially in forward flight, there still remains several unanswered questions. These questions include the efficacy of the validation with measurements, and the trades in performance between rotor designs that are optimized for hover versus forward flight. To this end, this section presents some suggestions for future work.

1. Validation of the aerodynamic modeling tools remains incomplete. In particular, while the performance of a coaxial rotor (thrust and power) can be predicted quite well, there are still questions about the ability to accurately predict the details of the interfering wake and the spanwise loadings on the blades. Unfortunately, there are no experimental data available for the airload distributions on the two rotors of a coaxial system, except perhaps from some indirect measurements that were made by NACA on coaxial propellers. There are also a dearth of wake measurements, particularly those that show the interactions of the wakes from the upper and lower rotors as they develop in the downstream region. In the future, it is recommended that more experiments with coaxial rotor systems should be conducted, including measurements of the spanwise loads on the blades and the interfering wake structures, such as by using flow visualization and velocity field measurement methods.

2. In the present study, the far wake in the free vortex wake method was modeled by using only tip vortices (although provision of a full-span inner wake is provided in the FVM) to reduce the computational cost of the analysis. Including the full-span wake currently would have made the overall analysis

prohibitively expensive expected with only secondary benefits in predictive capability. However, in the future the aerodynamic performance of coaxial rotors should be further analyzed by considering the effects of the full-span wake. In this respect, fast multipole methods (Ref. 41) could be used to enhance the computational performance by reducing the number of velocity field evaluations.

3. In the present study, emphasis was placed on the optimization of the blade twist, planform shape, and inter-rotor spacing. Different airfoils can also be optimized on both rotors to provide maximum performance in forward flight. Blade shapes with forms of linear taper were examined, but more complex blade shapes could also be studied such as with nonlinear taper distribution on both the rotors. The only restriction is in the development of the appropriate shape functions to describe the blade planform. Furthermore, in the present analysis the blade radius on both of the rotors was held constant. Varying the radius of the upper and lower rotors might be a further way of minimizing interference effects, and so in further improving the overall efficiency of a coaxial rotor system. While the engineering involved in designing rotors with different diameters (and different rotational speeds) will inevitably be more complicated and expensive than one using equal diameters, the trades between aerodynamic efficiency, weight, cost, etc. needs to be carefully explored. Alternate rotor design concepts like the syncropter (counterrotating intermeshing rotors on inclined shafts) can also be analyzed to study their

performance compared to parallel rotor coaxial design.

4. The problem of coaxial rotor optimization in forward flight has been only briefly examined in present work. The results suggest that while there may be some benefits in altering the shape of the blades for best forward flight performance, the range of conditions that the rotor must operate in suggests that there may be no one optimum that gives the best overall levels of aerodynamic efficiency. The real issue becomes, therefore, whether or not the rotor design choices made for best hovering performance are carried over into forward flight, or whether there are any adverse effects on performance. Similarly, the question is whether any best design in forward flight also retains an acceptable level of aerodynamic efficiency in hovering flight. Initial results suggest that these goals can be achieved, but there are other issues that need to be explored. This includes better validation of the aerodynamic modeling in forward flight.

Bibliography

[1] Boulet, J., *The History of the Helicopter as Told by its Pioneers 1907–1956*, Editions France-Empire, Paris, 1984.

[2] Liberatore, E. K., *Helicopters Before Helicopters*, Krieger Publishing, Malabar, FL, 1998.

[3] Lambermont, P., and Pirie, A., "Helicopters and Autogyros of the World," Cassel & Company Ltd., 1970.

[4] Chaney, M. C., "The ABC Helicopter", *Journal of the American Helicopter Society*, 14, (4), pp. 10–19, 1969.

[5] Lambert, M., "The Soviets explain the Ka-32 Helix," Interavia, Aug., 1985.

[6] Preator, R., Leishman, J. G., and Baldwin, G. D., "Conceptual Design Studies of a Mono Tiltrotor (MTR) Architecture," American Helicopter Society International 60th Annual Forum Proceedings, Baltimore, MD, June 7–11, 2004.

[7] Preator, R., Leishman, J. G., and Baldwin, G. D., "Performance and Trade Studies of a Mono Tiltrotor (MTR) Design," Proceedings of the 61st Annual Forum of the American Helicopter Society International, Grapevine, TX, June 1–3, 2005.

[8] Pines, D. J., and Bohorquez, F., "Challenges Facing Future Micro-Air-Vehicle Development, *Journal of Aircraft*, Vol. 43, (2), March–April, 2006, pp. 290–305.

[9] McAlister, K. W., Tung. C., Wilson, J. S., and Rand, O., "Experimental and Numerical Study of a Model Coaxial Rotor," American Helicopter Society International 62nd Annual Forum Proceedings, Phoenix, AZ, May 9–11, 2006.

[10] McAlister, K. W., and Tung. C., "Experimental Study of a Hovering Coaxial Rotor With Highly Twisted Blades," American Helicopter Society International 64th Annual Forum Proceedings, Montréal, Canada, April 29–May 1, 2008.

[11] Bohorquez, F., "Rotor Hover Performance and System Design of an Efficient Coaxial Rotary wing Micro Air Vehicle," Ph.D. dissertation, Department of Aerospace Engineering, University of Maryland, College Park, Maryland, 2007.

[12] Bagai, A., "Aerodynamic Design of the X2 Technology Demonstrator Main Rotor Blade," American Helicopter Society International 64th Annual Forum Proceedings, Montréal, Canada, April 28–May 1, 2008.

[13] Coleman, C. P., "A Survey of Theoretical and Experimental Coaxial Rotor Aerodynamic Research," 19th European Rotorcraft Forum Proceedings, Cernobbio–Como, Italy, September 14–16, 1993. Also published as NASA TP-3675, March 1997.

[14] Harrington, R. D., "Full-Scale Tunnel Investigation of the Static Thrust Performance of a Coaxial Helicopter Rotor," NACA Technical Note 2318, 1951.

[15] Dingeldein, R. C., "Wind Tunnel Studies of the Performance of a Multirotor Configurations," NACA Technical Note 3236, 1954.

[16] Andrew, M. J., "Coaxial Rotor Aerodynamics in Hover," *Vertica*, Vol. 5, 1981, pp. 163–172.

[17] Saito, S., and Azuma, S., "A Numerical Approach to Coaxial Rotor Aerodynamics," 7th European Rotorcraft Forum Proceedings, Garmisch–Partenkirchen, Germany, September 8–11, 1981.

[18] Zimmer, H., "The Aerodynamic Calculation of Counter Rotating Coaxial Rotors," 11th European Rotorcraft Forum Proceedings, London, England, September 10–13, 1985.

[19] Valkov, T., "Aerodynamic Loads Computation on Coaxial Hingeless Helicopter Rotors," Paper AIAA 90-0070, 28th Aerospace Sciences Meeting, Reno, NV, January 8–11, 1990.

[20] Leishman, J. G., and Ananthan, S., "Aerodynamic Optimization of a Coaxial Proprotor," American Helicopter Society International 62nd Annual Forum Proceedings, Phoenix, AZ, May 9–11, 2006.

[21] Bagai, A., and Leishman J. G., "Free-Wake Analysis of Tandem, Tilt-Rotor and Coaxial Rotor Configurations," *Journal of American Helicopter Society*, Vol. 41, (3), 1996, pp. 196–207.

[22] Leishman, J. G., Bhagwat, M. J., and Bagai, A., "Free-Vortex Filament Methods for the Analysis of Helicopter Rotor Wakes," *Journal of Aircraft*, Vol. 39, No. 5, September–October, 2002, pp. 759–775.

[23] Kim, H. W., and Brown, R. E., "Coaxial Rotor Performance and Wake Dynamics in Steady and Manoeuvring Flight," American Helicopter Society International 62nd Annual Forum Proceedings, Phoenix, AZ, May 9–11, 2006.

[24] Lakshminarayan, V. K., and Baeder, J. D., "Computational Investigation of Coaxial Rotor Aerodynamics in Hover," American Helicopter Society Specialist's Conference Proceedings on Aeromechanics, San Francisco, CA, January 23–25, 2008.

[25] Leishman, J. G., *Principles of Helicopter Aerodynamics*, Cambridge University Press, New York, 2006.

[26] Leishman, J. G., and Syal, M., "Figure of Merit Definition for Coaxial Rotors," *Journal of the American Helicopter Society*, Vol. 53, (3), July 2008, pp. 290–300.

[27] Leishman, J. G., and Ananthan, S., "An Optimum Coaxial Rotor System for Axial Flight," *Journal of the American Helicopter Society*, Vol. 54, (1), January 2009, pp. xx–xx.

[28] Froude, W., "On the Elementary Relation Between Pitch, Slip and Propulsive Efficiency," *Transactions of the Institute of Naval Architects*, 19, 1878, 00. 47–57.

[29] Gessow, A., "Effect of Rotor-Blade Twist and Plan-Form Taper on Helicopter Hovering Performance," NACA Technical Note 1542, 1948.

[30] Bhagwat, M., and Leishman, J. G.,"Accuracy of Straight-Line Segmentation Applied to Curvilinear Vortex Filaments," *Journal of the American Helicopter Society*, Vol. 46, No. 2, April 2001, pp. 166–169.

[31] Bagai, A., *Contributions to the Mathematical Modeling of Rotor Flow-Fields using a Pseudo-Implicit Free-Wake Analysis*, Ph.D. Thesis, University of Maryland, College Park, Maryland, 1995.

[32] Ananthan, S., *Analysis of Rotor Wake Aerodynamics During Maneuvering Flight Using a Free-Vortex Wake Methodology*, Ph.D. Thesis, University of Maryland, College Park, Maryland, 2006.

[33] Beddoes, T. S., "Representation of Airfoil Behavior," *Vertica*, Vol. 7, No. 2, 1983, pp. 183–197.

[34] Ananthan, S., *The Role of Filament Stretching in the Free-Vortex Modeling of Rotor Wakes*, M.S. Thesis, University of Maryland, College Park, Maryland, 2008.

[35] Bhagwat, M. J., *Mathematical Modeling of the Transient Dynamics of Helicopter Rotor Wakes Using a Time-Accurate Free-Vortex Model*, Ph.D. Thesis, University of Maryland, College Park, Maryland, 2001.

[36] Batchelor, G. K., *An Introduction to Fluid Dynamics*, Cambridge University Press, England, 1967.

[37] Johnson, W., *Helicopter Theory*, Princeton University Press, 1980.

[38] Vanderplaats, Garret N., *Numerical Optimization Techniques for Engineering Design*, McGraw-Hill, Inc., 1984.

[39] Taylor, M. K., "A Balsa-Dust Technique for Air-Flow Visualization and Its Application to Flow Through Model Helicopter Rotors in Static Thrust," NACA Technical Note 2220, 1950.

[40] McAlister, K. W., Tung, C., Wilson, J. S., and Rand, O., "Experimental and Numerical Study of a Model Coaxial Rotor," American Helicopter Society International 62nd Annual Forum Proceedings, Phoenix, AZ, May 9–11, 2006.

[41] Greengard, L., and Rokhlin, V., "A New Version of the Fast Multipole Method for the Laplace Equation in Three Dimensions," *Acta Numerica 6*, pp. 229–269, 1997.